PHD

Advanced Studies of Membrane Fouling

Investigation of Cake Fouling Using Fluid Dynamic Gauging

Lewis, William

Award date:
2015

Awarding institution:
University of Bath

Advanced Studies of Membrane Fouling: Investigation of Cake Fouling Using Fluid Dynamic Gauging

William James Towry Lewis

A thesis submitted for the degree of Doctor of Philosophy

University of Bath
Department of Chemical Engineering

November 2014

Declaration of Authorship

This is all my own work except where I have indicated via references or other forms of acknowledgement.
Experimental work performed with or by other researchers is as follows:

Chapter 5: electron micrographs and one set of experimental results were collected by MEng project students, Matthew Wilcox and Robert Chance, under supervision from this author.

Chapter 7: Work performed on lignin filtrations was conducted in partnership with Dr Tuve Mattsson of Chalmers University of Technology, Gothenburg, Sweden. Some experimental work for which results are detailed in section 7.5 was performed by MEng project students, Alexandra Agg and Adam Clarke, under supervision from this author.

Signature:

Date:

Abstract

Membrane filtrations are widely used in process industries but are almost always limited by fouling, a highly studied and significant problem. This is defined as unwanted material deposited on a membrane surface or within its pores, which can significantly impair performance and/or reduce operating life. The strategies to mitigate fouling include cleaning in place, modified membranes, and optimisation of operating conditions. In order to correctly select or target improvements to any such measures a detailed mechanistic understanding of the fouling process is important, which requires more than just performance data from unit operations. One key mechanism is that of cake fouling, which describes the build-up of particle layers on the surface of the membrane. Its growth and physical properties are difficult to assess.

In this project the technique of fluid dynamic gauging (FDG) has been explored as a means to study cake fouling. This simple, yet robust method allows for estimation of thickness and strength of cake fouling at high concentrations and opacity, without any prerequisite knowledge of feed properties. Studies described herein focused on microfiltrations through cellulosic membranes. FDG was used to track cake growth during filtrations of polydisperse yeast suspensions (which contained large agglomerates), demonstrating its capability to work with non-ideal, food-like substances. Later studies used more predictable suspensions of hollow glass spheres, which were used to assess various filtration models. The most effective was found to be an interpretation of the critical flux laws, which were used to successfully identify pore fouling during filtrations of Kraft lignin, an observation supported by FDG measurements.

Another novel achievement of this project was the development of an automated apparatus for performing FDG in cross-flow membrane filtration. This allowed for much faster acquisition of results, and demonstrated the potential for its development into an autonomous system capable of making thickness measurements on the fly during filtrations. The most reliable protocol for determining cake growth rates was by repeated filtrations in which destructive thickness testing was performed at selected time points. This was because continuous or even repeated thickness measurements during a single filtration were found to cause too much disturbance to the fouling layer.

Computational fluid dynamics was used to simulate shear stress profiles on the fouling layer, while also providing a more accurate means to calibrate the automated apparatus. Erosion caused by FDG readings, when viewed under a microscope, was found to conform to the shear stress profiles predicted by simulations.

Acknowledgements

I would like to express my sincerest gratitude to both my supervisors, Drs Y. M. John Chew and Michael R. Bird. Their support and guidance has been invaluable to me over the course of my PhD. I would also like to thank Dr Tuve Mattsson of Chalmers University of Technology in Gothenburg, Sweden, with whom I collaborated on some experimental studies detailed in this thesis. I am also particularly grateful for the resources which were provided by his institution and hope for further collaborative endeavours between Chemical Engineering at Bath and the Forest Products and Chemical Engineering group at Chalmers. I am also very grateful to the project students, Matthew Wilcox, Robert Chance, Alexandra Agg, and Adam Clarke, who obtained some of the data reported herein.

I am indebted to a number of technical staff at the university; particularly Paul Frith and John Bishop, who were instrumental in the production of a new piece of advanced apparatus. I have also received help and support from Fernando Acosta, Robert Brain, Suzanne Berkeley, Marianne Harkins, Daniel Lou-Hing, and Alex Cuipa.

Some equipment, support and advice was provided by the Department of Chemical Engineering and Biotechnology at the University of Cambridge. I am grateful in particular to Dr Ian Wilson, who allowed me to use some equipment there, as well as donating a piece of experimental apparatus for my work. Dr Patrick Gordon also very kindly provided help and advice on setting up and programming with LabView™.

There are countless colleagues and friends who have enriched my experience since I joined the university in 2010. They are too numerous to list completely here; although I would like to express my appreciation to Dr Sarah Jones, Iain Argyle, Peter Bechervaise, Dr Hannah Leese, Dr Kah Peng Lee, and Corinne Jeffs who all provided help and advice from the moment I began.

Finally my parents, siblings and friends deserve my thanks for all their love, support and understanding during my PhD.

Image removed for copyright purposes. Original image can be found at:
http://www.phdcomics.com/comics/archive.php?comicid=1139

"I seldom end up where I wanted to go, but almost always end up where I need to be."
Douglas Adams

Nomenclature

Roman

A_m	Membrane surface area	m^2
A, B, C, D	Constants used in parametric fits	-
C_d	Discharge coefficient	-
c	Particle/solute concentration	$kg \cdot m^{-3}$
c_b	Bulk particle/solute concentration	$kg \cdot m^{-3}$
c_m	Particle/solute concentration at the membrane	$kg \cdot m^{-3}$
c_p	Permeate particle/solute concentration	$kg \cdot m^{-3}$
$\widehat{D}[\phi]$	Diffusivity coefficient	-
D_{CP}	Diffusion coefficient for concentration polarisation	$m^2 \cdot s^{-1}$
D_S	Shear-induced diffusivity	$m^2 \cdot s^{-1}$
D	Duct width	m
d	Gauge tube inner diameter	m
$d_{3,2}$	Sauter mean diameter (of particle)	m
$d_{4,3}$	Volume mean diameter (of particle)	m
d_p	Particle diameter	m
d_t	Gauge nozzle throat diameter	m
$d_{V,i}$	Volume% cut-off diameter	m
F_N	Normal force on particle	N
F_R	Resistance force (to particle motion)	N
F_T	Tangential force on particle	N
g	Acceleration due to gravity	$m \cdot s^{-2}$
Ga	Galileo Number	-
h_0	Clearance of gauging nozzle from substrate	m
h_g	Height of the gauge tube exit used in CFD simulations	m
h	Clearance of gauging nozzle from a surface	m
H	Duct height	m
$h_{0,offset}$	Offset position of the membrane from $h_0 = 0$	m
$h_{0,Mi}$	Gauge position indicated by micrometer	m
J	Permeate flux	$m \cdot s^{-1}$
J^*	General limiting flux constant	$m \cdot s^{-1}$

J'_{rec}	Dimensionless flux recovery by rinsing	-
J_0	Initial flux	$m \cdot s^{-1}$
J_∞	Steady-state flux	$m \cdot s^{-1}$
J_{crit}	Critical flux	$m \cdot s^{-1}$
J_{final}	Flux at the end of an experiment	$m \cdot s^{-1}$
J_{rinse}	Flux following rinsing under relaxation	$m \cdot s^{-1}$
J_T	Transition flux (for a change between fouling mechanisms	$m \cdot s^{-1}$
K	Kozeny constant	-
k	Coefficient for flux decline models	(varies)
k'_c	Cake filtration constant	$m \cdot s \cdot kg^{-1}$
k_{CP}	CP mass transfer coefficient	$m \cdot s^{-1}$
L	Duct length	m
l_{eff}	Effective pipe length	m
M_c	Cake mass	kg
M_g	Mass of fluid from gauge	kg
m_g	Gauging mass flowrate	$kg \cdot s^{-1}$
M_p	Mass of permeate collected	kg
m_p	Permeate mass flowrate	$kg \cdot s^{-1}$
n	Power index for flux decline models	-
N_{array}	Array size (used in data acquisition)	-
N_{DOF}	Total number of degrees of freedom	-
n_s	Power law index for hindered settling	-
p	Pressure	Pa
p_{in}	Inlet pressure	Pa
p_{static}	Static pressure	Pa
Q_{duct}	Duct volumetric flowrate	$m^3 \cdot s^{-1}$
r	Radial distance from central axis of gauge tube	m
r, z	Coordinates in cylindrical space	m
R_c	Cake resistance	m^{-1}
R_{CP}	Concentration polarisation resistance	m^{-1}
Re_{duct}	Duct flow Reynolds number	-
R_f	Total fouling resistance	m^{-1}
$R_{f,final}$	Total fouling resistance at the end of an experiment	m^{-1}

$R_{f,rinse}$	Total fouling resistance following rinsing under relaxation	m^{-1}
R_m	Membrane resistance	m^{-1}
R_p	Pore fouling resistance	m^{-1}
R_{rev}	Resistance of fouling layer reversible by rinsing	m^{-1}
R_T	Total resistance	m^{-1}
S	Constant rate of back-transport from cake layer	$kg \cdot m^{-2} \cdot s^{-1}$
s	Nozzle rim width	m
S_i	Software controlled scale factor at a node	-
S_v	Surface area per unit volume	m^{-1}
t	Time	s
TMP	Transmembrane pressure	Pa
$t_{residence}$	Residence time	s
$\boldsymbol{u}$	Velocity vector	$m \cdot s^{-1}$
u	Velocity in x or r direction	$m \cdot s^{-1}$
$\bar{u}$	Superficial velocity through a packed bed	$m \cdot s^{-1}$
$u_{p,\infty}$	Particle terminal velocity	$m \cdot s^{-1}$
u_w	Slip velocity	$m \cdot s^{-1}$
V	Filtered volume	m^3
v	Velocity in y direction	$m \cdot s^{-1}$
v_{av}	Average y-wise velocity	$m \cdot s^{-1}$
v_{IL}	Inertial lift velocity	$m \cdot s^{-1}$
v_{max}	Maximum y-wise velocity	$m \cdot s^{-1}$
w	Velocity in z direction	$m \cdot s^{-1}$
w_{av}	Average z-wise velocity	$m \cdot s^{-1}$
w_{max}	Maximum z-wise velocity	$m \cdot s^{-1}$
x, y	Coordinates in Cartesian space	m
y	Distance in y direction	m
y^*	Dimensionless distance from membrane surface	-

Greek

ϕ	Particle volume fraction	-
σ	blocked surface area per unit volume of permeate	m^{-1}
μ	Viscosity	$kg \cdot m^{-1} \cdot s^{-1}$
κ	Permeability	m^2

ε	Packed bed porosity (void fraction)	-
δ	Deposit thickness	m
β	Surface friction coefficient	-
α	FDG nozzle angle	°
Π	Osmotic pressure	Pa
ϑ	Parameter for calculation of slip velocity	-
ω	Ratio of gap height to permeability squared	-
Δp_{ij}	Pressure drop between points i and j	Pa
Δp_c	Pressure drop across the cake	Pa
$\Delta p_{13,offset}$	Offset to gauge nozzle pressure drop	Pa
ϕ_w	Particle volume fraction at the wall	-
ϕ_c	Particle volume fraction of the cake	-
ϕ_b	Bulk particle volume fraction	-
ϕ_{ads}	Adsorbed particle volume fraction	-
φ_c	Specific cake resistance	$m \cdot kg^{-1}$
τ_w	Wall shear stress	$N \cdot m^{-2}$
$\tau_{w,max}$	Maximum wall shear stress	$N \cdot m^{-2}$
ρ_p	Particle wet density	$kg \cdot m^{-3}$
ρ_L	Fluid density	$kg \cdot m^{-3}$
κ_m	Membrane permeability	m^2
κ_c	Cake permeability	m^2
ε_m	Membrane surface porosity	-
δ_m	Membrane thickness	m
δ_m	Concentration polarisation layer thickness	m
δ_c	Cake thickness	m
$\dot{\gamma}$	Shear rate	s^{-1}
ρ	Density (of fluid, used in CFD)	$kg \cdot m^{-3}$
ε_{ij}	Strain rate tensor	-
τ_{ij}	Shear stress tensor	$N \cdot m^{-2}$

Acronyms

CA	Cellulose acetate
CFD	Computational fluid dynamics

CFV	Cross-flow velocity
CIP	Cleaning in place
CP	Concentration polarisation
CPU	Central processing unit
CSI	Chemical shift imaging
DOTM	Direct observation through the membrane
DVO	Direct visual observation
EIS	Electrical impedance spectroscopy
FDG	Fluid dynamic gauging
FDM	Finite difference modelling
FEM	Finite element modelling
FVM	Finite volume modelling
LVDT	Linear variable differential transformer
mAB	Monoclonal antibody
MF	Microfiltration
MWCO	Molecular weight cut-off
NF	Nanofiltration
NMR	Nuclear magnetic resonance
PA	Polyamide
PDE	Partial differential equation
PES	Polyethersulfone
PP	Polypropylene
PS	Polysulfone
PVDF	Polyvinylidene fluoride
RAM	Random access memory
RC	Regenerated cellulose
RO	Reverse osmosis
SEM	Scanning electron microscopy
sFDG	Scanning-mode fluid dynamic gauging
SID	Shear-induced diffusivity
TMP	Transmembrane pressure
UF	Ultrafiltration
UTDR	Ultrasonic time-domain reflectometry
VI	Visual interface

Contents

Declaration of Authorship ..... **I**
Abstract ..... **III**
Acknowledgements ..... **IV**
Nomenclature ..... **VI**
Contents ..... **XI**
List of Figures ..... **XVI**
List of Tables ..... **XIX**
List of Publications ..... **XX**

Chapter 1: Introduction **1**
1.1 Context **1**
1.2 Structure of this dissertation **2**
Chapter 2: Current state of the art **5**
2.1 Principles of membrane operations **5**
2.1.1 Types of membrane filtration operation 5
2.1.2 Membrane materials 6
2.1.3 Operating modes and configurations 7
2.2 Industrial applications of membrane separations **10**
2.2.1 Food and beverage processing 10
2.2.2 Pharmaceutical and White Biochemical Production 12
2.2.3 Water purification 14
2.3 Membrane Fouling and Cleaning **15**
2.3.1 Fouling 15
2.3.2 Cleaning 16
2.4 Modelling filtration and fouling **17**
2.4.1 Generalised filtration model 17
2.4.2 Estimating cake resistance, R_c 18
2.4.3 Concentration Polarisation 20
2.4.4 Modelling dead-end flux decline 22
2.5 Fouling models for cross-flow filtration **24**
2.5.1 Critical Flux Model 25
2.5.2 Particle Capture Model 26
2.5.3 Inertial Lift 28
2.5.4 Shear-induced Diffusivity 29
2.5.5 Summary 31
2.6 In-situ Methods for Monitoring Fouling Layer Development **31**
2.6.1 Direct Observation techniques 35
2.6.2 Laser Optics 37
2.6.3 Ultrasonic Time-Domain Reflectometry 39
2.6.4 Nuclear Magnetic Resonance (NMR) Imaging 40
2.6.5 Electrical Impedance Spectroscopy (EIS) 42
2.6.6 Radiation-based measurements 43
2.6.7 Summary 44

2.7 Fluid Dynamic Gauging (FDG) 46
2.7.1 Theory and Principles 46
2.7.2 Modes of operation 48
2.7.3 Strength measurement using FDG 49
2.7.4 Previous FDG studies 50
2.8 Conclusions 52
Chapter 3: Aims and Objectives 55
3.1 Aims 55
3.2 Objectives 56
3.2.1 Implementing the technique 56
3.2.2 Apparatus development 56
3.2.3 CFD studies 56
Chapter 4: Duct Flow Rig 59
4.1 Apparatus 59
4.1.1 FDG Gauge 59
4.1.2 Test section 59
4.1.3 Flow loop 61
4.1.4 Data Acquisition 61
4.2 Materials 62
4.2.1 Continuous media 62
4.2.2 Yeast Filtration 63
4.2.3 Ballotini filtration 65
4.3 Methods 68
4.3.1 Calibration 68
4.3.2 Yeast fouling experiments 69
4.3.3 Ballotini fouling experiments 72
4.4 Conclusion 75
Chapter 5: Results A – Yeast and ballotini filtration 77
5.1 Calibrations 77
5.2 Yeast Filtration 78
5.2.1 Flux decline 78
5.2.2 Destructive Thickness tests 82
5.2.3 Analysis of extracted cake 83
5.3 Ballotini fouling 86
5.3.1 Flux decline and thickness 86
5.3.2 Comparison of particle size/buoyancy 90
5.3.3 Visual inspection 92
5.3.4 Application of back-transport models 95
5.3.5 Critical flux model 98
5.4 Conclusions 103
Chapter 6: Automated Cross-flow Rig 105
6.1 Improved features of new apparatus 105
6.2 Apparatus 106
6.2.1 FDG gauge 106
6.2.2 Test Section 106
6.2.3 Flow loop 110
6.3 Data Acquisition 112
6.3.1 Wiring 113
6.3.2 Real-time data display and output 113
6.3.3 Stepper control system 116

6.3.4 Automated calibration 118
6.4 Summary of Experiments 121
6.4.1 TLF: Time-dependent Lignin Fouling 121
6.4.2 PLF: Pressure-dependent Lignin Fouling 121
6.4.3 BLF: Ballotini-Lignin mixture Fouling 121
6.5 Materials 121
6.5.1 Lignin Suspension 121
6.5.2 Membranes 124
6.6 Methods 125
6.6.1 Initial start-up 125
6.6.2 Calibration 125
6.6.3 Destructive thickness and strength testing 127
6.6.4 Cake extraction and weighing 127
6.6.5 Cleaning of apparatus 127
6.6.6 TLF studies 128
6.6.7 PLF studies 128
6.6.8 BLF studies 129
6.7 Conclusion 130
Chapter 7: Results and Discussion B: Lignin Fouling 131
7.1 Membrane calibrations 131
7.2 Thickness estimations from destructive testing 131
7.3 TLF studies 132
7.3.1 Data validation 132
7.3.2 Cake growth over time 134
7.3.3 Cake resistance 136
7.3.4 Cake volume fraction 138
7.3.5 Destructive thickness tests 140
7.3.6 Critical flux laws 143
7.4 PLF Studies 147
7.4.1 Data validation 147
7.4.2 Recovery flux and cake thickness 148
7.4.3 Fouling resistance 150
7.4.4 Destructive strength testing 152
7.4.5 Critical flux laws 154
7.4.6 Comparison with TLF studies 156
7.5 BLF Studies 157
7.5.1 Cake growth and flux decline 158
7.5.2 Destructive strength testing 161
7.6 Conclusions 163
7.6.1 Improvements to lignin filtration 163
7.6.2 Automation of FDG 164
Chapter 8: Computational Fluid Dynamics 165
8.1 Introduction 165
8.2 Components of numerical CFD modelling 165
8.2.1 Flow domain 165
8.2.2 Mathematical model 166
8.2.3 Coordinate systems 166
8.2.4 Discretisation methods 167
8.2.5 Computational grid (mesh) 167
8.2.6 Solution method and convergence tests 167
8.3 Numerical modelling applied to FDG 168

8.3.1 Equations solved 168
8.3.2 Discretisation method 169
8.3.3 Solver configuration and convergence criteria 169
8.4 Aims and Objectives 169
8.5 Simulation 1: duct flow with d_t = 1 mm gauge (Membrane flow) 171
8.5.1 Simulation parameters 172
8.5.2 Boundary Conditions 172
8.5.3 Finite element grid (mesh) 175
8.5.4 Results 176
8.6 Simulation 2: duct flow with d_t = 1 mm gauge (complete geometry) 179
8.6.1 Simulation parameters 179
8.6.2 Boundary Conditions 180
8.6.3 Finite element grid (mesh) 181
8.6.4 Results 181
8.7 Simulation 3: duct flow with d_t = 0.5 mm gauge 183
8.7.1 Simulation parameters 184
8.7.2 Boundary conditions 185
8.7.3 Mesh 186
8.7.4 Results 187
8.7.5 Conclusions 195
8.8 Simulation 4: 2D Axisymmetric flow with d_t = 0.5 mm gauge 196
8.8.1 Simulation Parameters 196
8.8.2 Boundary Conditions 197
8.8.3 Mesh 198
8.8.4 Results 199
8.9 Conclusions 203

Chapter 9: Conclusions and Future Perspectives 205
9.1 Implementation of FDG 205
9.1.1 Yeast, filtered by mixed cellulose ester membranes 205
9.1.2 Ballotini filtered by regenerated cellulose membranes 205
9.1.3 Lignin filtered by regenerated cellulose membranes 206
9.1.4 Mixed foulant systems filtered by regenerated cellulose membranes 207
9.1.5 Use of mathematical models 207
9.2 Limitations of current apparatus 208
9.2.1 Operating conditions 208
9.2.2 Membrane offset 210
9.2.3 Developing flow on a membrane surface 210
9.2.4 Limitations of the FDG procedure 210
9.3 Future studies using current apparatus 212
9.3.1 Optimisation of cross-flow lignin filtrations 212
9.3.2 Further investigations of pre-fouling layers 213
9.3.3 Fouling by TiO_2 particles 213
9.4 Future developments of membrane FDG devices 214
9.4.1 Enhancements to the automated FDG apparatus 214
9.4.2 Radial cross-flow FDG 218
9.4.3 Practical application in industry 220
9.5 Concluding Remarks 221

Chapter 10: Bibliography 223

Appendices

A. Derivations for calculations 2

A1. Calculation of ballotini particle density 2

A2. Correction for mass over-estimation 3

B. Algorithm for critical flux analysis 4

B1. Smoothing of flux data 4

B2. Processing of $f(J)$ 5

B3. Determine linear fit parameters where n = 0 5

B4. Determine linear fit parameters where n = 1 or 2 7

C. Membrane permeability tests 9

C1. Method 9

C2. Derivation for equation (A15) 10

D. Data acquisition and error calculation 11

D1. Data acquisition for duct flow rig 11

D1.1 Time, t 11

D1.2 Gauging flow, m_g: 12

D1.3 Permeate flow, m_p: 12

D1.4 Gauging pressure, Δp_{14}: 12

D1.5 Transmembrane pressure, TMP: 12

D1.6 Discharge Coefficient, C_d: 12

D1.7 Apparent height, h, and deposit thickness, δ_c: 13

D2. Data acquisition for automated cross-flow rig 13

D2.1 Time, t 13

D2.2 Data points specific to each variable, N_{var} 14

D2.3 Permeate flow, m_p 14

D2.4 Average differential pressure, Δp_{14} 14

D2.5 Average TMP: 14

D2.6 Gauging pressure, Δp_{13} 15

D2.7 Apparent height, h, and deposit thickness, δ_c: 15

D3. Error calculation for δ_c measurements 15

D4. Error calculation for τ_w 16

E. Design documents for automated cross-flow rig 17

List of Figures

Figure 2.1. Pore size and rejection behaviour of different membrane types. 5
Figure 2.2. Diagrams showing dead-end and cross-flow modes of operation 7
Figure 2.3. Process flow diagrams for filtration modes 8
Figure 2.4. Types of cross-flow membrane modules. 9
Figure 2.5. Publication trends 15
Figure 2.6. Concentration profile predicted during concentration polarisation. 21
Figure 2.7. Mechanisms of different fouling phenomena 23
Figure 2.8. Force balance on a particle resting against a porous surface 27
Figure 2.9. Diffusivity coefficients 30
Figure 2.10. Techniques for monitoring membrane fouling 35
Figure 2.11. Principles of laser-based fouling monitors 38
Figure 2.12. Principle of UTDR 39
Figure 2.13. Basic design of an EIS unit 42
Figure 2.14. Diagram of the apparatus used by Johansson and Theliander (2007) 43
Figure 2.15. Schematic and principles of FDG 46
Figure 2.16. General profile of C_d vs. h/d_t 48
Figure 4.1. Diagram and photograph of test section 60
Figure 4.2. Flow loop for duct flow apparatus 61
Figure 4.3. SEM Micrographs of mixed cellulose ester membrane 63
Figure 4.4. Microscope images of yeast suspension 65
Figure 4.5. Particle size distribution of yeast suspension 65
Figure 4.6. SEM Micrographs of *Schleicher & Schuell* RC59 membranes 66
Figure 4.7. Particle size distribution for Sphericel© 67
Figure 4.8. SEM micrographs of 110P8 ballotini particles 68
Figure 4.9. Example of determining $h_{0,offset}$ 70
Figure 4.10. Replacement of valve V2 with a weir. 72
Figure 5.1. Calibration plots for Δp_{13} discharge coefficient, C_d 77
Figure 5.2. Flux and TMP at operating TMPs of 35 mbar 79
Figure 5.3. Flux and estimated cake thickness against time during yeast filtration 80
Figure 5.4. Estimated thicknessand flux for filtrations using method M3 81
Figure 5.5. Estimated thickness, δ_c vs. $\tau_{w,max}$ 82
Figure 5.6. Side and overhead views of yeast fouling layer 83
Figure 5.7. SEM micrographs of the yeast fouling layer 85
Figure 5.8. Flux and estimated cake thickness against time 87
Figure 5.9. Final flux, and final estimated cake thicknessagainst TMP 87
Figure 5.10. Flux and estimated cake thickness against time 88
Figure 5.11. Summary of thickness tracking results using method M2 89
Figure 5.12. Flux and estimated cake thickness against time 90
Figure 5.13. δ_c vs. $\tau_{w,max}$ after 3600 s fouling 91

Figure 5.14. Cross-sections (perpendicular to flow) of fouling layer 93
Figure 5.15. Miscroscope image taken after fouling with 60P18 suspension 93
Figure 5.16. Miscroscope image and processing after fouling with 110P8. 94
Figure 5.17. δ_c vs. $\tau_{w,max}$, comparison with particle capture model 97
Figure 5.18. δ_c vs. $\tau_{w,max}$, comparison with inertial lift model 98
Figure 5.19. General trend seen in plots of $f(J)$ against J using equation (2.20) 99
Figure 5.20. Examples curves for $f(J)$ against J 100
Figure 5.21. $f(J)$ against J using equation (2.20) where n = 0 101
Figure 5.22. Transitional flux, J_T for filtrations of 60P18 ballotini 102
Figure 5.23. Gradient, k against initial flux, J_0 for filtrations of 60P18 ballotini 102
Figure 6.1. Schematic of the new gauge nozzle and dimensions 106
Figure 6.2. Schematic and photograph of the new test section 107
Figure 6.3. Photograph showing the components of the membrane cassette 109
Figure 6.4. Photograph, and schematic of the linear stepper assembly 110
Figure 6.5. Schematic and photograph of flow loop used with the new test section 111
Figure 6.6. Main VI window and data acquisition tab 114
Figure 6.7. Constants tab from the VI 115
Figure 6.8. Stepper controls for VI 117
Figure 6.9. Calibration tab used for automated calibration readings 119
Figure 6.10. Control flowchart for automated calibration procedure 120
Figure 6.11. Window and calibration curve used during automated calibration 120
Figure 6.12. Particle size distribution for lignin suspensions 123
Figure 6.13. SEM micrograph of *Whatman* RC58 membrane 124
Figure 6.14. Different types of filtration used in BLF studies 129
Figure 7.1. Repeat calibration readings during pure water filtration 131
Figure 7.2. Initial flux decline for lignin filtration at 100 mbar 132
Figure 7.3. Dry weight of cake per unit area against measured thickness 133
Figure 7.4. Cake thickness and flux vs. time. 134
Figure 7.5. Dry cake mass deposited and flux against time 135
Figure 7.6. Fouling resistanc against cake thickness. 137
Figure 7.7. Deposited mass of cake per unit area against measured thickness 139
Figure 7.8. δ_c vs. $\tau_{w,max}$ for lignin cakes. 140
Figure 7.9. Comparison between estructive thickness tests for lignin filtrations 141
Figure 7.10. Predictions for destructive strength testing for different mechanisms 142
Figure 7.11. $f(J)$ against J using (2.20) where $n = 0$ for a 2000 s filtration 144
Figure 7.12. $f(J)$ against J using equation (2.20) where $n = 1$, and $n = 2$. 145
Figure 7.13. Dry cake mass deposited and flux against time 146
Figure 7.14. Flux decline for lignin fouling experiments 147
Figure 7.15. Average flux after 2000 s filtration and recovery after rinsing 148
Figure 7.16. Mass of cake per unit area of membrane against measured thickness 149
Figure 7.17. Fouling resistance after rinsing against cake thickness 150
Figure 7.18. Contribution of different resistance mechanisms to total resistance 151

Figure 7.19. δ_c vs. $\tau_{w,max}$ for lignin cakes fouled at 50, 100, and 200 mbar TMP..... 153
Figure 7.20. Image and diagram of eroded region of lignin fouling layer..... 154
Figure 7.21. $f(J)$ against J using (2.20) where $n = 0$ for 2000 s filtrations 155
Figure 7.22. Comparison of flux decline behaviour between the TLF studies..... 157
Figure 7.23. Thickness and flux against time for mixture fouling M, B and BL..... 158
Figure 7.24. Images from of a fouling layer from BL experiments..... 159
Figure 7.25. Comparison of flux and thickness between M, TLF and B experiments 160
Figure 7.26. $\delta_c$vs. $\tau_{w,max}$ for M and BL experiments 162
Figure 8.1. Cartesian, cylindrical, and spherical coordinate systems 166
Figure 8.2. Examples of a structured, and unstructured mesh 167
Figure 8.3. Computational domain used to model duct flow FDG with a membrane . 171
Figure 8.4. Image of the mesh in the area around the gauge nozzle. 175
Figure 8.5. C_d vs. h/d_t from simulations and experiments..... 176
Figure 8.6. Simulated shear stress distributions at h/d_t = 0.15 and 0.25..... 177
Figure 8.7. Flux through the membrane just below the gauge at h/d_t = 0.06 178
Figure 8.8. Computational domain used to investigate flow disturbance..... 180
Figure 8.9. Streamlines and mean velocity profile 182
Figure 8.10. τ_w from simulation, along the surface representing the membrane.. 183
Figure 8.11. Computational domain used to model FDG in the new apparatus..... 184
Figure 8.12. Mesh configuration around the FDG nozzle region 186
Figure 8.13. Positioning of the additional radial lines on the y = 0 plane..... 187
Figure 8.14. 3D simulation results plotted against randomly selected calibrations..... 188
Figure 8.15. Simulated shear stress distributions at various h/d_t values..... 189
Figure 8.16. Simulated shear stress distributions at various h/d_t values..... 190
Figure 8.17. Simulations results vs. analytical model for $\tau_{w,max}$..... 191
Figure 8.18. Cylindrical coordinates of $\tau_{w,max}$ vs. h/d_t..... 192
Figure 8.19. 3D surface plots of simulated shear stress at various h/d_t values..... 193
Figure 8.20. Axisymmetric domain modelled in this simulation..... 196
Figure 8.21. Mesh structure for a simulation where h/d_t = 0.15..... 198
Figure 8.22. 2D and 3D simulation results for Δp_{13}, C_d vs. h/d_t 199
Figure 8.23. 2D axisymmetric simulation results for τ_w vs. r..... 201
Figure 8.24. Streamlines for a simulation at h/d_t = 0.15 showing 202
Figure 8.25. Simulation and analytical predictions for $\tau_{w,max}$ and r- coordinate..... 202
Figure 9.1. Presumed clearance, h, measured by FDG, over an uneven surface..... 211
Figure 9.2. Flowchart for end and fail sequences 216
Figure 9.3. Control flowchart for automated destructive strength tests..... 217
Figure 9.4. Concept schematic for a radial cross-flow FDG system. 219
Figure 9.5. Proposed implementation of FDG within an existing industrial process. . 220

List of Tables

Table 2.1. Typical properties of common polymeric membrane materials 6
Table 2.2 Examples of membrane use in industry 11
Table 2.3 Constants for equation (2.18) for three different fouling models 23
Table 2.4 Constants for equation (2.20) for three different fouling models 26
Table 2.5. Summary of in-situ methods for monitoring membrane fouling 33
Table 2.6. Comparison of FDG with other techniques 53
Table 4.1. List of inputs and outputs to and from the VI program 62
Table 4.2. Characterisation data for 5 μm mixed celloluse ester membranes 63
Table 4.3. Characterisation data for 0.6 μm regenerated cellulose membranes 66
Table 4.4. Particle size data for ballotini. 68
Table 4.5. Thickness tracking experiments 73
Table 5.1. Parameters used to fit experimental Δp_{13} vs h/d_t data to equation (5.1). ... 78
Table 6.1 Minimum, average, and maximum particle size data 123
Table 6.2. Characterisation data for 0.2 μm regenerated cellulose membranes 124
Table 7.1 Average values for the critical flux constants 154

List of Publications

Lewis, W.J.T., Chew, Y.M.J. & Bird, M.R. 2012a. The application of fluid dynamic gauging in characterising cake deposition during the cross-flow microfiltration of a yeast suspension. *Journal of Membrane Science,* 405–406**,** 113-122.

Lewis, W.J.T., Peck, O.P.W., Muir, A.C., John Chew, Y.M. & Bird, M.R. 2012b. The fouling and cleaning of surfaces in the food sector. *Food Science and Technology (London),* 26**,** 30-32.

Linkhorst, J. & Lewis, W.J.T. 2013. Workshop on membrane fouling and monitoring: A summary. *Desalination and Water Treatment,* 51**,** 6401-6406.

Mattsson, T., Lewis, W.J.T., Chew, Y.M.J. & Bird, M.R. In situ investigation of soft cake fouling layers using fluid dynamic gauging. *Food and Bioproducts Processing*. [In press, corrected proof]

Conference presentations

Lewis, W.J.T., Chew, Y.M.J. & Bird, M.R. 2011. Experimental and cfd studies of fluid dynamic gauging in cross-flow microfiltration systems, presented at *11th International Congress of Engineering and Food (ICEF11).* Athens, 22nd – 26th May 2011

Lewis, W.J.T., Chew, Y.M.J. and Bird, M.R., 2012, Investigating the influence of buoyancy on deposition and shear-induced removal during the cross-flow microfiltration of a model suspension, presented (by Chew, Y.M.J.) at *Suspension Processing & Suspension Engineering Rheology 2012*, Cambridge 10 – 11th September 2012.

Lewis, WJT, Chance, RMJ, Wilcox, MC, Chew, YMJ & Bird, MR, 2012, Investigations of Cake Fouling during the Cross-Flow Microfiltration of a Model Suspension: Influence of Buoyancy on Deposition and Shear-Induced Removal, presented at *Euromembrane 2012*, London, 23 – 27th September 2012.

Lewis, WJT, Wilcox, M, Chance, R, Chew, YMJ, and Bird, MR, 2013, Fluid Dynamic Gauging: A Practical Tool for Characterising Membrane Fouling (poster), presented at *ChemEngDayUK*, Imperial College London, 25 – 26th March 2013.

Mattsson, T., Lewis, W.J.T., Chew, Y.M.J. & Bird, M.R. (2014) In situ investigation of soft cake fouling layers using fluid dynamic gauging, presented (by Mattson, T.) at *Fouling and Cleaning in Food Processing 2014*, Cambridge, 31st March – 2nd April 2014

Chapter 1: Introduction

1.1 Context

A wide variety of industrial processes such as water purification, fractionation, solids removal or recovery, and dewatering can be performed using synthetic membrane filtrations. These membranes are selectively permeable barriers used to separate two fractions of a process stream based on size or sometimes electrochemical properties. In many cases this is the method of choice because it provides a more energy efficient alternative to conventional techniques such as evaporation, chromatography, or centrifugation; in some cases a more finely tuned selectivity can also be achieved (Foley, 2013). Over the past few decades, numerous advances and novel techniques have developed in the field of membrane technology (Al-Amoudi and Lovitt, 2007), and it is now a thriving industry (Freedonia, 2013).

Membrane fouling is defined as the deposition of solid particles or dissolved species on the external surface of a membrane which results in a decline in performance (Cui *et al.*, 2010). This is measured either by a reduction in the flowrate (commonly expressed as flux, J), or increase in the operating transmembrane pressure (TMP) required to achieve a constant flux. Industrial membrane operations employ a variety of cleaning methods to maintain performance which are often specific to individual processes (Li and Chen, 2010). It is also possible to ameliorate fouling by careful selection of operating conditions or the use of specially modified membranes with antifouling properties (Meng *et al.*, 2009).

Improvements to membrane cleaning protocols, operating conditions, and material modifications are best performed with an understanding of the fundamental fouling and/or cleaning mechanisms occurring at the surface or within the membrane. To do so requires advanced methods, which should ideally be capable of making in-situ, real time observations during a filtration. Here the technique of fluid dynamic gauging (FDG) is explored as a means to acquire information on the formation of filter cakes – fouling layers which develop on the surface of a membrane – in-situ and in real time during cross-flow microfiltrations. Not only is it capable of estimating fouling layer thickness, but also of assessing its cohesive and adhesive strength. In this work the methodology reported by previous researchers (Jones *et al.*, 2010b; Lister *et al.*, 2011) was refined, and new equipment has been developed with an aim towards producing an automated FDG measurement system. The capability of this device is reported, and it is

used to test mechanistic fouling models as well as providing information which can be used to inform potential improvements to specific membrane operations. As part of the development of this technique, computational fluid dynamics (CFD) was used to investigate otherwise immeasurable characteristics of the operation of FDG such as local fluid shear stress, velocity and pressures.

1.2 Structure of this dissertation

Chapter 2 gives an overview of membrane technology and the problem of fouling, as well as some of the current theory which describes the process. It also details other methods used to perform in-situ investigations of cake fouling. The technique of FDG is explained, along with a summary of the applications and advances since its original development.

Chapter 3 gives further detail to the aims of this work, and outlines the objectives through which they will be achieved.

Chapter 4 provides details of the experimental apparatus initially used in this work. This was a unit built to perform FDG measurements of cake fouling in cross-flow filtrations. Two studies were performed with this. The first was of the filtration of a yeast suspension, which demonstrated the applicability of FDG to membrane filtrations of food-type materials. The second was of inert spherical glass particles (ballotini), which present a much more ideal system to which mechanistic fouling models based on particle dynamics could be applied. The results of these studies are presented in Chapter 5, along with an assessment of the fouling models discussed in Chapter 2.

Chapter 6 details the design and operation of a new piece of FDG apparatus for cross-flow membrane filtrations. This FDG variant featured an automated system with enhanced precision compared to the original apparatus. The control systems in place are briefly discussed, as well as an account of the experimental methods used for studies in which it was employed. These studies focused on the fouling of a microfiltration membrane during filtrations of a suspension of Kraft lignin, a wood derivative. Some initial studies were also performed to identify the effect of combining the lignin suspension with ballotini particles. The results and discussion for this work are presented in Chapter 7, which also demonstrates how a combination of FDG and advanced data processing methods can elucidate the effect of different fouling mechanisms which occur during filtration.

Chapter 8 details the CFD studies used in this work to investigate aspects of FDG which would otherwise be very difficult to measure. These included the fluid

shear stress associated with strength measurements produced by FDG, and also predicted pressure profiles which were used directly in the operation of the new apparatus.

Chapter 9 closes the report with a summary discussion of the results produced in this work and also some perspectives on the future of FDG in membrane applications. This includes both recommendations for further work using the current apparatus, as well as a proposal for a new design of cross-flow membrane FDG system. The potential for FDG to be directly applied in an industrial setting is also discussed.

Chapter 2: Current state of the art

2.1 Principles of membrane operations

A membrane is a semipermeable barrier which selectively restricts the passage of suspended solids, dissolved solutes, or other chemicals. This can be based on size, molecular weight, or electrostatic characteristics of the rejected species. This allows for separations to take place with low energy input and at a finely tuned selectivity of products. Synthetic membranes, which are used in industrial separations (for which some examples are given in section 2.1.2), can be made from porous polymers, ceramics, metals, or even a liquid or gas phase (Mulder, 1996). They can have a homogeneous or heterogeneous structure, can carry electric charge, and be symmetric or include a support layer (asymmetric). Typically the driving force for flow through the membrane is transmembrane pressure (TMP).

2.1.1 Types of membrane filtration operation

Membrane filtration operations fall into four categories, namely: microfiltration (MF), ultrafiltration (UF), nanofiltration (NF), and reverse osmosis (RO), for which the size of rejected species decreases respectively. MF membranes are usually specified by pore size, whereas the others are generally described in terms of a molecular weight cut-off (MWCO) above which a particular membrane will reject macromolecules or particles of an equivalent size. Approximate pore size ranges and examples of rejected species are given in Figure 2.1. Smaller rejected species require use of a less permeable membrane with smaller pores, increasing the required operating pressure.

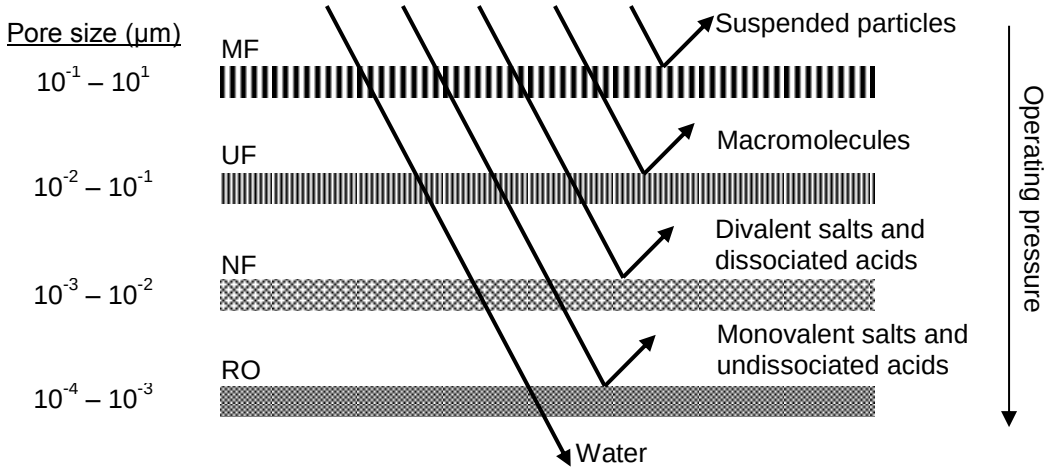

Figure 2.1. Pore size and rejection behaviour of different membrane types (Perry *et al.*, 1984). Operating pressure increases with decreasing pore size.

2.1.2 Membrane materials

In terms of their construction materials (leaving aside gas, liquid and metal membranes), membranes can be broadly categorised into two types: organic (polymeric) membranes, or inorganic (ceramic) membranes.

Organic (polymeric) membranes

Organic membranes can be made from a variety of polymers, some of which are listed in Table 2.1.

Table 2.1. Typical properties of common polymeric membrane materials (Cheryan and Cheryan, 1998; Cui *et al.*, 2010). Estimates for stable operating temperature readings are given based on available data. Chemical stability is a representation of how wide a pH resistance the material has and its tolerance of chlorine as well as range of resistances to various other cleaning agents.

Membrane material	Wetting property	Chemical stability	Thermal stability
Cellulose acetate (CA)	Hydrophilic	Poor	0-30°C
Regenerated cellulose (RC)	Hydrophilic	Medium	0-75°C
Polyamide (PA)	Hydrophilic	Medium	0-50°C
Polyethersulfone (PES)	Hydrophobic	Good	0-125°C
Polysulfone (PS)	Hydrophobic	Good	0-125°C
Polyvinylidene fluoride (PVDF)	Hydrophobic	Good	0-125°C
Polypropylene (PP)	Hydrophobic	Good	0-125°C

Hydrophilic membranes usually exhibit a higher flux and are less adsorptive, making them more resistant to fouling (Mulder, 1996). They are often less robust than hydrophobic membranes in terms of chemical and thermal stability however. The lower chemical resistance of the hydrophilic membranes, especially to chlorine, makes them less ideal where more intensive cleaning in place (CIP) protocols are required (Li and Chen, 2010). Cellulosic membranes (e.g. CA and RC) are cheap to produce (Cheryan and Cheryan, 1998) so periodic replacement can be more viable than using more robust, lower flux membranes. Hydrophobic membranes have significantly reduced flux compared with hydrophilic membranes but are the more common in process industries, especially in food processes where sterilisation protocols demand a higher chemical and/or thermal tolerance. An increasingly common practice is to coat membranes to

make them more hydrophilic. However such coatings can degrade over time (Li and Chen, 2010).

Inorganic (ceramic) membranes

Ceramic membranes have high mechanical strength and extremely high chemical and temperature resistance. For this reason they have a much greater lifespan and reliability compared with polymeric membranes. However they are also considerably more expensive (Cui *et al.*, 2010). They are commercially available as monolithic modules, of which the most common construction materials are γ-alumina, zirconia, and titania. Ceramic membranes will incur an approximate ten-fold increase in capital cost over polymeric systems but have been known to last over a decade, which might eventually recoup the difference (Cheryan and Cheryan, 1998).

2.1.3 Operating modes and configurations

There are two modes of operation in pressure-driven membrane systems, namely dead-end and cross-flow, the main features being shown in Figure 2.2. Dead-end filtrations (Figure 2.2a) are the simpler of the two, wherein all rejected material is deposited on the feed side of, or within the membrane. The preferred mode in a lot of cases is cross-flow (Figure 2.2b); here the feed flows parallel to the membrane surface, resuspending some of the rejected material, and exits in a more concentrated *retentate* stream. This allows sustained continuous operation, albeit with periodic cleaning measures required in a lot of cases (Richardson *et al.*, 2007b).

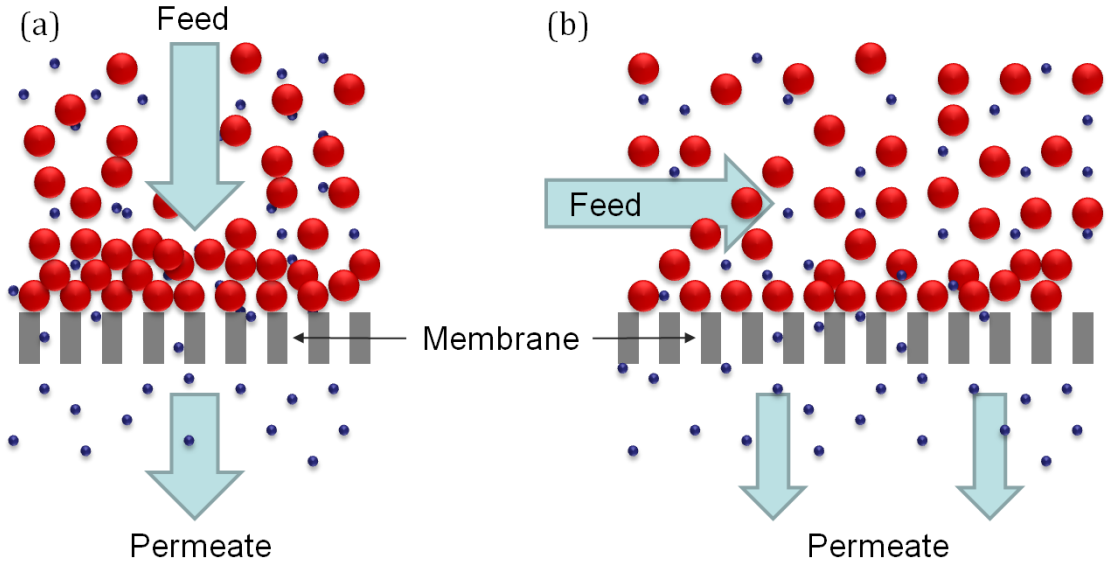

Figure 2.2. Diagrams showing (a) dead-end, and (b) cross-flow modes of operation

The way in which cross-flow filtrations are performed varies depending on the type of media separated and the desired product stream (i.e. permeate or retentate). The three main configurations are (Richardson *et al.*, 2007b):

Continuous single pass (Figure 2.3a): The feed is passed through the membrane unit once only. Units can be ordered in series to achieve the desired concentration.

Feed and Bleed (Figure 2.3b): The retentate is recycled back to the inlet of the unit, often via a feed tank. The retentate can then be recovered when it reaches the desired concentration. A disadvantage of this is that flux declines dramatically as concentration of the feed/retentate increases. This configuration is often used for dewatering.

Diafiltration (Figure 2.3c): In contrast to feed and bleed, clean water is added to the system at the same rate as permeate loss in order to 'wash' the retentate, as it is recirculated through the filtration unit. This is often performed when a dilute species must be completely removed, or is too precious to waste but must be separated from the solid material in the retentate (Miradlidhara, 2010).

(a)

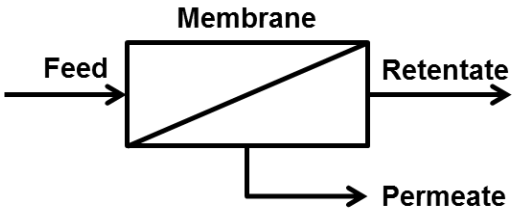

(b)

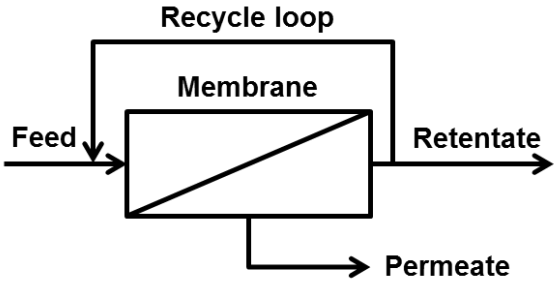

(c)

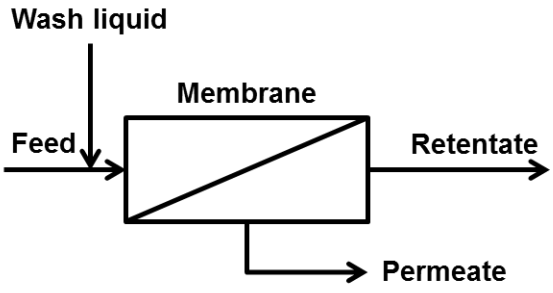

Figure 2.3. Process flow diagrams for (a) continuous single pass, (b) Feed and bleed, and (c) Diafiltration

The above processes can be achieved through a variety of different units to meet the demands of a particular process.

Filtration units

Industrial cross-flow filtrations units are often modular, and the most common types, shown in Figure 2.4, are described below:

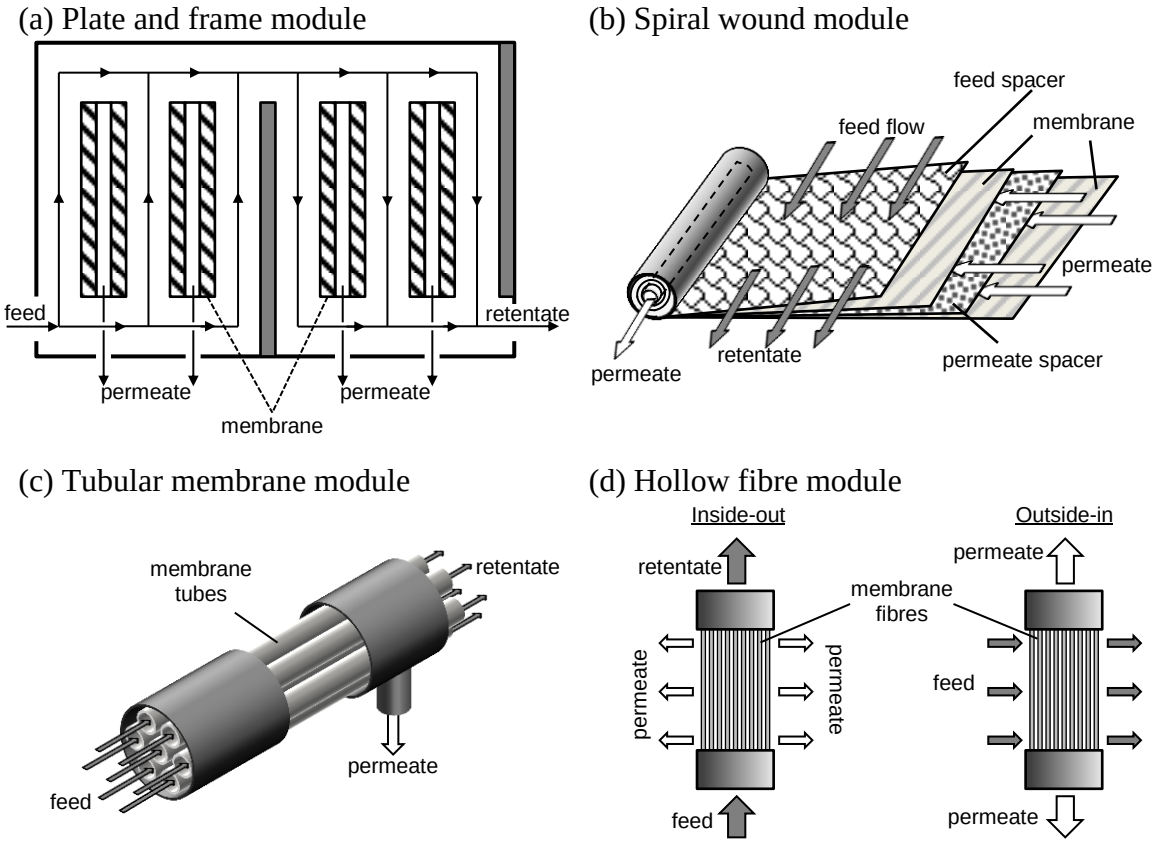

Figure 2.4. Types of cross-flow membrane modules (Richardson *et al.*, 2007b).

Plate and frame modules contain sets of flat sheet membranes with spacers sandwiched between the two to allow permeate outflow, as shown in Figure 2.4a. Feed flow is spread across all membrane surfaces in a tortuous path.

In *spiral wound* membranes, a tightly wound spiral contains repeating layers of a feed spacer, membrane, permeate spacer and membrane. Feed flows into the module inside the feed spacer, and permeate flows into a central tube in the module through the permeate spacer. The units are sealed at each end so that fluid must pass through the membranes to reach the permeate line. Figure 2.4b shows a diagram of a spiral wound module.

Individual *tubular* membranes are generally > 10 mm in diameter and supported within a porous tube. Feed solution flows through the inside of multiple tubes and permeate travels through the walls of the membrane into an external chamber, as shown in Figure 2.4c. A similar arrangement can be used with ceramic membranes.

Similarly to tubular membrane modules, *hollow fibre* modules contain a bundle of tubes, or fibres. These are much thinner and a lot more numerous, due to their size

they are also self-supporting. Hollow fibre modules can be run in two configurations: Inside-out, in which the feed enters the inside of the fibres and permeate flows into the external chamber; or outside-in, in which the feed enters the external chamber and permeate flows from the centre of the fibres. Both modes are shown in Figure 2.4d.

2.2 Industrial applications of membrane separations

A 2002 market study showed that production of membranes has been increasing steadily over the past decades, with MF occupying ~60% of both the total quantity of membranes (measured by surface area) and sales revenue in the US (Atkinson, 2002). UF and RO membranes were found to account for equivalent market shares of ~17%, whilst other membrane technologies (such as pervaporation, membrane contactors, and electrodialysis) made up the final 6%. Approximately 75% of industrial membranes manufactured are polymeric. Membrane technology has a relatively short history, with asymmetric membranes (now the staple of those available commercially) first becoming available in the 1960s (Miradlidhara, 2010).

There are strong financial incentives for the implementation of membrane separations within a process. For example, drying and/or evaporation steps can be replaced with much less energy intensive membrane separations. MF and UF often offer a more effective method for separating solid matter from process streams, as well as providing highly specific selectivity for the retention of valuable cells or macromolecules (such as in fractionation of whey proteins for dairy product). RO and NF can also be used for the concentration of aqueous streams such as dyes or food additives, producing high-quality water as a by-product which can then be recycled back to earlier processes. Membrane units are often fairly compact systems, with a modular design which allows for simple scale-up and process expansion, as well as installation within existing process plants. They can also be implemented synergistically with other separation and reaction operations, a process sometimes referred to as ‘hybridisation’; this is considered to be one the most important features of currently developing membrane technology (Miradlidhara, 2010).

A summary of some examples of membrane process applications in industry is given in Table 2.2, each of which is briefly summarised below:

2.2.1 Food and beverage processing

Ultrafiltration membranes can be used for clarification of a variety of beverages, such as beer (van der Sman *et al.*, 2012), fruit juice (Merry, 2010), or iced tea (Evans *et*

al., 2008). It has also been investigated as a potential replacement for various processing steps in edible oil production (Ladhe and Krishna Kumar, 2010b).

Table 2.2 Examples of membrane use in industry, (Ladhe and Krishna Kumar, 2010a; Merry, 2010) (Davies and Smith, 2010; Lipnizki, 2010)

Industry	Process examples	
Food and Beverage Processing	Clarification of apple juice	**UF**
	Concentration of Passata (tomato juice)	**RO**
	Bacteria removal and salt balancing for soy sauce	**MF, UF, NF, RO**
	Degumming, dewaxing and catalyst removal in vegetable oil process streams	**UF, MF**
	Microbe removal and whey protein concentration and fractionation in the dairy industry	**UF**
Pharmaceutical and White Biotechnology	Sterilisation of process buffers, feeds and intermediate products	**MF**
	Concentration of process streams	**UF**
	Separation of product from bulk fermentation broth.	**MF, UF, RO**
Water Treatment	Membrane bioreactors (MBR) for municipal water treatment	**MF**
	Reverse osmosis desalination	**RO**

Fruit juice processing

Reverse osmosis can be used to concentrate juice products by dewatering, as an alternative to evaporation. This is confined to niche products, however, as the maximum concentration is often too low and improvements to evaporation technology have eliminated any competitive edge RO may provide in this sector (Merry, 2010). It should also be noted that, due to the acidity of some fruit juices, more careful selection of membrane materials is necessary.

Soy sauce refining

Commercial membranes have been used for soy sauce production in Japan since the 1980s, and in China since the 1990s (which now produces 60% of the 8M tons, ~7.2M tonne, annual global production). Conventional refining steps after fermentation, which include heat pasteurisation, followed by sedimentation or packed bed filtration, can be replaced by membrane technologies (Wan *et al.*, 2010). MF and UF have been proven to deliver product with a high yield and long shelf life (Tien and Chiang, 1992),

while RO and NF can also be used for further refinements, delivering a product with lower salt content and paler colour (Luo *et al.*, 2009).

Edible oil production

Although it is not widely used in the edible oils industry, the application of membrane processes has been investigated over the last 40 years and it appears widely applicable, offering many advantages (Ladhe and Krishna Kumar, 2010a). It is projected that energy savings of over 50% could be achieved by the replacement of conventional deacidification and bleaching steps with membrane separations (Köseoglu and Engelgau, 1990). Although the overall production process for edible oils is long and complex, 5 steps have received specific attention, for which numerous studies of applicable membrane processes have been catalogued by Manjul and Subramanian (2006). These applications include:

- Degumming by UF and MF using ceramic (De *et al.*, 1998; Majid *et al.*, 2000), and polymeric (Ochoa *et al.*, 2001) membranes.
- Deacidifaction, for which membrane processes have yet to become economically viable (Bhosle and Subramanian, 2005).
- Bleaching, for which attempts to use membranes so far have been unsuccessful (Ladhe and Krishna Kumar, 2010b).
- Dewaxing, which is already being performed on an industrial scale in Japan using hollow fibre MF membranes (de Morais Coutinho *et al.*, 2009).
- Removal of Ni catalyst particles, for which ceramic membrane filtration has been proposed (Ladhe and Krishna Kumar, 2010b).

2.2.2 Pharmaceutical and White Biochemical Production

Pharmaceutical

Pharmaceutical products such as monoclonal antibodies (mABs) are often produced by harvesting products from cell cultures. Numerous separation and purification steps are employed downstream to achieve a product of extremely high purity, meeting strict regulatory requirements. Some of these steps are currently performed using membrane filtrations whilst others are performed using different methods, for which membranes are being explored as possible alternatives.

Current membrane technologies used in mAB production include dead-end MF of process buffers to minimise bacterial contamination, usually with 0.2 µm pore sizes (Davies and Smith, 2010). This process is often also applied to remove particles formed

in process media due to pH and other adjustments, as well as reducing the chance of bacterial contamination and improving holding lifetime. Cross-flow UF is also employed in the concentration of process streams, most often in the form of flat sheet (usually polyether-sulfone or regenerated cellulose) membranes arranged in cassette structures. Virus reduction can be performed using NF, as the primary mechanism for virus reduction is size exclusion; however, due to high membrane area requirements which escalate capital cost, it is crucial to perform these separations at stages in the process with the least possible throughput. Increasing concentrations leaving cell cultures are now imposing bottlenecks on existing mAB processes, providing incentives to look towards emerging membrane technologies such as membrane adsorbers, charged membranes, and high performance cross-flow membrane units (Davies and Smith, 2010).

Hollow fibre bioreactors are becoming an increasingly important tool in tissue engineering. Due to their high surface area to volume ratio it is possible to grow dense populations of adherent cells, providing nutrients through the capillary-like to mimic blood vessels (Wung *et al.*, 2014). These can potentially aid cell growth and support for regenerative medicine applications, in-vitro toxicology studies, artificial organs, and even in the production of cultured meat products. Recent developments have led to commercially available hollow fibre membrane bioreactors (FiberCell, 2008).

White biotechnology

The aim of industrial "white" biotechnology is to substitute chemical processes based around C_2 and C_3 chemistry with bioprocesses, the conversion process for this is most often bulk fermentation, with downstream processing costs often dominating the overall cost of production. The global market for such chemicals (excluding bioethanol) exists at around €20-25 billion per annum and it is estimated that in the coming years, 20% of all chemical products (a market of ~€250 billion) will come from bioprocesses (Lipnizki, 2010). Antibiotics are one of the most important of these, constituting a total market volume of around €8-11 billion, with the majority of production taking place in China and India (Elander, 2003). Other key products include organic acids such as acetic, citric, and lactic (in order of annual production); amino acids, vitamins, biopolymers, and yeast. Membranes have become well established in these processes since they were first introduced on an industrial scale in the 1970s. In most cases, cross-flow UF or MF is used as a primary separation step to remove biomass and cellular debris from the product of interest. Diafiltration has become particularly popular for

this, often with a RO or NF concentration step downstream, from which permeate can be recycled back as diafiltration water (Lipnizki *et al.*, 2002).

2.2.3 Water purification

The first large scale use of desalination for municipal drinking water was in the middle east, where the low rainfall continues to drive innovation in water supply (IST, 2014). This came in the form of thermal desalination, through evaporation and condensation. One of the first of such desalination plants was commissioned in Jeddah, which did not originally produce much water; however Kindasa water services now operates two RO facilities capable of producing almost 40,000 m^3/day of potable water from seawater (Kindasa, 2014). Significant improvements in RO membrane technology over the last half-century has made this by far the preferred method for new desalination plants (Greenlee *et al.*, 2009), and RO comprises 80% of desalination plants worldwide.

In order to reach the concentration requirements for potable water, such as the guideline limit of 1000 mg/L total dissolved solids (TDS) recommended by the World Health Organisation (WHO, 2008), membranes and processes of a particularly high salt rejection are required. Typical seawater RO plants have a rejection rate of 99.4 – 99.7%, and typically operate at TMPs of 5.5 – 8 MPa (Greenlee *et al.*, 2009) to achieve a total water recovery of 35 – 40%. This sometimes involves using extra passes to reduce permeate concentration (Sanz *et al.*, 2007). Brackish water can also be made into a viable source of potable water through RO desalination which, as a result of a much lower salt content than seawater, can be operated much more efficiently recovering between 75% and 90% of the feed water. Typically they operate at TMPs of 0.6 - 3 MPa using membranes with a salt rejection of 95 – 99%, this reduces capital and operating costs making them over 3 times cheaper per m^3 water than seawater filtrations.

To reduce disruption of the process by particulate fouling of the main units, RO desalination requires a pre-treatment step. The preferred method for this is also shifting towards membranes, with MF and UF being the primary choice in this case. Although this is still seen as the more expensive pre-treatment option, it does allow for the upstream removal of dissolved organics (which foul RO membranes through surface adsorption) by precipitation (Pearce, 2007).

2.3 Membrane Fouling and Cleaning

2.3.1 Fouling

Although membranes present the opportunity to perform many separations more efficiently, the reality is less straightforward. Deposition of filtered species in the pores or on the surface of the membrane can severely limit flux or, if the system is run at a constant flux, greatly increase transmembrane pressure. Unwanted deposition is known as fouling, and is the subject of a large proportion of membrane related research to date (see Figure 2.5). The nature and severity of fouling varies widely, and depends on the type of species filtered, operating conditions, and membrane properties. In RO treatment of inorganic feeds for example, concentration polarisation can lead to scaling on the membrane surface (Greenlee *et al.*, 2009), while in water treatment using membrane bioreactors biofouling is one of the most pertinent issues (Santos *et al.*, 2011). Often in microfiltration and ultrafiltration, the most significant fouling phenomenon is surface deposition (Cui and Muralidhara, 2010).

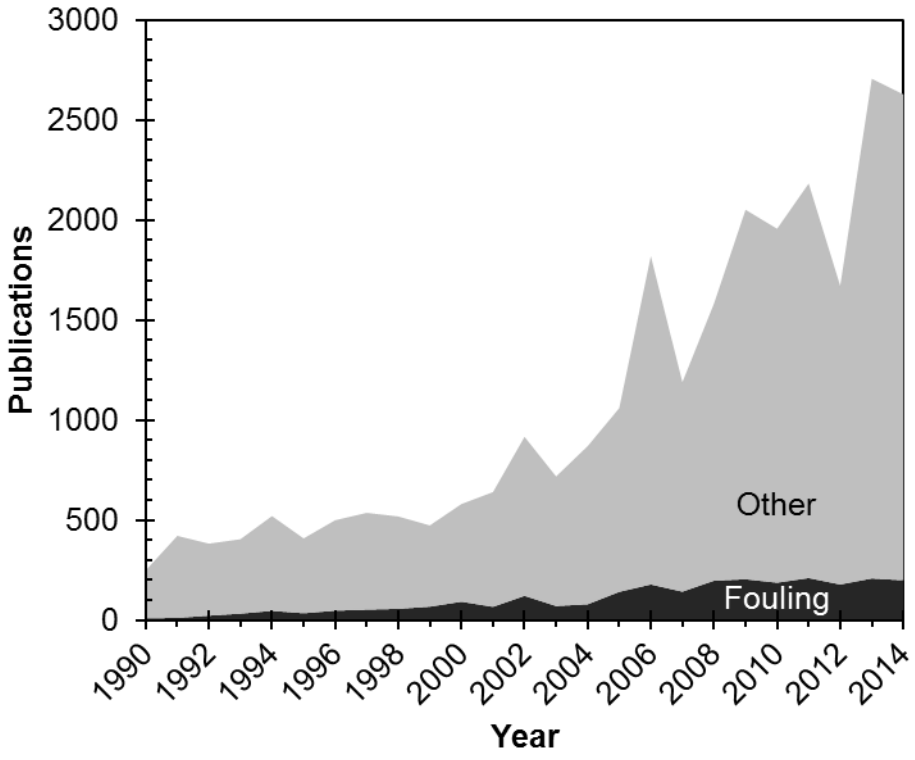

Figure 2.5. Publications in the two most prominent membrane-related journals, namely Journal of Membrane Science and Desalination. Number of publications is split into those with the keyword "fouling" (dark grey region), and all others (light grey region). Data collected using Scopus® (accessed 21/09/2014).

2.3.2 Cleaning

The approach towards fouling in industry is often a balance between prevention or attenuation, and cleaning. The former is attempted through the careful selection of operating conditions such as cross-flow velocity (De Bruijn *et al.*, 2002), transmembrane pressure (TMP) (Balakrishnan *et al.*, 2000), or temperature (Cassano *et al.*, 2007; Makardij *et al.*, 1999) as well as introducing shear enhancement mechanisms such as turbulence promoters (Krstićś *et al.*, 2004) or vibrations and ultrasound (Al-Akoum *et al.*, 2002; Muthukumaran *et al.*, 2007). In some cases pretreated (Argyle *et al.*, 2012) or functionalised membranes (Kroll *et al.*, 2010) are capable of limiting fouling phenomena.

Cleaning in place (CIP) is a generally accepted necessity in membrane processes (Muralidhara, 2010). Physical cleaning procedures can include flow reversal (e.g. backflushing (Kuberkar and Davis, 2001) or backpulsing (Sondhi and Bhave, 2001)), and ultrasound (Muthukumaran *et al.*, 2005). Chemical cleaning agents are many and varied, but generally a series of acid, alkali, and/or enzyme washes are required to solubilise or otherwise break down foulants on a membrane (Li and Chen, 2010).

The economic implications of cleaning cannot be neglected. Productivity is indicated by either an average process flux or energy input and must be balanced against the cost of cleaning. Any cleaning measures used will also require downtime, reducing productivity; however fouling will also reduce productivity by inhibiting production rate. Murildhada (2010) notes that membrane lifetime is also an important economic factor. As discussed in section 2.1.2, durable membrane materials such as polyethersulphone are hydrophobic so generally exhibit lower fluxes, whereas hydrophilic membranes such as regenerated cellulose allow higher fluxes but are more easily damaged. One must therefore consider the replacement cost of the membrane against the propensity towards fouling, cleaning frequency, and flux. Ceramic membranes are the most durable option, however a cost model presented by G.K. Pearce (Pearce, 2012) indicated that, due to their higher capital cost, a further 10% increase in flux must be achieved in order to make them more commercially viable than polymeric membranes.

In a recent workshop (entitled “Membrane Fouling and Monitoring”) gathering together experts in the field of membrane fouling, a general consensus was reached that membrane fouling phenomena are best understood and managed, rather than prevented (Linkhorst and Lewis, 2013). Research trends are moving towards this, and with effective cost-benefit analyses it should be possible to fine-tune the design of membrane

operations towards more efficient and economically viable practices. With a full mechanistic understanding of membrane fouling and cleaning, it will be possible to take into account the membrane material, physical and chemical cleaning operations, and operating conditions, to predict the best combinations of these variables for a specific process.

The graph presented in Figure 2.5 demonstrates how membrane related research has increased in output since 1990, as well as indicating how large a proportion of this is dedicated to the study of fouling. From 1990 to 1996 it occupied around 5-10% of membrane related research, but from 2000 onwards it makes up roughly 15% of publications. It should be noted that the data only gives a rough estimate and is subject to the limits of the search terms defined in the caption.

2.4 Modelling filtration and fouling

2.4.1 Generalised filtration model

In pressure driven membrane processes the flux, J, is usually expressed by Darcy's law (Mulder, 1996):

$$J = A_m \frac{dV}{dt} = \frac{TMP}{\mu} \frac{\kappa_m}{\delta_m} \tag{2.1}$$

where A_m, is the area of the membrane, V is the total volume of fluid filtered, μ is the fluid viscosity, κ_m is the permeability of the membrane, and δ_m is the membrane thickness. This is often expressed as a resistance model:

$$J = \frac{TMP - \Pi}{\mu R_T} \tag{2.2}$$

where Π is osmotic pressure[*] and R_T is the total resistance of the system, which includes that of the membrane and any other flux reducing phenomena such as fouling or concentration polarisation. It also encompasses within its definition the thickness of the membrane and fouling layer(s). These extra resistance terms can be added in series, similarly to standard heat transfer equations, to give the additive resistance model:

[*] Osmotic pressure acts against flux when the concentration of a dissolved species is significantly higher on the feed side than the permeate side.

$$J = \frac{TMP - \Pi}{(R_m + R_c + R_{CP} + R_p)\mu} \tag{2.3}$$

where R_m, R_c, R_{CP}, and R_p are membrane, cake, concentration polarisation, and pore-fouling resistances respectively. R_c, R_{CP}, and R_p will be discussed in later sections, the membrane resistance, R_m is given by:

$$R_m = \frac{\delta_m}{\kappa_m} \tag{2.4}$$

and can be determined easily by filtration of a pure solvent (usually water).

2.4.2 Estimating cake resistance, R_c

Estimation from flux data

In an ideal dead-end filtration system, in which all particles are rejected and form a cake layer on the surface, cake layer resistance can be described by:

$$R_c = \frac{\varphi_c V c_b}{A_m} \tag{2.5}$$

where φ_c is the specific cake resistance ($m \cdot kg^{-1}$), and c_b is the bulk particle concentration. Substituting equation (2.5) into (2.3), assuming osmotic pressure, concentration polarisation and pore fouling to be insignificant, gives the generally accepted dead-end filtration equation:

$$\frac{t}{V} = \frac{R_m \mu}{A_m TMP} + \left(\frac{\varphi_c c_b \mu}{2A_m^2 TMP}\right) V \tag{2.6}$$

By plotting t/V vs V, which should exhibit a linear correlation for filtrations at constant TMP, Suki *et al.* (1984) inferred – from the gradient of a linear regression fit – the specific resistance of Bovine Serum Albumin (BSA) protein deposits during dead-end ultrafiltration.

For cross-flow filtrations however, resistance calculations using equation (2.6) are not reliable, due to a non-linear relationship which develops between t/V and V. This is exemplified in results taken by Murase *et al.* (1995), who performed cross-flow filtrations of various granular suspensions using ceramic microfiltration membranes.

Estimation from particle size data

Specific cake resistance can also be related to porosity by adapting the Carman-Kozeny equation (Richardson *et al.*, 2007a) for flow through packed beds:

$$\bar{u} = \frac{\varepsilon^3}{KS_v^2(1-\varepsilon)^2}\frac{TMP}{\mu\delta_c} \tag{2.7}$$

where $\bar{u}$ is the superficial velocity through the cake, K is the Kozeny constant, S_v is the particle surface area per unit volume, ε is the packed bed porosity (estimated as 0.4 for tightly packed spheres), and δ_c is the cake thickness. By substituting $\bar{u}$ for J, equation (2.7) can be rewritten using equation (2.3), where R_c is the only resistance term, as:

$$R_c = \frac{K(1-\varepsilon)^2 S_v^2}{\varepsilon^3}\delta_c \tag{2.8}$$

Cake thickness, δ_c, can be converted to cake mass, M_c, per unit area by:

$$\frac{M_c}{A_m} = \delta_c(1-\varepsilon)\rho_p \tag{2.9}$$

where ρ_p is the wet density of a particle[*]. Given that:

$$\varphi_c = R_c\frac{A_m}{M_c} \tag{2.10}$$

specific cake resistance can be estimated by dividing (2.8) by (2.9) to give:

$$\varphi_c = \frac{K(1-\varepsilon)S_v^2}{\varepsilon^3\rho_p} \tag{2.11}$$

When applied to filtrations, a value of 5 is generally assumed for the Kozeny constant, K (Nakanishi *et al.*, 1987; Okamoto *et al.*, 2001). However, this assumption is known to cause discrepancies (Foley, 2006). McCarthy *et al.* (1998a; 1998b; 2002) have performed numerous studies on cakes formed from *K. marxianus* yeast cells. They were able to relate the Kozeny constant logarithmically to the aspect ratio of the cells, allowing for more accurate predictions of φ_c. The Kozeny constant has also been calculated from the solids fraction by Meireles *et al.* (2002) for purposes of computer simulations.

[*] The properties of many suspended particles, such as volume and density, can differ from those when dry; this is of particular concern when dealing with microbial cells. Ju and Ho (1988) have determined wet cell density by measuring dextran uptake.

Additional considerations

Foley (2006) reviewed the effects of a number of cake layer properties including compressibility, cell surface properties, morphology and ionic environment on R_c and φ_c. They highlighted that these studies have dealt with pressure drops across the membrane, when in fact the pressure drop across the cake, Δp_c, should be calculated separately as:

$$\Delta p_c = TMP - \mu R_m J \tag{2.12}$$

This means that the pressure drop across the cake would depend on the degree of fouling within the membrane pores. The author also makes the point that for compressible cakes formed from microbial suspensions, the cake properties may vary with position through the cake. Furthermore they state that cells closest to the membrane experience greater deformation, which could affect the level of pore blocking. A similar effect has been recorded by Mattsson *et al.* (2012a), who observed much higher resistances in cake layers closer to the membrane when performing dead-end microfiltrations of microcrystalline cellulose. They proposed that a 'skin layer' existed on the surface of the membrane, at the bottom of thick filter cakes, which had compressed much more than subsequent layers on top of it.

It is clear from the aforementioned studies that it is possible to estimate the resistance characteristics of filter cakes under different conditions for dead-end filrations. Such estimations become less applicable when dealing with cross-flow filtrations, where one must consider the back transport of particles away from the cake. Such models are explored in section 2.5.

2.4.3 Concentration Polarisation

During filtration, solutes or suspended particles are convected towards the membrane due to permeate flux, but due to their retention they will be present at a higher concentration closer to the membrane, which imposes a resistance to flux. This phenomenon is known as concentration polarisation (Cui *et al.*, 2010). When a balance is reached between convective drag of particles and/or solutes towards the membrane, and back-transport away from the membrane, a steady-state is reached and the concentration profile shown in Figure 2.6 is established, for which the following equation applies (Mulder, 1996):

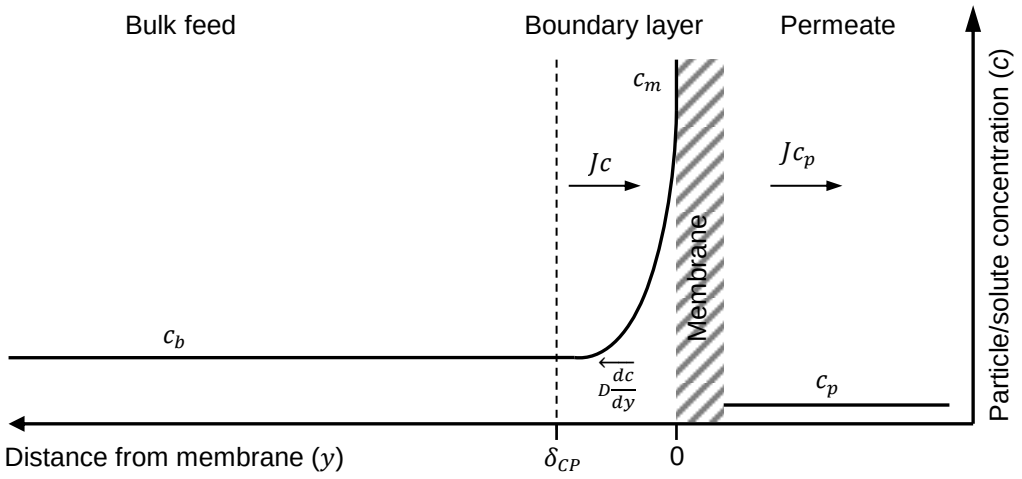

Figure 2.6. Concentration profile predicted during concentration polarisation under steady state conditions, adapted from (Mulder, 1996).

$$Jc + D_{CP}\frac{dc}{dy} = Jc_p \tag{2.13}$$

where c is the particle/solute concentration, y is the distance from the membrane, D_{CP} is the diffusion coefficient, and c_p is the concentration of the permeate. Upon integration this equation becomes:

$$\frac{c_m - c_p}{c_b - c_p} = e^{\left(\frac{J\delta_{CP}}{D_{CP}}\right)} \tag{2.14}$$

where $c_m$and c_b are the concentration at the membrane and concentration in bulk liquid respectively, and δ_{CP} is the thickness of the CP boundary layer. For a system in which complete retention occurs, equation 15 can be expressed as:

$$\frac{c_m}{c_b} = e^{(J/k_{CP})} \tag{2.15}$$

where k_{CP} is the mass transfer coefficient associated with concentration polarisation equating D_{CP}/δ_{CP}. A situation can be proposed in which flux becomes independent of TMP, and the concentration of solute or particles at the membrane surface at which it forms a gel-layer. This theory is known as the gel-polarisation model, for which a steady-state value of flux, J_∞, is predicted by:

$$J_\infty = k_{CP}\, ln\left(\frac{c_m}{c_b}\right) = k_{CP}(ln(c_m) - ln(c_b)) \tag{2.16}$$

Assuming c_m is constant and independent of bulk concentration, equation (2.16) suggests that k_{CP} and c_m could be determined from a linear correlation between J_∞ and c_b. In practice this has not been proven, as diffusivity appears to be dependent on c_b (Mulder, 1996). Further to this, osmotic pressure changes due to CP are not taken into account in this model.

At higher solute concentrations near the membrane, osmotic pressure is exerted against the permeate flow, which reduces the pressure driving force through the membrane and hence the permeate flux. CP is most significant when the process media contains dissolved salts and macromolecules, which induce a greater osmotic potential than larger matter, as well as being more susceptible to diffusion and convective forces. Thus CP is of more concern in RO, NF, and on the lower end of UF MWCOs, however dissolved macromolecules and other smaller particles in heterogeneous mixtures may contribute towards CP in MF operations as well.

2.4.4 Modelling dead-end flux decline

Sections 2.4.1 and 2.4.2 illustrate how cake resistance can be determined in dead-end filtration, and from this (assuming R_{CP} and Π to be negligible) one could infer pore resistance from equation (2.3) by:

$$R_p = \frac{TMP}{\mu J} - (R_m + R_c) \tag{2.17}$$

This does not, however, present any means to estimate how fast pore fouling will occur or the flux decline in the absence of any cake fouling. Furthermore, one cannot infer directly whether flux decline is occurring due to cake filtration, pore fouling, or both without an autopsy of the fouled membrane (Suki *et al.*, 1984).

Hermia (1982) presented a general model for constant TMP filtrations which can be used to describe flux decline due to various types of fouling phenomena, which are considered to occur in series. Their model takes the form:

$$\frac{d^2t}{dV^2} = k\left(\frac{dt}{dV}\right)^n \tag{2.18}$$

where k and n are variable constants, for which the values depend on the type of fouling phenomenon modelled, as summarised in Table 2.3. The phenomena, or *filtration laws*, are based around an assumption of uniform cylindrical pore distribution across a membrane surface. Referring to Figure 2.7 for a schematic, these laws are defined below.

(a) Standard blocking (n = 1.5) (b) Complete blocking (n = 2)

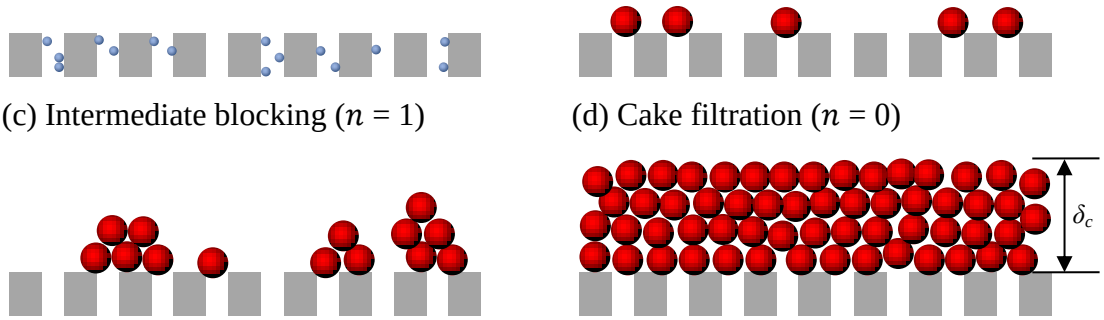

(c) Intermediate blocking (n = 1) (d) Cake filtration (n = 0)

Figure 2.7. Mechanisms of different fouling phenomena decribed by Hermia (1982), as used in equation (2.20)

Standard Blocking (n = 1.5)

This law considers internal pore fouling, as indicated by the smaller particles within the pores in Figure 2.7a. A typical example of this would be the sorption of macromolecules by the membrane material (Belfort *et al.*, 1994). In Hermia's (1982) formulation the pore volume is assumed to decrease proportionally to the total volume filtered, V, which in turn reduces flux.

Table 2.3 Constants for equation (2.18) for four different fouling models, where J_0 is initial flux, σ is the blocked membrane surface area per unit volume of permeate, and ϕ_{ads} is the volume of particles retained by pores per unit volume of permeate (Hermia, 1982).

Filtration law	k	n
Cake Filtration (Figure 2.7d)	$\frac{\varphi_c c_b \mu}{A_m^2 TMP}$	0
Intermediate blocking (Figure 2.7c)	$\frac{\sigma}{A_m}$	1
Standard blocking (Figure 2.7a)	$\frac{2\phi_{ads}}{\delta_m} A_m^{-0.5} J_0^{0.5}$	1.5
Complete Blocking (Figure 2.7b)	$J_0 \sigma$	2

Complete Blocking (n = 2)

This law assumes that each particle which reaches the surface of the membrane completely blocks a pore (Figure 2.7b), effectively reducing the available membrane surface area which allows flux. The resulting function considers the available surface area to decline proportionally to the total volume filtered volume, V.

Intermediate Blocking (n = 1)

This is similar to the complete blocking law above, but perhaps presents a more realistic mechanistic model for surface fouling. Here particles which reach open pores will block them, reducing the available surface area for flux. This law, however, allows for other particles to rest on top of these, as seen in Figure 2.7c wherein some open pores remain while particles are still deposited on top of others. The suspension is assumed to be homogeneous, such that particles are as likely to settle on open pores as on top of other particles. Hence the incremental decrease in available surface area is proportional to the area of unblocked membrane. This means flux should decline more slowly than under the complete blocking law.

Cake filtration (n = 0)

In this law the cake resistance, R_c is presumed to increase linearly with cake deposition, which is directly proportional to the volume filtered, as described by equation (2.5). This law is described by equation (2.6) which, when differentiated with respect to V gives. :

$$\frac{d^2t}{dV^2} = constant = k\left(\frac{dt}{dV}\right)^0 \tag{2.19}$$

which fits the general model of equation (2.18) where n = 0.

Implementation

Bowen *et al.* (1995) used this model to identify the type of fouling occurring during different stages of a bovine serum albumin (BSA) filtration. They determined n by reading the gradient from a log-log plot of d^2t/dV^2 against dt/dV.

2.5 Fouling models for cross-flow filtration

While the fouling rate for dead-end filtrations can be readily estimated, as described above, the methods for cross-flow filtrations are more complex. This is because one must consider the rate at which particles are resuspended into the bulk flow due to shear forces on the surface of the fouling layer, which occur due to cross-flow.

This phenomenon is often referred to as *back-transport* (Belfort *et al.*, 1994). In this section, four mechanistic models are explored which aim to predict flux decline taking back-transport mechanisms into account.

2.5.1 Critical Flux Model

The concept of critical flux was first introduced by Field *et al.* (1995), and is a principle still used in modern filtration processes. The basic premise is that below a critical flux, J_{crit}, no observable fouling will occur during cross-flow filtration. The authors proposed this theory based on a number of different microfiltrations of three types of media (yeast cells, yeast cell debris, and dodecane-water emulsion) through both tubular and flat sheet membranes. It is important to note that this principle applies at start-up in a system, so that if a filtration is run above critical flux (i.e. $J > J_{crit}$), fouling will still occur which may affect the flux or transmembrane pressure when it is returned to conditions below J_{crit}. One key industry to which this is appropriate is in munipal wastewater treatment, wherein operation below critical flux has been proven to allow for long term operation at a continuous flux without a loss of performance (Meng *et al.*, 2009).

Field *et al.* (1995) also incorporated this theory into a mathematical model based on the constant pressure laws developed by Hermia (1982) described in section 2.4.4. This takes into account the sequential blocking phenomena put forward by Hermia, using the general equation:

$$-\frac{dJ}{dt}J^{n-2} = k(J - J^*) \tag{2.20}$$

where J^* is a critical or limiting flux for a particular type of fouling law. n and k are constants which vary depending on the fouling law, for which the values and formulae are shown in Table 2.4. For complete blocking laws (where n = 2), $J^* = J_{crit}$, and at this flux no fouling will occur. In all other cases J^* represents a limiting flux specific to a particular blocking law. The description of the fouling mechanisms in Figure 2.7 and discussed in section 2.4.4 is still appropriate to this analysis. It should be noted, however, that the standard blocking mechanism (Figure 2.7a) is left out of this analysis because there is no back-transport mechanism due to cross-flow. As a result one must assume that, for equation (2.20) to work, this blocking mechanism does not take place.

Table 2.4 Constants for equation (2.20) for three different fouling models, where k_c' is a cake filtration constant, J_0 is initial flux, σ is the blocked membrane surface area per unit volume of permeate, and ε_m is the membrane surface porosity. Field *et al.* (1995)

Fouling law	k	n
Cake Filtration (Figure 2.7d)	$\frac{\varphi_c k_c'}{J_0 R_m}$	0
Intermediate blocking (Figure 2.7c)	σ	1
Complete Blocking (Figure 2.7b)	$\frac{J_0 \sigma}{\varepsilon_m}$	2

It is evident from equation (2.20) that by writing:

$$f(J) = -\frac{dJ}{dt} J^{n-2} \tag{2.21}$$

One should observe a linear plot of $f(J)$ vs. J, which would apply in the region where a particular fouling mechanism is dominant (Field and Wu, 2011). From this it should then be possible to estimate J^*, as well as other parameters from Table 2.4. Additionally it can be used to check that flux decline seen is concordant with a particular fouling model when validating experimental data.

2.5.2 Particle Capture Model

Broekmann *et al.* (2006) used a model originally reported by Foley which considers a force balance on an individual particle resting upon a membrane or cake. The general principle implied by the authors is that the particle will remain at rest against the porous surface unless the force from tangential flow is great enough to overcome the opposing frictional resistance of the surface. A diagrammatic representation of the force balance is presented in Figure 2.8.

The normal force on a particle held against a surface of a constant permeability, κ, was derived by Sherwood (1988) to be:

$$F_N = 3\mu J d_p 0.36 \left(\frac{\kappa}{d_p^2}\right)^{-\frac{2}{5}} \tag{2.22}$$

where d_p is the particle diameter. An estimate of the tangential force due to cross-flow is given by (Broeckmann *et al.*, 2006):

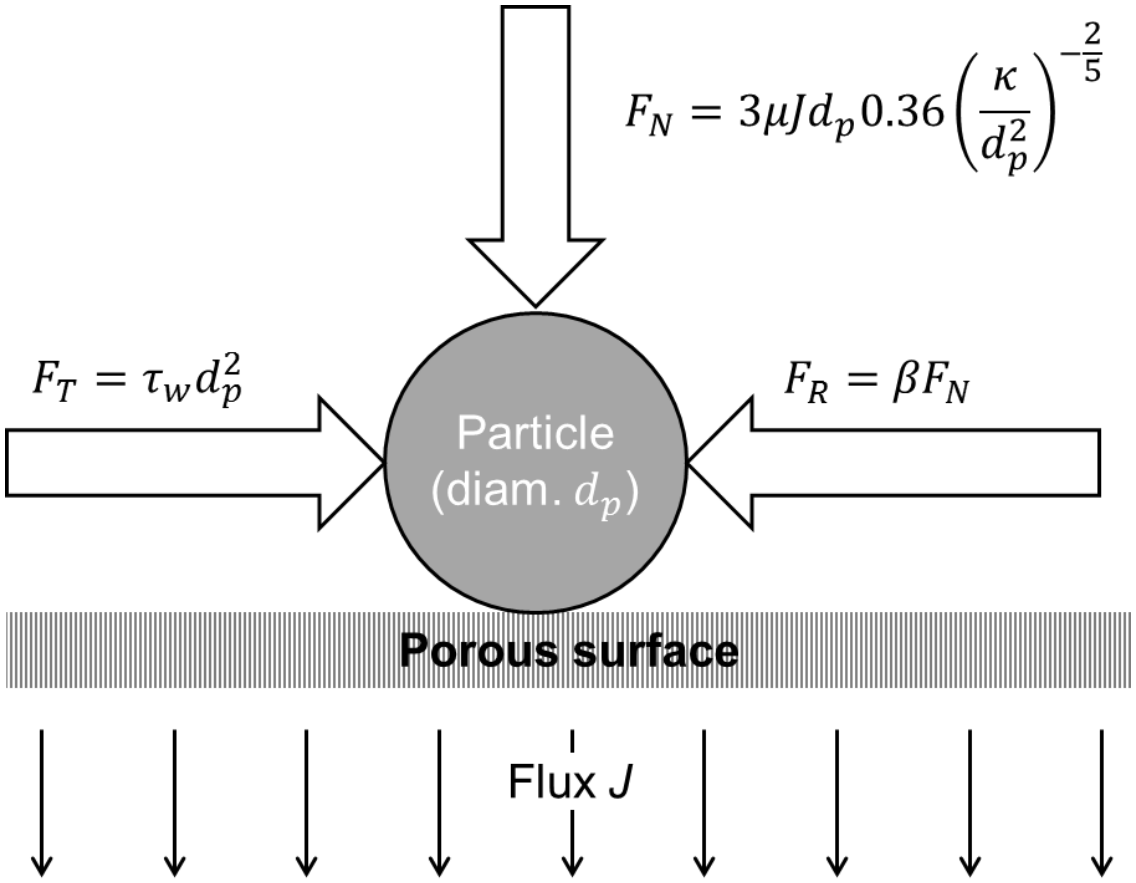

Figure 2.8. Force balance on a particle resting against a porous surface, as described by Broekmann *et al.* (2006)

$$F_T = \tau_w d_p^2 \tag{2.23}$$

where τ_w is the shear stress on the porous surface due to tangential flow, and d_p is the particle diameter. They estimate the frictional force resisting this movement (between the particle and the surface on which it rests), as a function of the normal force, to be:

$$F_R = \beta F_N \tag{2.24}$$

where β is a friction coefficient for the surface. A value of 0.03 was used by the authors, although this is an arbitrary approximation made by scaling a previously derived value for dust particles in air (Jeon and Jung, 2004) down by a factor of 10. In fact Jeon and Jung (2004) suggested values ranging from 0.1 – 0.3 for the dust particles; so for particles in a fluid it could be reasoned that a friction coefficient of: $\beta = 0.02 \pm 0.01$ should be used. This would imply a variation in F_R of up to 100%.

Combining equations (2.22) to (2.24) gives a condition for particle removal from the surface:

$$d_p\left(\tau_w d_p - \beta 3\mu J 0.36\left(\frac{\kappa}{d_p^2}\right)^{-\frac{2}{5}}\right) > 0 \tag{2.25}$$

The limitations of this model are:

1. Surface is completely flat
2. Frictional coefficient does not change between the membrane layer and the cake layer
3. Only a single sphere is considered, interactions with other particles, or shape factors, are not considered.
4. Limiting condition of $\kappa \ll d_p^2$

Broeckmann *et al.* (2006) fitted this model with experimental TMP vs. time data at a constant flux of 20 $L{\cdot}m^{-2}{\cdot}h^{-1}$ for a pilot-scale membrane bioreactor. They found that at higher flux the model under-predicted TMP, and at lower flux it over-predicted TMP.

2.5.3 Inertial Lift

Another method devised to estimate the rate of back transport of particles away from a membrane was proposed by Altena and Belfort (1984). Their 'inertial lift' model, derived using the Navier-Stokes equations, predicts the migration of particles away from a flat porous surface at low cross-flow velocity. Drew *et al.* (1991) later extended it to higher cross-flow velocities (although still under laminar flow conditions). The theory produces an inertial lift term, v_{IL}, describing the velocity of individual particles travelling away from the membrane, given by:

$$v_{IL} = \frac{f(y^*)\rho_L d_p^3 \dot{\gamma}^2}{128\mu} \tag{2.26}$$

where $f(y^*)$ is a function of dimensionless distance from the surface, ρ_L is the density of the fluid, and $\dot{\gamma}$ is the shear rate. A generally accepted value for $f(y^*)$ is given by Drew *et al.* (1991) as 0.577, pertaining to the maximum inertial velocity for fast laminar cross-flow systems. For flow in a duct with one porous surface, wherein cross-flow velocity is characterised by Re_{duct}, this equation is valid where the particle size is small relative to the height, *H*, of the duct i.e.:

$$\left(\frac{d_p}{H}\right) Re_{duct} \ll 1 \tag{2.27}$$

and fouling layers are relatively thin such that they do not significantly reduce H.

For steady-state systems in which the transport of particles towards the membrane is balanced by their removal; inertial lift velocity can be equated to permeate flux to give (using $f(y^*) = 0.577$):

$$J = v_{IL} = 0.0045 \frac{\rho_L d_p^3 \dot{\gamma}^2}{\mu} \tag{2.28}$$

It should be noted that the inertial lift velocity in this case is independent of the particle concentration in the fluid, however it is strongly dependent on particle size. Li et al (2000) tested this as a means to predict critical flux in cross-flow systems, however they found that it massively under-estimated its value.

2.5.4 Shear-induced Diffusivity

This technique is based on the principle that particles suspended in a fluid will tend to be displaced from areas of high shear to those of lower shear. This means that shear forces due to flow over a porous surface will drive particles away from it into the bulk flow.

In contrast to the inertial lift model, which is derived from constitutive equations; shear-induced diffusivity (SID) is a property of particles in a shear field determined purely by empirical means. By tracking radioactively labelled particle migration in a couette device, Eckstein *et al.* (1977) observed that particles tended to migrate from areas of high fluid shear to lower ones. They expressed particle movements in terms of a diffusivity term, D_s, which is related to the particle volume fraction, ϕ, and shear rate by:

$$D_s = \dot{\gamma} \left(\frac{d_p}{2}\right)^2 \widehat{D}[\phi] \tag{2.29}$$

where $\widehat{D}[\phi]$ is a diffusivity coefficient which increases linearly with particle volume fraction, ϕ, from 0 to 0.02 in the range $0 \leq \phi \leq 0.2$, and $\widehat{D}[\phi] \cong 0.025$ (within a factor of 2) in the range up to $\phi = 0.5$. This relationship is plotted in Figure 2.9a. Leighton and Acrivos (Leighton and Acrivos, 1986) performed similar experiments with smaller particles and determined the following approximation:

$$\widehat{D}[\phi] = \frac{1}{3}\phi^2\left(1 + 0.5e^{8.8\phi}\right) \tag{2.30}$$

In this other method they also observed short-term effects on fluid viscosity during their experiments using a couette device, however they still believed their results to under-predict particle diffusivity at lower concentrations. Equation (2.30) is plotted in Figure 2.9b.

Zydney and Colton (Zydney and Colton, 1986) used this principle to determine a steady-state flux for cross-flow microfiltrations through a duct of length, L, with a flat sheet membrane. Noting that the problem of mass transfer due to shear at a wall was analogous to heat transfer problems; they employed the Leveque solution to determine the flux, J_∞, at steady-state using equation (2.29) and $\widehat{D}[\phi] = 0.03$:

$$J_\infty = 0.078\left(\frac{d_p^4}{16L}\right)^{\frac{1}{3}}\dot{\gamma}\, ln\left(\frac{\phi_w}{\phi_b}\right) \tag{2.31}$$

where ϕ_w and ϕ_b are the particle volume fractions at the wall and in the bulk liquid respectively. The former of these can often be assumed to be the maximum packing density for the particles in suspension (Davis and Leighton, 1987).

(a) (b)

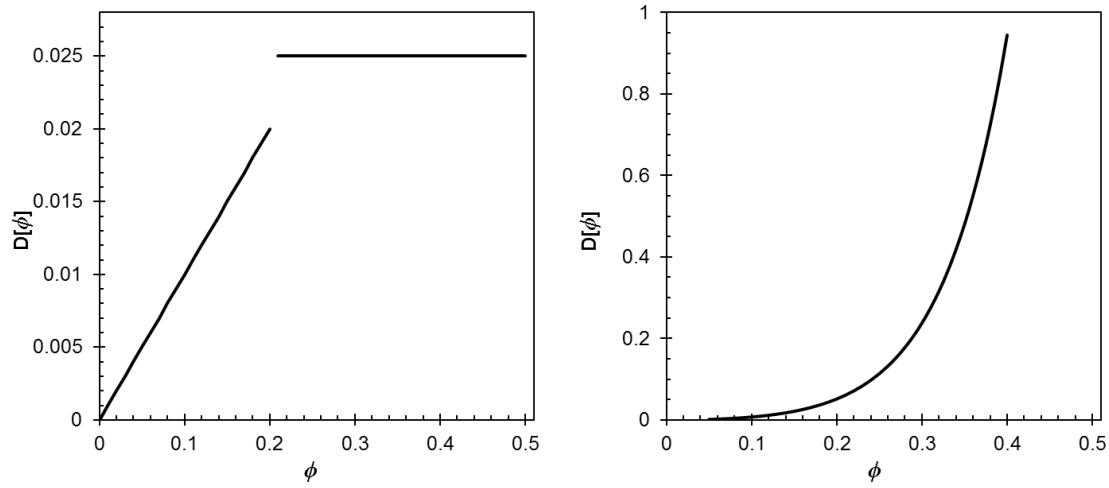

Figure 2.9. Diffusivity coefficient given by (a) Eckstein *et al.* (1977) and (b) equation (2.30), (Leighton and Acrivos, 1986).

Equation (2.31) was tested in the range $0.2 \leq \phi_b \leq 0.5$ by Zydney and Colton, using $\phi_w = 0.6$. For more dilute suspensions, Li *et al.* (2000) determined:

$$J = 0.0595\left(\frac{d_p^4}{16L}\right)^{\frac{1}{3}}\dot{\gamma}\, ln\left(\frac{\phi_w}{\phi_b}\right) \tag{2.32}$$

while Drew *et al.* (1991) used equation (2.30) to determine:

$$0.064\left(\frac{d_p^4}{16\phi_b L}\right)^{\frac{1}{3}}\dot{\gamma} \tag{2.33}$$

Li *et al.* (2000) have tested equations (2.31), (2.32), and (2.33) using a range of particles as a means of determining critical flux. Their results fitted best with equation (2.32).

2.5.5 Summary

The critical flux model described in section 2.5.1 relates the rate of flux decline to the type of fouling system thought to be occurring. An advantage of this is that it does not require the separate measurement of various properties of the suspension and/or membrane to be used in this way. It does provide a means to predict flux or cake growth under varied conditions, but allows for a qualitative assessment of the type of mechanics involved in different stages of fouling.

Of the three models which describe the behaviour of particles in a shear field (sections 2.5.2, 2.5.3, and 2.5.4), the most useful appears to be the shear-induced diffusivity model, because it uses empirical observations for real suspensions rather than considering the fluid dynamics around individual particles. All three, however, are likely to be unhelpful when describing more complex fouling systems, where inter-particle interactions may also play an important role.

2.6 In-situ Methods for Monitoring Fouling Layer Development

In order to verify such models as described in sections 2.4 and 2.5, or to derive parameters for them, it is necessary to perform experiments for which all necessary variables are known and/or measureable. Although flux decline or TMP increase are good indicators of fouling, they do not provide reliable measures for the extent of pore-fouling or the thickness of a cake layer. *Ex-situ* methods such as membrane 'autopsies', wherein a fouled membrane is recovered after a filtration, can provide important information about the thickness and structure of a filter cake (Nghiem and Schäfer, 2006; Sun *et al.*, 2011). This can, however, give misleading results as cakes could slump, and may be hard to extract in such a way that they are representative of the time-point at which a filtration was terminated. Furthermore it would involve dismantling filtration equipment. Hence numerous techniques have been developed over the last two decades in order to study cake fouling and initial deposition *in-situ*. Chen *et al.* (2004) provide a comprehensive review of such techniques, some of which are outlined in this

section, along with more recent developments. Table 2.5 shows a summary of these along with selected references for each method.

Table 2.5. Summary of in-situ methods for monitoring membrane fouling

Name	Operating principle	Key features	Limitations
Direct Observation Through Membrane (DOTM) (Li *et al.*, 1998, 2000, 2003a; Wicaksana *et al.*, 2012; Zhang *et al.*, 2006)	Use of microscope and CCD camera to monitor foulant deposition on membrane surface from underneath.	• Detects fouling before indicated by loss of performance • Can be used to estimate critical flux • Cross-flow and dead-end • Can provide relevant data for assessing SID models • Ideal for testing models which consider initial deposition	• No indication of cake thickness • Light must be transmissible through suspension and membrane. Deposition must also contrast against these to be seen. • Only provides information about initial deposition. • Limited by microscope resolution.
Direct Visual Observation (DVO) (Marselina *et al.*, 2009; Mores and Davis, 2001; Vrouwenvelder *et al.*, 2007; Wakeman, 1994)	Use of a microscope and CCD camera to monitor foulant deposition from overhead or across the membrane.	• Tracks particle movements on fouling layer • Cross-flow and dead-end • Has been applied to hollow-fibre membranes • Thickness measurements (hollow fibre and MPM only) to a resolution of ±10 μm • Can indicate flowing and stationary fouling layers	• Light must be transmissible through suspension. • (Flat sheet only) Light must be transmissible through or reflected from the membrane • (Flat sheet only) No indication of cake thickness • Hollow fibre studies limited to outside-in flow
Laser Triangulometry (Hamachi and Mietton-Peuchot, 2001; Mendret *et al.*, 2007; Schluep and Widmer, 1996)	An angled laser beam is directed towards the surface of the fouling layer. Cake growth is indicated by translational movement of the reflected beam.	• Real-time indication of cake thickness to a resolution of ±3 μm • Dead-end and cross-flow • Has also been used to indicate thickness change across the width of a duct	• Requires transmission of laser beam through suspension • Cake surface must reflect laser • Refractive index of suspension may change with concentration • Laser could damage photosensitive cakes

Table 2.5. Summary of in-situ methods for monitoring membrane fouling

Name	Operating principle	Key features	Limitations
Ultrasonic Time Domain Reflectometry (UTDR) (Li *et al.*, 2003b; Mairal *et al.*, 1999; Sim *et al.*, 2013a; Xu *et al.*, 2009a; Zhang *et al.*, 2003)	An ultrasonic signal is reflected from the surface of the membrane or cake. The time-delay between emission and reception of the sound	• Real-time indication of cake thickness to a resolution of ±0.1-0.75 μm (depending on frequenccy) • Has also been applied to spiral wound, tubular, and hollow fibre membranes. • Can be mounted on to existing equipment • Detects fouling before indicated by loss of performance • Dead-end and cross-flow studies • Works in opaque feeds	• Involves complex signal processing • Requires prerequisite knowledge of acoustic impedance of feed • Acoustic impedance of feed may alter with feed concentration • Ultrasound signals are reflected at an interface where acoustic impedance changes. This may not be well defined for cake fouling. • Ultrasound signals may potentially interfere with fouling
Nuclear Magnetic Resonance (NMR) imaging (Buetehorn *et al.*, 2011; Graf von der Schulenburg *et al.*, 2008; Yao *et al.*, 1995)	Maps distributions of free protons using pulsed radio frequencies in a magnetic field.	• Real-time indication of cake thickness to a resolution of ±10 μm • Also measures fluid velocity • Can generate 3D representation of fouling layers • Dead-end and cross-flow • Works with opaque feeds	• Expensive technique requiring high level of technical expertise • Only achievable with particular types of fouling • A purpose-built, non-metallic filtration unit must be mounted within constrained NMR equipment.
Electrical Impedance Spectroscopy (EIS) (Chilcott *et al.*, 2002; Coster *et al.*, 1996; Kavanagh *et al.*, 2009)	Measurement of the response of the membrane and fouling region when an alternating current is applied.	• Can be used to evaluate porosity and electrochemical properties of membranes. • Indicates scaling on RO membranes • Cross-flow and dead-end	• Very niche applications • Requires suitably conductive feed and membrane • No indication of cake thickness • Has not yet been applied to UF or MF
Radiography (Mattsson *et al.*, 2012a; Sedin *et al.*, 2003)	Impedence of γ radiation by a cake is used to indicate both thickness and porosity	• Indication of local porosity in real-time • Dead-end filtrations • Can indicate porosity at different cake heights	• Not yet applied to cross-flow • Does not explicitly determine cake thickness • Radiation can be hazardous to the user.

2.6.1 Direct Observation techniques

The simplest, and arguably one of the more robust techniques for monitoring cake fouling or surface deposition on membranes is by directly observing the process, usually with the aid of a microscope. The types of study and variations of the technique are represented in Figure 2.10a and discussed in this section.

Direct visual observation (DVO)

Direct observation of fouling in cross-flow filtrations was first reported by Romero and Davis (Romero and Davis, 1991). They used a cathetometer to monitor cake growth through a viewing window on the side of a cross-flow filtration module. A similar arrangement was employed by Mackley and Sherman (1992) who used a video camera at 15× magnification to capture and measure cake growth. Both of these studies were performed on particles of diameter $d_p > 100$ μm, which is larger than those typically found in industrial applications. Later, Wakeman (1994) used a high-speed camera to monitor fouling of microfiltration membranes by suspensions of calcite and anatase ($0.5 \leq d_p \geq 25$ μm) to track cake thickness over time. These studies all used an observation technique wherein cake fouling was viewed side-on through an observation window, in order to measure thickness (see Figure 2.10a). The general findings of all

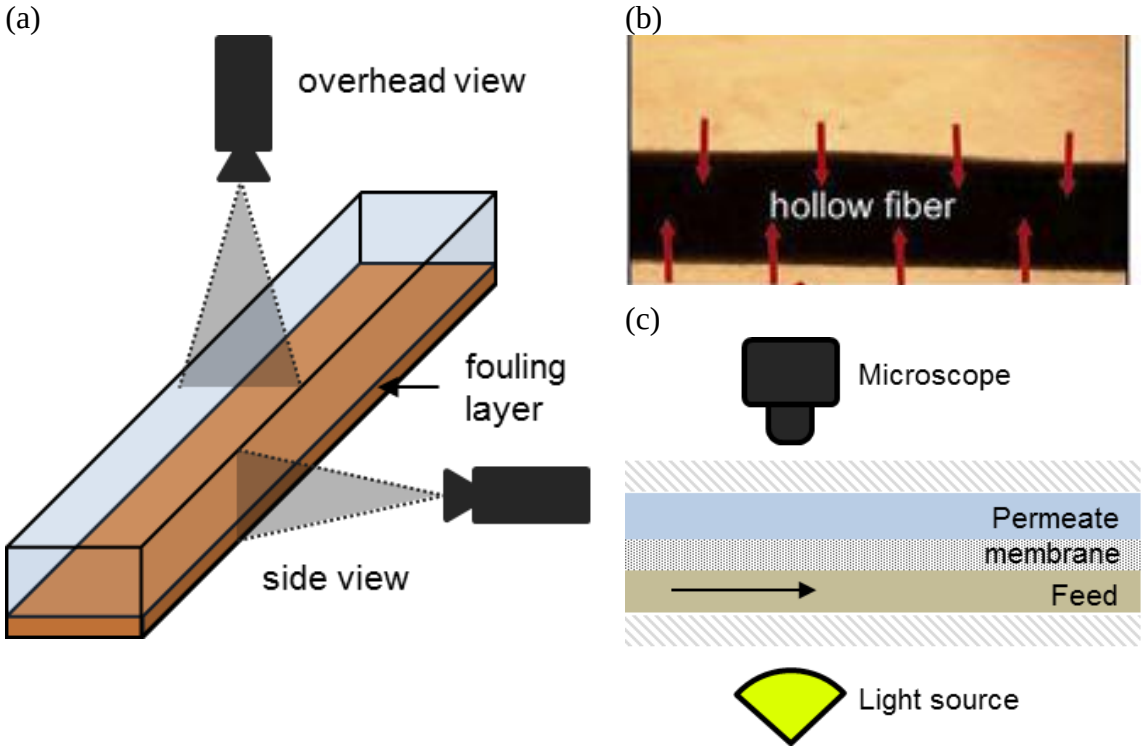

Figure 2.10. (a) General concept for direct observation techniques viewing from overhead and sideways (b) Direct observation of hollow fibre fouling, where red lines represent the direction of flux, reprinted from (Marselina *et al.*, 2008). (c) DOTM technique.

these have been that terminal cake thickness decreased with increasing cross-flow velocity and/or particle concentration. This method has not been widely adopted, however, as accuracy is limited by the precision of the viewing angle and the assumption that cake thickness at the viewing window is representative of the whole cake.

Mores and Davis (2001) used a microscope to monitor fouling from overhead on the feed side of the membrane (as indicated in Figure 2.10a), a technique they refer to as direct visual observation (DVO). Although it requires a light source to be shone through the membrane they have shown that this is possible using both transparent and non-transparent membranes (provided the membrane is at least partially translucent). They went on to use this method in the study and optimisation of backpulsing techniques (Mores and Davis, 2002a, b) and in later work, Knutsen and Davis (2006) used a similar set-up to track particles and measure their speed along a membrane surface. DVO has also been used with high pressure RO membranes to indicate the onset of microbial fouling (Huang *et al.*, 2010; Subramani and Hoek, 2008) and mineral scaling (2009; Uchymiak *et al.*, 2007). The effect of fouling on membrane feed spacers has also been investigated by Vrouwenvelder *et al.* (2007; 2006) using a "Membrane fouling simulator" which employs the overhead DVO principle, this time relying on reflected light from the surface of the membrane to contrast the fouled areas.

Hughes *et al.* (Hughes *et al.*, 2006a; Hughes *et al.*, 2006b, 2007) report a DVO technique in which three-dimensional images of the fouling layer could be attained during cross-flow filtrations. Their method involved using a standard optical microscope along with a multiphoton microscopy (MPM) excitation method (detailed in the above references) to illuminate fluorophore-stained yeast-cells in the cake. A disadvantage was that the images were obtained through a time-consuming scanning method which required that filtrations be halted in order to obtain a clear image.

A novel approach by Marselina *et al.* (2008; 2009), was to use a microscope and video camera assembly to capture the fouling of single polyvinylidene fluoride (PVDF) hollow fibre microfiltration membranes, which were mounted tightly in a crossflow module with an outside-in flow configuration. An example of an image acquired is shown in Figure 2.10b. In later work this technique was used to study removal mechanisms during backflushing, and also show evidence of different component parts (e.g. flowing and stationary) of a cake layer (Ye *et al.*, 2011).

Direct observation through the membrane (DOTM)

Li *et al.* (1998) reported a technique whereby they mounted a microscope and video camera assembly above a cross-flow filtration test cell, in which permeate flowed upwards through a transparent alumina membrane. This allowed them to view fouling from the permeate side of the membrane, as indicated in Figure 2.10c, such that they could observe foulant behaviour on the membrane surface. They went on to use this method to determine a critical flux in cross-flow filtrations, demonstrating how foulant deposition could be detected before significant indication by a loss of filtration performance (Li *et al.*, 2000). They also used this technique to assess the validity of inertial lift and shear-induced diffusivity models (which are described in sections 2.5.3 and 2.5.4). Their studies have included filtration of a variety of sizes of latex spheres, and fluorescently stained bacteria (Li *et al.*, 2003a). Zhang *et al.* (2006) used the same method with an inverted microscope to allow settling effects to take place, and used this to study microfiltrations of bidisperse mixtures of different sized latex spheres (Zhang *et al.*, 2006) and fractal hematite flocs (Zhang *et al.*, 2010). It has been used to determine critical flux and more complex initial fouling phenomena in filtrations of microalgae (Wicaksana *et al.*, 2012), as well as for determining a critical Peclet number for crossflow filtrations based on SID coefficients (Zamani *et al.*, 2014).

2.6.2 Laser Optics

The principle behind laser triangulometry, a positioning method used in a variety of applications outside the field of membrane fouling, is relatively simple. Diffuse reflection of an incident laser beam is used to indicate height changes of the reflective surface based on the angle at which it approaches a detector, as shown in Figure 2.11a. Schleup and Widmer (1996) used this to study cross-flow microfiltrations of yeast cell suspensions, and Altmann and Ripperger (1997) used similar apparatus to study cake deposition of diatomaceous earth and monodisperse silica particles. Mendret *et al.* (2007) reported an adaption where, instead of a single point on the surface, a laser sheet was projected across the width of the filtration cell, as shown in Figure 2.11b. The incident laser sheet was emitted at an angle, with a camera mounted directly above the area at which it reflected from the membrane/cake surface. The position of the reflected line on the surface relative to its position on a clean membrane was used (with image processing tools) to indicate cake height with a precision of about ±3 μm. They employed this technique to track cake growth during a dead-end filtration of a bentonite suspension. In later work they expanded their study to look at the effects of TMP on

deposit thickness (Mendret *et al.*, 2009), noting that initial deposition showed the highest resistance, and the cake only showed compressibility further from the membrane.

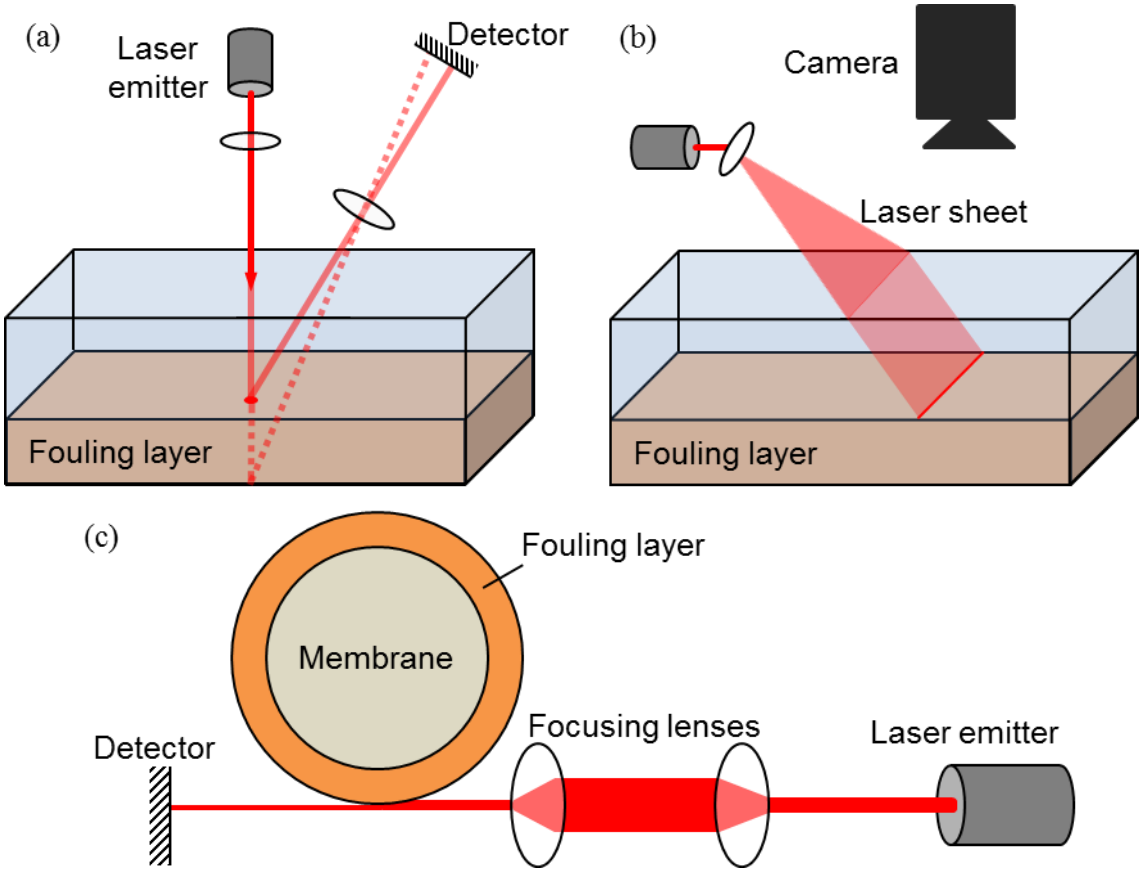

Figure 2.11. (a) Principle of laser triangulometry, where the solid line shows the path of the laser when there is a fouling layer, and the dashed line indicates the path for a clean membrane. (b) laser sheet adaption reported by Mendret *et al.* (2007). (c) Principle employed for tubular membranes, as reported by Hamachi and Mietton Peuchot (2001).

Another method using lasers has been demonstrated by Hamachi and Mietton Peuchot (2001), this time to monitor cake growth on a tubular membrane. They constructed a filtration apparatus which included a tubular ceramic membrane encased in a transparent cell. A laser was focused tangentially across the apex of the membrane or surface of the foulant layer, with a detector on the other side, as indicated in Figure 2.11c. During outside-in filtrations of bentonite, they were able to make high resolution thickness measurements in a range of 30 µm with a repeatability of about 10 µm, and could track growth above this range by adjusting the position of the laser emitter using a micrometer. In later work (Hamachi and Mietton-Peuchot, 2002) they demonstrated subsequent cake removal by increasing cross-flow velocity after a steady-state had been reached.

2.6.3 Ultrasonic Time-Domain Reflectometry

Ultrasound scanning has many industrial, military and medical applications, and works by exploiting acoustic impedance. When sound waves encounter an interface between two media of different density, a wave is reflected with an amplitude dependent on the difference in acoustic impedance. The time delay between emission of the incident wave and detection of the echoed wave can give an indication of the distance between the source and the interface, provided the acoustic impedance of the medium between the two is known. Using a high frequency it is possible to use this principle to detect multiple interfaces e.g. liquid-foulant, foulant-membrane, membrane-support etc. (Chen *et al.*, 2004). Figure 2.12a shows the methodology behind thickness measurements, where the time-domain responses of reflected signals A to C are shown in Figure 2.12b. The development of a signal response C, and its distance from A and B can be used to indicate the cake thickness. The movement of B must also be taken into consideration, due to the increased impedance caused by the cake slowing acoustic signals returned from the membrane surface. Hence it can be seen that the procedure can become quite complex.

UTDR was first applied to membrane filtration by Mairal *et al.* (1999), who demonstrated early detection of calcium sulphate scaling in RO membranes. In later work they also used it to track scale removal (Mairal *et al.*, 2000), proposing that UTDR could be developed into an effective tool for monitoring fouling layer development in real-time. It has since been used to study the fouling and cleaning of flat sheet membranes fouled with paper mill effluent and kaolin (Li and Sanderson, 2002; Li *et*

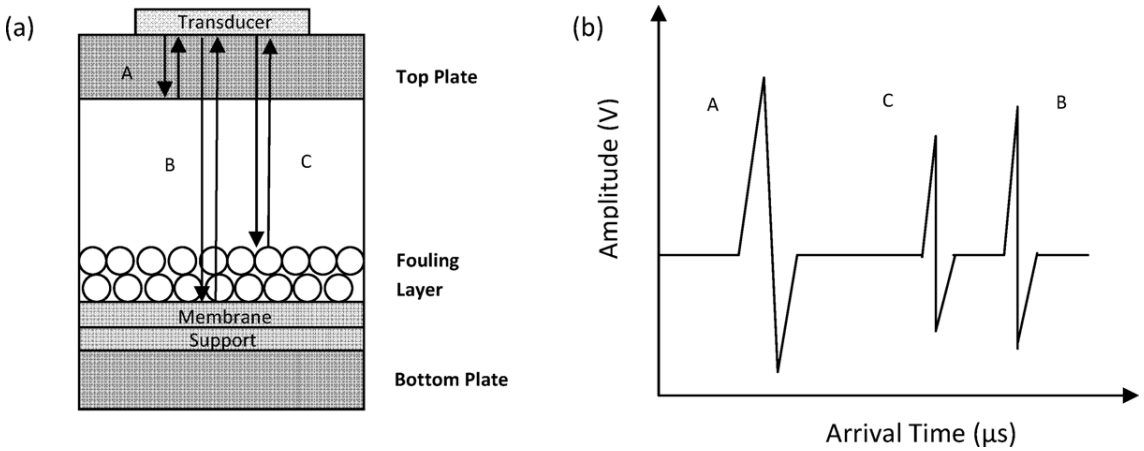

Figure 2.12. Principle of UTDR, where (a) represents the experimental technique, wherein a transducer sends an acoustic signal which is reflected at the shell/liquid interface at A, from the membrane at B, and the top of the fouling layer at C. The resulting response signals are shown in (b). Reprinted from Sim *et al.* (2012)

al., 2002a; 2002b). More advanced modelling and data analysis methods for interpreting time-domain response graphs have since been developed, demonstrating how it can also provide qualitative information about the structure of the fouling layer (Li *et al.*, 2003b). Its applications have expanded to include monitoring fouling in spiral wound (An *et al.*, 2011; Zhang *et al.*, 2003), tubular (Li *et al.*, 2006), and hollow fibre membranes (Liu *et al.*, 2006; Xu *et al.*, 2009a; 2009b).

More recently, 3D scanning ultrasonic measurements have also been made possible in both dead-end (Cheng *et al.*, 2011) and cross-flow (Lin *et al.*, 2013) filtrations, by mounting a transducer on a moving stage. UTDR has developed into a choice experimental method for studying important aspects of membrane fouling. For example Sim *et al.* (2012) selected it for studying the glass-transition of colloidal silica particles concentrated at the membrane surface during cross-flow filtrations. They were also able to enhance the technique for monitoring biofouling by dosing feeds with colloidal silica (Sim *et al.*, 2013b). Another innovation has been the installation of an array of UTDR transducers along the entire length of a submerged hollow fibre filtration module (Li *et al.*, 2014).

UTDR is a versatile tool which has shown many improvements over the last 15 years. Unlike the two previously described methods it can be operated with entirely opaque feeds; however the method is more complex than direct observation or laser optics. As far as can be ascertained from the literature, thickness measurements are either the result of some degree of manual interpretation of UTDR signals or advanced signal processing algorithms. Thus the method is still a highly specialised technique. In experimental comparisons with the laser sheet method outlined in section 2.6.2, performed by Loulergue et al (2011), it was noted by that the two methods can produce differing thickness measurements in the same filtration. This was linked to differences in cake density, and possible presence of a concentration polarisation layer. This brings to light an important point of both measurement techniques: that the thickness reading is representative of a point where a signal (either optical or acoustic) will be reflected, and this will depend on the nature of the fouling layer.

2.6.4 Nuclear Magnetic Resonance (NMR) Imaging

Images obtained using NMR are generated by mapping distributions of free protons (H nuclei), mainly from water and hydrocarbon compounds. The representation of each proton is weighted by its spin behaviour when subjected to pulsed radio frequencies in an applied magnetic field. It is completely non-invasive, and can generate

3-dimensional images of samples which are optically opaque down to a resolution of 10 μm or below. Because of this the application of NMR imaging has extended beyond clinical radiology to studies of various industrial processes.

One of the first attempts to apply this to membrane fouling was in the cross-flow filtration of oil-water emulsions through bundled hollow fibre microfiltration membranes (Yao *et al.*, 1995). The authors successfully produced reliable velocity profiles for flow within the membranes. By using selective Chemical Shift Imaging (CSI) they were able to produce cross-sections showing the distribution of oil or water. They used CSI to analyse CP layers and in later work identify oil droplets within the membrane pores (Pope *et al.*, 1996). From the flux profile and thickness of the polarisation layer they went on to determine its specific resistance. They were also able to obtain spatially localised values by taking readings at various axial planes along the membrane. The same research group has also presented NMR studies of CP in colloidal silica filtrations through tubular membranes (Airey *et al.*, 1998).

Very few NMR studies of membrane fouling have been reported, most likely due to the complexity and expense of the technique. Graf von der Schulenburg *et al.* (2008) used NMR with an industrial spiral wound RO membrane module, as well as a custom-built NF cell, to study biofouling of membrane feed spacers. They later expanded this work to cleaning studies (Creber *et al.*, 2010b), and for evaluating 3D simulations of flow disturbances due to fouling (Creber *et al.*, 2010a). Buetehorn *et al.* (2011) used NMR to observe cake growth and velocity profiles at different positions along a submerged holler fibre MF membrane, achieving cake thickness estimates with a resolution of ±17.6 μm through image processing.

Although it is capable of providing an extensive set of data for a filtration, NMR is a particularly laborious procedure, requiring the use of non-metallic apparatus capable of fitting into a NMR machine. The programming and data extraction is also very complicated and must be optimised to compromise between resolution and time sensitivity, requiring specialist support (Chen *et al.*, 2004). NMR is also limited by the characteristics of the foulant, requiring special considerations and adaptions to the technique (Airey *et al.*, 1998; Buetehorn *et al.*, 2011).

2.6.5 Electrical Impedance Spectroscopy (EIS)

By applying an alternating current of varying amplitude and frequency across a material, and measuring the amplitude and phase difference of the resulting electric potential across it, it is possible to infer a number of its physical properties (Coster *et al.*, 1996). Figure 2.13 shows the basic design of device which can perform this test. Local porosity, and electrochemical properties of both the skin-layer and sub-layer of a heterogeneous membrane can be inferred by comparing these measurements to those which would be observed in an ideal system of capacitors and resistors (Cañas *et al.*, 2001). Watkins and Pfromm (1999) showed that it was possible to monitor fouling of an ion exchange membrane in real-time by measuring the capacitance change at the electric double-layer between the solution and the membrane. Park *et al.* (2006) have used EIS to study BSA fouling of commercial ion-exchange membranes, and Kavanagh *et al.* (2009) have shown how it could also be applied to pressure-driven RO processes. Recently, a commercially available EIS unit was developed which can perform in-situ characterisation of RO membranes, as well as acting as an early warning system for fouling layer development (Panco-GmbH, 2012). This apparatus has since been used to study calcium carbonate scaling in RO filtration (Antony *et al.*, 2013), and also model

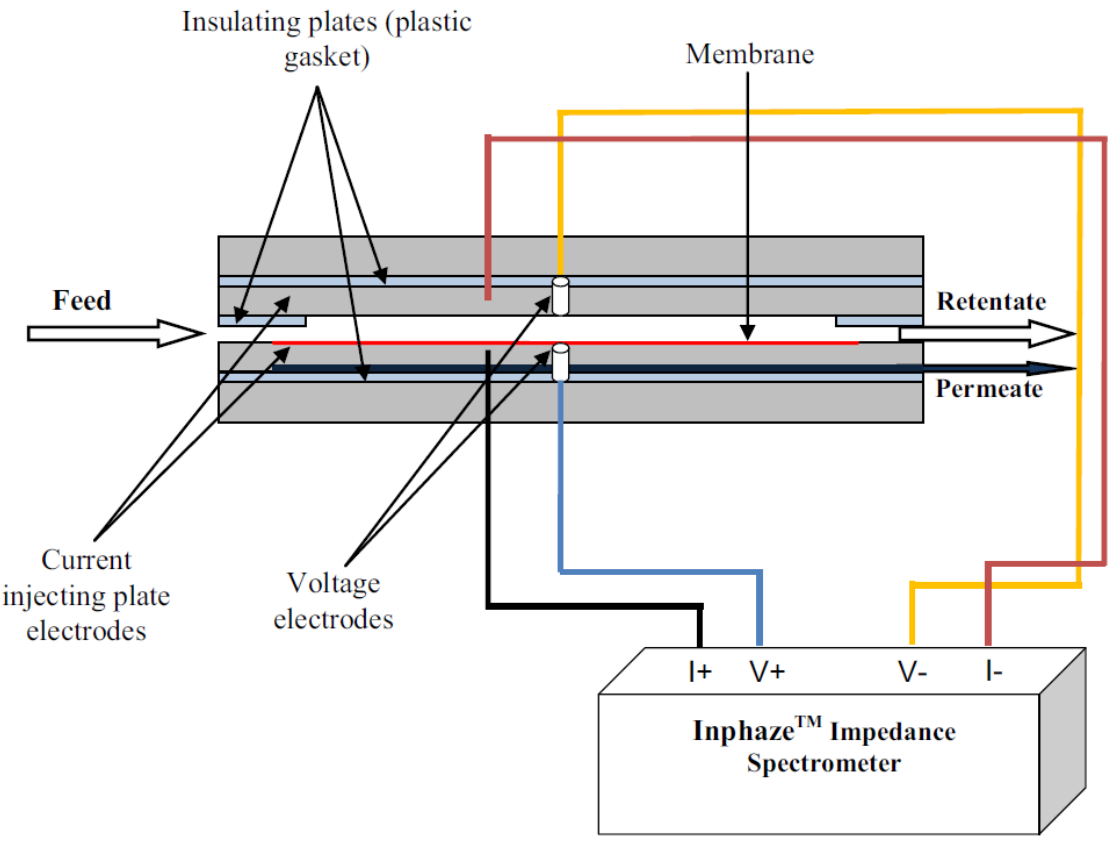

Figure 2.13. Basic design of an EIS unit, Reprinted from (Panco-GmbH, 2012).

solutions of BSA, silica, and a mix of the two (Sim *et al.*, 2013a). There are no notable studies on pressure driven MF and UF fouling by EIS as of yet, probably due to the need for conductive membranes and a suitable ionic feed concentration. There have also been no reports featuring a quantitative estimate of deposit thickness. This method has fairly niche applications, and requires a carefully designed module to achieve. Furthermore the interpretation of data gives an indication of fouling, but not an immediately available measure of its extent. The technology still appears to be in its infancy, requiring precursory studies to identify the characteristic EIS responses of different foulants.

2.6.6 Radiation-based measurements

Perhaps due to the inherent danger to the user, radiological measurements are not particularly popular as a means to perform in-situ studies of membrane fouling. Though some studies have looked at the porosity of cakes during sedimentation (Bergström, 1992), or performed radiography studies ex-situ (Lin and Miller, 2000), only one group of researchers based in Gothenburg appears to have attempted the use of such methods in-situ during filtration. Sedin *et al.* (2003) reported the use of γ-ray attenuation to measure the solid fractions of cakes formed during high pressure dead-end filtrations of kaolin, calcium silicate, and lignin suspensions. They used a cylindrical chamber with piston-driven flow to filter the suspension, with a radiation emitter and detector

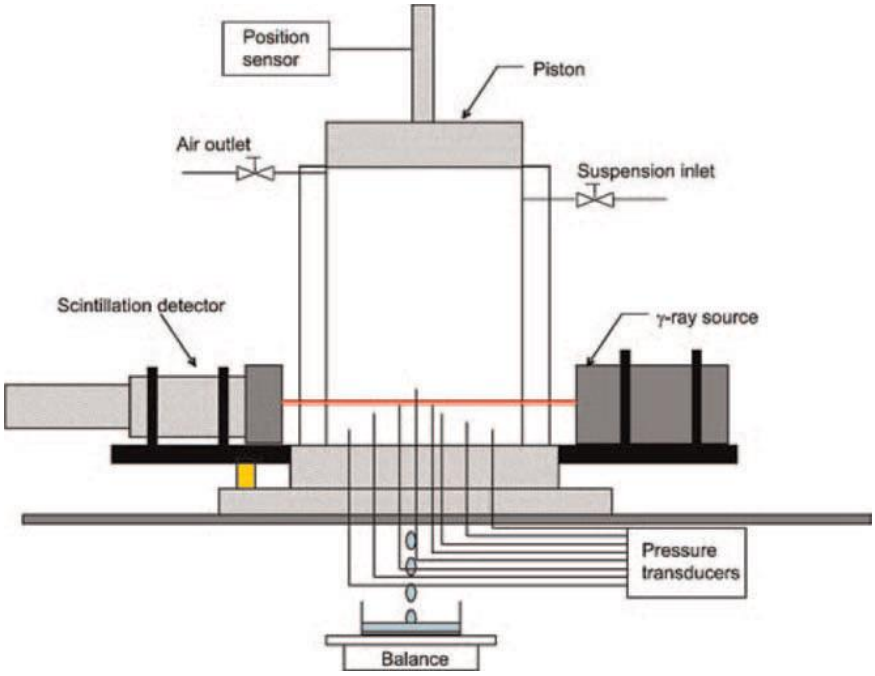

Figure 2.14. Diagram of the apparatus used by Johansson and Theliander (2007) and others to study porosity of fouling layers in dead-end filtration. Reprinted from (Johansson and Theliander, 2007).

mounted on opposite sides of the unit. These were vertically mobile, so that the volume fraction of solids in the cake could be estimated for different heights. Another addition they made to the system was a number of capillary tubes protruding to different heights through the membrane at the base of the chamber. This allowed them to measure local pressures through the cake, which could be related back to porosity. A diagram showing the setup of this apparatus, as reported by Johansson and Theliander (2007), is shown in Figure 2.14. Porosity estimations are made using the Beer-lambert law for both the liquid and solid phase, which relates the absorption of photons to the distance travelled and literature-sourced attenuation coefficients of a material.

Sedin *et al.* (2003) used this technique to look at cake compressibility, comparing it with constitutive relationships for specific cake resistance. It has since been used by Mattsson *et al.* (2011) to investigate the influence of zeta-potential on the properties of TiO_2 cakes, who produced further studies on the intricacies of dead-end filtrations of microcrystalline cellulose (2013; Mattsson *et al.*, 2012a, b). Of particular interest is their observation of a dense "skin" layer of particles closer to the surface of the membrane in some of their experiments. This is concordant with results published by Mendret *et al.* (2009), who reported this part of the cake to be incompressible. Mattsson *et al.* (2012a) expanded on this concept by showing how the type of membrane used or operating pressure could also have a significant influence on the formation of a skin layer.

Because this method has been performed in dead-end, it is possible to infer cake thickness from the volume fraction of the cake and the total permeate volume filtered. Not much emphasis is placed on the cake thickness, however, rather its local characteristics. Their use of radiation-based in-situ measurements for cake fouling in filtrations appears to be the only prominent example in the literature, and could conceivably be applied to cross-flow filtrations in the same manner.

2.6.7 Summary

A range of non-invasive tools have been developed to detect and characterise fouling in membrane filtrations. In quite a few cases the purpose of their use has been to advance the understanding of some of the underlying phenomena associated with fouling e.g. (Knutsen and Davis, 2006; Mattsson *et al.*, 2012a; Wakeman, 1994) and, where applicable, assess some of the mathematical models to describe the process e.g. Li *et al.* (2000; 2012). A common conclusion seems to be that there is some degree of fit with a model, but is often very specific and tailored to a particular feed which, in

these experimental circumstances, is often homogeneous and clearly defined. Hence it is unlikely that a one size fits all mathematical approach can yet be developed for modern industrial filtrations, in which a variety of different physical processes may be taking place concurrently.

Instead a more reasonable approach might be to develop early warning systems for industrial processes; for instance Li *et al.* (2014; 2012) have demonstrated detection of fouling layers when operating below critical flux, where fouling was not indicated by a TMP increase. Likewise Li *et al.* (2003a) reported that DOTM can detect surface fouling before standard process indicators would. The possibility of early detection is in fact a selling point of the commercially available EIS technique (Panco-GmbH, 2012). The challenge when designing an early warning device is how to implement it within existing apparatus. If it is impossible to install sensing apparatus on to existing modules, one tactic could be to mount a unit parallel to the main filtration system to give a representative indication of the extent of fouling.

Another more general use for these types of technique is to help optimise operating parameters for a process. An example of this are the direct observation studies for hollow fibres (Ye *et al.*, 2011), wherein backwashing principles could be explored at laboratory scale. For use in more industrially relevant systems however, all those mentioned above present one of two main drawbacks. The first is that some kind of light transmission is needed, so that they will not work with opaque feeds. The second is the requirement for more specialist and expensive equipment and expertise to attain and interpret data, often requiring specific knowledge of the feed properties beyond concentration and density.

The development of accurate techniques is of great benefit to the fundamental understanding of membrane fouling, but equally important are tools which allow a process to be characterised on-the-fly, and with little need for detailed prior characterisation of the feed. It must be able to indicate the speed and intensity at which surface fouling occurs, and also be able to assess how easily it can be removed. It is the purpose of this project to explore the potential of fluid dynamic gauging as a means to study membrane fouling with a greater efficiency and versatility than by the measures described above.

2.7 Fluid Dynamic Gauging (FDG)

Fluid dynamic gauging (FDG) was first developed by Tuladhar *et al.* (2000) as a means to measure the thickness of soft deposits on solid surfaces, such as whey protein fouling on stainless steel. It is based on the concept of pneumatic gauging, which was at one time a popular tool in engineering metrology (Evans and Morgan, 1964). The pneumatic gauging method employed the pressure-drop effect of a gas directed through a constriction between a nozzle and a surface. In FDG however, the flow is reversed, and the method operates by suction of a liquid instead of ejection of a gas. It has been used to study fouling for a variety of applications; ranging from scaling in heat exchangers (Chew *et al.*, 2005a) to fouling by food substances (Gordon *et al.*, 2012).

2.7.1 Theory and Principles

FDG operates using basic principles of fluid mechanics, based around pressure drops due to flow through a constriction and divergent nozzle. Figure 2.15a shows a schematic of an FDG gauge, which consists of a tapered nozzle affixed to the end of a tube. This is suspended above a surface in a liquid medium. When applying a constant differential pressure, Δp_{14}, between the surrounding liquid region (1), and an arbitrary point down the length of the gauge tube (4), fluid flows into the nozzle. The flowrate, m_g, is governed by the size of two contractions in the flow path. Between (1) and (2)

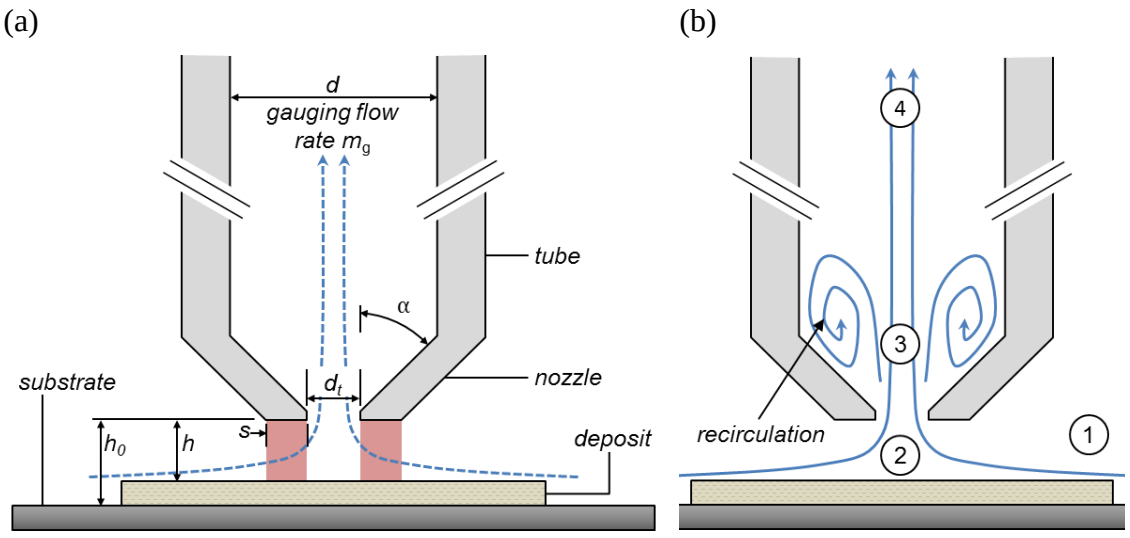

Figure 2.15. (a) Schematic of FDG gauge, consisting of tube of diameter, *d*, a nozzle with throat diameter, d_t, taper angle, α, and rim width *s*. The tip of the nozzle is suspended at a known height h_0 from a substrate, and its height above the surface of a deposit can be inferred from the mass flow m_g into the gauge. The area shaded red indicates the region of interest where thickness and strength measurements are made. (b) Flow paths within the gauge showing the recirculation region. Points 1-4 represent critical locations between which pressure changes are of particular relevance to the theory.

the flow constriction is related to the clearance, h of the nozzle from the surface below. Between (2) and (3) the flow constriction is related to the nozzle orifice diameter, d_t. As shown in Figure 2.15b, recirculation occurs within the nozzle at point (3), due to the downstream expansion after the orifice. For this reason the height at which (4) is defined is important, as it must be assumed that flow at this point is laminar and fully developed.

The flowrate, m_g can be characterised by a dimensionless discharge coefficient, C_d, defined as (Tuladhar *et al.*, 2000):

$$C_d = \frac{actual\ mass\ flowrate}{ideal\ mass\ flowrate} = \frac{4m_g}{\pi d_t^2 \sqrt{2\rho_L \Delta p_{13}}} \tag{2.34}$$

which scales the actual flowrate against an ideal prediction using the Bernoulli equation, which neglects viscous effects. Here ρ_L is the density of the fluid, and Δp_{13} is the pressure drop between points (1) and (3). Δp_{13} cannot be measured directly, so instread it is determined using the Hagen-Poiseuille equation to approximate pressure drop between points (3) and (4), Δp_{34}:

$$\Delta p_{13} = \Delta p_{14} - \Delta p_{34} = \Delta p_{14} - \frac{128 \mu m_g l_{eff}}{\pi d^4 \rho_L} \tag{2.35}$$

where μ is the viscosity of the fluid, and l_{eff} is the effective length of a tube with diameter d between point (3) and a pressure tapping at (4). l_{eff} takes pipe contractions and bends into consideration.

The general relationship between C_d and a dimensionless measure of clearance from the surface, h/d_t, is shown in Figure 2.16. C_d exhibits a strong dependence on h/d_t at where $h/d_t < 0.25$, labelled on Figure 2.16 as the *incremental zone*. Within this region the flow restriction is dominated by the clearance, h, from the surface below. Above this value, C_d tends towards an asymptote, where flow becomes limited primarily by the nozzle throat diameter, d_t, and not h. Tuladhar *et al.* (2000) determined this ratio analytically using Bernoulli's principle for flow through a contraction, and went on to demonstrate this empirically. It stands to reason that when using FDG to make thickness measurements, it should be operated in the incremental zone.

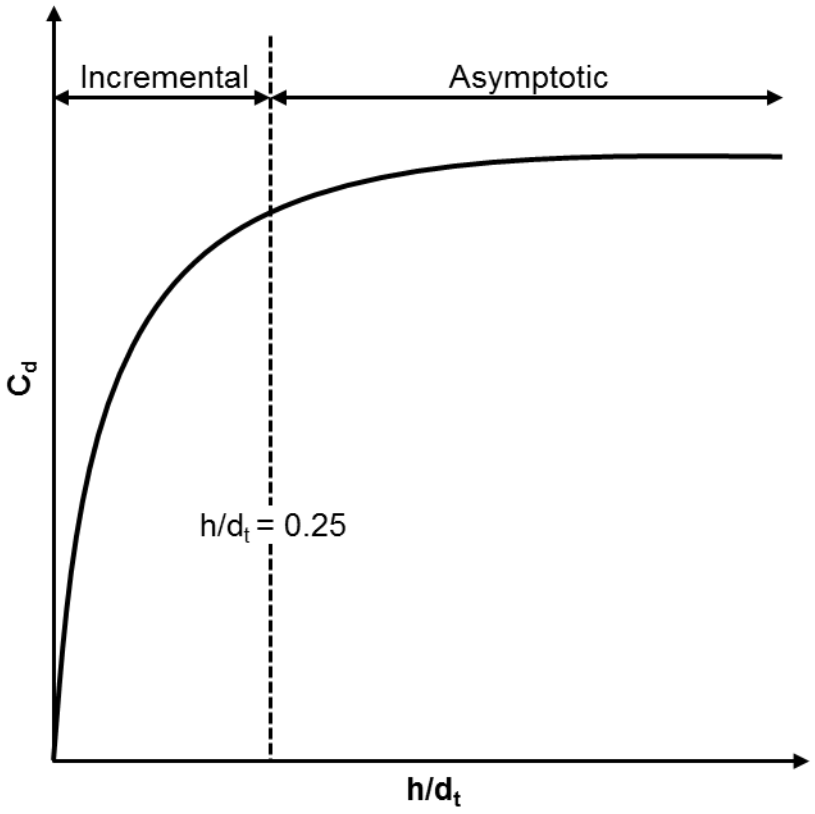

Figure 2.16. General profile of C_d vs. h/d_t, where the dashed line indicates the transition point, at h/d_t = 0.25, between incremental and asymptotic behaviour.

They also demonstrated that the same relationship for C_d vs. h/d_t could be achieved over a stainless steel substrate and a variety of deposits of known thickness, approximating the relationship by the following equation:

$$C_d = A\left(1 - e^{-B\frac{h}{d_t}+C}\right) \tag{2.36}$$

where A, B and C are constants. By using measurements of Δp_{14} and m_g to calculate C_d using equation (2.34), it is then possible to back-calculate using (2.36) to estimate the clearance, h, from a deposit when the gauge nozzle is at a known clearance, h_0, above the substrate. The thickness of the deposit, δ, is then given by:

$$\delta = h_0 - h \tag{2.37}$$

2.7.2 Modes of operation

There are two modes of operation by which fluid dynamic gauging measurements can be performed, *mass flow mode* and *pressure mode*.

Mass flow mode

This is the original configuration developed by Tuladhar *et al.* (2000) wherein a differential pressure between points (1) and (4) on Figure 2.15 is achieved using hydrostatic pressure. The flowrate, m_g is used to calculate C_d and from this, deposit thickness is estimated using equations (2.36) and (2.37). Because the flow must be discharged to atmosphere for measurement, this limits the pressure under which an FDG system can be operated. There is also no way to control the rate at which fluid is lost from the system due to gauging flow, this can create practical issues when operating the technique, as a constant pressure head must be maintained in the FDG environment for mass flow mode.

Pressure mode

Instead of controlling Δp_{14} and measuring m_g, it is possible to set a constant gauging flowrate using an adjustable valve and measure Δp_{14}. Equations (2.36) and (2.37) can again be used to estimate deposit thickness, or h/d_t can be inferred directly from a plot of Δp_{13} vs. h/d_t. This is the preferred mode for studies of fouling in flowing environments because it can be performed at significantly higher pressures and with a small and controlled rate of removal from the system so as not to affect the overall flow conditions (Gu *et al.*, 2011a).

2.7.3 Strength measurement using FDG

Although non-contact, FDG cannot be described as truly non-invasive. This is because inherent in all measurements, there is a fluid shear stress exerted on the surface of the fouling layer. This is most significant in the area directly beneath the nozzle tip, corresponding to the shaded region in Figure 2.15a, and is the main cause of the pressure drop between (1) and (2), Δp_{12}. With accurate determination of this, however, one can investigate the response of fouling layers to fluid shear at a large range of values. Coupled with thickness readings, it is also possible to track the removal of foulant at elevated fluid shear. This concept was first explored by Chew *et al.* (2004a), who used CFD to predict shear stress distributions and went on to demonstrate the shear-induced removal of tomato paste from a stainless steel substrate (Chew *et al.*, 2004b). From this they were able to infer a yield strength of the deposit corresponding to the adhesion strength to the surface. Further studies were performed for polymeric fouling in quasi-static systems (Chew *et al.*, 2005b; 2006), also for inorganic scaling of stainless steel plates in duct flow systems (Chew *et al.*, 2005a).

CFD studies by Chew *et al.* (2004a), and Gu *et al.* (2009b) both showed good agreement with an analytical model for the shear stress, τ_w, on the surface underneath the nozzle within the area of interest. This is a solution to the Navier-Stokes equations for converging flow between parallel discs, derived by Middleman (1998):

$$\tau_w = \frac{3\mu m_g}{\rho_L \pi h^2}\frac{1}{r} \tag{2.38}$$

where r is the radial distance from the central axis of the gauge tube. For FDG, the maximum shear stress, $\tau_{w,max}$ will occur around the inner edge of the nozzle rim at $r = d_t/2$. Equation (2.38) is derived assuming creeping flow, where inertial effects are ignored. The criteria for this is defined as (Fryer *et al.*, 1985):

$$\frac{m_g h}{24\rho_L \pi r \mu} \ll 1 \tag{2.39}$$

The validity of equation (2.38) will be explored in more depth in Chapter 8.

2.7.4 Previous FDG studies

The original study by Tuladhar *et al.* (2000) demonstrated that thickness measurements could be made for whey protein, butter and sticky foam on a stainless steel surface. They also investigated the cleaning of whey protein deposits from the surface using NaOH, demonstrating how the deposits swelled over time before being removed. These tests were performed with the fouled surface suspended in a static volume of liquid, where the only flow in the system was through the gauge by means of a siphon effect. This mode of operation is herein referred to as a *quasi-static* system.

In further studies, the authors used FDG to demonstrate the cleaning-in-place (CIP) of whey protein fouling in a *duct flow* environment (Tuladhar *et al.*, 2002a, b, 2003). They achieved this by attaching an FDG gauge to a heat-transfer module, and operating it in mass-flow mode.

Quasi-static FDG

Although investigations of fouling in a flowing environment are more representative of industrial processes, quasi-static FDG remained a very useful tool for investigating surface fouling phenomena. Chew *et al.* (2004a) reported its successful application to non-Newtonian fluids; and have also developed a rig in which the gauge can be moved along an axis parallel to the surface. This latter FDG design was also capable of taking pressure readings at a point on the surface itself using a manometer

(Chew *et al.*, 2004b), which they used to verify CFD simulations. They used this rig to make strength measurements of food deposits and calcium sulphate scaling on stainless steel plates (Chew *et al.*, 2005a). Solvent-based cleaning of polymeric fouling has been studied using FDG in a rig specially designed for processing solvents (Chew *et al.*, 2005b; 2006).

Sahoo *et al.* (2008) mounted a quasi-static FDG rig above a confocal microscope and used this apparatus to provide simultaneous mechanical, chemical and microstructural properties of whey protein gels. Another recent adaption to quasi-static systems is the implementation of scanning mode FDG (sFDG), which was first proposed by Chew (2004). Gordon *et al.* (2010) demonstrated how multiple samples or different areas of fouling can be analysed on a surface by moving it along *x* and *y* axes. They used this FDG configuration to study the removal of gelatine films and egg yolk using enzyme-based cleaning agents (Gordon *et al.*, 2011a; 2011b). Peck *et al.* (2013) have also used qausi-static FDG to investigate biofilm adhesion to different surfaces.

A combination of experimental and CFD studies was employed by Peralta *et al.* (2011a, b) to investigate different nozzle geometries and develop an analytical method for selecting the appropriate nozzle design for a particular application. By adapting the shape of the nozzle they showed it was possible to create a relatively flat shear stress profile on the surface below the gauge. Another important adaption to a quasi-static gauging system was made by Yang *et al.* (2014). In the first published use of pressure-mode FDG for a quasi-static system, Yang *et al.* described the use of a syringe pump to control m_g and a differential pressure transducer to measure Δp_{14}. By operating the syringe pump in different directions they were able to test the adhesion of petroleum jelly to a stainless steel surface under two different conditions, namely suction and ejection mode. Stark differences were seen in the response of fouling layers between these two modes. They dubbed this *zero discharge FDG* due to it being a closed system.

Duct flow FDG

Following on from the work of Tuladhar *et al.* (2003), Hooper *et al.* (2006) investigated the use of duct flow FDG for studies of protein fouling, comparing it to its quasi-static counterpart. Gu *et al.* (2007; 2009b) performed CFD simulations of duct flow FDG. They found good agreement between CFD predictions and experimental data for C_d vs. h/d_t profiles. Their simulations showed that strength measurements could also be performed in duct flow systems. This work has led on to the development of a FDG technique for application to annular flow sections for studying fouling and cleaning in heat exchangers (2011a; 2011b; Gu *et al.*, 2009a), who also demonstrated

the first use of pressure-mode FDG. This design was later adapted by Ali *et al.* (2013) to work at higher temperatures and pressures.

Membrane FDG studies

Chew *et al.* (2007) showed how a few small adaptions to a previous FDG rig allowed measurements of particle fouling during dead-end filtration, which led towards recent studies of membrane fouling (including the present work). They also combined this with an inverted microcope to view fouling from the permeate side of a transparent membrane (Chew *et al.*, 2010). The first FDG studies on cross-flow filtration were pioneered by Jones *et al.* (2010a; 2010b; 2012), who performed real-time thickness measurements of fouling layers during cross-flow microfiltrations of sugar beet molasses through flat sheet polysulphone membranes. These studies were all performed at high cross-flow velocity under turbulent conditions, and used mass-flow mode FDG. Lister *et al.* (2011) have demonstrated the use of duct flow FDG in cross-flow membrane filtrations (under laminar flow conditions) of model suspensions of spherical glass beads by pressure-mode FDG. They also reported preliminary CFD simulations used for strength measurements, which include consideration of membrane flux. They concluded that FDG can be successfully applied to membranes and porous surfaces in a flowing environment.

2.8 Conclusions

Membrane fouling is a widely studied and varied field. A number of models exist to describe cake fouling and removal based on known properties of a feed. To test such models and to investigate various fouling phenomena requires novel techniques to elucidate the fouling mechanisms taking place. Ideally such techniques need to provide an indication of cake thickness in-situ and in real-time.

Table 2.6 provides a comparison between FDG and the methods discussed earlier in this chapter. A rating out of five is given for each based on the following factors:

- *Operability:* A higher rating indicates a higher ease of operation and lower technical expertise required to use.
- *Cost:* A higher rating indicates a lower cost to assemble the apparatus
- *Versatility:* Lower ratings mean there are fewer fouling systems which can be investigated.
- *Accuracy:* How accurately cake thickness can be estimated.

Table 2.6. Comparison of FDG with other techniques, where a maximum of five stars is allocated for the most desirable quality in each category (e.g. for high operability and accuracy, and low cost).

Method	**Operability**	**Cost**	**Versatility**	**Accuracy**
DOTM	☆☆	☆☆	☆	☆☆
DVO	☆☆	☆☆	☆☆	☆☆
UTDR	☆☆☆	☆☆☆	☆☆☆☆	☆☆☆☆
Laser-optics	☆☆☆	☆☆☆☆☆	☆☆	☆☆☆☆☆
EIS	☆	☆☆☆	☆	N/A
Radiation-based	☆☆☆	☆☆☆	☆☆☆☆	N/A
FDG	☆☆☆☆☆	☆☆☆☆	☆☆☆☆☆	☆☆☆

While other methods such as UTDR and laser optics can potentially produce a more reliable estimate for cake thickness, FDG offers advantages in cost, versatility, and operability. With further developments it should be possible to develop equipment in which it can operate almost completely automatically. This would make it one of the most feasible and reliable techniques for gaining an insight into the fouling behaviour of complex and otherwise uncharacterised foulants.

Chapter 3: Aims and Objectives

Membrane fouling is a phenomenon which, although extensively studied, is not fully understood or predictable. Ultimately, a comprehensive, constitutive model to describe membrane fouling and the reduction, prevention or amelioration thereof, would be of great importance to all industry sectors in which membranes are used. This, however, would require intrinsic knowledge of many different properties of the process feed which determine how foulants interact with the membrane. Such properties may be impossible to determine accurately or require specialist equipment to do so. Some models, as discussed in sections 2.4 and 2.5, have been developed to describe various mechanisms of foulant deposition and/or removal. In addition a variety of lab-based techniques have been developed (see section 2.6) which can be used to elucidate some of the behaviour such models describe. Some common drawbacks of these techniques are the need for translucent feeds, specialist support and/or analytical equipment, and specific properties of the feed not readily available. While providing a means to test underlying theory, they do not lend themselves immediately to a straightforward monitoring and testing protocol which could be used within industrial filtration processes.

3.1 Aims

Fluid dynamic gauging is a technique which can be used to estimate cake fouling thickness and strength properties in-situ. It requires little or no precursory knowledge of the feed properties, and is cheap to install and operate. The aim of this work is to further the development of FDG as a tool to study membrane fouling, with emphasis on its development as a tool for industrial purposes. This means ensuring that it can work in opaque, non-ideal feeds and potentially test food-related foulants. It must also be easily operable and demonstrate the ability to provide useful information about a membrane fouling system.

A smartly designed FDG system should allow for faster improvement and optimisation of membrane unit operations by providing a better indication of the effects of different cleaning protocols or operating conditions. If installed in-line with an ongoing filtration it would also allow for real-time adaption to changing feed streams, so that cleaning agents could be more appropriately selected.

3.2 Objectives

The overall aims described above were realised by three approaches. Primarily by further implementation of the technique to demonstrate its efficacy and investigate how it relates to existing mathematical models for cake fouling. Secondly, a new piece of FDG apparatus was developed as part of this project with enhanced automation features. Finally, CFD techniques were applied to enhance understanding of FDG operations.

3.2.1 Implementing the technique

FDG was used to monitor cake thickness and perform strength tests in cross-flow microfiltrations of both ideal (homogeneous spherical particles) and non-ideal (food-like or organic) suspensions. Commercially available cellulosic membranes were used in all experiments. This included studying cake growth at a variety of transmembrane pressures and cross flow velocities. Strength tests were used to identify how difficult cake layers closer to the membrane surface were to remove by fluid shear forces when compared to those on the cake surface. Using results from FDG the fouling models described in section 2.5 were assessed for their viability.

3.2.2 Apparatus development

A new cross-flow filtration apparatus has been developed with an automated FDG system. It includes features to read thickness measurements on-the-fly and improve upon previous designs used by Jones *et al.* (2010b) and Lister *et al.* (2011). This apparatus can, through LabView™ (or other suitable data acquisition and instrument control) programming, eventually be capable of performing FDG measurements automatically, making it ideal for practical applications in industry. This report gives details of the user interface developed in order to make this possible.

This system will also implement a smaller nozzle, half the size of the aforementioned designs, in order to minimise the overall footprint of the FDG gauge in the flow channel. This will increase the upper limit of shear stress at which measurements can be performed, and increase the precision of thickness measurements.

3.2.3 CFD studies

Computational fluid dynamics (CFD) was employed to produce calibration profiles for FDG more accurately than could be achieved experimentally. In addition, CFD was used to estimate shear stress profiles on the surface of fouling layers when

making strength measurements using FDG. This helped to assess the viability of such measurements and also test the applicability of the model described by equation (2.38) for predicting surface stress.

Chapter 4: Duct Flow Rig

The equipment used by previous researchers (Chew *et al.*, 2005a; Lister *et al.*, 2011) for duct flow FDG studies was recommissioned to study filtrations of two different types of suspension. The first, yeast, was used to verify that FDG could be used to monitor the growth of soft, food-like fouling deposits on membranes. The second, inert glass microspheres (ballotini), was investigated in order to assess different models which describe foulant removal.

4.1 Apparatus

4.1.1 FDG Gauge

In these experiments an FDG gauge with the following dimensions was used (see Figure 2.15a): d = 4 mm, d_t = 1 mm, α = 30°, s = 0.5 mm

4.1.2 Test section

The test section, shown in Figure 4.1, is similar to that used by Lister *et al.* (2011). The main body was constructed from Perspex to form a square duct of 15 mm cross-section at the entrance. The membrane (M) was supported on a stainless steel mesh spacer (S) and held in place between the top and bottom parts of the test section using a rubber seal (RS) to prevent leakage around the membrane. As evident in Figure 4.1a, the membrane is fitted at the bottom of a 3 mm recess within the duct. Permeate was collected from the bottom of the test section and a bleed point (BP) was used to remove air from the underside of the membrane and spacer. Transmembrane pressure was measured by a differential transducer, dP_1 (*Omega Engineering*, PX26-005DV, ±1 mbar), connected to pressure tappings (PT) via flexible tubing. An FDG gauge (G) is suspended above the membrane through an o-ring sealed hole in the test section. Gauge height was adjusted and measured using a micrometer screw, Mi (*Mitutoyo*, ±5 μm), supported by a guide rail and spring (SP). The outlet from the gauge was connected by a short flexible coupling (FC) to an X-piece (X). Δp_{14} was measured using a differential transducer, dP_2 (*Omega Engineering*, PX26-001DV, ±0.25 mbar), which was connected by flexible tubing to the X-piece and a pressure tapping (PT) into the duct. A bleed point (BP) on the top of the X-piece was used to remove air bubble from the system, and needle valve (NV) downstream was used to control gauging flow, m_g.

(a)

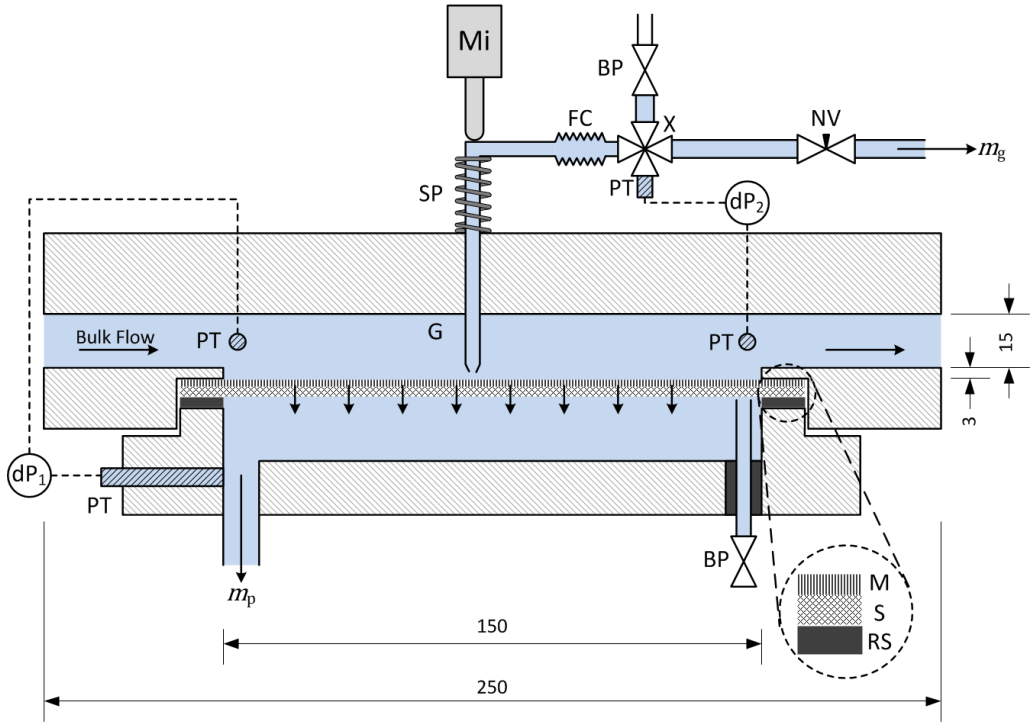

(b)

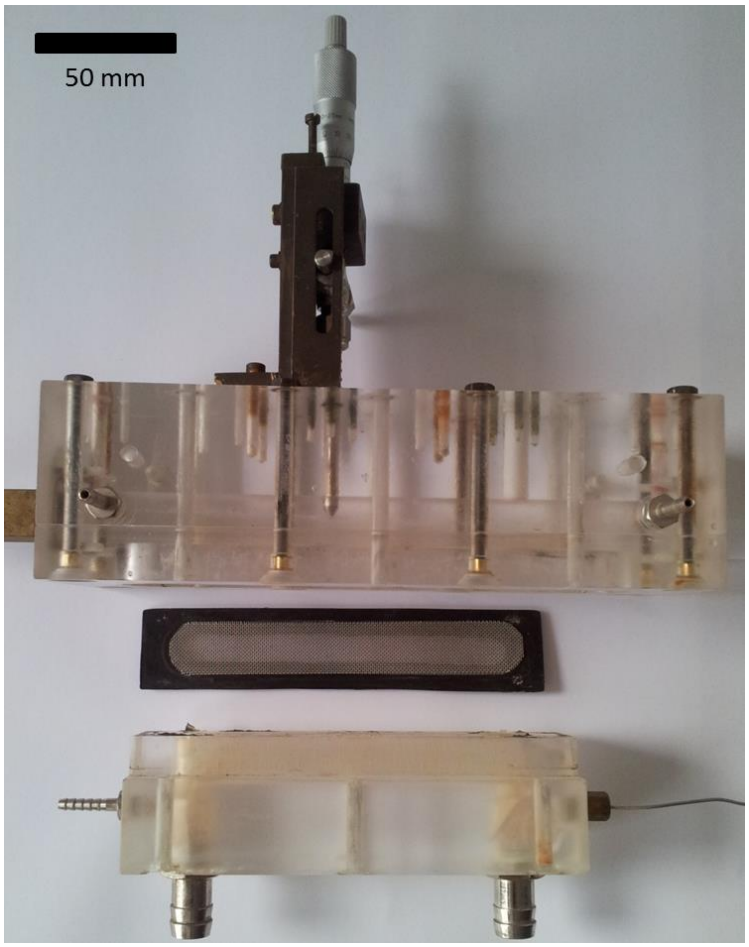

Figure 4.1. (a) Diagram of duct flow test section NV – Needle Valve, PT – Pressure Tapping, FC – Flexible Coupling, Mi – Micrometer, X – X-Piece, SP – Spring, BP – Bleed Point, G – Gauge, M – Membrane, S – Spacer, RS – Rubber Seal. Dimensions are in mm. (b) Photograph of test section, split apart to show the spacer and rubber seal between the two halves.

4.1.3 Flow loop

The flow loop was set up as shown in Figure 4.2. Process media was stored in a 15 L stirred tank, and circulated through the system by a regenerative pump (*Totton*, HPR 6/11). Flowrate into the test section was measured by a variable area flowmeter (*KDG Instruments*, Rotameter Series 1100), and controlled by V1 and a needle valve attached to the flowmeter. A 500 mm long square duct of 15 mm cross-section forms an entry section immediately prior to the test section, which exists to ensure a fully developed flow at the entrance. V2 was used to control TMP, however for ballotini filtrations this was replaced with a Y-piece of variable height, creating a weir for more accurate pressure control (shown in Figure 4.10). Permeate flow, m_p, and gauging flow, m_g, were recorded using electronic balances (*A&D*, FX-3000i, ±0.005 g) connected to a data-logging PC. In order to prevent any suction beneath the membrane from the permeate line, a Y-piece was fitted downstream of the permeate outlet. It was open to atmosphere such that a constant liquid head could be maintained level to membrane.

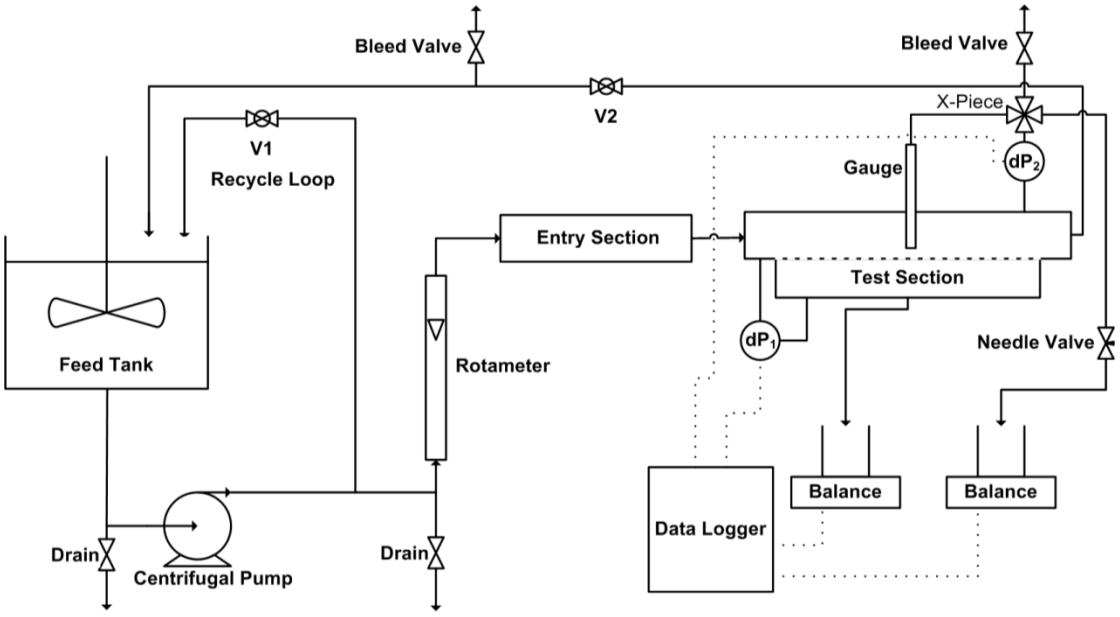

Figure 4.2. Flow loop for duct flow apparatus

4.1.4 Data Acquisition

The pressure transducers used contain a small piezoresistive element, which changes resistance under applied stress. Pressure is indicated by measuring an output voltage under an applied excitation voltage. A constant potential of 10V was supplied to the transducers and the output voltage was amplified by three orders of magnitude for

reading with a data acquisition (DAQ) device (*Advantech*, ADAM 4019+). Balances were connected to the PC via RS-232 interface.

Experimental data was timed and logged in a specially developed visual interface (VI) using LabView™ 2010. Readings from each pressure transducer and balance were logged every 0.75 s (the highest frequency at which the VI was stable) in a constantly running command loop. Table 4.1 summarises the input and output data processed by the VI. A more thorough description of how output data is calculated is given in appendix D1.

Table 4.1. List of inputs and outputs to and from the VI program. Superscripts show: RT – data shown in Real-Time, OC – data updated On-Command, † – implemented in ballotini experiments only.

Inputs	**Outputs**
Gauge height h_0	Pressures TMP and Δp_{14} from transducers [RT]
Height offset $h_{0,offset}$ [†]	Mass readings, M_g, and M_p, from balances [RT]
Voltage signals from transducers dP_1 and dP_2	Mass flow from gauge, m_g [RT]
Mass readings as data strings from balances	Mass flow of permeate, m_p [RT]
Fluid properties ρ_L and μ	Discharge coefficient, C_d [OC]
FDG dimensions and effective length d, d_t and l_{eff}	Errors for m_g, m_p, TMP and Δp_{14} readings [RT]
Membrane area A_m	Estimated height, h [RT, †]
Time, t (from internal PC clock)	Estimated deposit thickness δ_c [RT, †]
C_d vs. h/d_t correlation parameters [†]	Flux, J [RT, †]
Array size (N_{array}) for m_g, m_p, TMP and Δp_{14} readings [†]	Arrays (Ar) and/or graphs (Gr) of the following data: • C_d vs. h/d_t [Ar, Gr, OC] • J and TMP vs. t [Ar, Gr, RT, †] • C_d vs. h/d_t calibration plot with data overlay [Gr, OC, †] • All output data vs. time [Ar, OC, †]

4.2 Materials

4.2.1 Continuous media

Foulants were suspended in reverse osmosis water (conductivity 7-10 μS) in all experiments, obtained from an on-site RO unit (*Veolia*, Sirion Midi). The water was de-aerated using a cylindrical vacuum chamber (*Island Scientific*) connected to a 2-stage rotary vacuum pump (*Edwards*, E2M2). All experiments took place at ambient temperatures of 15-18°C.

4.2.2 Yeast Filtration

Membranes

Mixed cellulose ester membranes of 5 μm nominal pore size (*Millipore UK*, SMWP29325) were used in this study, which were provided as 293 mm circular sheets. These were hydrophilic, symmetric membranes. The membrane permeability was characterised by dead end filtration (described in appendix C.), and thickness also estimated using electron microscopy. The characterisation data is summarised in Table 4.2, from which it is clear that the permeability measured in the lab is over 50% higher than that indicated by the manufacturer. The reasons for this are unknown.

Table 4.2. Membrane characterisation data from manufacturer (Millipore, 2014) and experiments. Tolerance range of these values is indicated where known.

	δ_m (μm)	Flux at 0.7 bar ($mL \cdot min^{-1} \cdot cm^{-2}$)	κ ($\times 10^{-13}\ m^2$)	R_m ($\times 10^{8}\ m^{-1}$)
Millipore specs	135	580	1.87	7.22
Experiments	145	846 ± 26	2.85 ± 0.09	5.08 ± 0.15

Scanning electron miscroscopy micrographs taken of the membrane (using a *JEOL* JSM648LV electron microscope), are shown in Figure 4.3. It is clear from SEM analysis that the membrane exhibits a networked pore structure, with some surface pores appearing to be larger or smaller than the nominal diameter of 5 μm. As a result it is plausible that during filtrations particles larger than the nominal pore size could still block pores.

(a) (b)

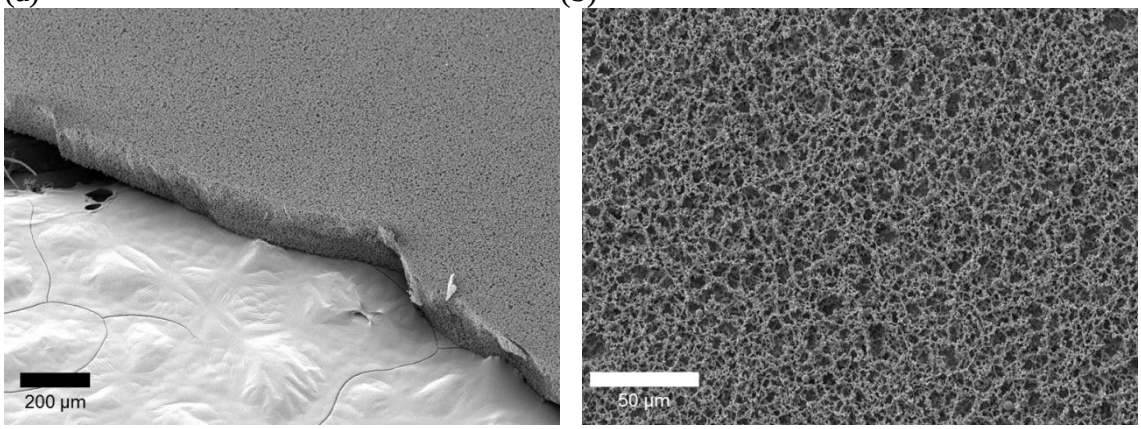

Figure 4.3. SEM Micrographs of *Millipore* SMWP mixed cellulose ester membrane. (a) shows a fractured edge of the membrane at 80× magnification. The adhesive surface used to secure the membrane can be seen at the bottom left of the image. (b) shows the membrane surface at 500× magnification. Both images are taken at 5 kV and membranes were gold-sputtered prior to microscopy.

Yeast suspension

Dried inactive *S. Cerevisiae* yeast powder (*Sigma-Aldrich UK*, 51475) was suspended in de-aerated RO water at a concentration of 1 $g \cdot L^{-1}$ (0.09 vol%). The de-aeration procedure was performed to prevent air bubbles developing in the gauging apparatus which could affect FDG readings. The pH of the suspension was 5.9, measured using a handheld meter (*Hanna instruments*, p-HEP). Yeast cells are known to flocculate most at an isoelectric point of pH 3.6 (Narong and James, 2006). Single cells of this type of yeast are reported to be typically ovoid in shape, with a diameter in the region of 6 μm (Narong and James, 2006). This was confirmed by imaging the yeast suspension under a microscope (*Nikon*, Diaphon 300) and using ImageJ to manually estimate cell dimensions. Cells imaged had lengths of 5-8 μm, and widths of 3-5 μm. Examples of microscope images are shown in Figure 4.4, in which it is clear that some significant cell flocculation occurred. Increasing pH using NaOH was found to limit flocculation (images not shown here) although this was not utilised in experiments. Flocculation of yeast cells could also be due to the presence of "sticky" substances which become adsorbed on to cell walls in the drying process (Guillemot *et al.*, 2006).

The particle size distribution of the suspension was characterised using a laser diffraction particle sizer (*Coulter*, LS230)[*]. The sample was fed to the device as a dry powder into an RO water reservoir, and also as a pre-mixed suspension. A Mie scattering model was used to fit the data, using a refractive index of 1.38, as determined by Malone (2010).The results, shown in Figure 4.5, display good repeatability for each method. It is clear from the graph, however, that there are more particles greater than 100 μm diameter for the samples tested by adding a pre-mixed suspension to the device. Despite this, cumulative data (not shown) indicated that more than 50% of the particles were < 20 μm diameter, and around 75% or more were < 100 μm diameter. The main peak for each set of data between 5.5 and 6.5 μm corresponds well with the observations made by optical microscope (Figure 4.4) for single cells and also shows reasonable agreement with size data reported by other authors (Li *et al.*, 1998; Mores and Davis, 2002b; Narong and James, 2006).

[*] This work was carried out with assistance from Zlatko Saracevic at the University of Cambridge

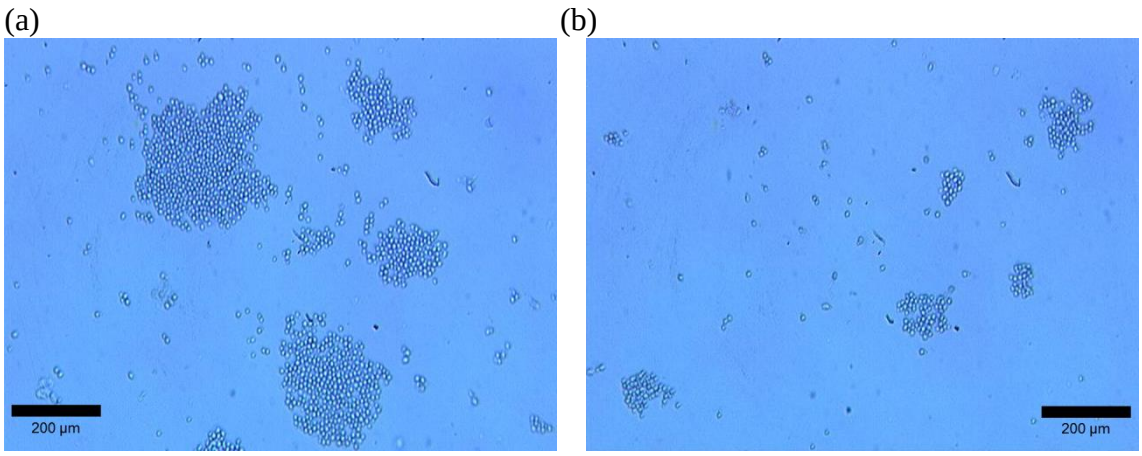

Figure 4.4. Microscope images of yeast suspension taken at 20× magnification. (a) shows examples of larger flocs, (b) shows more typically sized flocs.

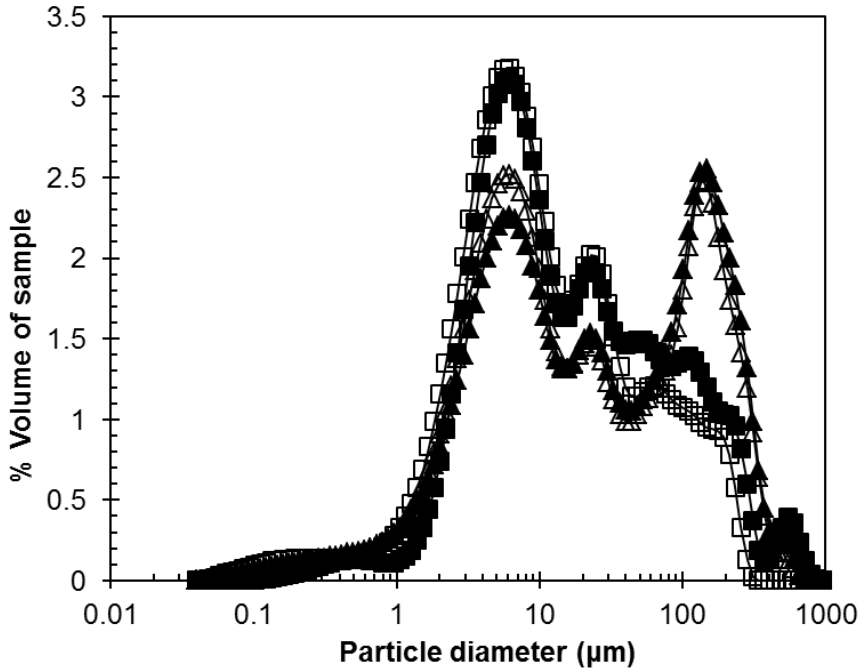

Figure 4.5. Particle size distribution of yeast suspension using two methods: powder added directly to the sample chamber (squares), and addition of a pre-mixed suspension to the sample chamber (triangles). Solid and open symbols correspond to repeats of each method.

4.2.3 Ballotini filtration

Membranes

Regenerated cellulose membranes of 0.6 µm nominal pore size (*Schleicher & Scheull*[*], RC59) were used in these experiments, available in A4-sized sheets. These are symmetric, hydrophilic membranes. Their permeability was characterised by dead end filtration (described in appendix C.) and thickness was estimated from SEM

[*] Now GE Whatman™, There is no manufacturer data available for these membranes as the product has been discontinued.

micrographs (see Figure 4.6). The data is shown in Table 4.3, where it is compared with initial flux data from cross-flow experiments. Clean-water flux observed in cross-flow experiments indicated a higher resistance than measured in dead-end filtrations, however there is reasonable agreement at the extremes of the error margins.

Table 4.3. Membrane characterisation data from dead-end experiments, and using initial, clean-water flux data from cross-flow experiments. Flux for dead-end experiments is calculated from the derived R_m value. Tolerance range of these values is indicated where known.

	δ_m (μm)	Flux at 50 mbar ($L \cdot m^{-2} \cdot h^{-1}$)	κ ($\times 10^{-14}$ m^2)	R_m ($\times 10^{9}$ m^{-1})
Cross-flow	57	5400 ± 700	1.70 ± 0.21	3.35 ± 0.42
Dead-end	57	6500 ± 100	2.06 ± 0.04	2.77 ± 0.05

(a) (b)

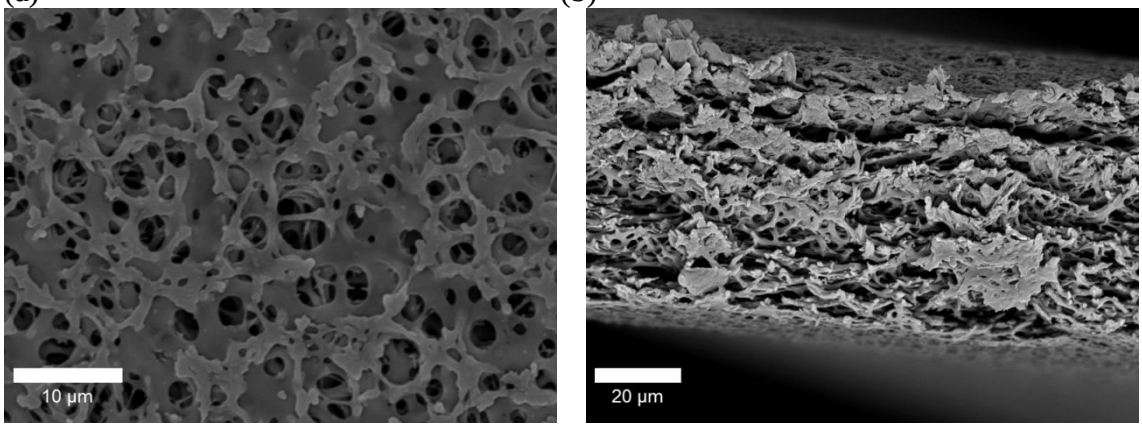

Figure 4.6. SEM Micrographs of *Schleicher & Schuell* RC59 membranes, taken at 15 kV. (a) Overhead view at 2500× magnification, (b) Cross-section at 1000× magnification. Images obtained by MEng project students Matthew Wilcox and Robert Chance (during academic year 2011/12).

Ballotini suspension

Ballotini – hollow glass spheres employed as an additive in paints – as used by Chew *et al.* (2007) and Lister *et al.* (2011), was selected as a model foulant to test the FDG set-up and investigate the applicability of the models outlined in section 2.5. It is manufactured by Potters inc. and was obtained in powder form from Blagden Speciality Chemicals©. Two types were used in this study, namely Sphericel® 110P8 and 60P18, which are, by manufacturer specification, neutrally and positively buoyant respectively. These types were selected to compare the behaviour of relatively similar sized particles with different buoyancy. Ballotini suspensions of bulk volume fraction ϕ_b = 0.2% were used in all experiments.

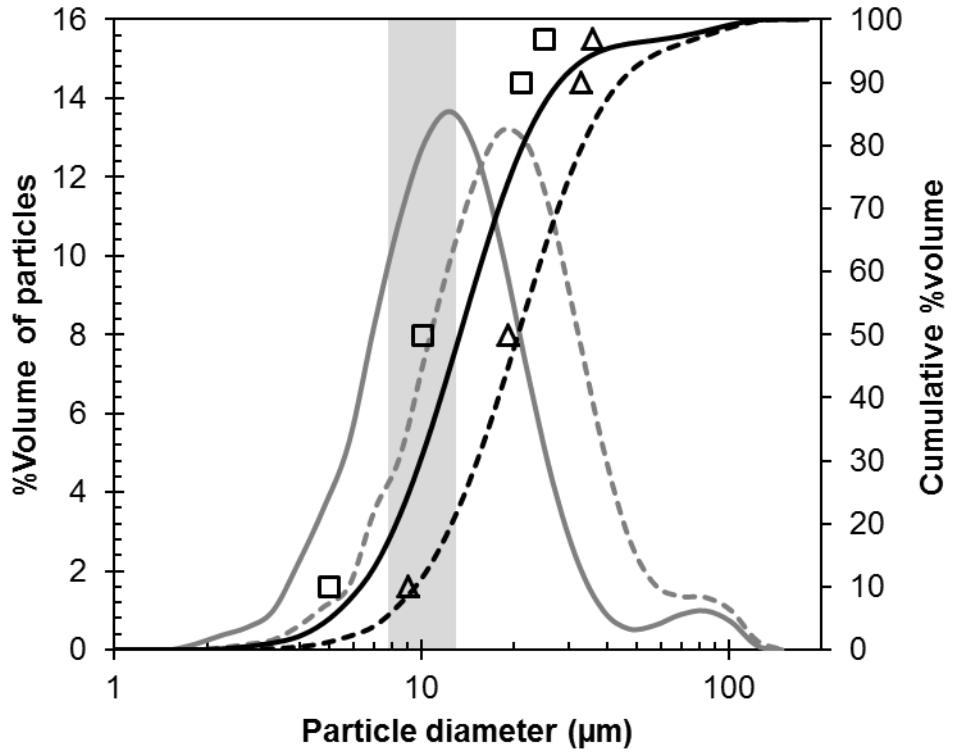

Figure 4.7. Particle size distribution for Spherical© 110P8 (Solid) and 60P18 (dashed). Grey lines indicate %volume for individual diameters and black lines indicate cumulative distribution. The shaded region indicates the size range considered to be neutrally buoyant, as calculated in appendix A1. Manufacturer data for cumulative distribution is also shown, where squares and triangles represent 110P8 and 60P18 respectively.

The size distribution of the particles, suspended in RO water, was characterised by laser diffraction (*Malvern*, Mastersizer X); this used the Mie scattering with a refractive index of 1.55 for borosilicate glass (a value provided within the device software). The buoyancy of the particles was related to their size by assuming a constant wall thickness as described in appendix A1, particles are considered to be neutrally buoyant in the region where $900 \leq \rho_p \leq 1100$ kgm^{-3}.

The particle size distribution is shown in Figure 4.7, mean diameters and distributions of buoyant particles are summarised in Table 4.4. The specifications from the manufacturer were given as cumulative distributions (Potters, 2011) and are also plotted (symbols). Both types of particle exhibit strong single peaks at 12.4 and 18.2 μm for 110P8 and 60P18 respectively; approximately 20% higher than their Sauter mean diameters, $d_{3,2}$. A smaller peak exists for both at around 80 μm, however this is thought to be an artefact as later studies using SEM (see Figure 4.8) did not indicate the presence of such large particles. Just over three quarters of the 60P18 particles are considered to be in the buoyant region, while for the 110P8 this is just over half. All of

the particles are at least twice the nominal pore size of the membrane used so complete rejection can be expected.

Table 4.4. Particle density, ρ_p, as given by manufacturer, Sauter and volume mean diameters, and distribution of weighted, buoyant, and neutrally buoyant particles in each ballotini suspension (to nearest 1%). Mean diameters calculated as the average values reported in 3 separate runs.

	ρ_p	$d_{3,2}$	$d_{4,3}$	**Weighted**	**Neutral**	**Buoyant**
	kg·m^{-3}	**(µm)**	**(µm)**	**d_p < 7.7 µm**	**7.7 ≤ d_p ≤ 12.9 µm**	**d_p > 12.9 µm**
60P18	600	15.6	22.9	5%	16%	78%
110P8	1100	10.1	15.4	17%	31%	52%

(a) (b)

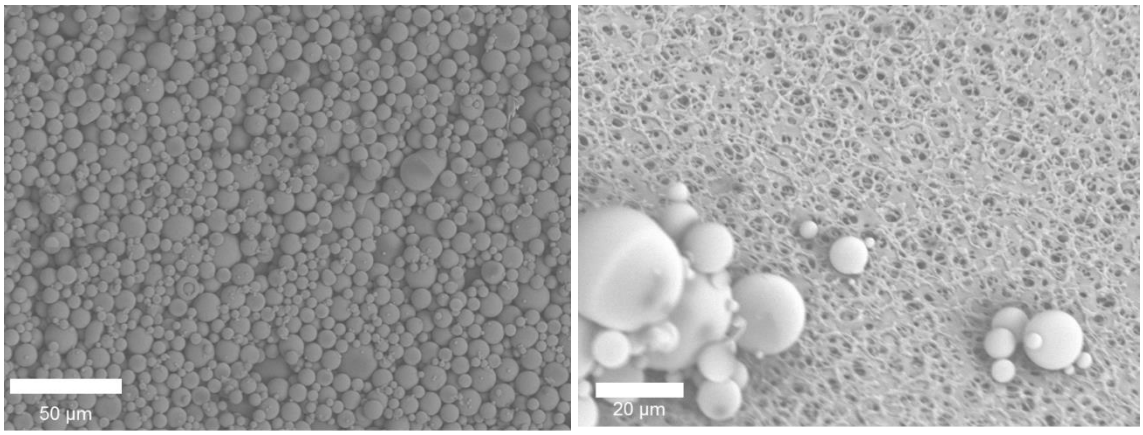

Figure 4.8. SEM micrographs of 110P8 ballotini particles taken at 15 kV. (a) shows a sample of particles, (b) shows particles resting on the surface of the membrane after filration. Images were obtained by MEng project students Matthew Wilcox and Robert Chance (during academic year 2011/12).

4.3 Methods

All experiments were performed at ambient temperature, which varied between 17 and 19°C. Differences in viscosity and density of the solvent within this range are negligible, as is the temperature shift incurred by the pressure transducers.

4.3.1 Calibration

Impermeable substrate

In order to infer h/d_t from pressure readings, and hence deposit thickness, a set of calibration data was required. To do this the membrane and spacer were replaced with a stainless steel sheet secured in the test section shown in Figure 4.1. The gauge nozzle was brought into contact with the surface, and the micrometer set to read zero.

The flow loop described in section 4.1.3 was filled with degassed RO water, and the pressure transducer ports were flooded to remove air bubbles (which in preliminary experiments were found to offset measurements). With the pump running, a constant duct flow rate was set using V1, and a constant static pressure, p_{static}, within the test section, indicated by dP_1 was set using V2. The position of the gauge was adjusted to h_0 = 1 mm using the micrometer, and gauging flow, m_g, was set using the needle valve.

A succession of pressure reading were taken at a range of h/d_t values, where in this case $h = h_0$, and h_0 was indicated by the micrometer. More readings were taken in the range $h/d_t < 0.3$ in order to improve the resolution where the most significant change in the C_d vs. h/d_t profile was expected. The needle valve required periodic adjustment to maintain a constant m_g within an acceptable margin of error of ± 0.01 g·s^{-1}. This was performed for a number of different values of m_g, p_{static}, and Re_{duct}.

Membrane calibration

Due to small irregularities in the membrane support, and its deformation under pressure, the position of the membrane relative to the gauge was not repeatable. This meant that the position read by the micrometer at which the nozzle would touch the membrane (i.e. $h_0 = 0$) needed to be ascertained. Contact with the nozzle could damage or deform the membrane surface however, so a non-contact technique was developed for this. A C_d vs. h/d_t (later Δp_{13} vs. h/d_t) plot was produced in the same way as described above, being careful not to allow Δp_{13} to reach a value corresponding to $h/d_t < 0.05$. The resulting plot was displayed on the VI alongside the original calibration plot. An adjustable value of $h_{0,offset}$, (where $h_0 = h_{0,Mi} - h_{0,offset}$) was varied on the VI until the two plots aligned. $h_{0,Mi}$ in this case represents the value read from the micrometer. This conept is illustrated in Figure 4.9.

4.3.2 Yeast fouling experiments

A new membrane sample was cut for each experiment and pre-wetted in RO water before being sealed into the test section. The flow loop was primed with degassed RO water, ensuring all air bubbles were purged from the system, particularly around the gauge. Air beneath the membrane was removed through the bleed point on the permeate side while tilting the test section. TMP and Re_{duct} were set using V2 and V1, then gauging flow was set at m_g = 0.2 g·s^{-1}, a different gauging flowrate was used for ballotini fouling experiments. The pressure indicated by dP_2 was checked against

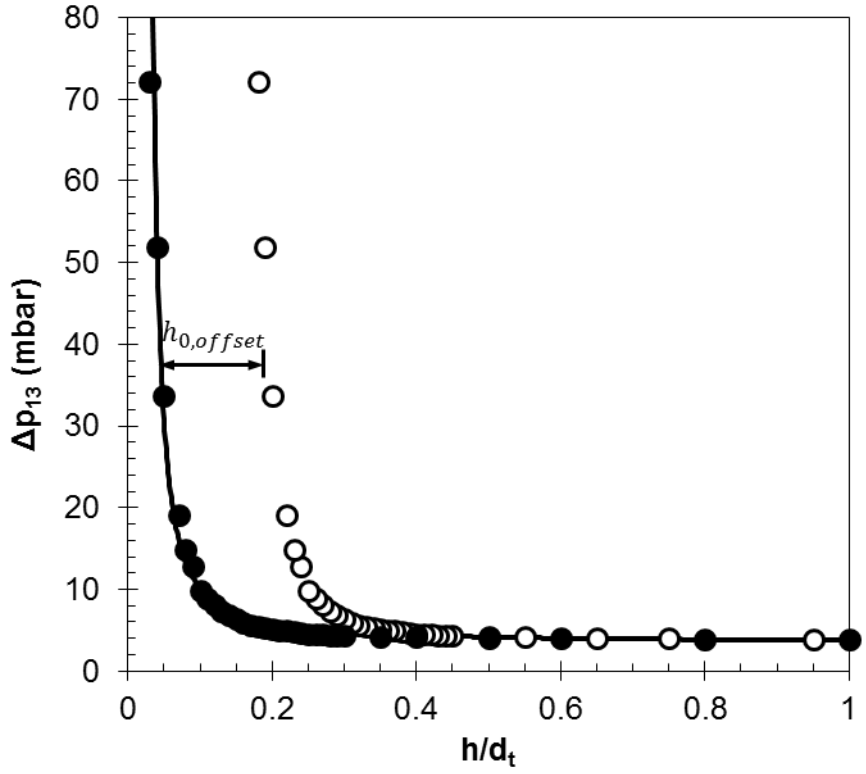

Figure 4.9. Example of determining $h_{0,offset}$, The offset is defined using the displacement in h/d_t from the predicted curve produced from previous calibration data. Experimental data for Δp_{13} vs. h/d_t is plotted where open and closed symbols represent the same data before and after offset correction.

previous experiments to ensure repeatable readings, where discrepancies usually indicated incomplete removal of air bubbles from the system. After this initial set-up, a membrane calibration, as described above, was performed. The resulting $h_{0,offset}$ was used in the experiment to correct h_0 values.

Yeast powder was added directly to the tank with the filtration running at the desired conditions. The overhead stirrer for the feed tank was set at a speed where turbulent mixing occurred, and it is assumed that mixing occurred instantaneously. There was in fact some delay between the addition of the yeast and fouling of the membrane while the suspension reached the test section, this is shown in the results for this study. A handheld pH meter (*Hanna instruments*, p-HEP) was used to monitor pH change due to the addition of yeast. During fouling, periodic adjustment of V1 and V2 was required to maintain Re_{duct} and TMP. The fouling layer was analysed using 3 different methods (M1-M3) in separate experiments, two of which (M2 and M3) were used to track cake layer growth as it occurred.

M1: Destructive testing of preformed layer

The yeast fouling experiment was run with h_0 > 10 mm and no gauging flow for 30 minutes. At this point a quasi-steady flux value was reached, where deposition should be balanced by removal due to shear flow. Gauging flow was maintained at 0.2 g·s^{-1} and the gauge was lowered towards the surface of the membrane making continual C_d readings until a value corresponding to $h/d_t \leq 0.25$ was reached. At this point a reasonably accurate estimation of cake thickness could be made. The gauge was moved closer towards the membrane surface in 20 μm increments, taking a reading at each step. A thickness and stress value could be determined for each of these steps, allowing for the study of the fouling layer's thickness decline in response to fluid shear stress.

Using this method prevented any interference with cake growth, and can be used to describe the cohesive and adhesive strength of the cake layers. It does not however, provide any indication of cake growth rate.

M2: Tracking cake growth at constant h

In this method, cake growth was monitored throughout the experiment. Before adding the foulant, the gauge was lowered to a point where $h/d_t = 0.2$ as indicated by C_d, where in this case $h = h_0$. The apparent height, h, was monitored continuously during fouling, and h_0 was increased as this decreased, attempting to maintain h/d_t between 0.2 and 0.25.

This method allows for continuous readings of cake thickness against time, maintaining the gauge at an optimal clearance from the surface, where a reasonable accuracy can be achieved while minimising disturbance to the cake layer. Some interference with cake growth is expected however, and the need for constant adjustment of the gauge height makes this technique quite labour-intensive.

M3: Tracking cake growth at constant h_0

This mode was also used to produce plots of δ_c vs. time, however the accuracy of readings increases with δ_c. Instead of performing regular adjustments to h_0 in order to maintain a constant h/d_t, the position of the gauge was set at the start of the experiment prior to addition of the foulant. C_d was constantly recorded during the fouling run and, as δ_c increased, h/d_t decreased; this produced far more precise readings at higher thicknesses. The needle valve downstream of the gauge did, however, require periodic adjustment in order to maintain m_g at 0.4 g·s^{-1} during the experiment.

Four different set heights were used in separate experiments, namely: $h_0 = 260$, 300, 350, and 400 μm.

The advantage of using this method is that it eliminates the possibility of gauge movements causing any sudden interference with cake growth. At lower h_0 values this method allows for a more steady determination of the initial cake growth rate, however at higher cake thicknesses a higher shear stress is imposed on the cake. When using higher h_0 values, the cake thickness cannot be resolved at lower thicknesses because $h/d_t > 0.25$.

Extraction of the fouled membrane

For the purpose of SEM studies and other imaging of the fouling layer, the cake was extracted from the test section. In order to preserve the cake structure, water held up in the test section after the experiment was drained through the membrane by applying a vacuum through a Buchner flask. The test section was then dismantled to retrieve the cake and membrane.

4.3.3 Ballotini fouling experiments

Alterations to apparatus

Some alterations were made to the operation of the VI used in these experiments. The most notable of these was that h/d_t readings were made from interpolation of a Δp_{13} vs. h/d_t calibration rather than C_d, although the original data for the calibration remained the same. A modification to the rig was also made, in which the valve control method for TMP was replaced by a weir of adjustable height. This construction is indicated in Figure 4.10, and consists a Y-piece, open to atmosphere, mounted on a vertical bar with a vertically adjustable clamp.

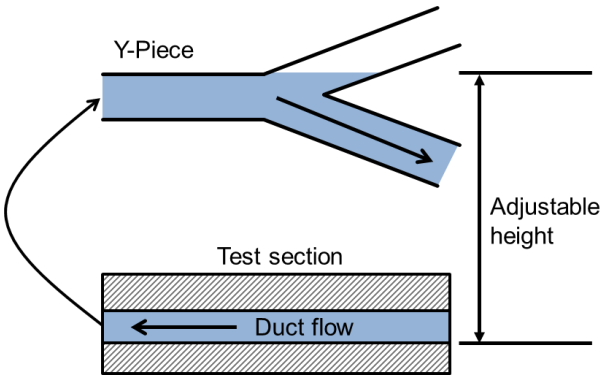

Figure 4.10. Replacement of valve V2 with a weir by means on a Y-piece for more accurate control of TMP. Not to scale.

Startup

As with the yeast experiments, a new piece of membrane was cut for each run and pre-wetted before installation into the test section. After bleeding air from the system and ensuring both ends of each pressure transducer were fully wetted, Re_{duct} and TMP were set using valves V1 and V2. After checking Δp_{14} against a standard value, a membrane calibration, as described in section 4.3.1, was performed. Prior to the experiment, gauging flow was stopped by closing the needle valve, and the gauge was retreated to a clearance where h_0 > 10 mm. The water in the feed tank was constantly agitated under turbulent conditions.

Ballotini was added to the system 30 seconds after setting a timer, so the decline from clean-water flux could be recorded. Two types of experiment were conducted for these ballotini filtrations: a thickness tracking experiment, and destructive strength test. After selected experiments the fouled membrane was recovered for microscopy and/or SEM analysis. These procedures are outlined below.

Cake thickness tracking

Similarly to method M2 described above, thickness was tracked using the same value of h/d_t. In these experiments, however, the gauge was not used to measure thickness continuously. Instead the gauge was maintained at a high clearance from the membrane between periodic readings.

After 4 minutes of filtration, gauging flow was set to 0.4 g·s^{-1}, and the gauge was moved towards the membrane, pausing at stages closer to the surface to allow a steady-state Δp_{13} value to be read. Once a value of $h/d_t \leq 0.2$ was reached, a steady-state reading was recorded to indicate cake thickness. m_g was set to zero again by closing the needle valve, and the gauge was retreated back to its original position where h_0 > 10 mm. This process took between 1 and 2 minutes, and was commenced at the start of every fourth minute from the beginning of the filtration. The experiment was terminated at 60 minutes, at which point the flux had reached a quasi-steady-state value.

Table 4.5. Thickness tracking experiments performed for each type of particle suspension.

		TMP (mbar)		
		30	**50**	**75**
Re_{duct}	**550**	60P18	60P18	110P8,60P18
	1000		110P8, 60P18	
	1550		60P18	

This experiment was performed for both types of ballotini suspension, and at 3 different TMP and Re_{duct} values. A summary of the experiments performed for each type of particle is shown in Table 4.5. Each experiment was performed at least 3 times, with 60P18 used as the primary suspension for making direct comparisons between filtrations at different TMP and Re_{duct} values.

Destructive strength testing

Similarly to the M1 measurement method detailed in the previous section, a filtration was allowed to proceed for an hour so that flux could reach a quasi-steady-state value. With the filtration continuing, a destructive thickness/strength test was performed using the same procedure as in M1, by the following steps:

1. Opening needle valve and setting gauging flow, m_g, to 0.4 g·s^{-1}
2. Locating the surface of the fouling layer by moving the gauge towards the membrane in small increments until $h/d_t \cong 0.25$, as indicated by Δp_{13} (interpolation is performed within the VI).
3. Moving the gauge in 20 μm increments towards the membrane and taking a reading once a steady-state Δp_{14} value is reached.
4. Repeating step 3 until Δp_{14} nears, but does not exceed TMP[*].

All strength testing experiments were performed at a TMP of 50 mbar and Re_{duct} of 1000.

Recovery of fouled membrane

At the end of each experiment, the fouled membrane was recovered by partially drying it. The test section was gradually emptied to drain, and fluid held up on the feed side of the membrane was removed through the cake by applying a vacuum (through a Buchner flask) to the permeate side of the test section. The fouled membrane, still wet, was left open to atmosphere for between 12 and 20 hours to allow most of the retained moisture to evaporate. Too much or too little moisture caused the fouling layer to disintegrate on removal.

Optical microscopy was performed on cross-sections of the fouling layer, as described in section 5.3.3.

[*] When Δp_{13} exceeds TMP, reverse flow may occur through the membrane in the area directly beneath the gauge; this phenomenon is predicted by CFD simulations (discussed in section Chapter 8). Ensuring Δp_{14} is less than TMP will prevent this from happening.

4.4 Conclusion

An existing piece of FDG apparatus was recommissioned for the purpose of thickness and strength studies for both a non-ideal (yeast) and ideal (ballotini) foulants on membrane surfaces. The results of such experiments, which are detailed in the next chapter, were then used to inform design decisions for an improved, more accurate, and automated device.

Chapter 5: Results A – Yeast and ballotini filtration

The apparatus and methods described in Chapter 4 were used to produce thickness and strength estimates for two types of foulant. The first being a suspension of inactive yeast cells, and the second inert ballotini particles. The results of initial calibration tests, and subsequent filtrations and cake characterisation are reported and discussed in this chapter.

5.1 Calibrations

Results of calibrations performed by measuring Δp_{13} at various known clearances, h (where $h = h_0$), over a stainless steel plate are shown in Figure 5.1. The C_d vs. h/d_t profile is similar to that observed by previous researchers using FDG (Gu *et al.*, 2009b; Tuladhar *et al.*, 2000). Earlier work (Lewis *et al.*, 2011) showed that Re_{duct} and static pressure had no significant influence on the shapes of these curves.

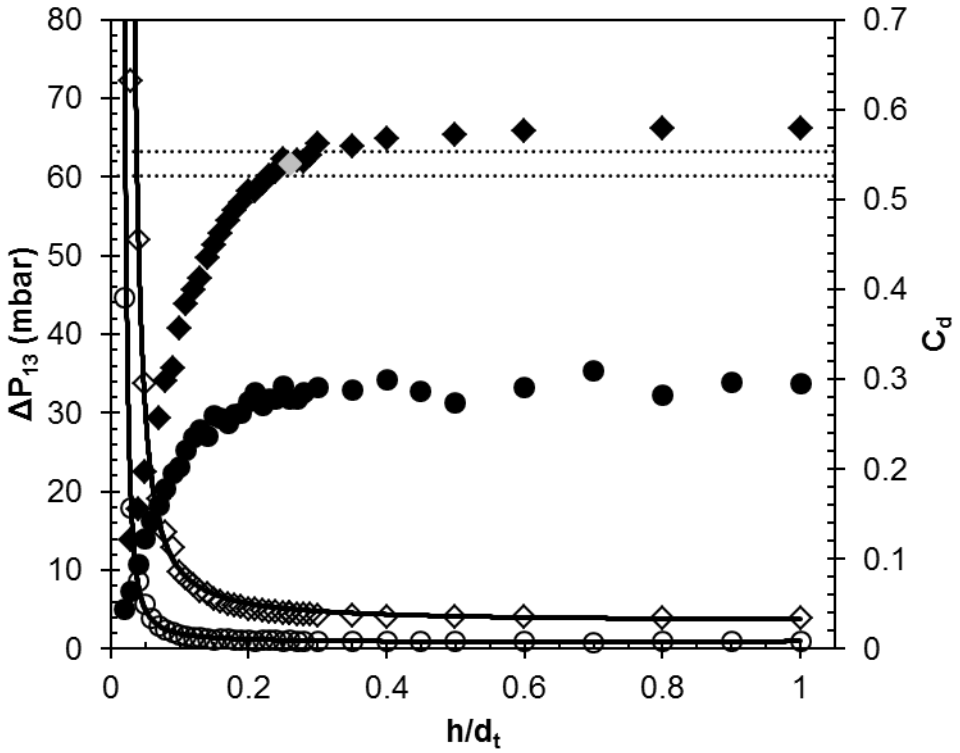

Figure 5.1. Calibration plots for Δp_{13} (open symbols) and discharge coefficient, C_d (closed symbols), against h/d_t, taken at gauging flows of m_g = 0.1 g·s^{-1} (circles) and 0.4 g·s^{-1} (diamonds) and at known clearances, h, over a stainless steel plate. The solid lines represent lines fitted to the data using equation (5.1). The grey marker shows the data point for h/d_t = 0.26 at m_g = 0.4 g·s^{-1}. Dotted lines above and below this point show the effect of a 0.01 g·s^{-1} shift in m_g up and down from the original value of 0.4 g·s^{-1}.

The pressure drop across the gauging nozzle, Δp_{13}, was used for estimating h/d_t (and by extension cake thickness) during filtrations because C_d was found to be very sensitive to small changes in m_g. An example of this is shown in Figure 5.1 where the value of C_d varies considerably when a change in m_g of ± 0.01 g·s^{-1} is applied to the raw data. Because m_g readings rely on transient balance readings, it is practical to remove such variations as a potential source of error. The alteration to Δp_{13} due to this same variation (in which m_g influences Δp_{34} (as discussed in section 2.7.1) is negligible, as were alterations to Δp_{14} of ± 0.25 mbar (the error in transducers) with a constant m_g value of 0.4 g·s^{-1}.

The fit curves shown in Figure 5.1 were determined by fitting the data, using the Matlab™ curve-fitting package, to the following parametric equation:

$$\Delta p_{13} = Ae^{\frac{-B}{h/d_t}} + Ce^{-\frac{-D}{h/d_t}} \tag{5.1}$$

for which the derived parameters are shown in Table 5.1:

Table 5.1. Parameters used to fit experimental Δp_{13} vs h/d_t data to equation (5.1).

m_g (g·s^{-1})	A (mbar)	B	C (mbar)	D
0.1	0.755	-0.0953	1.329	2.241
0.4	3.316	-0.1114	11.36	4.328

So that Δp_{14} measurements performed at $h/d_t \leq 0.2$ are within the instrument error in the pressure transducer dP_2 (as labelled on Figure 4.1) of ±0.25 mbar, the higher gauging flowrate of 0.4 g·s^{-1} was used to estimate cake thickness in all ballotini fouling experiments using this apparatus. Yeast fouling experiments employed data from a calibration of C_d vs. h/d_t at m_g = 0.2 g·s^{-1}, for which the method is reported elsewhere (Lewis *et al.*, 2012).

5.2 Yeast Filtration

These studies form the preliminary work which aided the improvements to subsequent design and operation of the newer apparatus (described in section 6.2).

5.2.1 Flux decline

Typical flux decline curves for experiments performed at 35 and 50 mbar are shown in Figure 5.2. Flux decreased significantly to less than 300 L·m^{-2}·h^{-1} within the first 300 s of the filtration, which was accompanied by a noticeable rise in TMP due to

the change in volumetric flow of retentate. Despite a difference in TMP, the final flux in all cases was recorded in the range of 75-95 $L \cdot m^{-2} \cdot h^{-1}$.

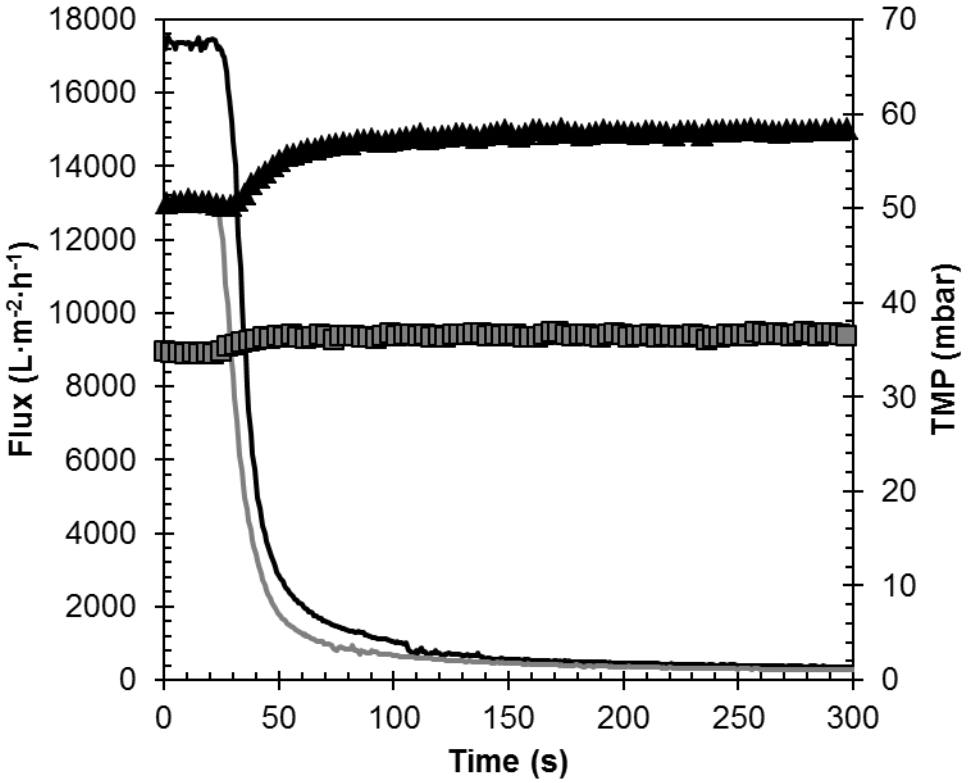

Figure 5.2. Flux (lines) and TMP (symbols) at operating TMPs of 35 mbar (grey) and 50 mbar (black).

The starting flux was also found to vary considerably between experiments, ranging from 9000 to 16000 $L \cdot m^{-2} \cdot h^{-1}$ at 35 mbar. This was attributed to background fouling of the membrane due to particles retained in the flow loop from previous experiments and possible inconsistencies in TMP readouts from dP_1 (Figure 4.1).

Cake growth was monitored over time during fouling at a TMP of 35 mbar using two different methods, M2 and M3, as described in section 4.3.2. Cake thickness after 1800 s filtration was also measured by destructive testing, as described by method M1.

Method M2: Constant h

The estimated thickness using this method is plotted in Figure 5.3 along with h_0 and estimated h associated with each reading. A small drop in estimated thickness is evident around 520 s, when h_0 was increased prematurely (due to misinterpretation of fluctuating values). As could be expected of a typical filtration (Wakeman, 1994), the cake appears to grow asymptotically as flux declines towards a quasi-steady-state value of about 90 $L \cdot m^{-2} \cdot h^{-1}$ within 1800 s of filtration. A limiting thickness of ~120-130 μm is observed, where the rate of deposition due to flux is presumed to match the rate of back-transport due to cross-flow.

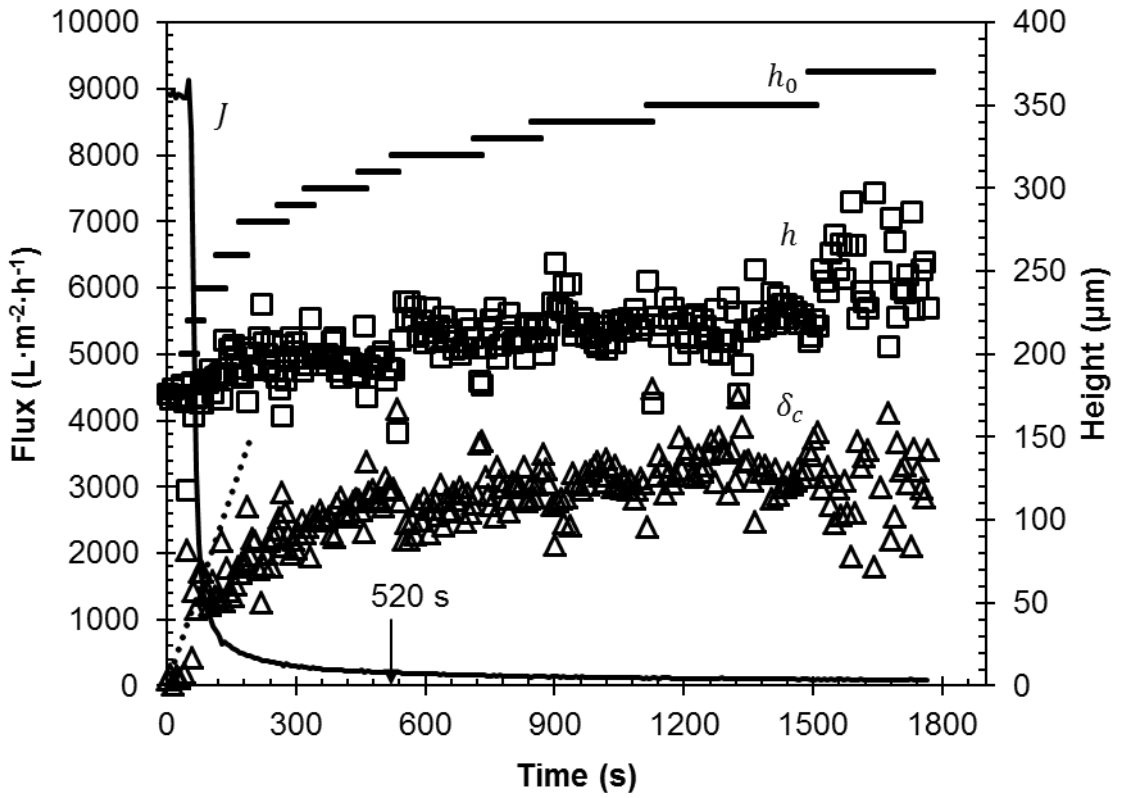

Figure 5.3. Flux (solid line) and estimated cake thickness (triangles) against time during filtration of yeast cells at 35 mbar TMP. Estimated height, h is indicated by squares, and the gauge clearance from the membrane, h_0 is indicated by black horizontal lines. The dotted line indicates the estimated initial cake growth rate.

Method M3: Constant h_0

Figure 5.4 shows estimates for cake thickness, δ_c, against time using method M3. As should be expected, the most accurate readings (i.e. those which exhibit the least scatter) are shown in (a), where $h/d_t < 0.15$ by 300 s. h/d_t is inferred from the graph by:

$$\frac{h}{d_t} = \frac{h_0 - \delta_c}{d_t} = \frac{260 - 140}{1000}\ (\mu m) \tag{5.2}$$

Although the initial flux varied significantly between experiments, a similar growth profile and terminal thickness is seen for the cake in (a), (b), and to some extent (c). The thickness estimates made at the highest clearance, h_0 = 400 µm (d), showed the greatest degree of scatter as in this case it was very likely that $h/d_t > 0.25$.

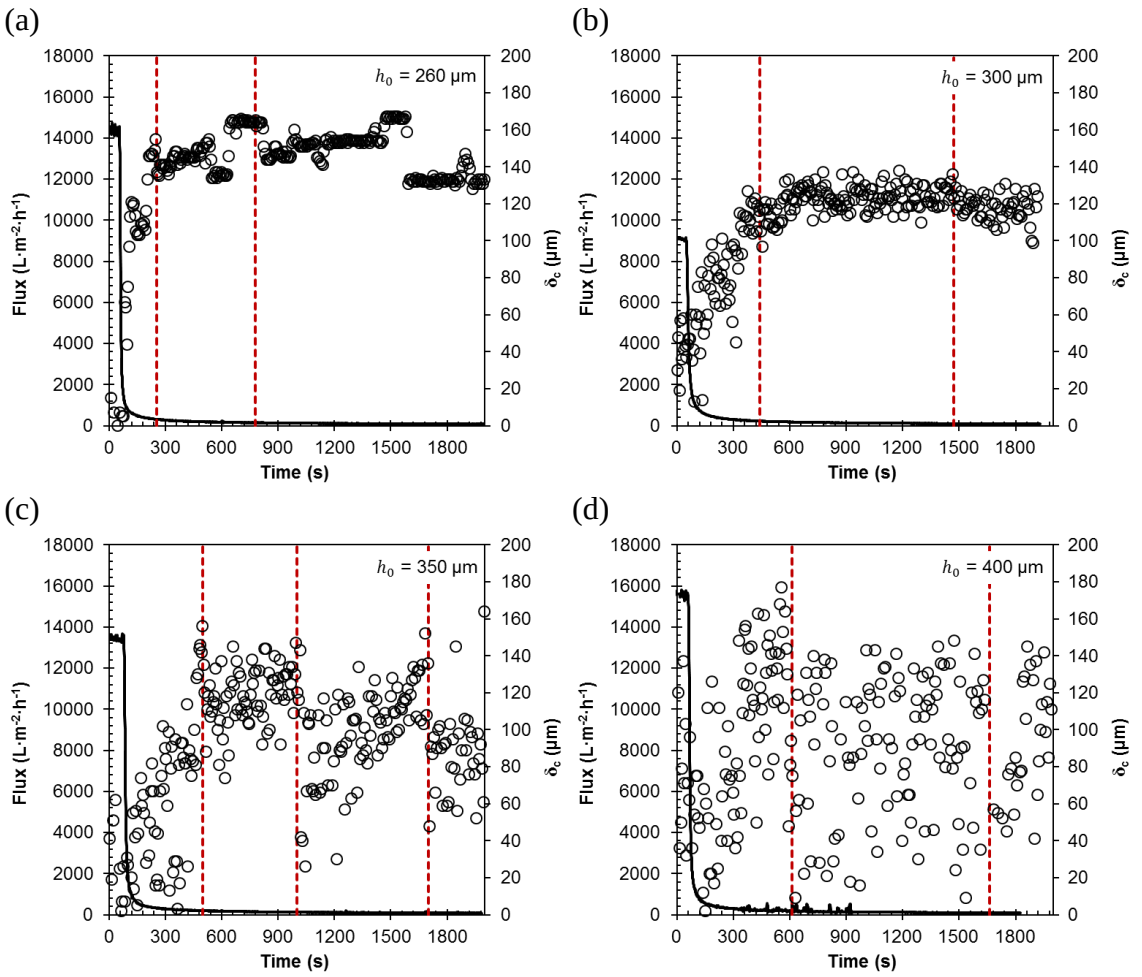

Figure 5.4. Estimated thickness (symbols) and flux (black line) for filtrations using method M3 to estimate cake thickness. Results shown here show filtrations at TMP = 35 mbar and Re_{duct} = 1000, where thickness is estimated at constant h_0 values of (a) 260 µm, (b) 300 µm, (c)350 µm, and (d) 400 µm. Dashed lines indicate time points at which adjustments to the needle valve were recorded.

The points at which the needle valve controlling m_g was manually adjusted (in order to maintain m_g = 0.2 g·s^{-1}) are marked by dashed lines on the graphs. The effect of this is seen most clearly in Figure 5.4a, where the estimated thickness decreased slightly due to the small increase in m_g when the needle valve was opened. A similar effect is seen on the same graph at around 1590 s where, without any manual adjustment to the needle valve, the estimate thickness decreased (accompanied also by a small increase in m_g). The gauging flow, m_g, is intrinsically linked to variations in cake thickness, as a decrease in h/d_t would restrict flow as well as increasing Δp_{13}. Knutsen and Davis (2006) have observed particles rolling on the surface of filter cakes, and constant capture and displacement of particles on the surface is very likely to be responsible for sudden changes in cake thickness.

5.2.2 Destructive Thickness tests

Using method M1 (see section 4.3.2), the position of the top surface of the yeast cake was ascertained, giving a thickness reading. Further incremental steps of the gauge nozzle towards the membrane caused removal of cake material. As indicated by Figure 5.5, the stress required to cause such removal was greater as the cake became thinner. It stands to reason from equation (2.22) that particles closer to the membrane will experience a higher normal force holding them to the surface (because F_N increases with decreasing local permeability, κ), resulting in a higher tangential force (e.g. τ_w) required for their removal. A layer is also observed (at 80-90 μm at 35 mbar TMP, and 30 μm at 50 mbar TMP) which cannot be removed at the maximum $\tau_{w,max}$ applied. While there is little difference in the initial thickness measured under each pressure (~250 μm), the height of this less deformable layer shows greater variation. It should be expected to be thicker at 50 mbar TMP as the force holding particles against the surface of the cake should be greater, however this adverse condition is attributed to random filtration behaviour in this case.

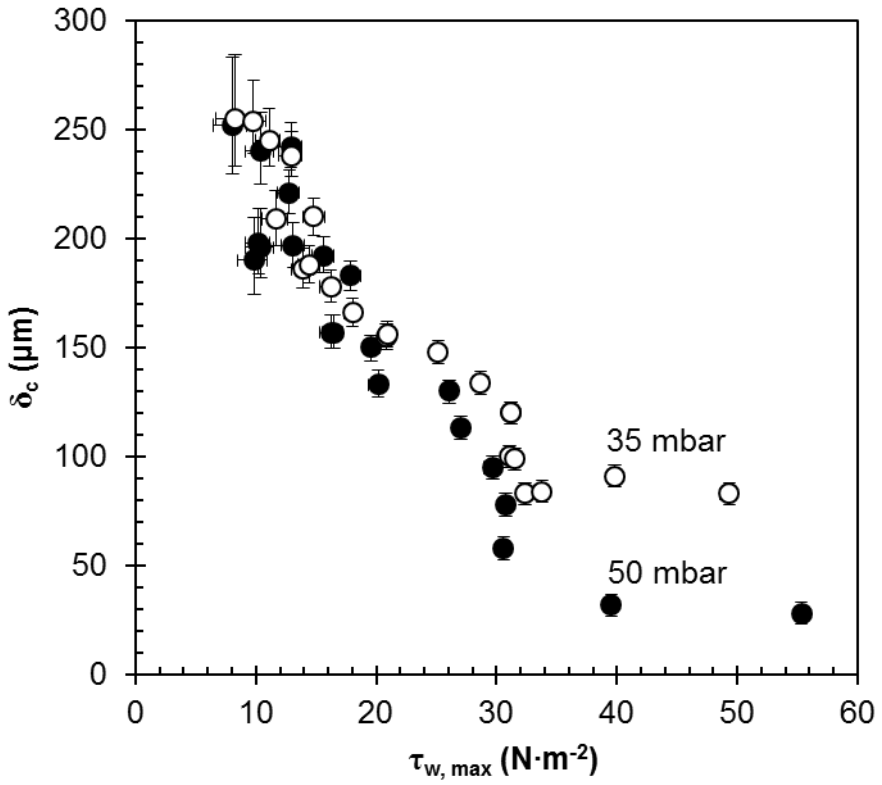

Figure 5.5. Estimated thickness, δ_c vs. estimated maximum wall shear stress, $\tau_{w,max}$ after 1800 s fouling with yeast at Re_{duct} = 1000, and TMP = 50 (closed symbols) and 35 (open symbols) mbar. Error bars are calculated as described in appendix D. .

It is also important to note that the first thickness value measured for TMP = 35 mbar, as shown by the open symbols on Figure 5.5, indicates the final

thickness after 1800 s fouling. This exceeds the limiting thicknesses recorded by methods M2 and M3 (see Figure 5.3 and Figure 5.4) by over 100 μm. It is therefore reasonable to conclude that the continued stress exerted by the gauging flow on the surface of the fouling layer when using methods M2 and M3 restrict cake growth during its development.

5.2.3 Analysis of extracted cake

Subsequent to fouling experiments the membrane (and cake) was removed for further analysis.

Visual analysis

On removal of the fouled membrane from the test section it was immediately obvious that both the geometry of the test section and the implementation of FDG had a strong impact on the way in which yeast was deposited on the membrane. Particularly evident was the increased deposition at the inlet of the flow channel at higher cross-flow velocity, as seen by comparison between Figure 5.6 (a) and (b). This indicates a strong tendency of particles to be dragged along the surface of the cake in cross-flow conditions. In addition to the deposition at the inlet side of the test section, the presence

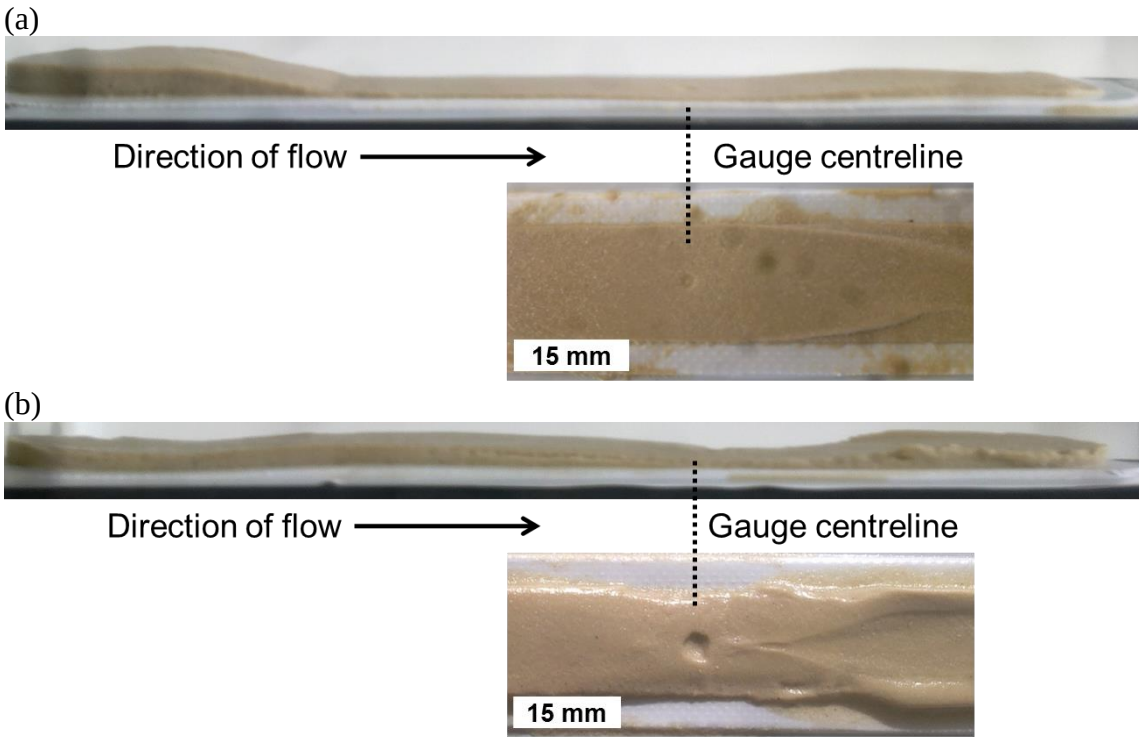

Figure 5.6. Side and overhead views of yeast fouling layer after filtrations at TMP = 35 mbar and Re_{duct} = (a) 1000, and (b) 1550. These images were taken after performing destructive strength tests, as described by M1 in section 4.3.2.

of the gauge also had a strong effect on settling downstream, creating the fork-like pattern seen to the right of the gauge centreline in Figure 5.6b. These can be attributed to recirculation and flow disturbance caused by the gauge, as discussed in section 8.6.

The shape of the eroded region at the gauge centreline for Re_{duct} = 1000, (Figure 5.6a) matched well with the geometry of the gauge, having a diameter of ~1.5 mm. A much larger indentation is seen in (b), due to the much thicker layer of deposited material on the membrane. The thickness of this layer was found to be unreadable however, as the deposit was too easily removed by fluid flowing into the gauge.

Impact of particle settling

The potential impact of settling on particle deposition is considered by estimating terminal velocity, $u_{p,\infty}$, using the correlation for particle suspensions given by Richardson *et al.* (2007b):

$$u_{p,\infty} = \frac{\mu}{\rho_L d_p}(2.33Ga^{0.018} - 1.53Ga^{-0.016})^{13.3}\left(1 + 2.4\left(\frac{d_p}{D}\right)\right)^{-1}(1-\phi_b)^{n_s} \qquad (5.3)$$

where ρ is the fluid density, g is the acceleration due to gravity, d_p is the particle diameter, μ is the dynamic viscosity of the fluid, Ga is the Galileo number, ϕ_b is the bulk particle volume fraction, and n_s is a power-law index which scales the terminal velocity with particle concentration. The duct width, D, is used as the limiting region for which wall effects are considered. The residence time , t_{res}, for particles flowing through the apparatus including the entry section and test section up to the end of the membrane (a total length of 850 mm) is given by:

$$t_{res} = 850[mm]\frac{\rho D}{\mu Re_{duct}} \qquad (5.4)$$

which is 12.7 s and 8.2 s for Re_{duct} values of 1000 and 1550 respectively. Using the residence time it is possible to produce a vague estimate for the degree of particle settling within the apparatus; a more detailed quantification of the total rate of settling is beyond the scope of this study. A condition can be specified for which particles that enter the flow duct at half its height will become trapped due to settling, before they reach the outlet of the test section:

$$u_{p,\infty} < \frac{D}{2t_{res}} \tag{5.5}$$

Using equation (5.3) this leads to cut-off diameters of 124 and 102 μm for Re_{duct} values of 1000 and 1550 respectively. These account for ~20% and ~25% (based on largest estimates) of the suspension. It can be concluded that a significant proportion of yeast particles are likely to have settled from suspension during flow through the apparatus. The degree to which this was apparent was markedly higher at an increased cross-flow velocity. Hence it is probable that difference between the profiles of the fouling layer shown in Figure 5.6 occurs due to carriage of the particles which had settled in the entry section and along the membrane.

Electron Microscopy

After removal from the test section, fouled membrane samples were freeze dried in liquid nitrogen and snapped to create clean cross-sections. They were sputter coated with gold before SEM analysis (*JEOL*, SEM6480LV). The resulting micrographs from cross-sections are shown in Figure 5.7.

(a) (b)

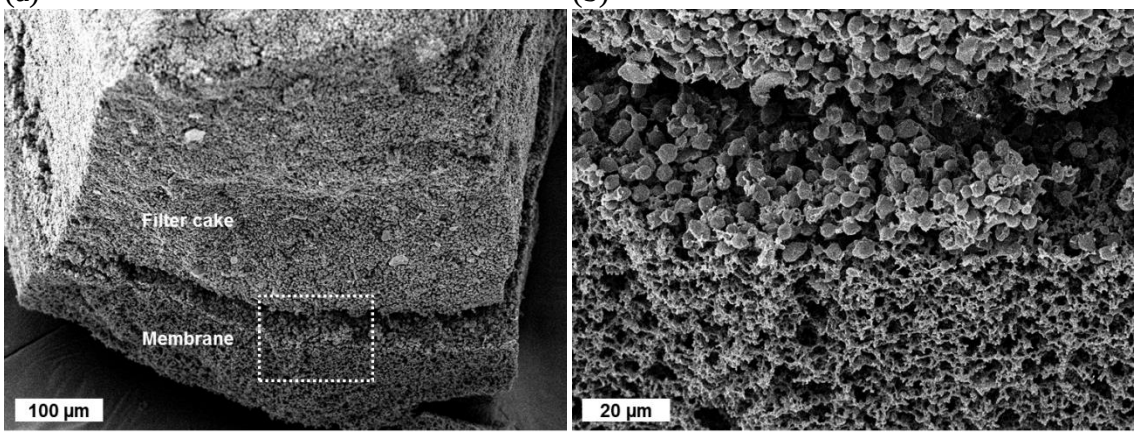

Figure 5.7. SEM micrographs of the yeast fouling layer developed on mixed cellulose ester membrane (5 μm nominal pore diameter) by fouling with 1 g·L^{-1} yeast suspension for 1800 s at TMP = 50 mbar and Re_{duct} = 1000. (a) shows an angled cross-section at 200× magnification, and (b) shows a 1000× magnification of the area indicated by the box in (a). SEM performed at 5kV.

The thickness of the fouling layer in (a) shows good agreement with the highest value estimated in Figure 5.5 for 50 mbar TMP. Although it appears as though the fouling layer has broken away from the membrane in the figure, closer analysis (see Figure 5.7b) indicates that some yeast cells have become embedded in the surface of the membrane structure. These would greatly reduce flow through the membrane by pore blocking, explaining the sharp flux decline shown in Figure 5.3 and Figure 5.4. This

also suggests a possible explanation for the trend seen in Figure 5.5, wherein at higher shear stresses, a much tougher layer remained on the membrane. The close tessellation between the yeast cells and membrane pore structure seen in Figure 5.7b would provide a lot more friction than between individual cells and agglomerates.

5.3 Ballotini fouling

The ballotini fouling experiments were performed to show, for a more monodisperse and predictable particle suspension, how FDG can be used to investigate small changes to flow conditions. The use of particles with a much more clearly defined morphology than yeast, and which did not form larger agglomerates, allowed for the investigation of the fouling models described in section 2.5. It should be noted that transient thickness data for ballotini was acquired periodically, rather than by methods M2 or M3, as described in section 4.3.2.

5.3.1 Flux decline and thickness

Although to a slightly lesser extent than seen for yeast fouling experiments, the initial flux was quite variable due to background fouling. Subsequent flux decline curves were repeatable however, and matched well following the initial steep decline immediately after addition of the foulant to the feed tank. The effect of TMP and cross-flow velocity (as characterised by Re_{duct}) on filtrations of the more buoyant (60P18) ballotini was also investigated.

Effect of TMP

The influence of TMP (30, 50, and 75 mbar) on fouling behaviour is shown in Figure 5.8. The estimated cake thickness, δ_c, increased asymptotically towards a steady-state thickness in all cases, matched in kind by an asymptotic decrease in flux. The final thickness and flux were, unsurprisingly, higher at increased TMP, as shown in Figure 5.9. No correlation could be established between final thickness values and initial fluxes, and there was no significant variation in final flux values for repeat experiments. A limiting thickness was also reached faster at a lower TMP, which agrees with the model described in section 2.5.2, wherein a higher normal force due to TMP - holding particles against the surface of the membrane or fouling layer – would increase the minimum shear stress required for their removal and re-entrainment into the bulk suspension. It is interesting to note, however, that while the estimated thickness reached a steady, unchanging value, the flux continued to decline up to the end of the experiment. The additional flux decline could be an indication of particle deposition too

loose to measure by FDG, or which does not deposit in the region where the gauge takes measurements. As discussed in section 5.2.2 for the yeast fouling experiments, there is a possibility that the use of the gauge limits cake growth in the region where measurements are taken. This is explored in sections 5.3.2 and 5.3.3.

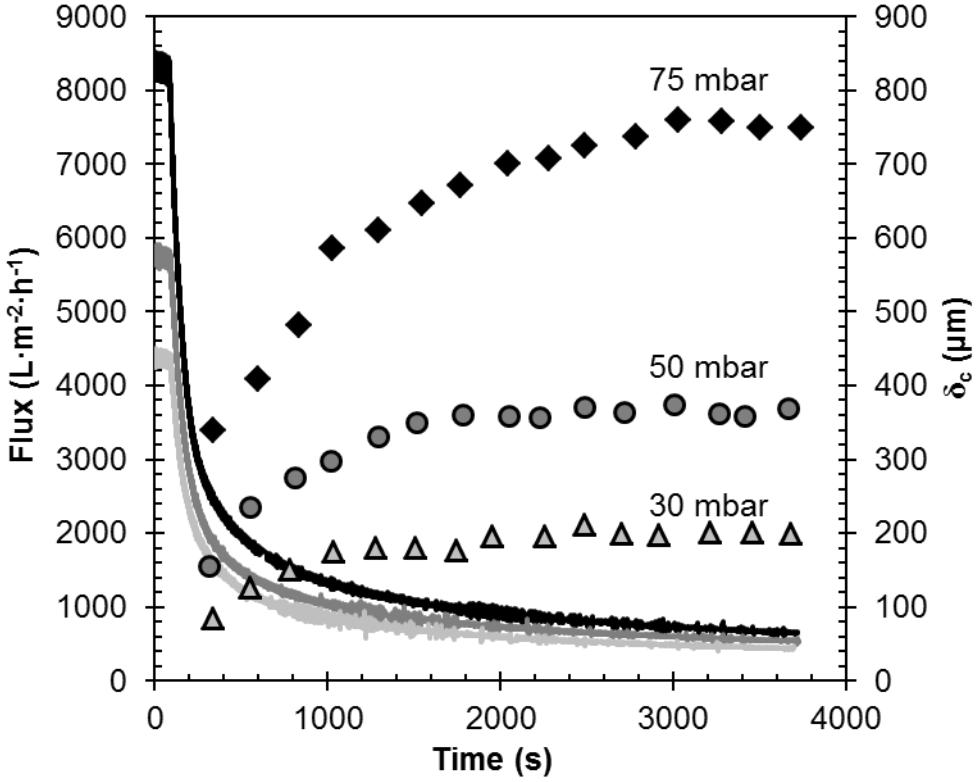

Figure 5.8. Flux (lines) and estimated cake thickness, δ_c (symbols), against time. Re_{duct} = 1000, and TMP = 30 mbar (light grey, triangles), 50 mbar (dark grey, circles), and 75 mbar (black, diamonds).

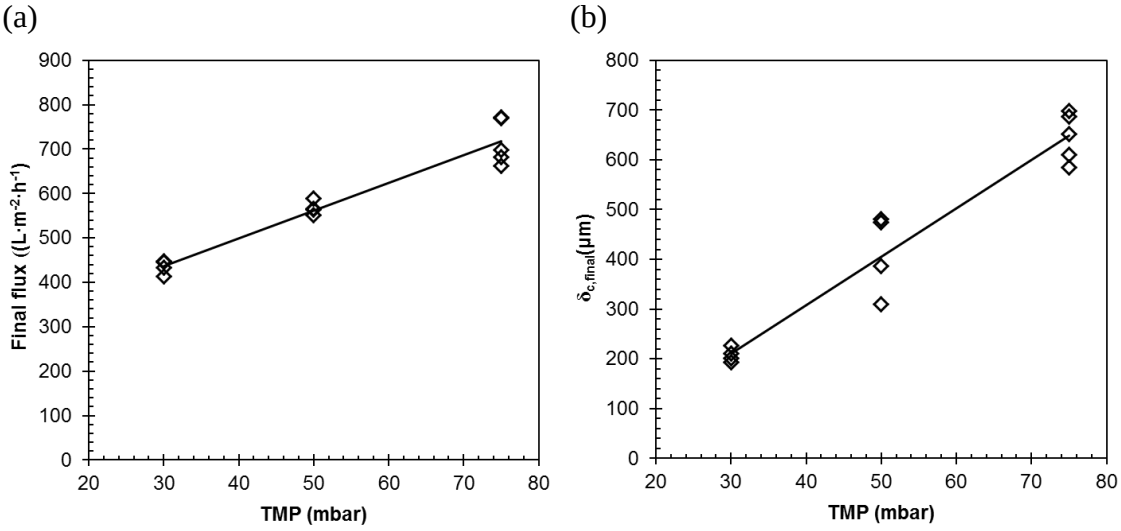

Figure 5.9. (a) Final flux, and (b) Final estimated cake thickness, $\delta_{c,final}$, against TMP for filtrations of the more buoyant 60P18 ballotini suspension at Re_{duct} = 1000.

Effect of Re_{duct}

Although increasing cross-flow velocity should reduce cake fouling thickness by imposing a higher shear stress on the surface, the opposite is apparent in this work. Figure 5.10 shows that, for the highest cross-flow velocity where Re_{duct} = 1550, a faster growing cake layer is observed, which does not reach a steady-state thickness as fast as at Re_{duct} = 1000. Increased cross-flow velocity did not appear to have a significant impact on flux decline, as evidenced by the close match of all three curves after the addition of foulant. The initial flux at Re_{duct} = 550 was noticeably lower than at the two higher values however, which suggests that an increased cross-flow velocity may limit background fouling. Initial fluxes for Re_{duct} values of 1000 and 1550 were both an average of 5600 L·m^{-2}·h^{-1}.

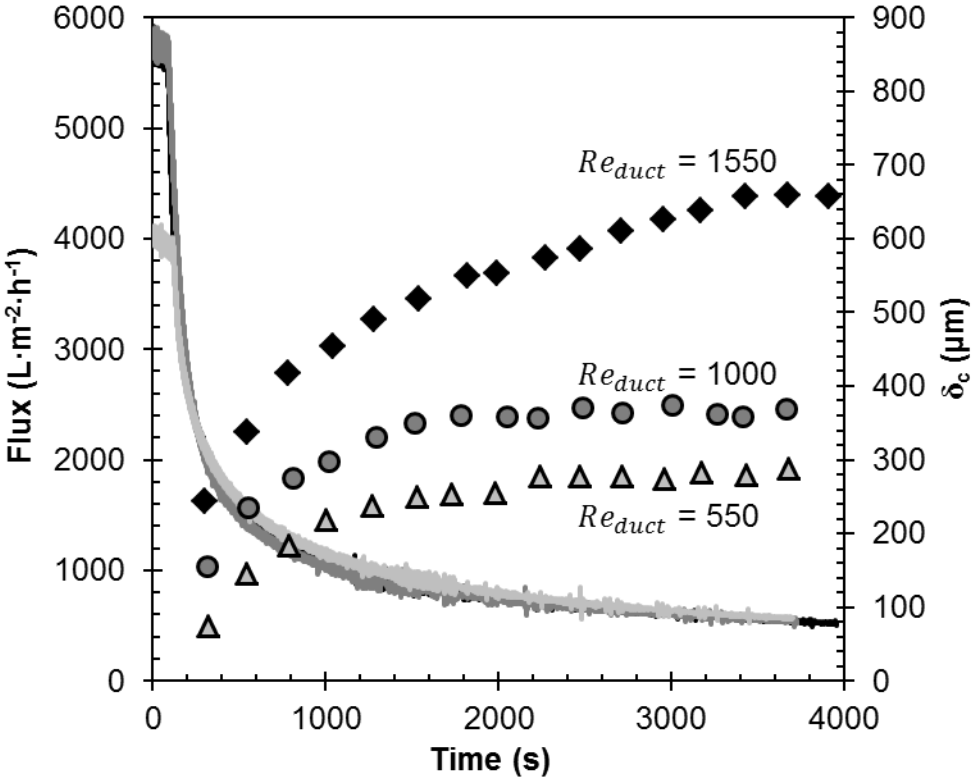

Figure 5.10. Flux (lines) and estimated cake thickness, δ_c (symbols), against time. TMP = 50 mbar, Re_{duct} = 550 (light grey, triangles), 1000 (dark grey, circles), and 1550 (black, diamonds).

The final flux after 3600 s was found to be consistent across all three Re_{duct} values as indicated for repeat experiments by Figure 5.11a. The positive trend for final cake thickness with increasing Re_{duct} is also fully evident in Figure 5.11b. Hence a much thicker cake is apparent at higher cross-flow velocity without an increased resistance. Three explanations for this are proposed:

1. The increased cross-flow velocity increases cake thickness by fluidisation, increasing its permeability.

2. Cake layer deposition is uneven, as has been shown for yeast filtrations by Figure 5.6. Higher cross-flow velocity reduces this effect.
3. FDG readings interrupt cake growth and even remove some particles in the process. At higher cross-flow velocity the cake structure beneath the gauge regenerates faster.

While 1 cannot be explored with the apparatus available, exploring the likelihood of 2 and 3 can eliminate this as a viable explanation. Deposition was found to be uneven in the case of all experiments, supporting the first assumption in 2. Due to recirculation (caused by the 3 mm recess to the membrane surface) at the inlet and outlet of the test section some extra deposition was seen at these points (similarly to that discussed in section 5.2.3), however the extent to which this contrasted at different cross-flow velocities was not measured.

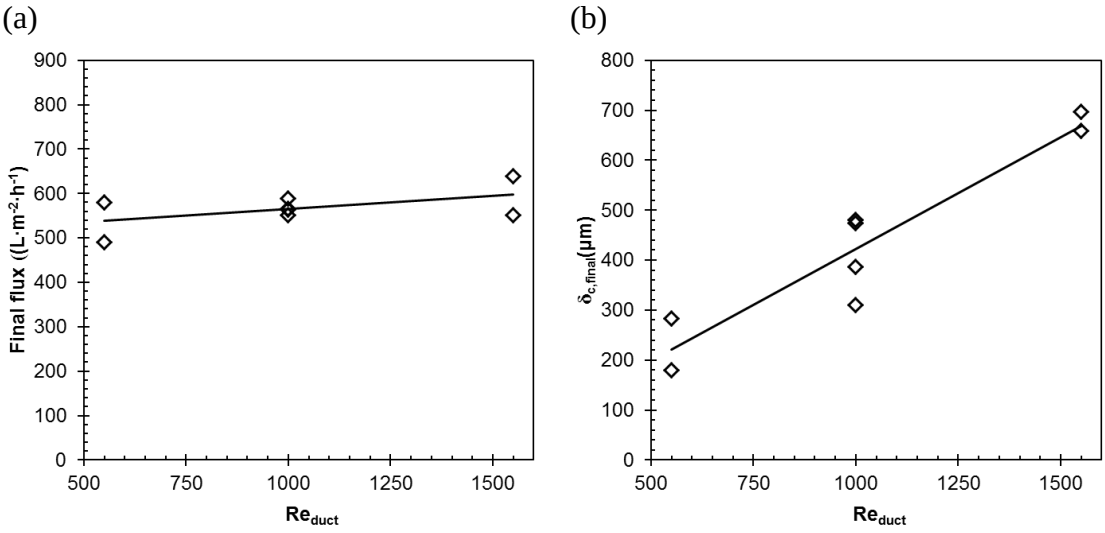

Figure 5.11. Summary of thickness tracking results using method M2, comparison of Re_{duct} at TMP = 50 mbar. These graphs show results for the more buoyant 60P18 ballotini suspension of (a) Final flux against Re_{duct}, and (b) Final estimated cake thickness, $\delta_{c,final}$ against Re_{duct}.

The higher final cake thickness measured at greater Re_{duct} values was confirmed by visual inspection, as demonstrated in section 5.3.3. This directly disputes explanation 3 above by verifying the trend set out in Figure 5.11b. Visual inspection of the fouling layer subsequent to these thickness tracking experiments (discussed later in section 5.3.3), along with the destructive thickness tests in Figure 5.13, also confirmed that periodic cake thickness measurements were lower than the actual thickness of the cake.

5.3.2 Comparison of particle size/buoyancy

Flux decline and thickness

Figure 5.12 shows that the larger, more buoyant 60P18 ballotini exhibited an 80% higher terminal flux compared with the smaller, neutrally buoyant 110P8 ballotini. The final cake thickness of the 60P18 was also less than half that of the 110P8. The Carman-Kozeny equation (2.7) would predict a higher resistance (leading to lower flux) for smaller particles, and the particle capture model (see section 2.5.2) predicts a higher rate of back-transport for larger particles. Both mean that just based on particle size, the 110P8 ballotini should be expected to form a thicker, more flow-resistant cake layer. Settling of 110P8 particles was less likely to be an important factor, as implementation of equation (5.3) suggests that most of the particles are too small to settle within the duct. The effects created by the 3 mm recess to the surface of the membrane were still observed in these experiments however, which is probably related to the low flow and recirculation at the recess towards the inlet. This is discussed in section 8.6.

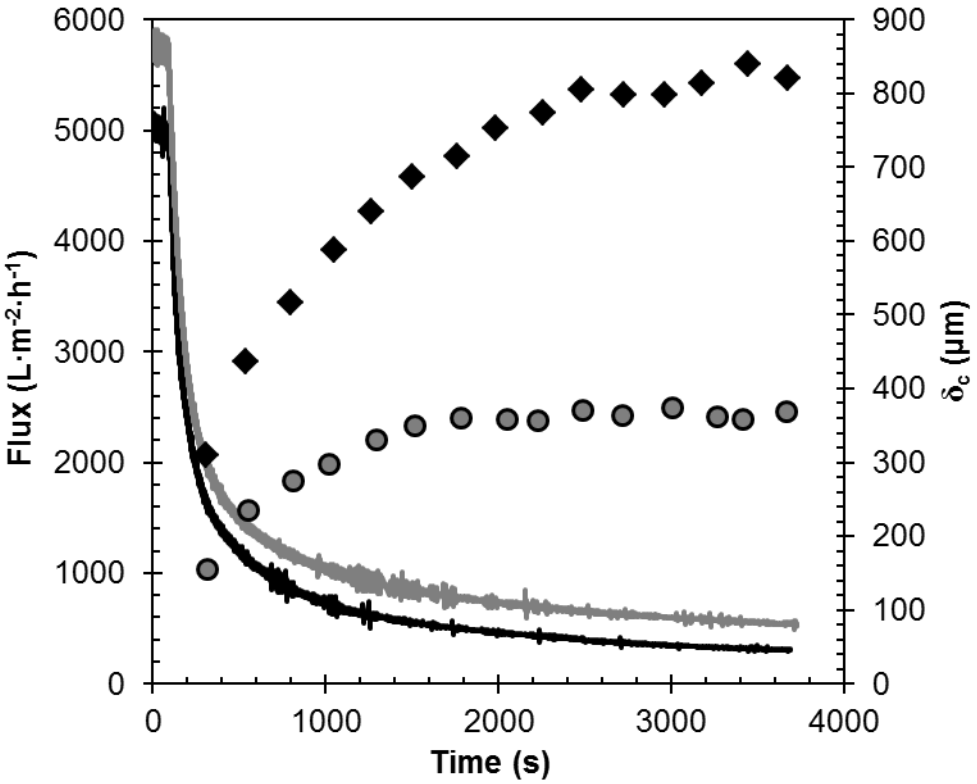

Figure 5.12. Flux (lines) and estimated cake thickness (symbols) against time for filtrations of 110P8 (black, diamonds) and 60P18 (grey, circles) at TMP = 50 mbar and Re_{duct} = 1000.

Destructive strength testing

Both types of ballotini exhibit a pattern shown in Figure 5.13 wherein the fluid shear stress, indicated by $\tau_{w,max}$, required to reduce the thickness of the cake layer is

greater closer to the membrane. This appears to occur in two different regions: the first, indicated by dashed red lines on the graph, has a much shallower gradient than the second which is indicated by the dashed blue lines. The transition between the two gradients can be interpreted as a yield stress for the cake, above which more significant removal takes place. Both types of particle also appear to be completely removed from the membrane surface when $\tau_{w,max}$ reaches 80 N·m^{-2}. Although the gradients on the graph are approximately equivalent, the 60P18 ballotini shows lower cohesion strength under fluid shear. This is evident both by the lower yield point of 22 N·m^{-2} compared with a value of 34 N·m^{-2}, as well as a near constant difference of approximately 20 N·m^{-1} between the two sets of data below the yield point of the 60P18 particles. The adhesion strength of the two appears to be similar, however. A small, possible monolayer of 60P18 particles appears to be present until the stress reaches 70-80 N·m^{-2}, after which they were completely removed.

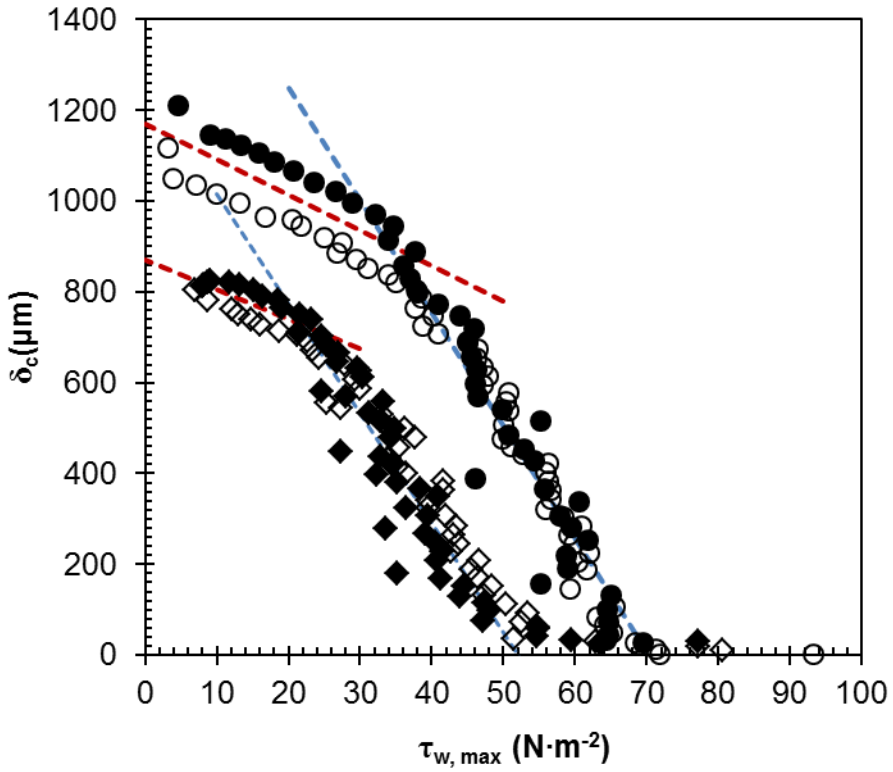

Figure 5.13. Estimated cake thickness, δ_c, vs. estimated maximum wall shear stress, $\tau_{w,max}$, after 3600 s fouling at TMP = 50, Re_{duct} = 1000 with 110P8 (circles) and 60P18 (diamonds) ballotini. Open and closed symbols represent separate runs of the same experiment. Dashed lines indicate linear fits to both sets of data (red) before and (blue) after estimated yield point of fouling layer.

Another observation from Figure 5.13 is that the starting thickness (i.e. that measured at the lowest shear) was greater than the maximum thickness shown for each type of ballotini under the same experimental conditions in Figure 5.12, where periodic

thickness measurements were made during growth. Although the actual difference was approximately similar (~300-400 μm thicker cakes were recorded by destructive testing in each case), as a percentage difference it is much more significant for the thinner layers formed by 60P18. The 110P8 ballotini cake also reached a steady state later than the 60P18, as seen in Figure 5.12. The FDG process likely interferes with cake growth less for 110P8 particles than 60P18, which is supported by the theory discussed in section 2.5.

5.3.3 Visual inspection

Methodology

Subsequent to selected experiments, cross-sections of the fouling layer were viewed using an optical microscope (*Nikon*, AZ100). Fouled membranes were partially dried inside the test section before extraction. Cross sections were made by fracturing the fouling layer along a line perpendicular to flow, approximately 5 mm prior to the location of the gauge nozzle. If the cake was too wet it would disperse with the retained water, or bend instead of fracturing. If it was too dry it would disintegrate or become impossible to mount for viewing. Thus very few samples were successfully measured by this technique.

Effect of Re_{duct}

Figure 5.14 shows cross-sections of cakes formed during filtrations at different Re_{duct} values, the results for which are presented in Figure 5.10 and Figure 5.11. The trend shown in Figure 5.11b is confirmed here, whereby the final cake thickness was observed to be higher at greater cross-flow velocity (i.e. higher Re_{duct}). Visual inspection confirmed this pattern for Re_{duct} = 1000, however no successful cross-sections were produced from those experiments.

The measurements here of 540 and 970 μm correspond to measured values of 287 and 659 μm presented at Re_{duct} = 550 and 1550 in Figure 5.13. In both cases the final thickness of the cake layer was significantly higher when measured optically rather than by FDG.

(a)

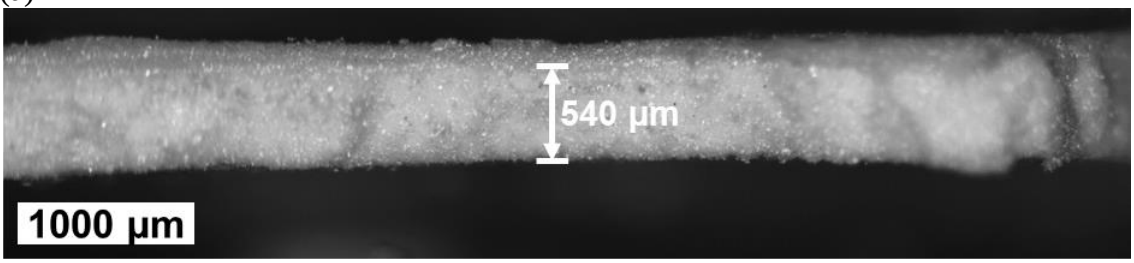

(b)

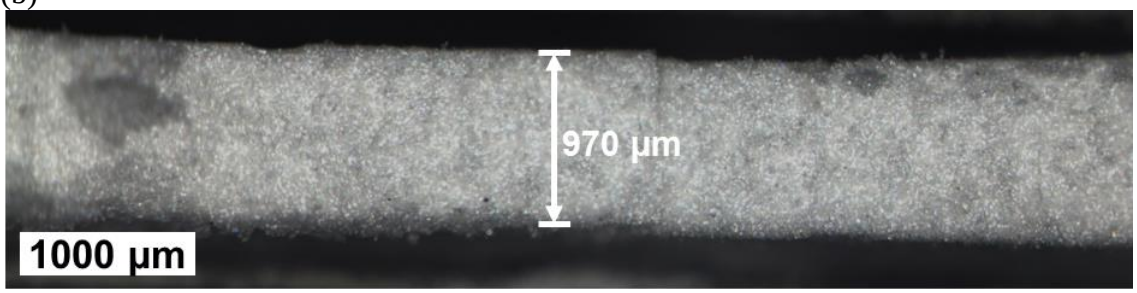

Figure 5.14. Cross-sections (perpendicular to flow) of fouling layer (at a location ~5 mm prior to the gauge nozzle) developed during 3600 s filtrations of 60P18 ballotini at 50 mbar TMP and Re_{duct} values of (a) 550, and (b) 1550. Estimated thickness (given to the nearest 10 µm) is superimposed. In both cases the surface which was in contact with the membrane is on the bottom.

Influence of FDG on thickness measurements

After each thickness tracking experiment with ballotini, a small circular impression was left on the cake, directly below the FDG nozzle. This confirmed the observations made above, which suggested that the repeated FDG measurements hindered cake growth and resulted in a lower final thickness than what was actually

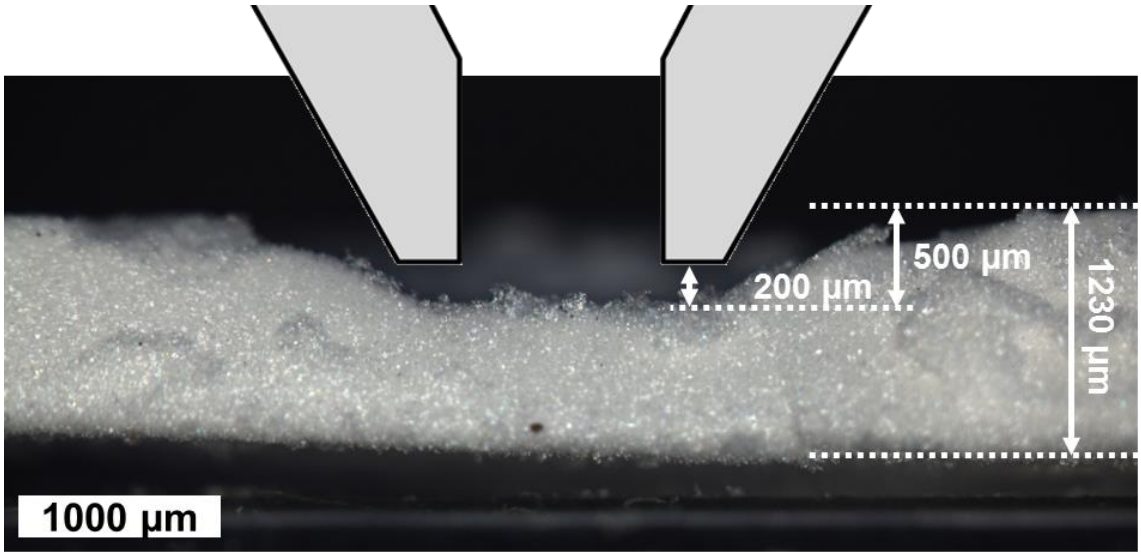

Figure 5.15. Miscroscope image taken after fouling with 60P18 suspension for 3600 s at TMP = 75 mbar and Re_{duct} = 1000. Periodic thickness measurements were made during this time. This shows a cross section (perpendicular to flow) of the fouling layer directly beneath the gauge, of which a scale drawing is superimposed to show its position at a clearance where h/d_t = 0.20. Estimated thickness measurements are shown to the nearest 10 µm.

present. Attempts were made to produce a cross-section by fracturing the cake perpendicular to flow directly central to the gauging nozzle position after performing thickness tracking experiments. The most successful of these is shown in Figure 5.15.

Height estimations displayed on the figure suggest a thickness of the area directly beneath the gauge where FDG readings were taken, to be ~730 μm, while the actual value measured by the gauge was 690 μm. This confirms that the thickness readings themselves are probably accurate, albeit with clear evidence that they are not truly representative of the rest of the cake.

(a)

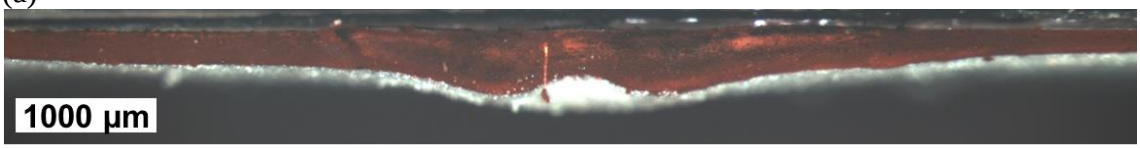

(b)

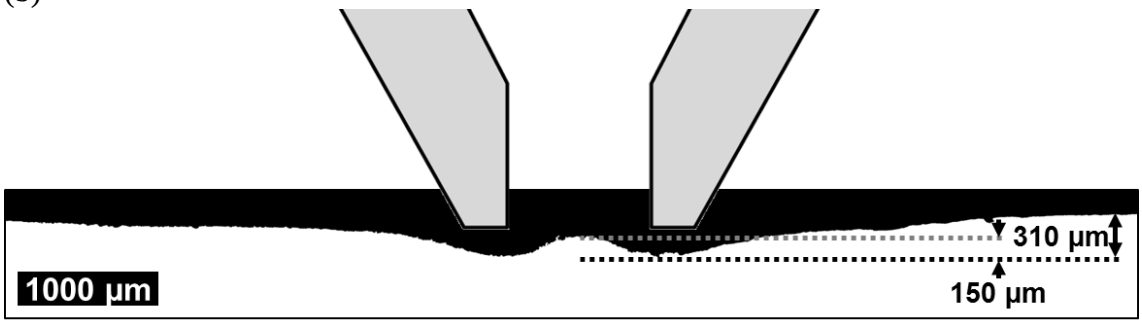

Figure 5.16. Miscroscope image and processing after fouling with 110P8 suspension for 3600 s at TMP = 75 mbar and Re_{duct} = 1000 (a) Superglue cast of the eroded region beneath the gauge, which was cross-sectioned perpendicular to flow at the centreline of the gauge position and coloured with a red marker. (b) Post-processed image to indicate the surface morphology of the ballotini fouling layer (in white) by inversion of the red-stained cast (now shaded black). As in Figure 5.15 a scale drawing of the tip of the gauge nozzle, in position at h/d_t = 0.20 is shown on the diagram. The estimated distance of 310 μm indicates the distance between the cake surface and the surface perceived by FDG measurements, while that of 150 μm indicates the height of the peak which formed at the centre.

A small peak was also observed in the centre of the circular impression left by the gauge. A more accurate morphological characterisation was performed by taking a cast of the cake surface below the gauge using superglue. The cast was then scored and snapped along a line central to the gauge nozzle. Colouring the cross-sectional face of this cast allowed subsequent ImageJ processing to give a clear representation of the surface morphology, as shown in Figure 5.16. Here the difference in height between this peak and the region beneath the tip of the gauge nozzle is estimated to be 150 μm, and the difference between the height measured by FDG and actual height of the fouling layer at 310 μm.

An important unknown factor in FDG measurements is whether the shape of the eroded region, as indicated by Figure 5.15 and Figure 5.16 significantly affects the estimation of h/d_t compared to that over a flat surface. This would require a more thorough study of the morphology of this region over multiple experiments, which is beyond the scope of this project. The use of superglue as a casting material is not optimal, as it forms a malleable solid structure and may entrain particles as it flows into the eroded region formed as a result of FDG tests. The possible further work in this area would require a combination of CFD and more reliable topography techniques for determining this geometry.

5.3.4 Application of back-transport models

Particle capture model

The particle capture model discussed in 2.5.2 produced a limiting condition for particle removal to take place, described by equation (2.25). To make a direct comparison to the results shown in Figure 5.13 a steady-state condition is assumed for each reading, wherein the particle capture model would give:

$$d_p\left(\tau_{w,max}\, d_p - \beta 3\mu J 0.36\left(\frac{\kappa}{d_p^2}\right)^{-\frac{2}{5}}\right) = 0 \tag{5.6}$$

such that the shear force imposed by FDG balances that holding the particles against the surface of the cake.

The local permeability, κ, and flux, J, through the eroded region beneath the gauge are assumed to be dependent on thickness, specifically that measured by FDG. Assuming that only cake resistance, R_c, and membrane resistance, R_m, contribute significantly to flux decline, κ can be calculated. Using the law of additive resistances (equation (2.3)), local flux is given by:

$$J = \frac{TMP}{\mu(R_m + R_c)} = \frac{TMP\kappa}{\mu(\delta_c + \delta_m)} \tag{5.7}$$

and cake permeability, κ_c, is given by:

$$\kappa_c = \frac{\delta_{c,max}}{R_c} \tag{5.8}$$

This leads to:

$$\kappa = \frac{\delta_c + \delta_m}{R_m + \frac{\delta_c}{\kappa_c}} \tag{5.9}$$

where δ_m and R_m are determined as described in appendix D1. κ_c is given by equation (5.8) using the maximum cake thickness, $\delta_{c,max}$, shown in Figure 5.13 and a value of R_c calculated with equation (2.3) using the final flux in the filtration. Because the ballotini particles are spherical and resilient against high external pressures (Potters, 2011), the assumption of a constant κ_c is reasonable.

Using the value the Sauter mean particle diameter, $d_{[3,2]}$ of each type of ballotini particle, and a value of $\beta = 0.03$, $\tau_{w,max}$ was determined for varying δ_c values by substituting equations (5.7) and (5.9) into (5.6) to give:

$$\tau_{w,max} = 3 d_p \beta \frac{TMP}{(\delta_c + \delta_m)} 0.36 \left(\frac{\delta_c + \delta_m}{\left(R_m + \frac{\delta_c}{\kappa_c}\right) d_p^2} \right)^{3/5} \tag{5.10}$$

It should be noted that a term for buoyant forces (in the case of 60P18 particles) or gravitational (for 110P8) can also be included in this formulation, however the effects were found to be negligible.

Equation (5.6) is plotted in Figure 5.17 for both types of ballotini, between which there is negligible difference in predicted removal behaviour. Noting the scale on the horizontal axis and the thicknesses measured by FDG, it is immediately apparent that this under-predicts the strength of the cake by over two orders of magnitude when compared with Figure 5.13.

CFD simulations, detailed in section 8.6, for the apparatus used predicted shear stress on the surface beneath the gauging nozzle to be ~0.035 $N \cdot m^{-2}$ (see Figure 8.10). Estimates for δ_c using equation (5.10) give 246 and 230 μm for 60P18 and 110P8 ballotini respectively. Hence it can be concluded that this model also under-predicts thickness when considering the low shear stress on the cake surface within the duct. It is therefore inappropriate for predicting limiting cake thickness during growth or removal due to shear.

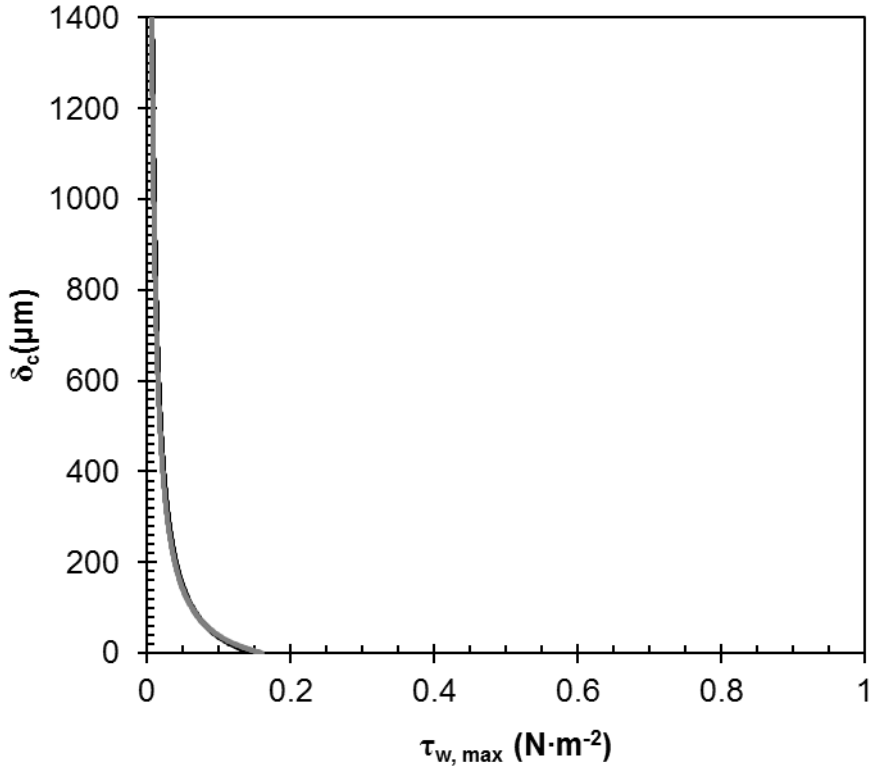

Figure 5.17. Cake thickness, δ_c, against maximum wall shear stress, $\tau_{w,max}$, calculated using equation (5.6) to predict the behaviour shown in Figure 5.13, where TMP = 50 mbar. Black and grey lines represent predictions for 60P18 and 110P8 ballotini respectively. Symbols show experimental data from Figure 5.13 for 60P18 (diamonds) and 110P8 (circles) ballotini.

Inertial lift model

Similarly to the particle capture model, a local flux predicted by the inertial lift model (described in section 2.5.3) is used to estimate a steady-state cake thickness under various shear stresses. Again the highest thickness measurement, along with the flux measured after 3600 s filtration, is used to estimate the cake permeability, κ_c. Assuming a steady-state thickness and local flux through the cake region just below the gauge, under a shear stress, $\tau_{w,max}$, equation (2.28) is rearranged using (5.7) and (5.8) to give:

$$\delta_c = \kappa_c \left(\frac{TMP\mu^2}{0.0045\rho_L d_p^3 \tau_{w,max}^2} - R_m \right) \tag{5.11}$$

This is plotted in Figure 5.18 alongside experimental data. The inertial lift model shows greater consistency with experimental studies than the particle capture model, however still drastically overestimates the extent of cake removal due to shear while also overestimating the maximum thickness at lower shear stresses.

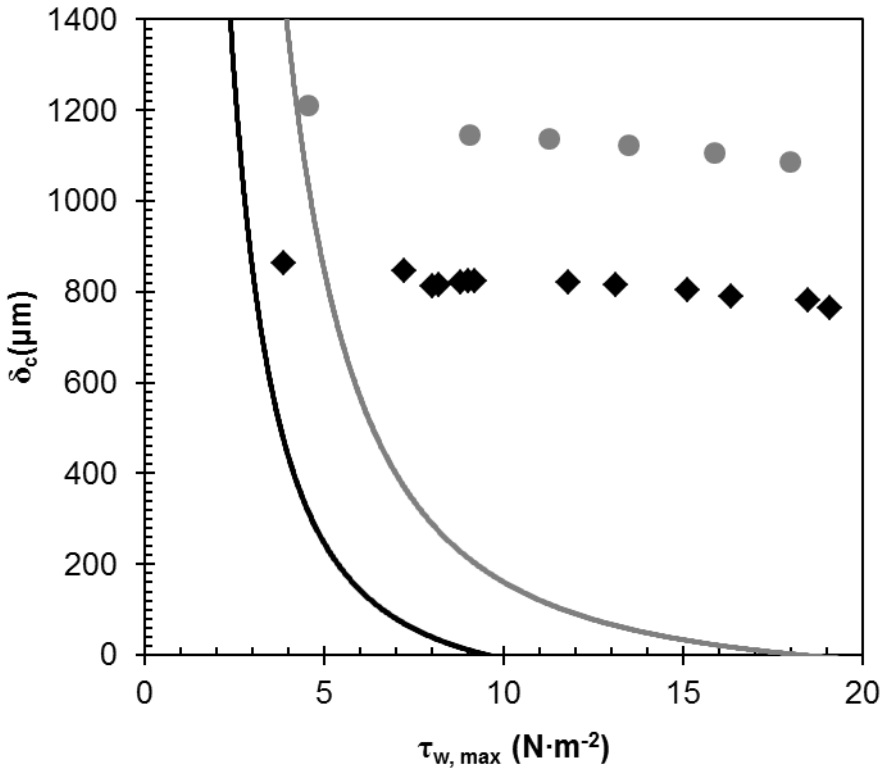

Figure 5.18. Cake thickness, δ_c against maximum wall shear stress, $\tau_{w,max}$, calculated using equation (5.11) to predict the behaviour shown in Figure 5.13, where TMP = 50 mbar. Black and grey lines represent 60P18 and 110P8 ballotini respectively. Symbols show experimental data from Figure 5.13 for 60P18 (diamonds) and 110P8 (circles) ballotini.

This discrepancy is not entirely unexpected, however, as neither model takes into account the effect of particle packing, rather the forces acting on individual particles. It is very likely that to disrupt an already formed cake would require higher shear than to prevent its growth, as it would need to overcome particle-particle static forces in the cake as well. For these results, the inertial lift model is more appropriate for estimating a critical flux, although previous researchers (Li *et al.*, 2000) noted that it under-estimates this value.

These back-transport models for filtrations of particle suspensions are limited considerably by the fact that they rely on accurately modelling the underlying physics of their behaviour in flow fields. A more general model which considers flux decline behaviour was assessed using the additional information provided by FDG, is discussed below.

5.3.5 Critical flux model

The analysis developed by Field *et al.* (1995) as described in section 2.5.1, was used to assess which type of fouling mechanism was dominant. The model considers the rate of flux decline during filtrations to describe behaviour in terms of three possible

mechanistic models. In this work, the critical flux model was applied using plots of $f(J)$ vs. J, where $f(J)$ is described by equation (2.20), which took the forms shown in Figure 5.19. The flux decline laws (e.g. complete blocking ($n = 2$), intermediate blocking ($n = 1$), or cake filtration ($n = 0$)) are applicable where a linear trend is identified between $f(J)$ and J. This was located algorithmically on these plots using a Matlab® script, which is described in appendix B. .

The key parameters identified through this process were a limiting flux, J^*, which corresponds to the x-axis intercept from the linear fit; the gradient, k, and a transition flux, J_T, representing the point where the flux decline mechanism changes to cake filtration ($n = 0$).

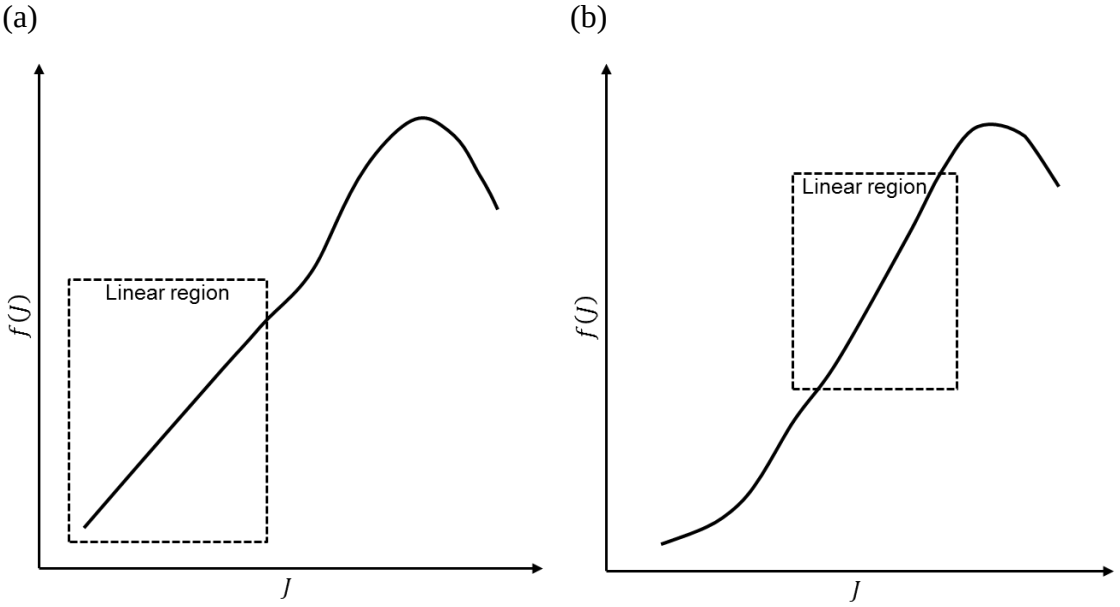

Figure 5.19. General trend seen in plots of $f(J)$ against J using equation (2.20) where (a) $n = 0$, or (b) $n = 1$ or 2.

Utilisation of resulting parameters

Example data for 60P18 ballotini filtrations using the cake filtration ($n = 0$), and intermediate blocking ($n = 1$) laws is shown in Figure 5.20. Through processing flux decline curves from all experiments, it was clear that the best linear fits of $f(J)$ vs. J occurred where $n = 0$. These were also applicable between the minimum flux and a relatively high transition flux, J_T, which corresponded to a time point early on in filtrations. This indicates, as should be expected for this system, that cake formation was the dominant fouling mechanism. Theoretically, the terminal flux, J_∞, should be predicted by J^* from equation (2.20) when $n = 0$. In general this gave reasonable predictions however there was considerable variation in this derived parameter, mostly due to increased data scatter at lower fluxes. The limiting flux, J^*, for intermediate

(n = 1) and complete blocking (n = 2) laws might also be construed as an indication of the upper limit of flux for the cake fouling (n = 0) model. The linear fit shown in Figure 5.20b demonstrates, however, that although a high goodness of fit can be achieved there is an obvious curvature to the data. Added to this, the resulting parameters for (n = 1) and (n = 2) were quite similar.

(a) (b)

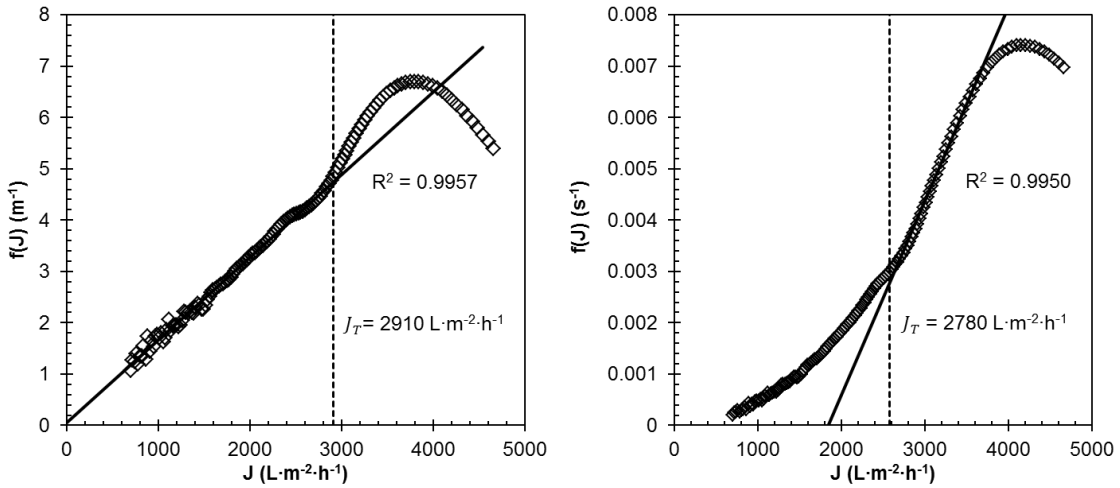

Figure 5.20. Examples curves for $f(J)$ against J used to determine critical flux parameters where (a) n = 0 and (b) n = 1. Vertical dashed lines indicate the transition flux, J_T, and the solid lines represent the linear trends identified using a Matlab® script. Data shown here is for a filtration of 60P18 ballotini at TMP = 50 mbar and Re_{duct} = 1550.

An arguably more important parameter derived in this analysis was in fact the transition flux, J_T, which represents the flux at which the dominant fouling phenomenon changes. For the three different types, n = 0 to 2, a good agreement was achieved for this value, with that predicted by the cake fouling model (n = 0) always slightly higher. An estimate for J_T was determined by taking an average between all three models. Here J_T now represents the flux at which cake fouling can be considered the dominant mechanism contributing to flux decline.

Influence of TMP

Figure 5.21 shows fits of $f(J)$ vs. J (using equation (2.20) and n = 0) for the three flux decline curves shown in Figure 5.8 for TMPs of 30, 50 and 75 mbar. In all cases a reasonable linear fit is achieved for a significant portion of the data, indicating that cake fouling is the dominant mechanism responsible for flux decline under all three conditions. The transition flux, J_T for each pressure (2490, 2960, and 3950 L·m^{-2}·h^{-1} for TMPs 30, 50, and 75 mbar respectively) occurred before the first thickness reading was taken. The trend in J_T with TMP is shown in Figure 5.22 wherein an average of all the

results, including those using n = 1 and 2, is shown. A clear positive trend is shown, although there was significant spread in the data.

Another clear observation to be made from Figure 5.21 is that the gradient, k, from equation (2.20), decreases with increasing TMP. From Table 2.4, it can be seen that for cake filtration, when n = 0:

$$k = \frac{\varphi_c k_c'}{J_0 R_m} \tag{5.12}$$

which implies a strong dependence on the initial flux, J_0. This is supported by experimental findings, as indicated by Figure 5.23, which demonstrates an inverse relationship between k and J_0. This should not be expected to be linear however, as the parameter k_c' in equation (5.12) contains the limiting flux, J^*. Due to the inherent variability of this quantity, and the lack of sufficient data for predicting the specific resistance of the cake, φ_c, no further analysis was performed for ballotini filtrations. Equation (5.12) can be used to identify an assumed constant back-transport rate of particles from the cake, this is explored further in section 7.3.6.

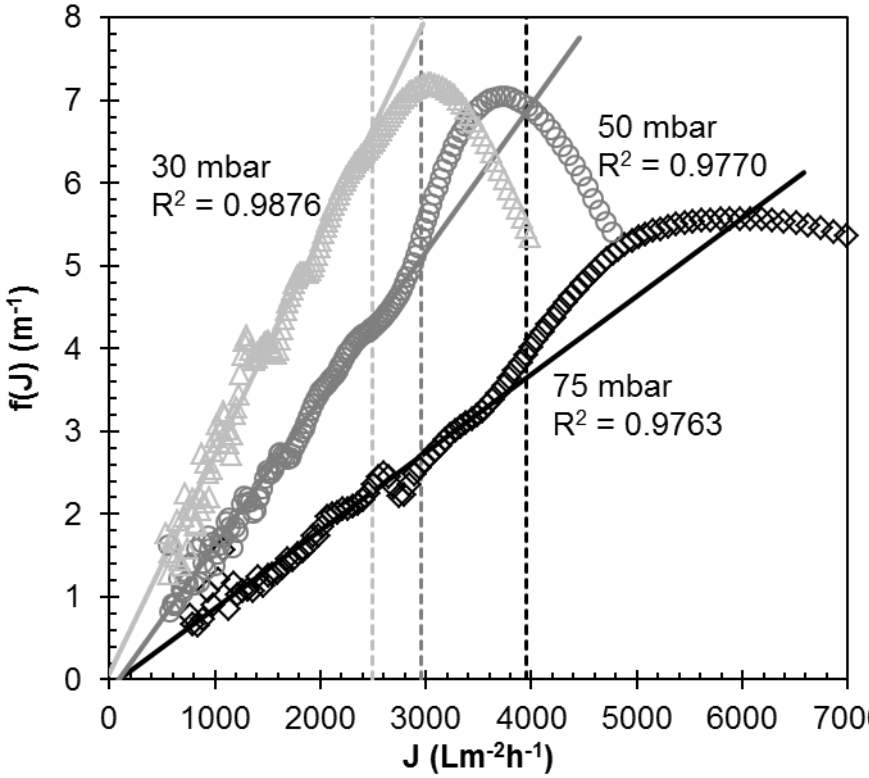

Figure 5.21. $f(J)$ against J using equation (2.20) where n = 0 for flux decline curves shown in Figure 5.8 where Re_{duct} = 1000 and TMP = (light grey, triangles) 30, (dark grey, circles) 50, and (black, diamonds) 75 mbar. The fits determined using the method described in appendix B. are indicated by the solid lines, and the associated J_T values are indicated by the dashed lines. In this case J_T = 2490, 2960, and 3950 L·m^{-2}·h^{-1} for TMPs of 30, 50, and 75 mbar respectively.

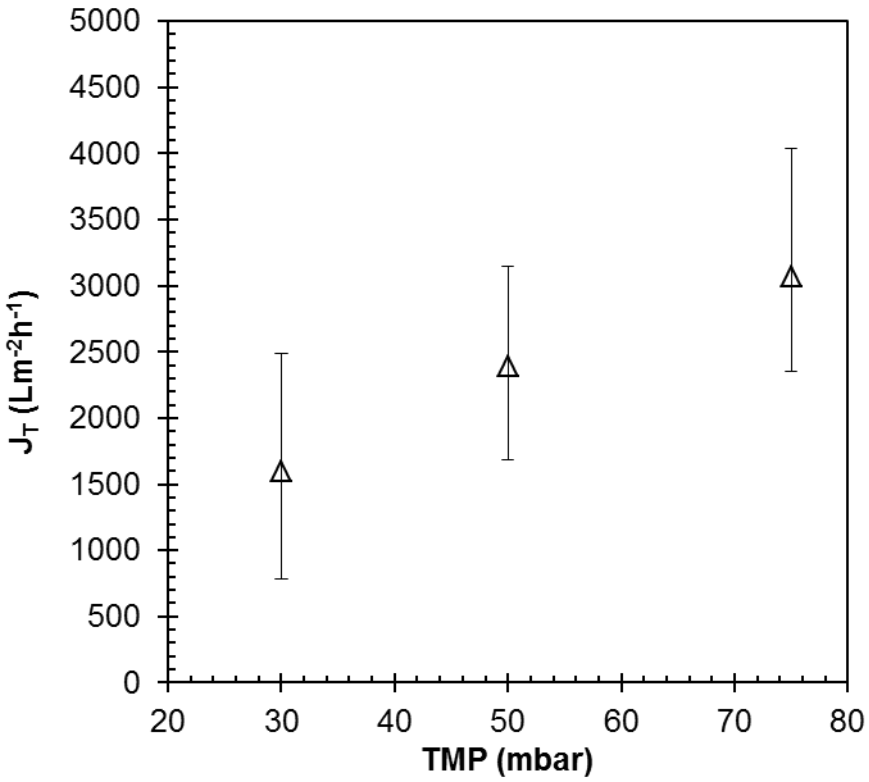

Figure 5.22. Transitional flux, J_T for filtrations of 60P18 ballotini at Re_{duct} = 1000 and varying TMP. Results shown here are averages taken from those derived by the method described above for n = 0, 1 and 2. Error bars depict the overall span.

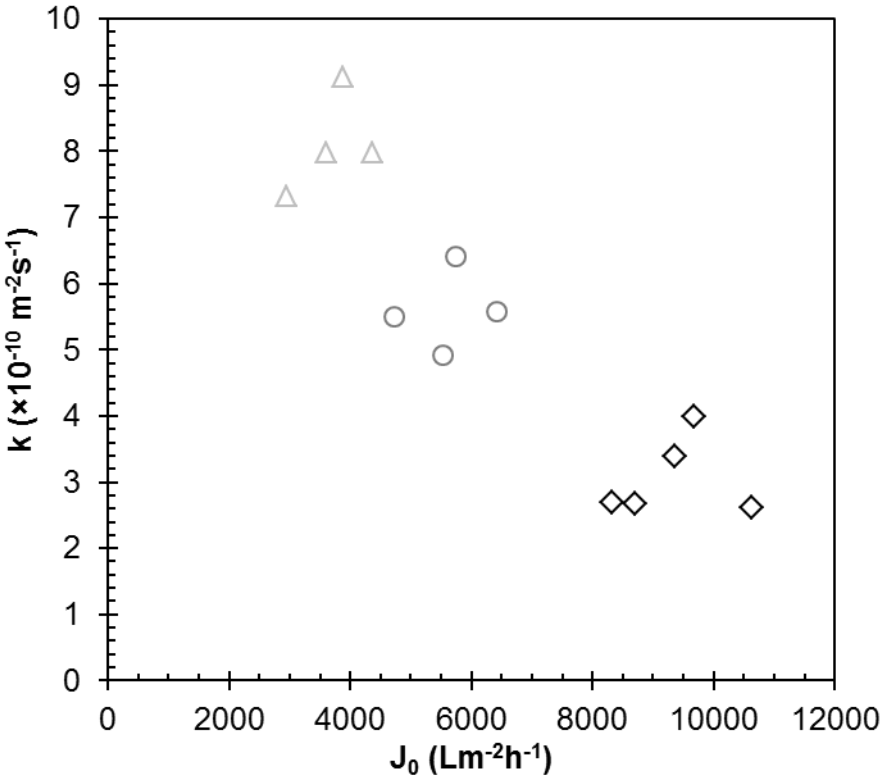

Figure 5.23. Gradient, k against initial flux, J_0 for filtrations of 60P18 ballotini at Re_{duct} = 1000 and TMP = 30 mbar (triangles), 50 mbar (circles) and 75 mbar (diamonds).

Using this analysis it can be concluded that a cake fouling mechanism becomes the dominant cause for flux decline within the first 200 s of a filtration, which is supported by a clear indication using FDG (Figure 5.8) of a fouling layer exceeding 50 μm measured at 240 s.

5.4 Conclusions

FDG has been demonstrated with both a non-ideal, polydisperse, foulant (yeast) and more monodisperse, ideal foulant (ballotini). The initial studies with yeast indicated that methods where cake thickness was measured constantly were not ideal and caused too much disruption to the formation of the cake layer. This method was improved upon in filtrations of ballotini particles, wherein that accuracy of thickness estimates was explored further. It was identified that making periodic estimates of cake thickness still caused too much disruption to the fouling layer, which was confirmed by viewing cross-sections of the cake under a microscope. Thickness measurements taken after a fouling layer was formed, however, provided a better representation of the fouling layer. In addition these tests were able to provide information about the strength of fouling layers when subjected to high fluid shear forces. An aspect of cake fouling which cannot be readily investigated using other techniques.

Investigation of various models to describe cake fouling in cross-flow conditions showed that the inertial lift and particle capture models were ineffective for describing cake removal. They also did not give satisfactory predictions for a terminal cake thickness. The critical flux model does not provide a means to predict cake thickness; however it provides the most useful analysis for these filtrations. As was shown for the ballotini filtrations it can be used to determine whether cake fouling is the most dominant cause of flux decline. With confirmation from FDG readings, it could also be used to determine the influence of pore-fouling mechanisms on flux decline. This is demonstrated later in section 7.3.

Chapter 6: Automated Cross-flow Rig

The results reported in the previous section highlighted some weaknesses of the apparatus used. Namely the 3 mm recess to the membrane surface which caused uneven deposition, and the time taken to manually adjust h_0. A higher precision for FDG thickness measurements is also desirable, which can be achieved using more advanced equipment and a smaller gauge nozzle. An automatically controlled measurement system would also reduce the time taken to perform experiments.

6.1 Improved features of new apparatus

To address some of the issues identified previously, a new test section was developed for cross-flow FDG studies which included the following improvements:

1. Automation of FDG for membrane calibrations by use of PC-controlled equipment using a LabView™ visual interface.
2. More precise measurement of cake thickness by implementation of:
    a. A smaller gauge nozzle, with d_t = 0.5 mm
    b. A linear stepper assembly to move gauge in smaller graduations of <1 µm
    c. A Linear Variable Differential Transformer (LVDT) for high accuracy measurement of gauge position (± 0.5 µm)
3. Smaller gauge has lower footprint within the duct flow channel and hence lower impact on flow. This also increased the range of $\tau_{w,max}$ which could be studied.
4. Reduction of step-down to membrane from duct entry (3 mm to 1 mm) and chamfering of this step to significantly prevent recirculation at the entrance and exit of the duct (see section 8.6).
5. Use of a syringe pump to control m_g, which led to the following advantages:
    a. Removed any significant inaccuracy from such readings due to the use of a needle valve, which risked clogging by foulant due to flow constriction.
    b. Zero net removal of process media from the feed side of the test section. This allows for sterile operation.
    c. More accurate control of shear stress imposed by gauging flow.
    d. Can be incorporated into an automated control system.

6. Capability for mounting membranes on curved supports.
7. Needle valve for more accurate control of TMP.
8. Automation system which allows experiments to be performed at a greater frequency.

This updated apparatus was used to study filtrations of Kraft lignin, a non-ideal fouling material, and then subsequently filtrations of a mixture of lignin and ballotini. One of the main purposes of these studies was to demonstrate how efficiently this new setup can be used to collect data for membrane filtrations.

6.2 Apparatus

6.2.1 FDG gauge

A smaller FDG gauge was used for this apparatus than has previously been used in any other FDG studies. A diagram of the nozzle is shown in Figure 6.1, and a full mechanical drawing is included in appendix E. .

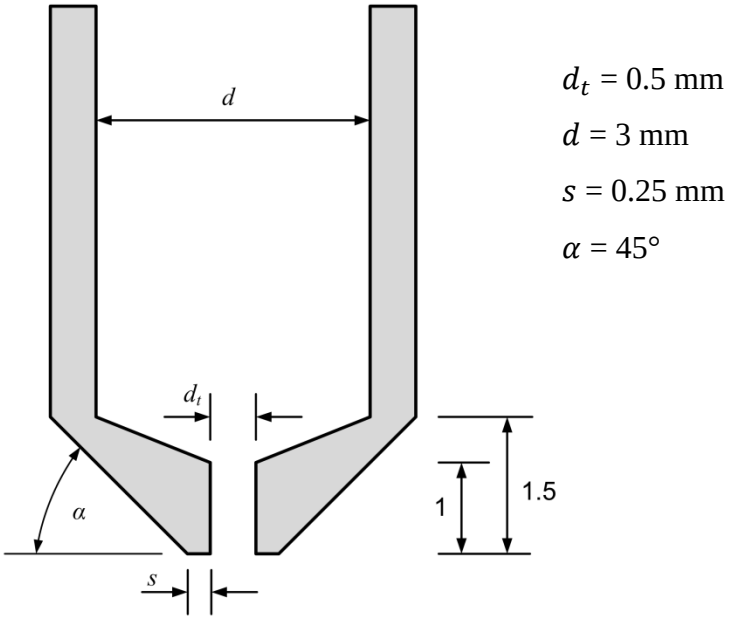

Figure 6.1. Schematic of the new gauge nozzle and dimensions (in mm).

6.2.2 Test Section

A schematic and photograph of the new test section is shown in Figure 6.2, its design was based on the apparatus described in section 4.1. The main body of the test section was made from polycarbonate, and contained a single square channel of 15 mm cross-section through which the feed suspension flowed over the membrane. The bottom section of this was removable, such that a membrane "cassette", detailed below, could be inserted (and later removed). The resulting filtration cell was a 150 mm long

channel, 15 mm wide by 16 mm high, with a membrane at the bottom surface. Here the 3 mm drop to the membrane, as described in section 4.1, was replaced by a 1 mm tapered drop by means of a chamfered edge on the membrane cassette. TMP was measured by a differential pressure transducer, dP_1 (*Omega Engineering*, PX26-005DV, ± 1 mbar), which was attached to pressure tappings into the feed and permeate side by flexible tubing. Δp_{14} was also measured by a differential pressure transducer, dP_2 (*Omega Engineering*, PX26-001DV, ±0.25 mbar), connected by flexible tubing to a tapping into the duct, and a y-piece upstream of the gauge nozzle.

The gauge was positioned directly in the centre of the duct, i.e. with its central axis 75 mm from each end of the filtration cell and 75 mm from each side. Two more positions were available for mounting the gauge towards the entrance or exit of the flow

(a)

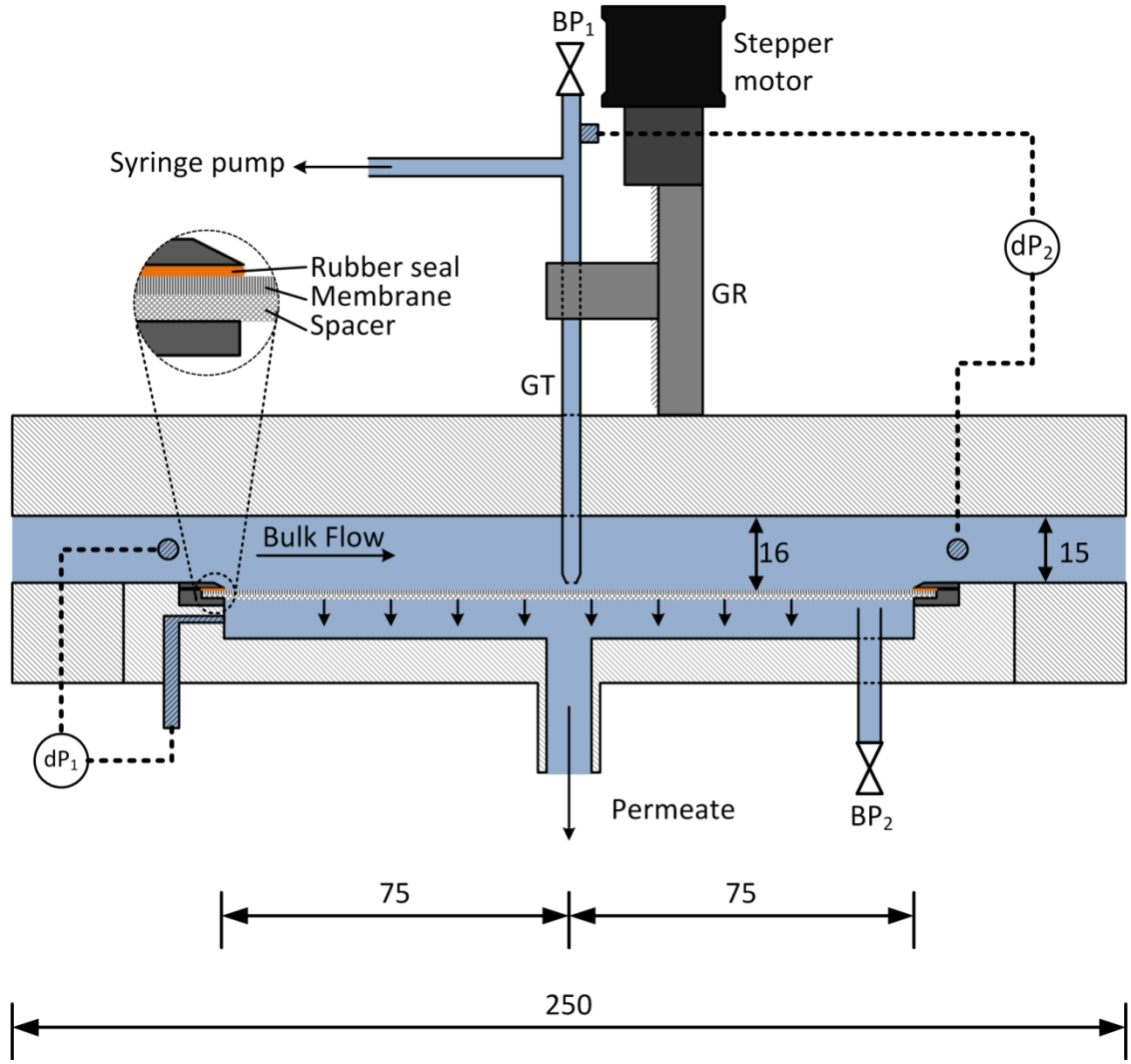

Figure 6.2. (a) Schematic, and (b) photograph of the new test section, where dP_1 and dP_2 are pressure transducers, BP_1 and BP_2 are bleed points with pinch valves. GT is the gauge tube, GR is the linear guide rail from the stepper system and V7 is a needle valve used to control TMP. Dimensions are in mm.

(b)

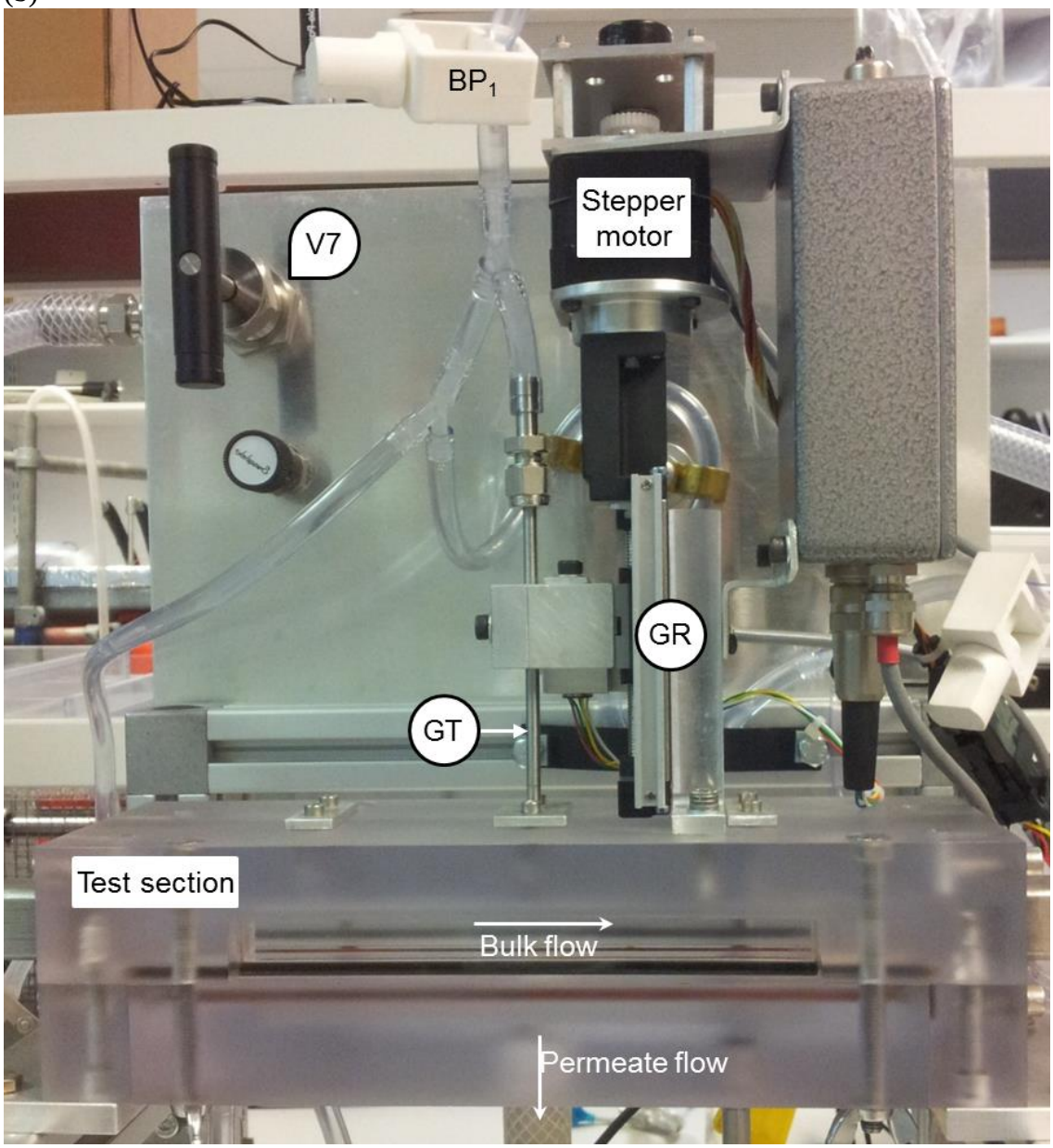

Figure 6.2. (a) Schematic, and (b) photograph of the new test section, where dP_1 and dP_2 are pressure transducers, BP_1 and BP_2 are bleed points with pinch valves. GT is the gauge tube, GR is the linear guide rail from the stepper system and V7 is a needle valve used to control TMP. Dimensions are in mm.

cell, each 60 mm from the central position. The gauge was inserted through the top of the test section with an o-ring seal, and its height controlled by a linear stepper assembly (described below). A bleed point was fitted beneath the membrane. This consisted of a retractable tube inserted through the bottom of the test section, with flexible tubing and a pinch valve at the end.

Full design drawings of the new test section are provided in appendix E. [*].

[*] The mechanical drawing and construction of the apparatus was performed by Paul Frith (Faculty of Science) based on original concept schematics produced by this author.

Membrane cassette

The membrane was mounted between a rubber seal and stainless steel mesh spacer, clasped tightly within a stainless steel frame to form a cassette with a 15×150 mm porous surface. The structure of the cassette is indicated in Figure 6.2a (inset), and the different parts are pictured in Figure 6.3. This design meant that a membrane could be more easily removed for further analysis after fouling. The spacer used in this work was flat, but was interchangeable with curved spacers.

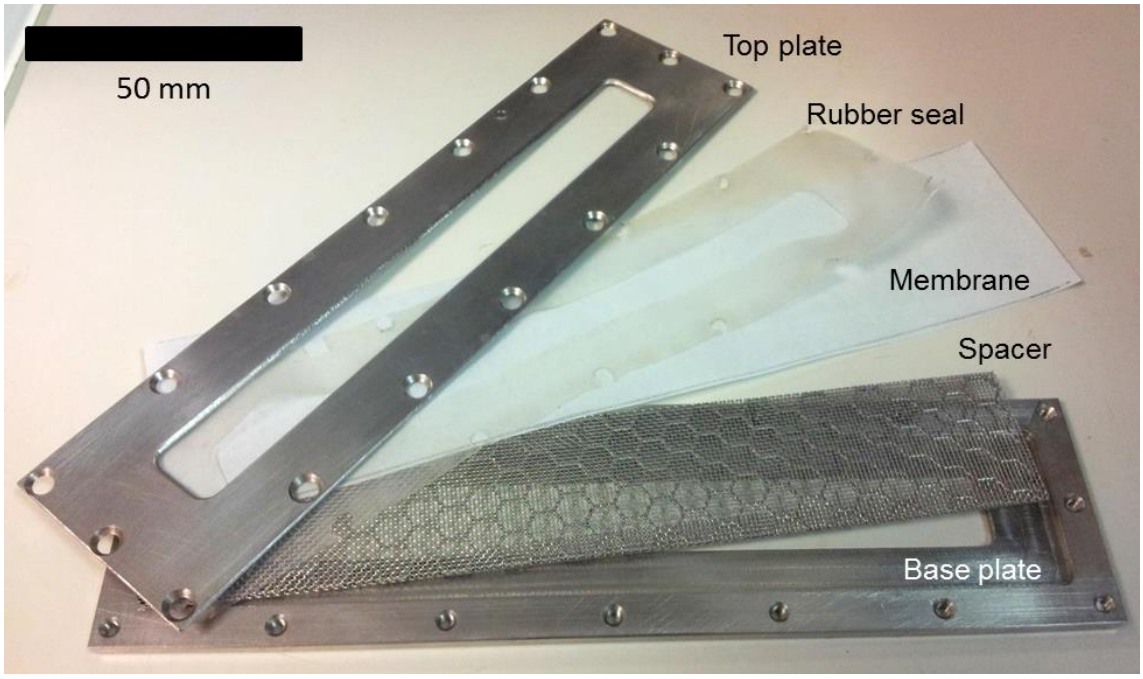

Figure 6.3. Photograph showing the components of the membrane cassette, which was screwed together tightly when used for filtrations.

Linear stepper assembly

A schematic and photograph of the linear stepper assembly are shown in Figure 6.4. The position of the gauge was adjusted using a stepper motor (*Nanotec*, ST4209S1006-B), attached to a linear guide rail (*THK*, KR1501AM). With these components, a single step size of 0.325 μm was achievable. The position of the gauge was read by two methods, namely a potentiometer and a linear variable differential transformer (LVDT). The LVDT (*RS Components*, SM-series LVDT, ± 0.5 μm) indicated the position of the gauge to a high accuracy within a limited range of 2 mm. The potentiometer (*Vishay*, Spectrol 534) was geared to the stepper motor such that it could indicate the position of the gauge, independently from the LVDT, within the entire movement range of the guide rail (75 mm). This set-up allowed the gauge to be removed far from the membrane when readings were not taken, and then quickly returned to a closer position for taking thickness readings.

(a) (b)

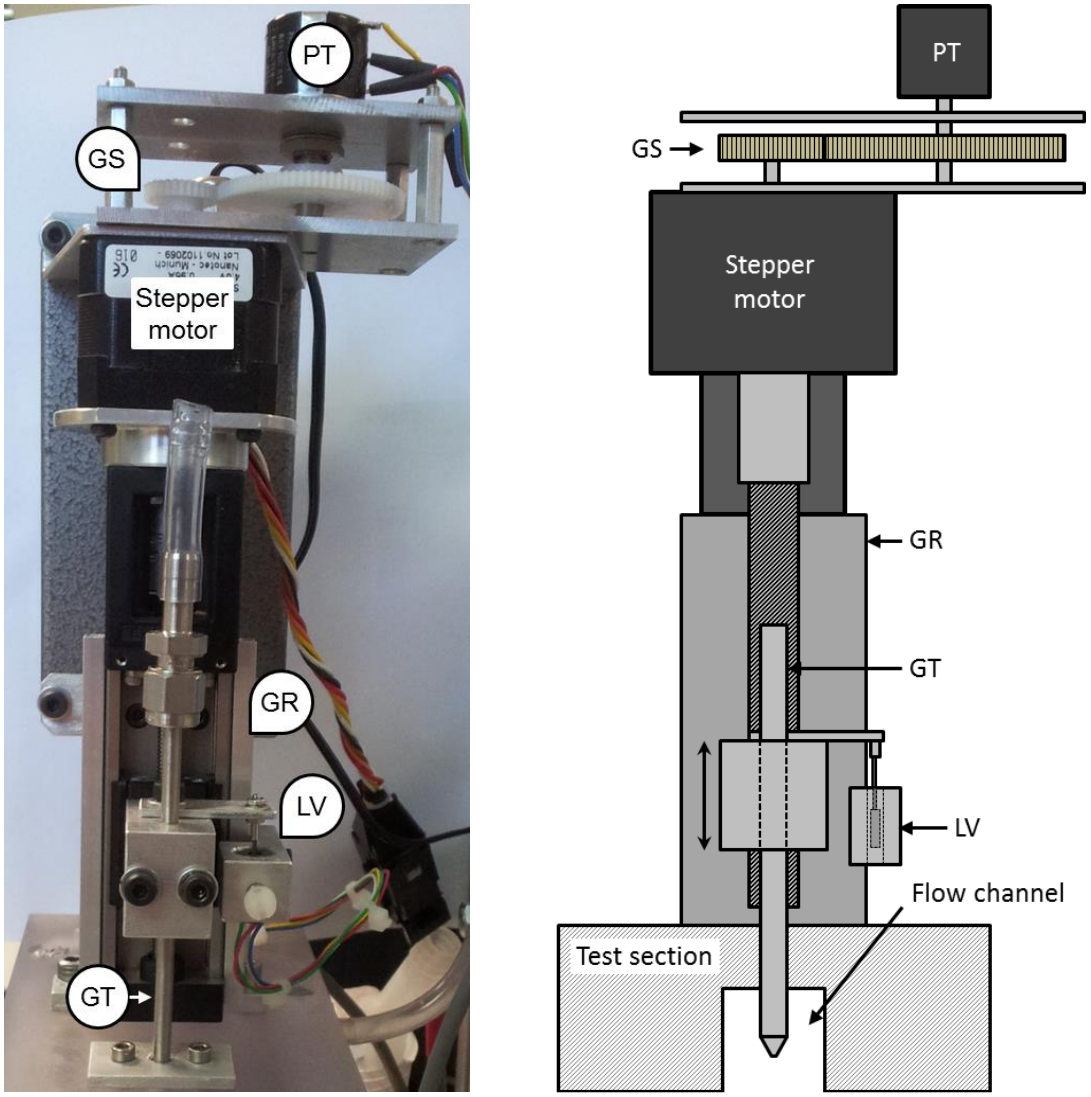

Figure 6.4. (a) Photograph, and (b) schematic of the linear stepper assembly mounted on to the test section. PT – potentiometer, GS – gearing system, GR – linear guide rail, LV – LVDT, GT – gauge tube.

6.2.3 Flow loop

The test section was installed into a recirculation rig, shown in Figure 6.5. The suspension was stored in a 20 L feed tank and circulated through the system using a centrifugal pump (*Charles Austen*, P16)[*]. A 500 mm long entry section of 15 mm square duct was attached to the inlet of the test section to ensure fully developed flow on entry. Cross flow velocity, characterised by Re_{duct}, was measured by a variable area flowmeter (*KDG Instruments*, Rotameter Series 1100) and controlled by adjustment of valves V2 and V5. TMP was controlled by adjustment of V7, and V6 could be shut in order to prevent permeate flow completely. The retentate was returned to the feed tank,

[*] This was later replaced with a regenerative pump (*Totton*, HPR6/11), however the operation of the rig remained unchanged.

(a)

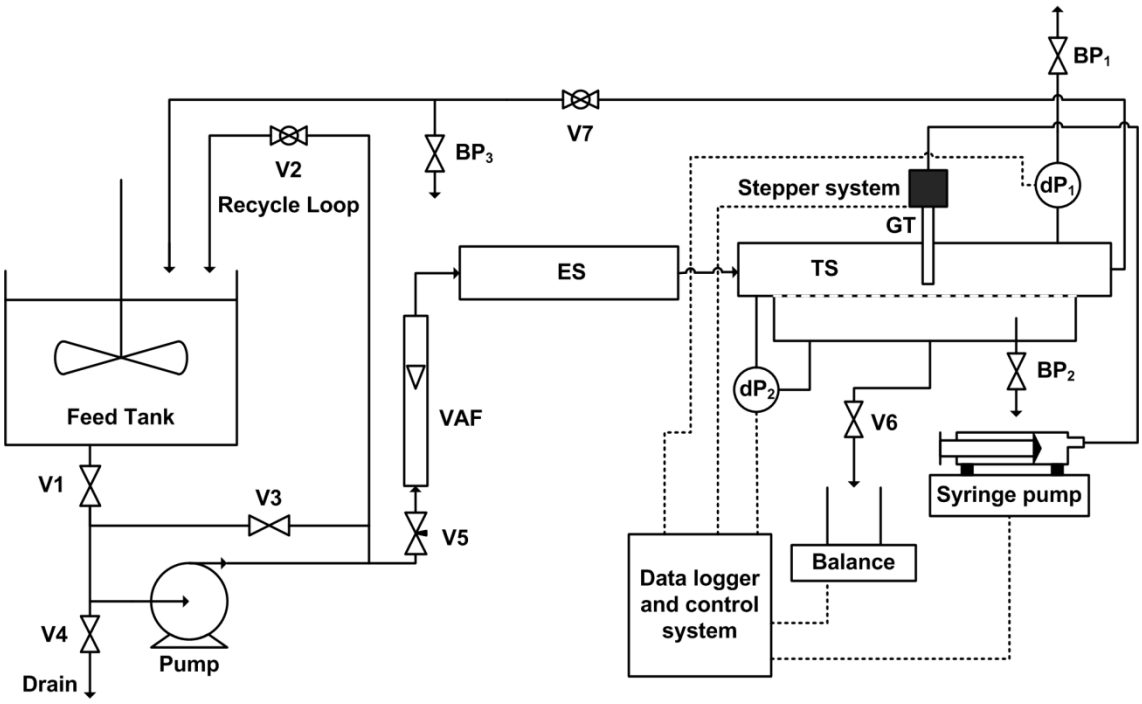

(b)

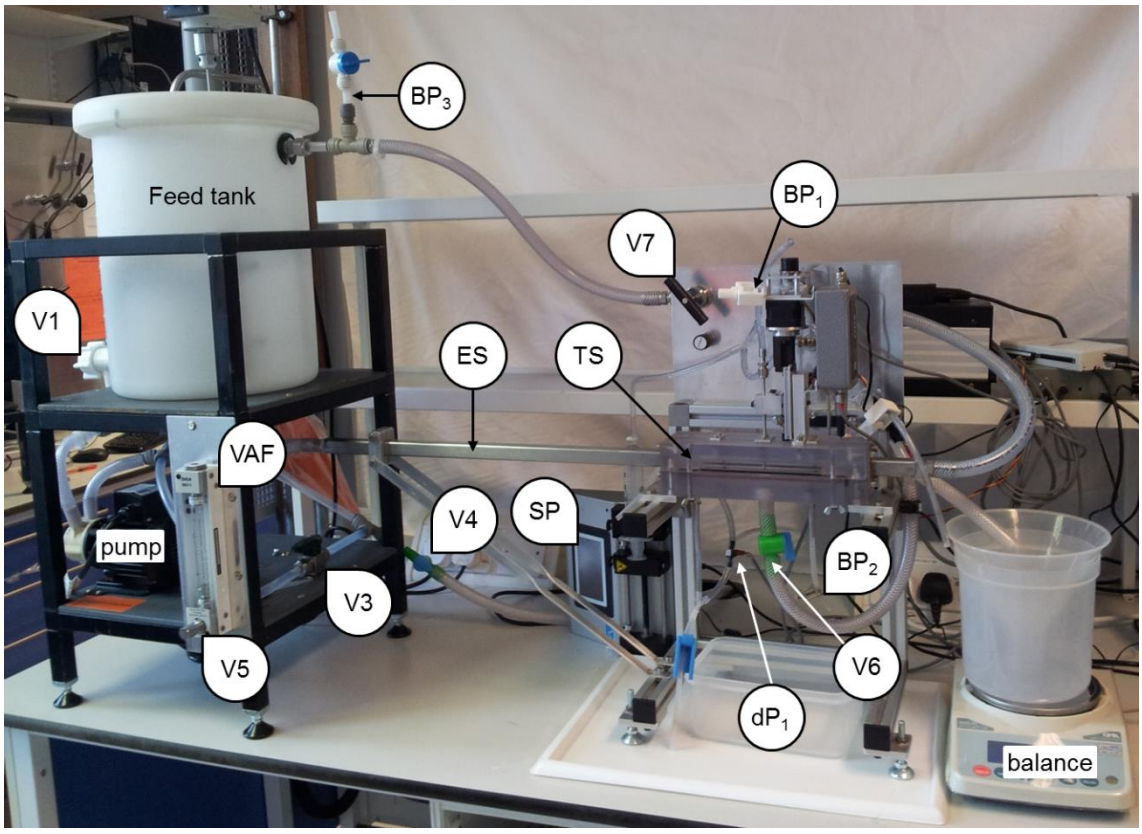

Figure 6.5. (a) schematic, and (b) photograph of flow loop used with the automated cross-flow apparatus. V1 to V7 are valves. BP_1 to BP_3 are bleed points. dP_1 and dP_2 are differential pressure transducers. GT is the gauge tube, ES is the entry section, VAF is a variable area flowmeter, SP is the syringe pump, and TS is the test section described in section 6.2.2.

while permeate was collected and weighed on an electronic balance (*A&D*, FX-3000i, ± 0.005 g). In order to prevent any negative pressure from a liquid head below the permeate outlet on the test section, a static weir was created using a Y-piece before the balance, at the same level as the membrane. Extra bleed points (not labelled) were installed on both sides of each pressure transducer to allow removal of any air bubbles.

The pressure transducers, balance, syringe pump and linear stepper assembly were all connected to a data-logging PC for measurement and control. The details of this are covered in the next section.

6.3 Data Acquisition

To meet the objective of progressing FDG for membranes towards a more automated and user-friendly technique, advanced control systems need to be employed. As a form of prototype, a LabVIEW™ 2010 Visual Interface (VI) was developed for easy recording and interpretation of data. Reducing the reliance on post-processing raw data or taking manual readings, the VI confers the following advantages:

- Estimations of gauge clearance, h/d_t, and deposit thickness, δ_c, are displayed in real-time
- The user can record individual data points on-demand, separate from a time-related data sheet
- Average and standard deviation of gauging pressure (Δp_{13}) measurement is determined across an adjustable time-period, such that steady-state readings within acceptable error margins can be recorded
- Safeguards prevent gauge movement which would damage the membrane or apparatus
- Collection of membrane calibration data is automated
- Tabbed format allows easy navigation and control of different data processes and control systems.

While a full description of the VI operation and programming is not provided in this dissertation, the most important operating principles relevant to an automated FDG system are outlined below. Some details of calculations used in data acquisition are also given in appendix D2.

6.3.1 Wiring

The pressure transducers (which use piezoresistive elements) were used under a constant 10 V excitation voltage, and their output voltage passed through an amplification circuit to a data acquisition (DAQ) device (*National Instruments*, NI USB-6210). A ± 10 V signal from the LVDT (transferred via a signal converter) was also read by the DAQ device. The stepper motor was controlled through a constant current drive (*Nanotec*, SMC42) by a programmable circuit board* (*Arduino*, ATmega2560), which also read the voltage of the potentiometer. All devices were connected to the PC via USB.

6.3.2 Real-time data display and output

The main VI screen and data acquisition tab are shown in Figure 6.6. This was used for monitoring pressures and balance readings and adjustment of acquisition timings. All of the data acquisition and processing took place within a process loop which ran every 0.5 s. This frequency – which was adjustable, as shown at item 5 – allowed fast response to changes in pressure and flow whilst maintaining the stability of the program for long-running experiments.

Syringe pump control

The syringe pump was capable of operating in withdrawal (drawing fluid from the test section) or infusion (infusing to the test section from the syringe) mode and at flowrates from 5 $pL \cdot min^{-1}$ to 220.97 $mL \cdot min^{-1}$. These processes, along with their respective flowrates, could be controlled from the VI. The status of the syringe pump could also be output on command, which was used during automated processes where the quantity of fluid within the syringe was important. 60 mL syringes (*BP Plastipak*) were used with the pump, however only a 40 mL working volume was used to allow a 10 mL buffer at each end before the full and empty extremes.

Average Pressures

Within this process loop, average pressures were taken across an adjustable timeframe (items 4 and 8 on Figure 6.6). In this work a 5 s timeframe was used for both, meaning that at 0.5 s loop intervals 11 consecutive data points were considered. The standard deviation for each was also recorded and displayed. Taking average values ameliorated the effects of minor flow pulses from the pump, and provided more reliable

* This was wired and programmed by John Bishop (a member of the Faculty of Engineering technical staff), and responded to string commands sent from LabVIEW™

data for thickness estimates. It also meant that error margins were not just assumed from the manufacturer data on the transducers, but directly evident during operation.

Flux calculation

Permeate flowrate was recorded by taking a mass difference between balance readings across an adjustable interval (item 7 on Figure 6.6) for which 9 s was used in this work. The membrane area was stored in the VI, which remained constant at 0.00225 m^2 for all experiments.

Δp_{13} calculation

Δp_{13} was calculated by equation (2.35), using l_{eff} = 200 mm. The latter value was arbitrary because an offset to Δp_{13} was required, as described in section 6.6.2. The standard deviation was considered to be the same as for Δp_{14}, given that the error in m_g was negligible when using the syringe pump. An indicator light (item 3 in Figure 6.6) showed whether the error was below an adjustable target (specified in item 1); this was

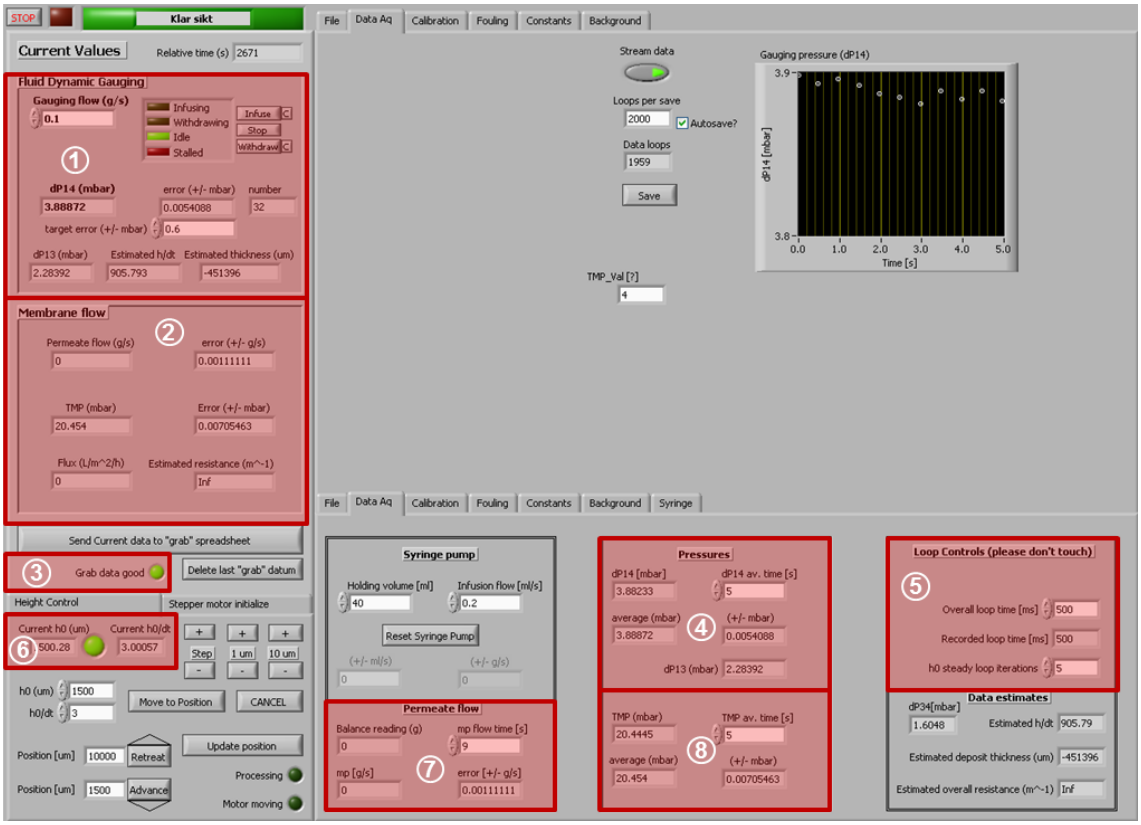

Figure 6.6. Main VI window and data acquisition tab, where numbered items are: 1. Syringe pump control, FDG related readings, and adjustment of target error; 2. Membrane filtration data; 3. Indicator light showing if Δp_{14} error is within limit; 4. Δp_{14} immediate, average, and standard deviation readings, plus time interval control for averaged readings; 5. Overall loop time control; 6. h_0 values and indicator light for steady readings, set in the height control tab; 7. Permeate flow values and time interval control. 8. TMP immediate, average, and standard deviation readings, plus time interval control for averaged readings.

also used as a condition in the automated calibration procedure described in section 6.3.4.

h_0 monitoring

The distance, h_0, between the gauge nozzle and the membrane was displayed in the bottom left corner of the VI screen, item 6. The indicator light in this item was used to show whether 5 consecutive readings (a number adjustable in item 5), all within an error of ± 0.5 μm had been made. This served to ensure that the gauge position was stationary and safeguard against random reading errors affecting gauge movements. The indicator was also used in the stepper control procedures described in section 6.3.3. Because the LVDT used to indicate the gauge position could only do so within a 2 mm range, readings from it were ignored when the potentiometer indicated that h_0 was outside this range (i.e. voltage > 11).

Thickness estimation

A linear interpolation function was used to predict h/d_t values from a set of data points for Δp_{13} vs. h/d_t. The data was plotted in a "constants" tab in the VI, shown in

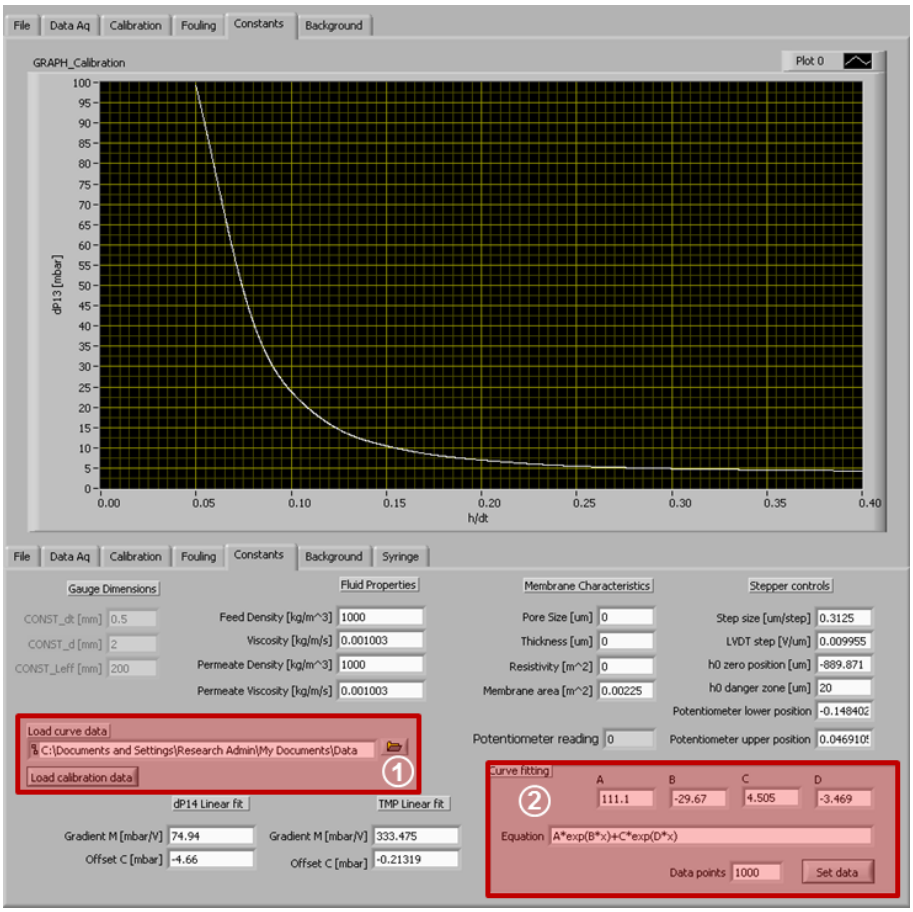

Figure 6.7. Constants tab from the VI, in which the graph shows the calibration plot for Δp_{13} vs. h/d_t defined by either 1: a tab-delimited text file, or 2: a coefficient equation.

Figure 6.7. These data points could be generated from a user-defined function, as in the box indicated by item 2, or from a spreadsheet (item 1). The latter of these was found to be the most accurate method as it allowed the use of a spline fit to CFD data. As described in section 8.7, this was the closest fit to calibration data and so produced the most accurate thickness estimations possible using this apparatus.

Data logging

All the above readings were recorded in an output data file, and aligned to the mid-point of their specified interval so that the time they apply to is accurately represented. For example: an average Δp_{14} value recorded across 5 seconds between 200 and 205 s would appear for 202.5 s. A full description of how the values above were calculated and aligned is given in appendix E. .

6.3.3 Stepper control system

Gauge movement speed was adjustable, however the positioning was often less accurate when moving at higher speeds. For this reason faster, less accurate adjustments were used to move the gauge at greater distances (e.g. $1 < h_0 \leq 12$ mm) far outside of the range used for making thickness measurements. Lower speeds were used for more accurate adjustments. Three different types of movement command were made available, the controls for which are shown in Figure 6.8, along with flowcharts outlining their respective control systems. The commands were as follows:

1. Immediate adjustment of h_0 by 1 step (~0.325 μm), 1 μm, or 10 μm. This did not account for backlash on the guide screw, so movements were not always of the exact distance.
2. Accurate positioning of the gauge. Here the nozzle height, h_0 could be specified directly. If the gauge position – as indicated by the LVDT – was greater than 0.5 μm from the target, further adjustments were made in a repeating loop until this was no longer true.
3. Fast movement of the gauge to specified "advance" and "retreat" positions. This process included speed adjustment for faster movement of the motor. The preliminary checks in this case also failed if h_0 was already within 500 μm of the target.

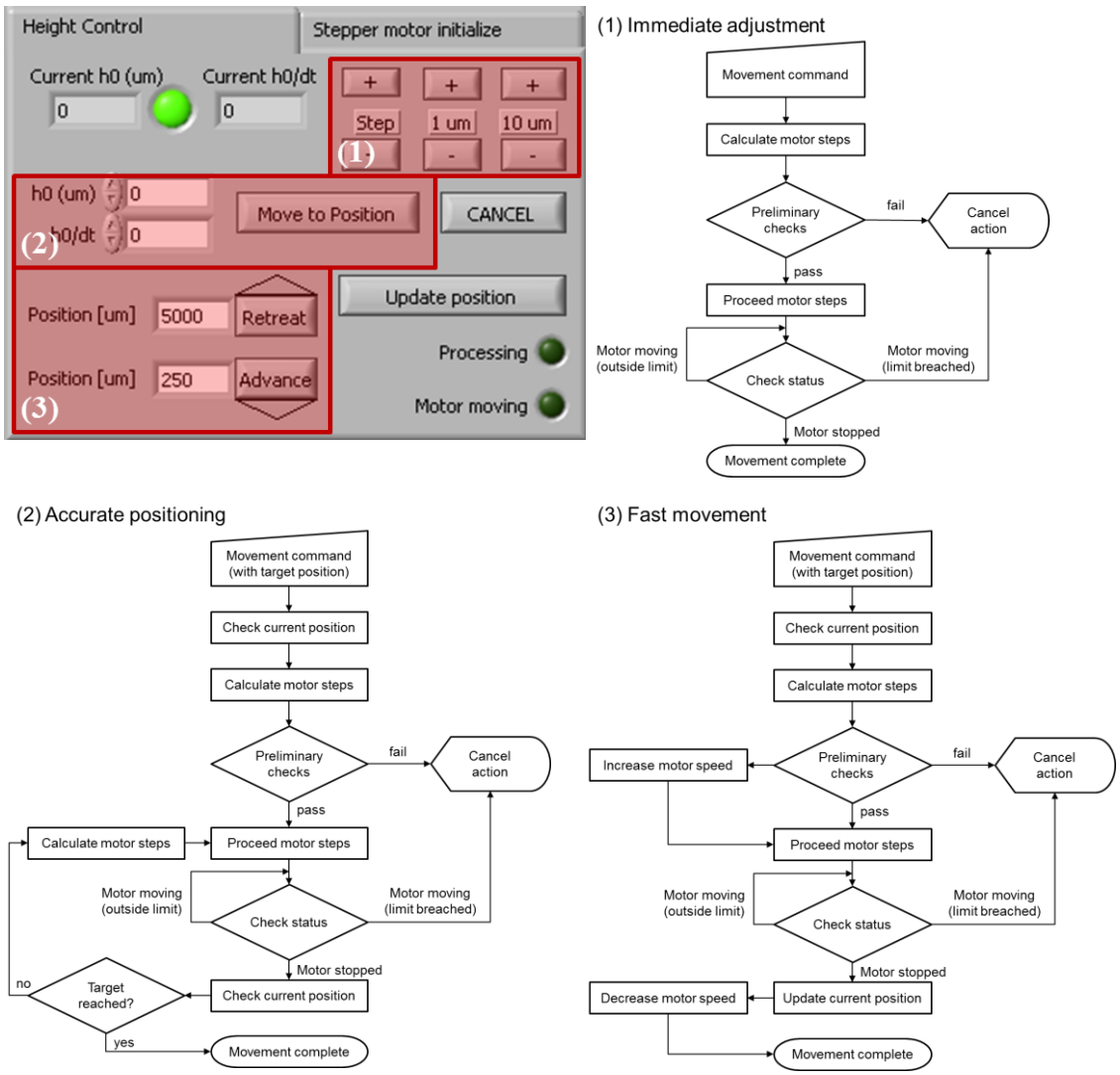

Figure 6.8. Stepper controls for VI, where boxes (1), (2) and (3) represent the different types of movement command described above. The corresponding control flowcharts for each are shown.

Movement safeguards

All of these control systems included preliminary and ongoing status checks to safeguard against movements which might bring the gauge into contact with the membrane. An adjustable maximum h_0 value (set at 20 μm in this work) was defined, below which the control system would not allow any movement. The ongoing status check relied on using the inbuilt timer of the main VI loop, along with h_0 estimation from the LVDT and step readings from the programmable circuit board, to continuously check if the motor was still moving. It also triggered an immediate cancellation of the motor movement if h_0 was below the minimum.

The preliminary checks were run prior to any movement operations, and a cancellation (or fail condition) would occur if any of the following conditions were met:

- Stepper motor is not enabled

- h_0 readings are unsteady (i.e. > 0.5 μm variation across five consecutive readings)
- A potentiometer reading has not been recorded to check the gauge is in the right position
- Target position is below maximum h_0
- Specific to the following movement commands from Figure 6.8:
    2. Potentiometer and LVDT readings confirm the gauge nozzle is within 2 mm of membrane
    3. Target h_0 >500 μm from current position

In addition to these safeguards, a 'CANCEL' button, as shown in Figure 6.8a allowed the user to abort movement at any time.

6.3.4 Automated calibration

A calibration tab within the VI, shown in Figure 6.9, was used to set calibration steps and display Δp_{13} vs. h/d_t values (item 2) against a standard calibration curve (item 1). The calibration curve could be input into the VI either in the form of an equation and accompanying coefficients, or directly from a data-file (see Figure 6.7). The VI was programmed such that the user could create a list of h_0/d_t values (item 4) using the controls in item 5, for each of which it would determine Δp_{13}. The order in which the values were attained could be altered between advancing (towards the membrane) and retreating (away from the membrane) modes, as shown in item 7.

A flowchart for the automated calibration process is shown in Figure 6.10. The process utilised movement command 2, as described above, and launched a separate window (Figure 6.11a) upon commencement to show progress and troubleshooting information. An additional feature was put in place to empty the syringe if it reached a maximum, set on the VI (item 6 on Figure 6.9). The process involved stopping the syringe pump, retreating the gauge far from the surface (using movement command 2, described in section 6.3.3) and infusing fluid from the pump slowly so as to avoid any interference with the position of the membrane. The gauge was then advanced closer to the surface, the syringe pump started, and the automated calibration proceeded from the next h_0/d_t target value. The data points generated by this process were displayed on the calibration tab alongside the calibration curve, as shown in Figure 6.9. The offset $h_{0,offset}$ was adjusted manually using the controls indicated by item 3 in Figure 6.9. Changes immediately shifted the data displayed on the graph, so adjustments could be

made until the calibration data matched precisely with the standard curve (see Figure 6.11b).

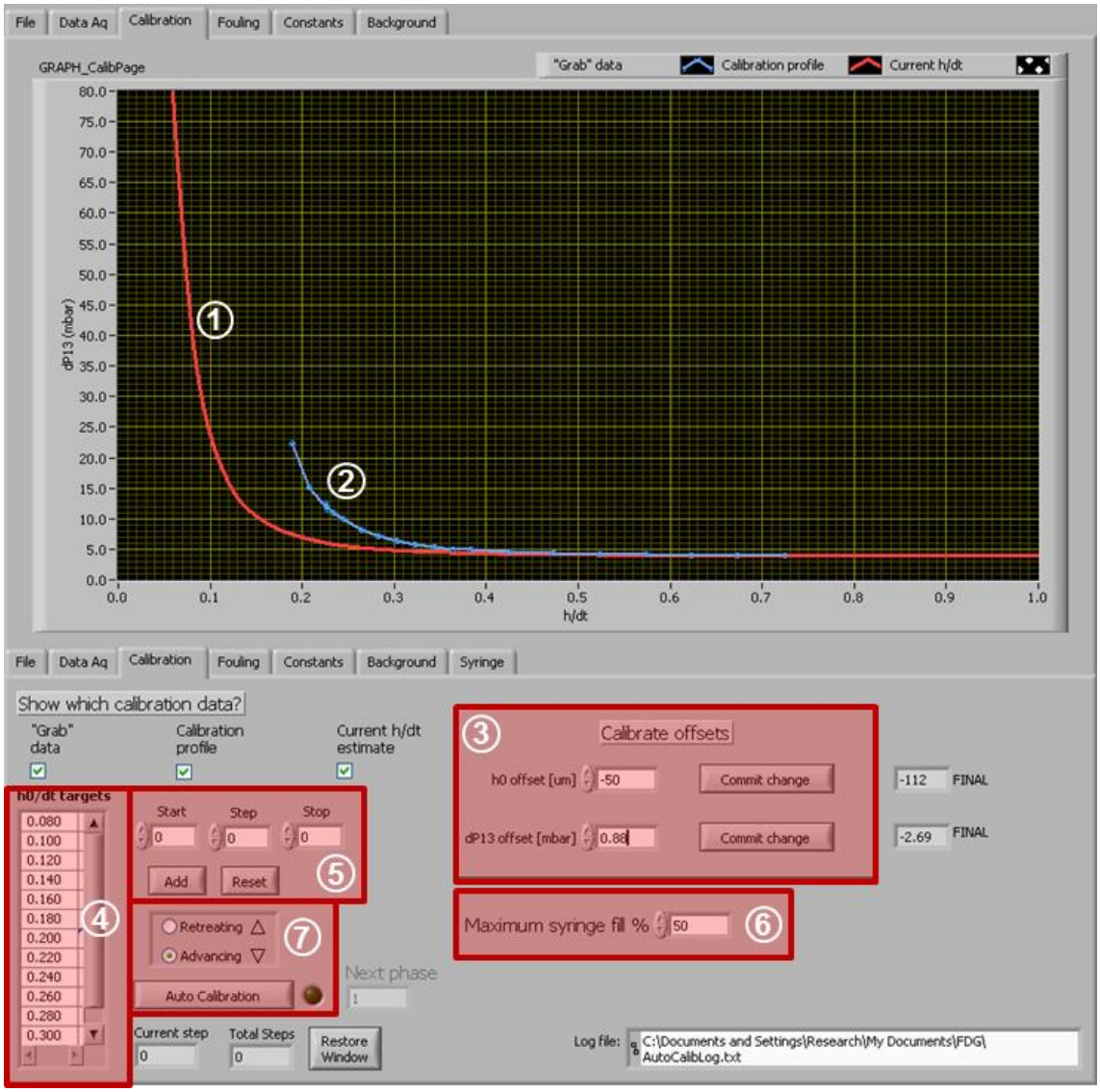

Figure 6.9. Calibration tab used for automated calibration readings and adjustment of offsets. Numbered items indicate: 1. Calibration curve (as described in section 6.3.2); 2. Calibration data gathered by the VI; 3. Calibration offset controls; 4. List of h_0/d_t targets; 5. Controls for setting h_0/d_t targets; 6. Control for maximum syringe capacity during automated calibration; 7, Control for direction of movement, and commencing automated calibration process.

In preliminary calibration experiments it became evident that small offsets to Δp_{13} were also required. This was due to minor shifts in the position of the transducer and possibly small changes in temperature which would affect the piezoresistive element inside it. Any change in Δp_{13} was found to present as a systematic error, so with a defined offset, $\Delta p_{13,offset}$, applied to readings, reliable thickness estimations could still be made. This was also included in the VI, shown by item 3 in Figure 6.9.

Once the calibration data matched the curve, the offsets were set for the current experiment by clicking the "commit change" button. The specified offsets were applied to subsequent h_0 and Δp_{13} readings.

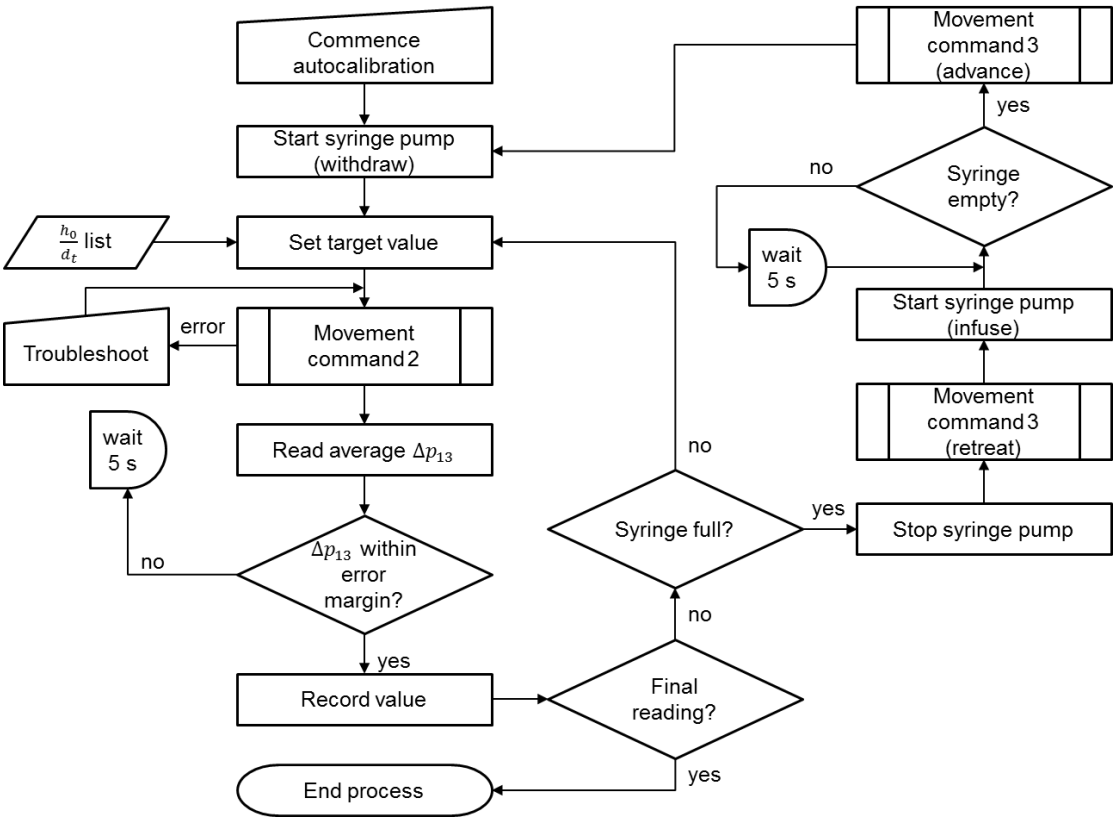

Figure 6.10. Control flowchart for automated calibration procedure, where movement commands 2 and 3 are represented in Figure 6.8.

(a) (b)

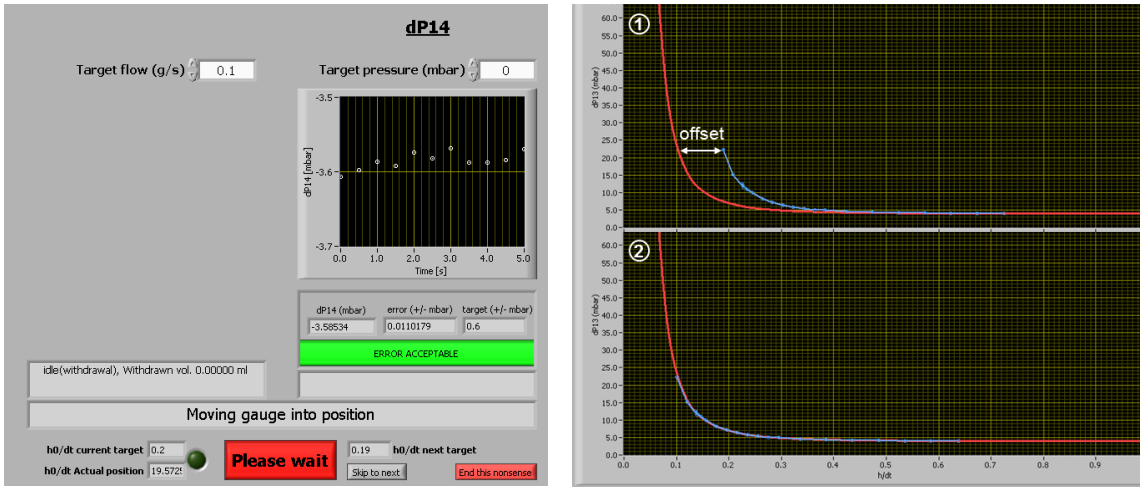

Figure 6.11. (a) Pop-up window used during automated calibration procedure. The blank space on the left was originally used for monitoring m_g, when an electronic balance was used instead of the syringe. (b) Example of offset adjustment for calibration curves where 1 and 2 show the same data before and after $h_{0,offset}$ has been altered.

6.4 Summary of Experiments

6.4.1 TLF: Time-dependent Lignin Fouling

In these experiments the thickness of fouling layers during filtration of a Kraft lignin suspension was studied, looking specifically at the build-up of cake against time. This work was performed in collaboration with with Dr Tuve Mattsson, of Chalmers University of Technology.

6.4.2 PLF: Pressure-dependent Lignin Fouling

The pressure-dependence of cake thickness and strength during Kraft lignin filtrations was studied. This work was also performed in collaboration with Dr Tuve Mattsson, of Chalmers University of Technology.

6.4.3 BLF: Ballotini-Lignin mixture Fouling

In experiments performed by MEng project students Adam Clarke and Alexandra Agg, a mixture of lignin and ballotini was filtered. The effect of introducing ballotini to the filtration process before the lignin was also investigated. The work was supervised by this author and results shown in section 6.6.8 are reprocessed from the original files output by the VI.

6.5 Materials

6.5.1 Lignin Suspension

Kraft Lignin was used as a model suspension for complex, food-like soils. It is separated from cellulose and hemicellulose in wood pulping and paper-milling processes (Wallberg *et al.*, 2003). Due to its aromatic chemistry it has also been proposed as a renewable source for bio-derived polymers (Laurichesse and Avérous, 2014). Depending on the source material, its treatment and extraction, lignin can have various chemical compositions and properties (Laurichesse and Avérous, 2014). In this work, a washed softwood Kraft lignin derived using the *Lignoboost*™ process – wherein it is precipitated under acidic conditions (Öhman *et al.*, 2008) – was used. The samples were obtained by collaborators at Chalmers University of Technology.

The lignin was suspended in RO water (conductivity 7-10 μS), obtained from an on-site RO unit (*Veolia*, Sirion Midi). The water was adjusted to pH 3.7 using sulphuric acid to ensure that all lignin remained precipitated in experiments – Kraft lignin is

known to be alkali-soluble (Öhman *et al.*, 2007a). The same quantity of acid was used in each experiment. The particle density was measured at 1350 kg m^{-3} using a gas pycnometer (AccuPyc II 1340, *Micromeritics*)[*], and particle size distribution was measured for each experiment by laser diffraction (*Malvern*, Mastersizer X). Suspensions of 0.02 vol% were prepared by dilution of 2 vol% stock suspensions.

Stock solution preparation

Stock solutions were prepared by mixing Kraft lignin powder with pH adjusted RO water. Because the powder retained some moisture, the weight used was adjusted to account for this. After drying a sample of powder for 24 hours in a vacuum oven at 70°C, it was found to be 61% (by weight) lignin and 39% water. A concentration of 44 g·L^{-1} was used to make 0.8 L stock solutions to 2 vol%.

Initially stock solutions were mixed only by a magnetic stirrer for at least 48 hours before use. Only TLF experiments used these stock suspensions. The rest of the experiments described in this section used a stock suspension which was first mixed using a homogeniser (*IKA*, T25) at 9000RPM for 2 hours. The suspension was kept agitated using a magnetic stirrer for at least 24 hours before use.

Particle size distribution

Table 6.1 shows minimum, average, and maximum particle size data for all experiments. Distribution plots of suspensions from three experiments most closely matching $d_{3,2}$ values at the average and two extremes are shown in Figure 6.12. In general, all data showed similar peaks at the lower end of the distribution, at around 3-5 μm. The most distinctive variation was found to be in the proportion of larger particles > 10 μm diameter. This variation in particle size appeared to be due to the mechanical treatment (e.g. stirring) of the suspension, as longer stirring times often resulted in a significant reduction in $d_{V,0.9}$. This suggests that larger agglomerates of lignin particles break down under applied fluid shear; however a full study of this behaviour was not performed in this work, and such behaviour could not be reproduced consistently.

[*] This work was performed by collaborators at Chalmers University of Technology, Gothenburg, Sweden.

Table 6.1 Minimum, average, and maximum values for each particle sizing criteria. $d_{V,i}$ represents the diameter below which a volume fraction, i, of the particles are smaller. $d_{3,2}$ and $d_{4,3}$ are the Sauter mean and volume moment mean diameters.

	$d_{V,0.1}$ (µm)	$d_{V,0.5}$ (µm)	$d_{V,0.9}$ (µm)	$d_{3,2}$ (µm)	$d_{4,3}$ (µm)
Minimum	1.60	4.93	15.51	3.58	8.74
Average	1.73	6.12	35.48	4.15	14.11
Maximum	2.04	10.31	95.54	5.41	27.21

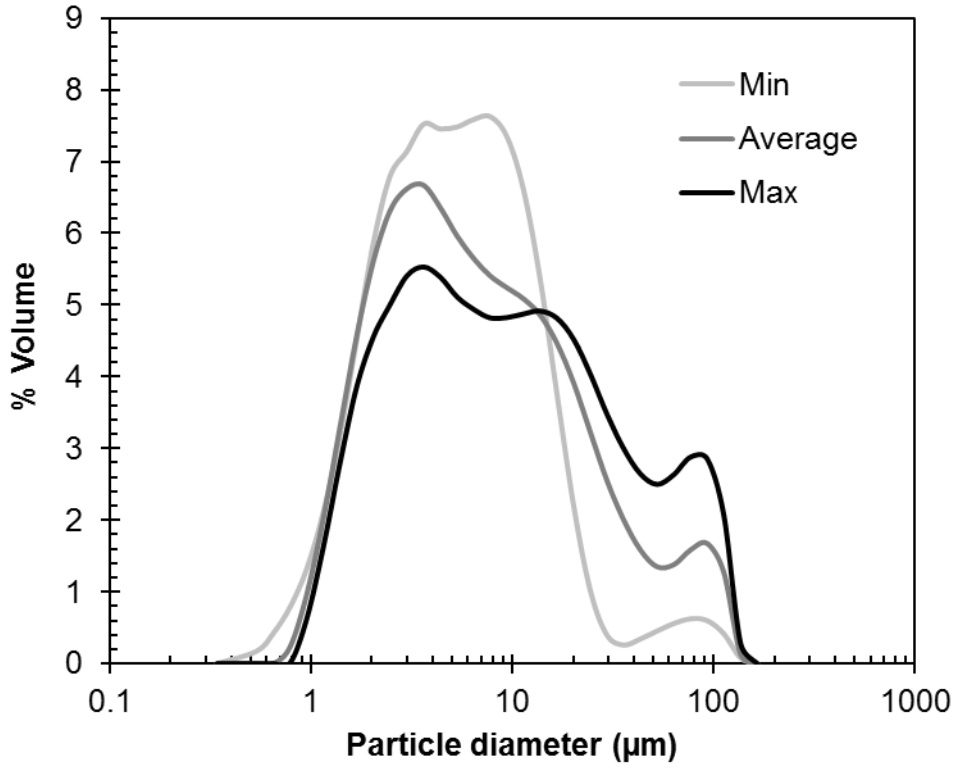

Figure 6.12. Particle size distribution (characterised by laser diffraction) for lignin suspensions corresponding to the minimum, average, and maximum $d_{3,2}$ readings across all suspensions.

Ballotini-lignin mixtures

The BLF studies used the same procedure to prepare lignin suspensions as described above. Ballotini particles (*Potters inc.*, Sphericel 110P8), which are described in 4.2.3, were added at the same volumetric concentration as lignin i.e. 0.02 vol%. The resulting suspension therefore had a total solids concentration of 0.04 vol%.

6.5.2 Membranes

All experiments described in this section used regenerated cellulose membranes of 0.2 µm nominal pore diameter, which are shown in Figure 6.13. These are symmetric, hydrophilic membranes of < 100 µm thickness. Those used in TLF experiments (*Schleicher & Scheull*, RC58) had a slightly higher resistance than those in the BLF and PLF experiments (*Whatman*, RC58). The resistance of each membrane, characterised by dead-end filtration as described in appendix C. , is shown in Table 6.2. The resistance of the newer Whatman RC58 membranes was lower than that indicated by the manufacturer specifications. This could be due to compressibility of the membrane pore structure, as pressure used by the manufacturer was almost two orders of magnitude higher than in the dead-end filtrations. Resistance calculations were not made at the same TMP used by the manufacturer.

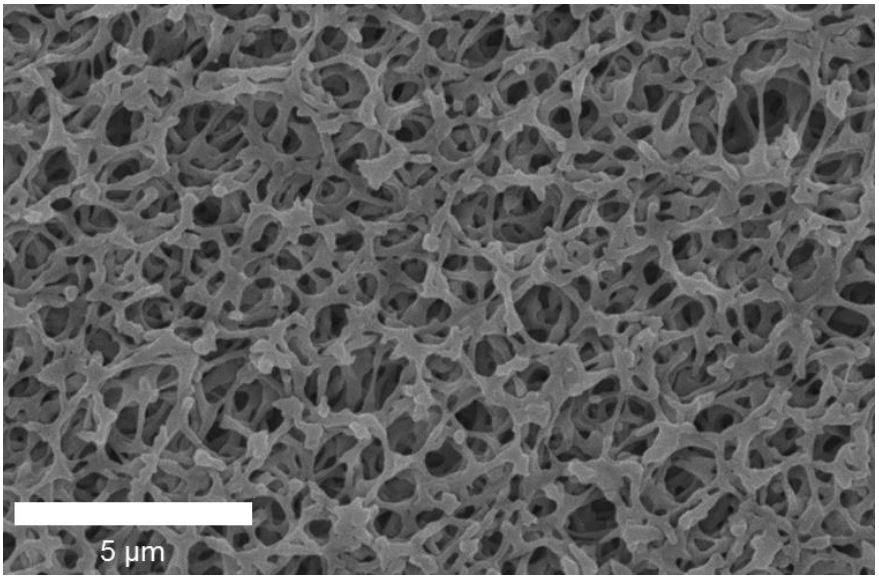

Figure 6.13. SEM micrograph of *Whatman* RC58 membrane taken at 6000× magnification and 15kV excitation voltage. This image was acquired by MEng Project students Alexandra Agg and Adam Clarke

Table 6.2. Membrane characterisation data from manufacturer and dead-end filtration experiments. Tolerance ranges represent standard deviation across repeat experiments

	δ_m (µm)	Flux at 0.9 bar ($s \cdot 100mL^{-1} \cdot 12.5cm^2$)	κ ($\times 10^{-15}\ m^2$)	R_m ($\times 10^{10}\ m^{-1}$)
Whatman specs	75	14	4.78	1.57
Exp. S&S	75*		4.30±0.03	1.75±0.01
Exp Whatman	75*		6.50±0.20	1.16±0.03

*These values are assumed to be the same as given by the manufacturer. Due to the slightly compressible nature of the membranes, and that they are likely to swell when wet, measurements were not possible

Wetting time

The membranes appeared to be instant wetting, a property also stated by the manufacturer. In order to eliminate the possibility of any long-term effects of wetting on the membrane structure, a sample was also tested after soaking in RO water for 24 hours, no change in resistance was observed outside the error range stated in Table 6.2.

Pure water flux

Some very minor flux decline during pure water filtration was noted. This amounted to a resistance increase of 0.04×10^{10} m^{-1} over a 3.5 hour time-period. This could be attributed to mild compaction of the membrane into the stainless steel support, minor background fouling (e.g. dust particles or contaminants in the flow loop), or even a slight drift in pressure transducer readings over time. Regardless of the cause, the resistance change attributed to this was insignificant compared to those later observed for the foulants studied.

6.6 Methods

(Refer to Figure 6.5 for valve identification)

6.6.1 Initial start-up

Membranes were soaked in RO water for at least one minute prior to their installation in the membrane cassette and subsequently into the test section. All experiments were commenced by filling the system and starting the flow loop described in section 6.2.3. The feed tank was filled with pH adjusted RO water, which was circulated by the pump to prime the flow loop. The test section required tilting to remove air bubbles from the top of the duct. Bleed points, as described in section 6.2.3 were used to remove air bubbles downstream of the gauge, from the permeate side of the test section, and from the tubes connected to the pressure transducers. TMP and Re_{duct} were set before performing calibrations.

6.6.2 Calibration

Impermeable Substrate

Calibration tests were performed using a plastic sheet in place of the membrane, to determine a benchmark Δp_{13} vs. h/d_t plot for the apparatus. To maximise the length of time during which readings could be taken without stopping the syringe, a low gauging flowrate of m_g = of 0.1 $g{\cdot}s^{-1}$ was selected. Below this the change in Δp_{14} was

too small (< 0.25 mbar) for cake thickness in the region $0.2 < h/d_t \leq 0.25$ to be accurately measured.

To prime the system, the feed tank was filled with RO water, and the test cell was flooded. With the pump active, and water circulating through the system (with no permeate flow), air bubbles were bled from the tubes downstream of the gauge and those connecting to the pressure transducers. On the first instance of this test the gauge position at which $h_0 = 0$ (i.e. the nozzle tip in contact with the surface) was also set. With the gauge tube loose from the bracket securing it to the guide rail, the stepper system was adjusted so that $h_0 = 0$. The gauge nozzle was gently pressed against the impermeable surface and the bracket tightened around the gauge tube.

Δp_{13} was measured for a selection of h/d_t (where $h = h_0$) values using the automated calibration process described in section 6.3.4. More data points were taken in the region where $h/d_t \leq 0.30$ where Δp_{13} showed the greatest dependent on the nozzle clearance.

Membrane Calibrations

Prior to every fouling experiment, a membrane calibration was performed to determine the position of the membrane relative to the gauge. A secondary purpose of this was to confirm that the FDG apparatus was operating correctly. With a filtration running, the automated calibration procedure described in section 6.3.4 was run in advancing mode (steps taken towards the membrane). The standard set of points used was: $0.06 \leq h_0/d_t \leq 0.26$ at 0.02 intervals, then $0.3 \leq h_0/d_t \leq 0.6$ at 0.05 intervals. Because of the possibility that $h_{0,offset}$ was positive (i.e. the membrane was higher than expected, the calibration was halted if Δp_{13} became too large. If further steps towards the membrane were required, they were performed using the height controls and further data points were recorded using the manual controls. Following this calibration run, adjustments were made to the offset values using the interface built into the VI (item 3 on Figure 6.9).

Following this calibration step, the gauge was retreated to a position where h_0 = 12 mm for fouling experiments. The syringe was also emptied back into the test section in infuse mode, ready for thickness readings.

6.6.3 Destructive thickness and strength testing

All experiments described in this chapter used the method described below to estimate the thickness of the cake layer and investigate the cohesive and adhesive strength of the cake.

The gauge was first moved to a position within the reading range of the LVDT (i.e. h_0 < 1.8 mm). The syringe pump was started in withdrawal mode and, while constantly monitoring the estimated h/d_t, h_0 was decreased stepwise until $h/d_t \leq 0.2$. A reading was logged when Δp_{13} was within acceptable error (± 0.6 mbar), as indicated by the VI (item 3 in Figure 6.6). h_0 was decreased in 20 µm steps using immediate movement commands (command 1, see section 6.3.3). For each of these steps, data was logged once a steady-state was reached. Smaller steps of 5-10 µm were used when $h/d_t \leq 0.1$.

This entire process was conducted during one fill of the syringe. This allowed a window of up to 400 s to make a full set of readings. After these tests the syringe pump was stopped and the gauge retreated to the high-clearance position of h_0 = 12 mm.

6.6.4 Cake extraction and weighing

Cakes were recovered after fouling experiments for further analysis including optical and electron microscopy, as well as drying and weighing for porosity estimates. After filtrations, valve V6 was closed, and bleed points BP_3 and BP_2 were opened. While using a syringe on BP_2 to maintain a TMP sufficient to hold the cake against the membrane, the system was drained backwards through the test section. Any remaining water held up in the test section was drained through the cake and membrane using a syringe at BP_2. The membrane cassette was subsequently removed and dismantled.

The filter cakes often exhibited some additional deposition (due to particle settling) at the inlet and outlet sides of the membrane surface. The fouled membrane was trimmed by around 1 cm at each end (the final length was measured) in order to prevent overestimation of deposition in the area beneath the gauge. The cake on the remaining membrane sample was rinsed off and dried for 24 hours in a vacuum oven at 70°C before weighing.

6.6.5 Cleaning of apparatus

Kraft lignin is known to be alkali-soluble (Öhman *et al.*, 2007a), so 0.1 wt% NaOH was used as the cleaning agent after all filtrations. Prior to chemical cleaning, the flow loop and test section were emptied, rinsed, and reassembled. The cleaning solution

was flowed through the test section (which no longer contained a membrane) without recirculation. After this it was rinsed through once more with RO water.

6.6.6 TLF studies

These experiments were all performed at a TMP of 100 mbar and Re_{duct} of 1550. A working volume of 15 L suspension was used, with 14 L pH adjusted RO water present in the system before addition of the foulant. Following a calibration, lignin from a stock suspension was mixed with pH adjusted RO water to a quantity of 1L. At the start of fouling experiments, this was added to the feed tank along with any permeate collected during calibrations. From this point forward, no permeate was returned to the feed tank and the system remained in feed-and-bleed mode. Following addition of the lignin, some adjustments to valves V5 and V8 were necessary to maintain Re_{duct} and TMP. The latter of these was kept within 5 mbar of the target.

In previous studies of ballotini and yeast fouling (Chapter 5), there was evidence that thickness readings taken during filtration affected subsequent cake growth. In order to circumvent this the filtration was performed with the gauge retreated to a clearance of h_0 = 12 mm until an allotted time, at which point destructive thickness and strength testing (described in section 6.6.3) was performed. This was undertaken for times of 750, 1000, and 2000 seconds with at least two repeats for each. Two more were performed at 3000 and 4000 s with no repeats.

Once complete, the membrane cassette was removed and the cake weighed and analysed as described in section 6.6.4.

6.6.7 PLF studies

These experiments were set up in feed and bleed mode as described above, with TMPs of 50, 100 and 200 mbar. In all cases the membrane was fouled for 2000 s at a cross flow where Re_{duct} = 1550 and the gauge nozzle retreated 12 mm from the membrane surface during the experiment.

Rinsing under relaxation

In all PLF experiments, and one TLF experiment, a different protocol was used when making thickness measurements.

After 2000 s, instead of performing a thickness measurement directly, the membrane was rinsed under relaxation (i.e. no permeate flow) with clean RO water. Permeate flow was halted by closing valve V6. The pump was stopped and the test section cut off from the rest of the flow loop by closing valves V5 and V7. The feed

tank was rinsed out, and the suspension replaced with pH adjusted RO water. The feed loop was restarted at the same cross-flow velocity and the test section rinsed through with the clean water, draining through BP_3 for 30 s until no more lignin was visible in this stream. This rinsing was continued for a further 270 s before opening V6 and readjusting TMP to the previous value. In all cases this resulted in a small increase in permeate flux compared with that at 2000 s. A destructive thickness and strength test (see section 6.6.3) was then performed, then the membrane was removed and a sample of the cake recovered for weighing as described in 6.6.4.

6.6.8 BLF studies

In this set of experiments, the effect of introducing an inert component (ballotini) to the filtration was investigated. Fouling layers formed by ballotini in previous studies (section 5.3) exhibited lower cohesive and adhesive strength than lignin, so could potentially be used as a buffer to make lignin fouling layers easier to remove.

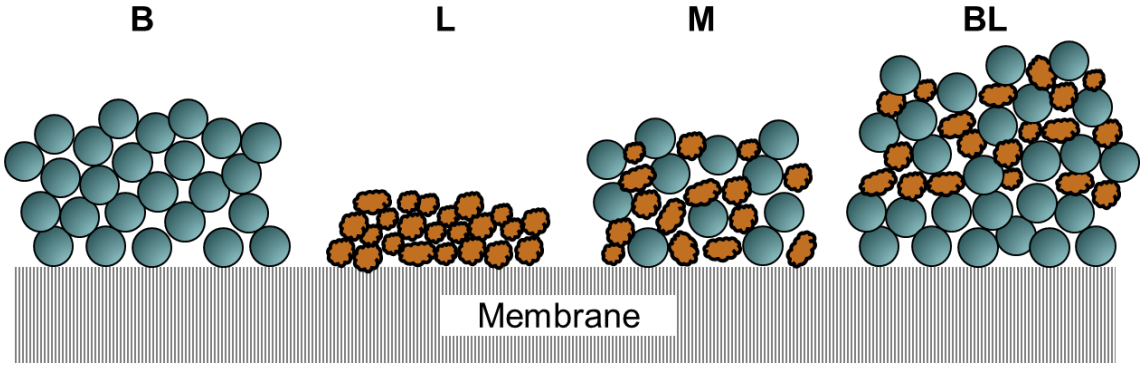

Figure 6.14. Different types of filtration used in BLF studies, as described in the text below.

Four different filtrations (as shown in Figure 6.14) were considered in this set of studies, namely:

L: Fouling with lignin only

A 0.02 vol% lignin suspension was filtered. Destructive testing was performed after 1500 and 4500 s of fouling.

BL: Ballotini then lignin

Initially only ballotini was added with acidified RO water to the feed tank in 200 ml of a concentrated suspension at the start of the filtration. This created a 14.2 L working volume with 0.02 vol% ballotini. At 300 s the lignin was added, along with a small amount of ballotini in 800 ml of concentrated suspension to make a final working volume of 15 L in the system containing 0.02 vol% of each component. This method does not account for the change in concentration due to rejected ballotini and permeate

volume. Destructive thickness and strength testing was performed at filtration times of 750, 1500, 3000, and 4500 s.

A total mass of 3.3 g ballotini was used for each experiment, and 150 mL of a 2 vol% stock suspension of lignin.

M: Filtration of the ballotini and lignin mixture

Here the ballotini and lignin were added in a 1 L concentrate to the feed tank at the same time. This resulted in filtration of a 0.04 vol% suspension of equal volumes ballotini and lignin, with a 15 L working volume. Destructive thickness and strength tests were performed at filtration times of 750, 1500, 3000, and 4500 s.

B: Fouling with ballotini only

A 0.02 vol% ballotini suspension was filtered. Destructive testing was performed after 1500 and 4500 s of fouling.

6.7 Conclusion

An improved apparatus for studying FDG was designed and commissioned. This included a smaller gauging nozzle for more accurate thickness measurements, as well as many automated features allowing for experiments to be performed with much lower user input required. Improvements were also made to the procedures used to make thickness measurements over time. The results of these are presented in the next chapter.

Chapter 7: Results and Discussion B: Lignin Fouling

The new automated FDG apparatus described previously was used to perform thickness and strength measurements of cakes formed during cross-flow filtrations of Kraft lignin. This chapter presents details of the results and data processing methods used to elucidate some of the fouling properties.

7.1 Membrane calibrations

To ensure reliable FDG thickness estimations, repeat calibration tests were performed every hour during a three hour pure water filtration at constant TMP. As shown in Figure 7.1, there was very good agreement between all calibration plots. In all cases where h_0/d_t < 0.2, the resulting h estimate was below 10 μm. This also indicated that there was no background fouling during pure water filtration.

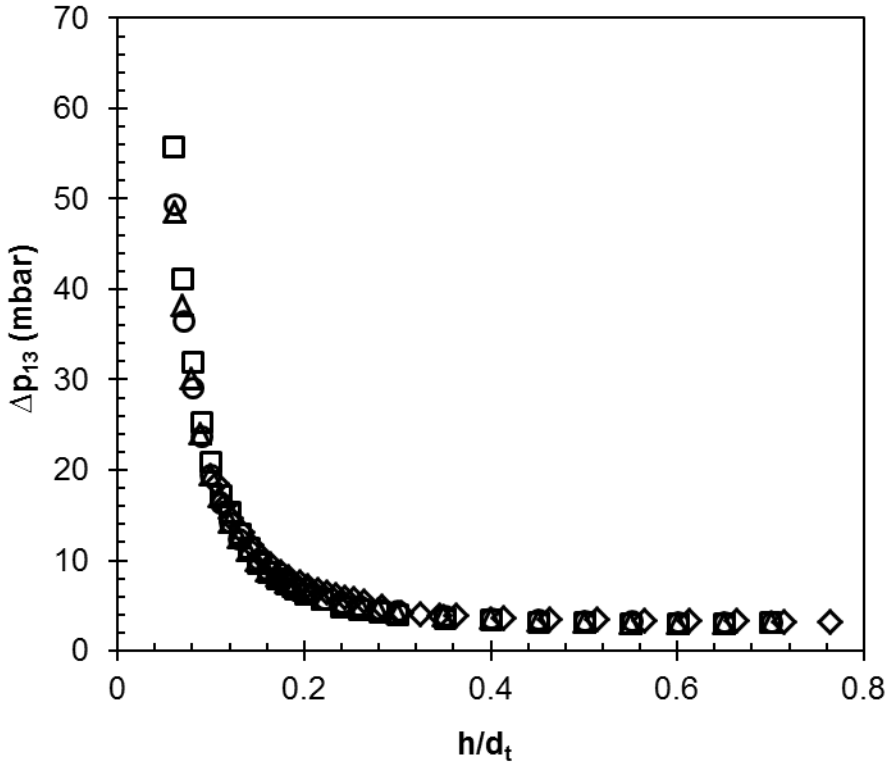

Figure 7.1. Repeat calibration readings performed during a pure water filtration at TMP = 100 mbar, Re_{duct} = 1550, at the beginning (diamonds), and after 1 (squares), 2 (triangles) and 3 (circles) hours of filtration. Gauging flowrate, m_g, was 0.1 g·s^{-1}

7.2 Thickness estimations from destructive testing

The calibration curve used to fit data was changed from a 4-parameter exponential equation to a spline fit after the TLM and PLM studies were completed.

The results from these were subsequently reprocessed to fit the more accurate spline curve described in section 8.7. This also affected the h/d_t estimations, meaning that earlier results had under-predicted this value. Thickness readings were therefore only included where $h/d_t \leq 0.25$. The first recorded data point within this limit was quoted as the measured cake thickness.

7.3 TLF studies

An example of a flux decline curve is shown in Figure 7.2. The initial increase in flux coincides with a TMP rise, which was due to a small increase in head pressure upstream of the pump when foulant was added to the feed tank.

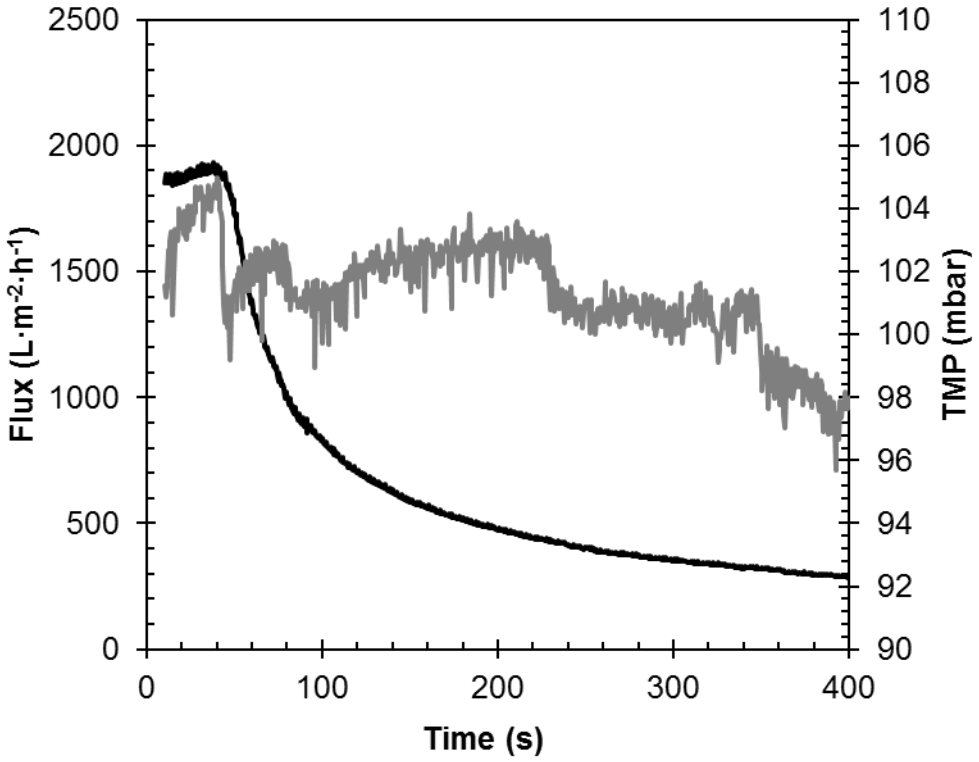

Figure 7.2. Initial flux decline during first 400 s of a 750 s lignin filtration at 100 mbar. Flux is shown in black and TMP in grey.

7.3.1 Data validation

At least 6 runs were performed for each of the following filtration times: 750, 1000, and 2000 s. There was very good concordance between flux decline curves for most of the runs. Those which deviated significantly from the curve shown in Figure 7.2 were discarded to ensure that thickness and strength measurements reported here were truly representative of repeatable flux decline behaviour. Deviation from this standard behaviour was likely to occur if there was contamination of or damage to the

membrane, or if it was improperly sealed in the test section. It could also be attributed to an abnormal particle size distribution in the suspension. There was however, no clear evidence of which of these were responsible when experimental data was discarded.

The initial flux was found to vary slightly; with an average value of 1900 $L \cdot m^{-2} \cdot h^{-1}$ and maximum deviation 160 $L \cdot m^{-2} \cdot h^{-1}$. This was most likely a result of small changes in the available membrane surface area due to stretching of the rubber seal (see Figure 6.3), but may also have been due to fluctuations in TMP or compression of the membrane into the support mesh. These fluctuations in initial flux were much lower than those reported in Chapter 5.

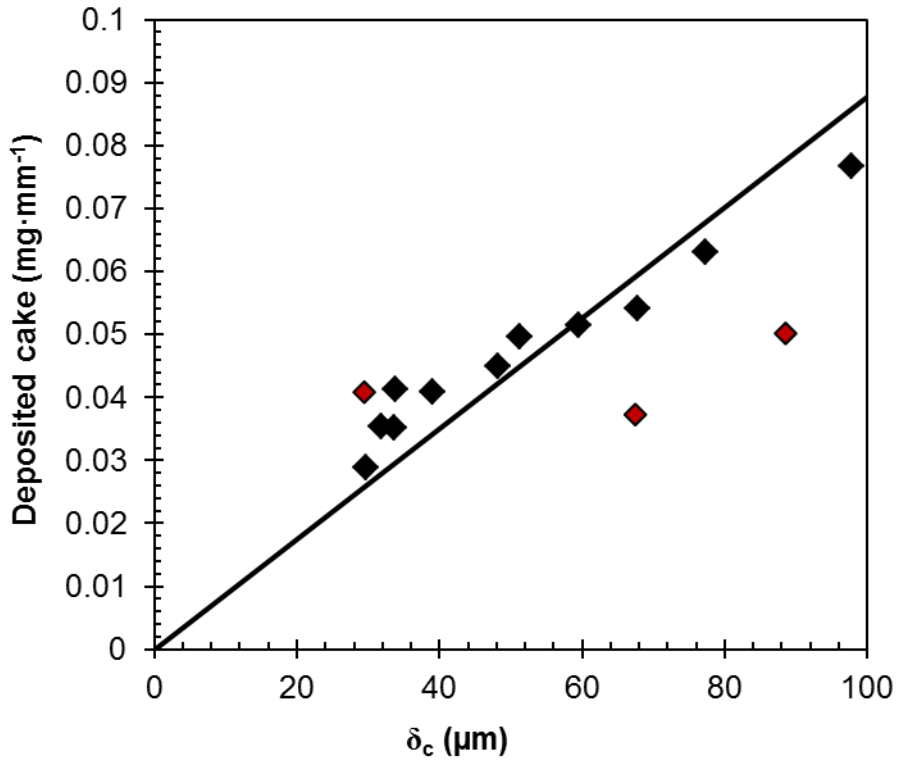

Figure 7.3. Dry weight of cake per unit area against measured thickness for all experiments. Red symbols indicate data points considered to deviate too far from the expected linear trend.

Further to this, thickness measurements were compared with measurements of the dry weight of cake deposited. Assuming the cake voidage to be relatively constant throughout, a linear trend should be expected between the deposited cake mass per unit area and the measured thickness. Readings which deviated from this trend (as indicated in Figure 7.3) were also discarded.

7.3.2 Cake growth over time

As shown in Figure 7.4, the flux decline curves exhibit very good concordance between different experiments. Over a ten-fold decline in flux is evident within the first 1000 s fouling, and it continues to decline steadily to about 85 $L \cdot m^{-2} \cdot h^{-1}$ at 4000 s.

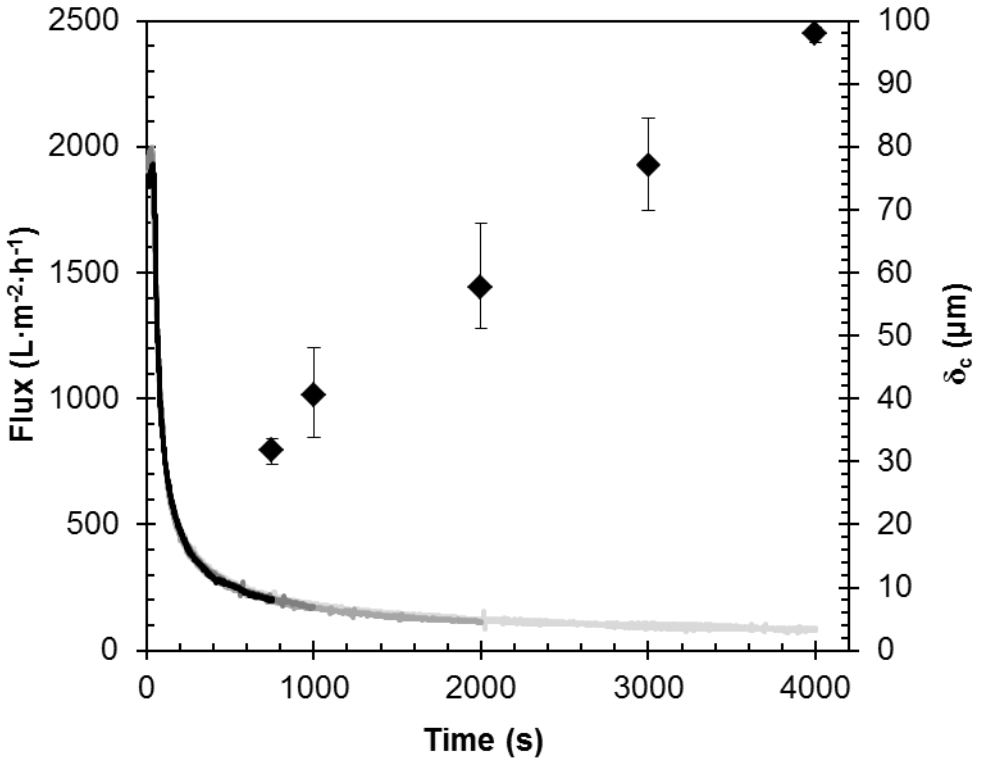

Figure 7.4. Cake thickness (symbols) and flux (lines) vs. time. Error bars for 750, 1000, and 2000 s indicate span of data across repeat experiments. Those for 3000 and 4000 s indicate measurement error. The black, dark, medium and light grey lines indicate flux curves for separate experiments ending at times 750, 1000, 2000 and 4000 seconds respectively.

Thickness Readings

The thickness readings (indicated by the symbols in Figure 7.4) at 750, 1000, and 2000 s represent average values for the experiments considered valid. Error bars for these three data points indicate the maximum and minimum values. The data points at 3000 and 4000 s show error bars corresponding to standard deviation of Δp_{13} readings, calculated as described in appendix D2. Despite the majority of flux decline having occurred by 750 s, the cake more than doubles in thickness by 4000 s and does not appear to have reached a steady-state thickness. This indicates a significant proportion of flux decline is due either to pore blockage or a more highly resistant, thinner layer of lignin closer to the membrane surface. This may be similar to the "skin layer" observed by Mattsson *et al.* (2012a).

Mass measurements

The mass of cake deposited per unit area of membrane is shown in Figure 7.5. The trend matches well with that shown in Figure 7.4. Included in this graph is the result from a single experiment in which the cake was rinsed under relaxation for 300 s (as described in 6.6.7) after fouling for 2000 s. Evident from the dashed line is that the flux is recovered to 225 $L \cdot m^{-2} \cdot h^{-1}$ after rinsing, which is slightly higher than that after 750 s, at which time the average flux between multiple experiments was 195 $L \cdot m^{-2} \cdot h^{-1}$. The deposited cake mass of 0.032 $mg \cdot mm^{-2}$ was also in the range measured for 750 s filtrations. This is not represented by the thickness measurement for this experiment however, which was 51.6 μm and close to the average thickness values measured at 2000 s without prior rinsing. This therefore indicates a fouling layer which cannot be measured using FDG due to its easy removal by shear, yet contributes significantly to flux decline. This is likely to be a loose flowing layer of particles, as observed on hollow fibre membranes by Marselina *et al.* (2008).

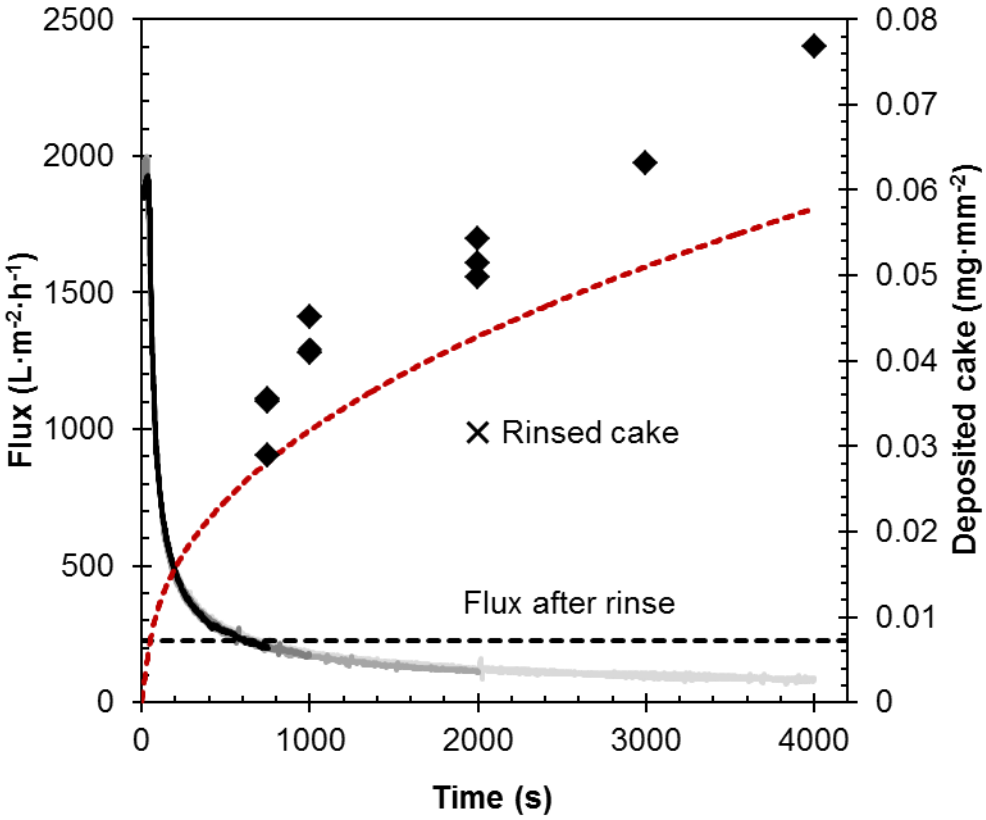

Figure 7.5. Dry cake mass deposited per unit area of membrane (symbols) and flux (lines) against time. Black, dark, medium and light grey lines represent fluxes for 750, 1000, 2000 and 4000 s respectively. The dashed black line indicates the flux through the cake after rinsing, and the cross indicates the deposited cake mass after rinsing. The dashed red line indicates the quantity of cake predicted by equation (7.1) for the 4000 s experiment.

Correction for mass overestimation

The discrepancy between thickness and deposited mass could also be attributed in part to the extra lignin held in the test section which could have been deposited on the membrane during its recovery. This would lead to an overestimation of the mass measurement for cake deposition per unit area of the membrane.

Based on the total volume of fluid in the test section, a generous estimate of 0.00675 mg·mm^{-2} is suggested as a systematic error in this measurement, the derivation of which is shown in Appendix A2. This accounts for roughly one third of the difference between the mass measurement before and after rinsing.

Estimation for cake growth

Assuming that there is no back-transport of material from the cake into the bulk media, the mass of cake, M_c, on the membrane can be predicted as follows:

$$\frac{M_c}{A_m} = \int_0^t J c_b \, . dt \tag{7.1}$$

where c_b in this case is the bulk concentration of lignin (0.27 kg·m^{-3}). The result for this is shown by the dashed red line in Figure 7.5, wherein it clearly under-predicts the mass of cake deposited on the membrane. This is still the case if a correction, as described above, is applied. Hence it is possible that cake deposition is enhanced by particle settling or some other particle capture mechanism on the surface of the cake. The former of these was tested by running a similar experiment with an impermeable substrate instead of a membrane. Particle deposition was found to be minimal, however due to the nature of this experiment it was not possible to recover it for weighing.

7.3.3 Cake resistance

The total fouling resistance, R_f, is given by the resistance-in-series model (equation(2.3)), by:

$$R_f = R_T - R_m \tag{7.2}$$

where R_T is the total resistance, and R_m is the membrane resistance (1.75×10^{10} m^{-1} as quoted in section 6.5.2). Fouling resistance is plotted against thickness in Figure 7.6, which indicates a linear gradient between the two. An intercept at R_f = 5.1×10^{10} m^{-1} is evident, which could be attributed to pore blocking or a skin layer formation, this will be discussed below.

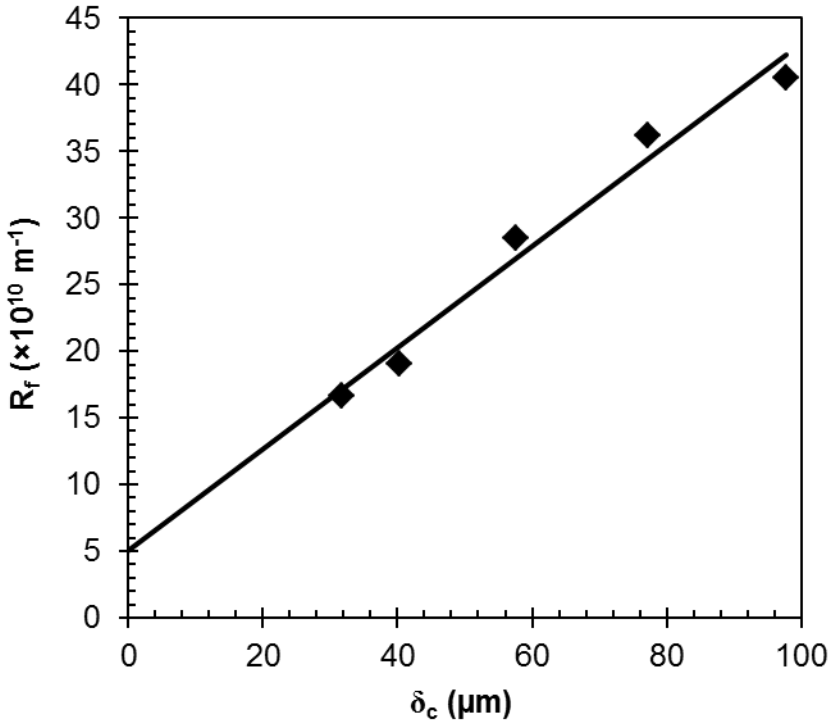

Figure 7.6. Fouling resistance, R_f against cake thickness. The line indicates a linear regression fit. Values shown here are from average thickness and flux data where multiple valid experiments were considered (e.g. for 750, 1000 and 2000 s).

Cake permeability

Cake permeability, κ_c, is related to its resistance, R_c, by:

$$\kappa_c = \frac{\delta_c}{R_c} \tag{7.3}$$

meaning that it should be equal to the inverse gradient of the trend line in Figure 7.6. This gives κ_c = 2.57×10^{-16} m^2. Estimating cake permeability using the Carman-Kozeny equation (2.7) yields a value of 1.27×10^{-14} m^2 when using the minimum Sauter mean diameter, $d_{3,2}$, measured for the suspensions, and a value of 0.4 for cake voidage, ε. This is over one order of magnitude lower than the measured value. This analysis assumes densely packed uniform spheres, which is unlikely to accurately reflect the nature of lignin cakes. Endo *et al.* (2002) provide theoretical consideration for shape factor and particle size distribution, however such models will not be considered in this work due to a lack of data for the former of these properties.

Pore blocking/skin formation

Extrapolation of the fit line in Figure 7.6 to δ_c = 0 is indicative of two possible fouling mechanisms, which are not necessarily mutually exclusive:

1. A thin fouling layer of lower permeability is formed close to the membrane. Mattsson *et al.* (2012a) observed such a phenomenon during dead-end filtrations of microcrystalline cellulose. This would present in an increased gradient as $\delta_c \to 0$.
2. The intercept of this graph could be considered as the resistance due to pore blocking, R_p. This is quite conceivable despite the smallest lignin particles exceeding the nominal pore size of the membrane. As evident from the layered mesh structure of the regenerated cellulose membrane, shown in Figure 6.13, larger surface pores exist in which the smaller lignin particles may become trapped.

Assuming only the latter of these, the pore blocking resistance was estimated to be $R_p = 5.10\times10^{10}$ m^{-1}. Assuming no cake fouling, this mechanism could still be responsible for a flux decline to 500 L·m^{-2}·h^{-1} which is reached within 200 s of fouling. Thus pore blocking is a plausible fouling mechanism during these filtrations.

7.3.4 Cake volume fraction

The particle volume fraction in the cake, ϕ_c, can be determined as follows:

$$\phi_c = \frac{M_c}{A_m}\frac{1}{\rho_p \delta_c} \tag{7.4}$$

where M_c/A_m is the mass of cake per unit area of membrane. The average result for this across valid experiments (disregarding that which included the rinsing cycle) was 0.72. Applying the correction for overestimation of deposited mass, as described in section 7.3.2, gave an average of 0.60.

This can also be estimated from Figure 7.3 by a linear fit to those data points considered valid. This must assume an intercept at zero, such that ϕ_c is constant through the cake. By this method ϕ_c was calculated at 0.65, with a value of 0.57 when applying a correction for deposited mass. The two datasets (before and after correction) are shown in Figure 7.7 along with the associated linear fits.

It should be also be noted that mass measurements here do not account for the deposited mass which contributes to pore blocking and not cake thickness. A rough estimate for this is formed by presuming this mass to equate to that of a monolayer of uniform particles densely packed on a flat surface. Assuming the average Sauter mean diameter for the suspensions of $d_{3,2}$ = 4.11 μm, and a void fraction of 0.4, this gives a

value of 0.0033 mg·mm^2. Subtracting this from mass measurements further reduces the estimated volume fraction of the cake to 0.53 from a linear fit.

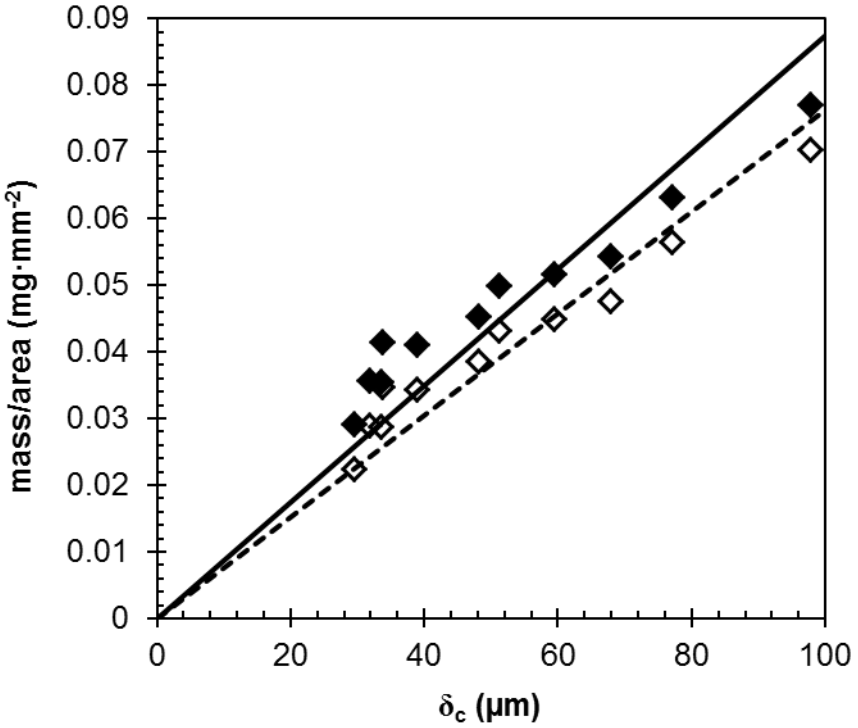

Figure 7.7. Deposited mass of cake per unit area against measured thickness. Closed symbols represent original data and the solid line indicates the linear fit to this. Open symbols represent data which has been corrected against mass overestimation, and the dashed line indicates the associated fit.

There is no existing data in the literature for the volume fraction which should be expected of lignin cake layers. The powder used to create the suspension was found, as reported in section 6.5.1 to contain 39 wt% water, which gives a volume fraction for lignin of 0.54 (due to its density exceeding that of water). It is unlikely that the filtered cake would exhibit a higher solids fraction than this; hence the most reasonable estimation for the cake volume fraction would appear to be under the assumption of both pore blocking and a significant portion of extra deposition during the cake recovery process.

An under-estimation of cake volume fraction could also occur due to the thickness being under-estimated by FDG. This is equally, if not more likely, as all FDG readings will interfere with the cake more significantly than cross-flow velocity. Additionally, in the case where the cake was rinsed under relaxation prior to thickness measurements (for which the deposited mass is indicated by the cross in Figure 7.5), the cake volume fraction was $\phi_c = 0.46$, with the measured thickness in the same range as for non-rinsed cakes. Thus despite the applied corrections, there is still strong evidence for a loose flowing layer of particles on the surface of the cake during filtration.

7.3.5 Destructive thickness tests

Cake thickness is plotted against the maximum shear stress imposed by the gauge, $\tau_{w,max}$, in Figure 7.8. The graphs show data for all experiments considered valid as outlined in section 7.3.1. The thinner cakes formed in shorter, 750 s filtrations exhibited some degree of swelling under the shear force imposed by the gauge, as indicated by Figure 7.8a, where the cake grows by roughly 10 μm between 30 and 70 $N{\cdot}m^{-2}$. This effect is seen for one of the 1000 s experiments, shown by triangles in (b), and not at all for the thicker cakes at filtrations of 2000 s and above. This could indicate stretching or other deformation of the cake layer without removal.

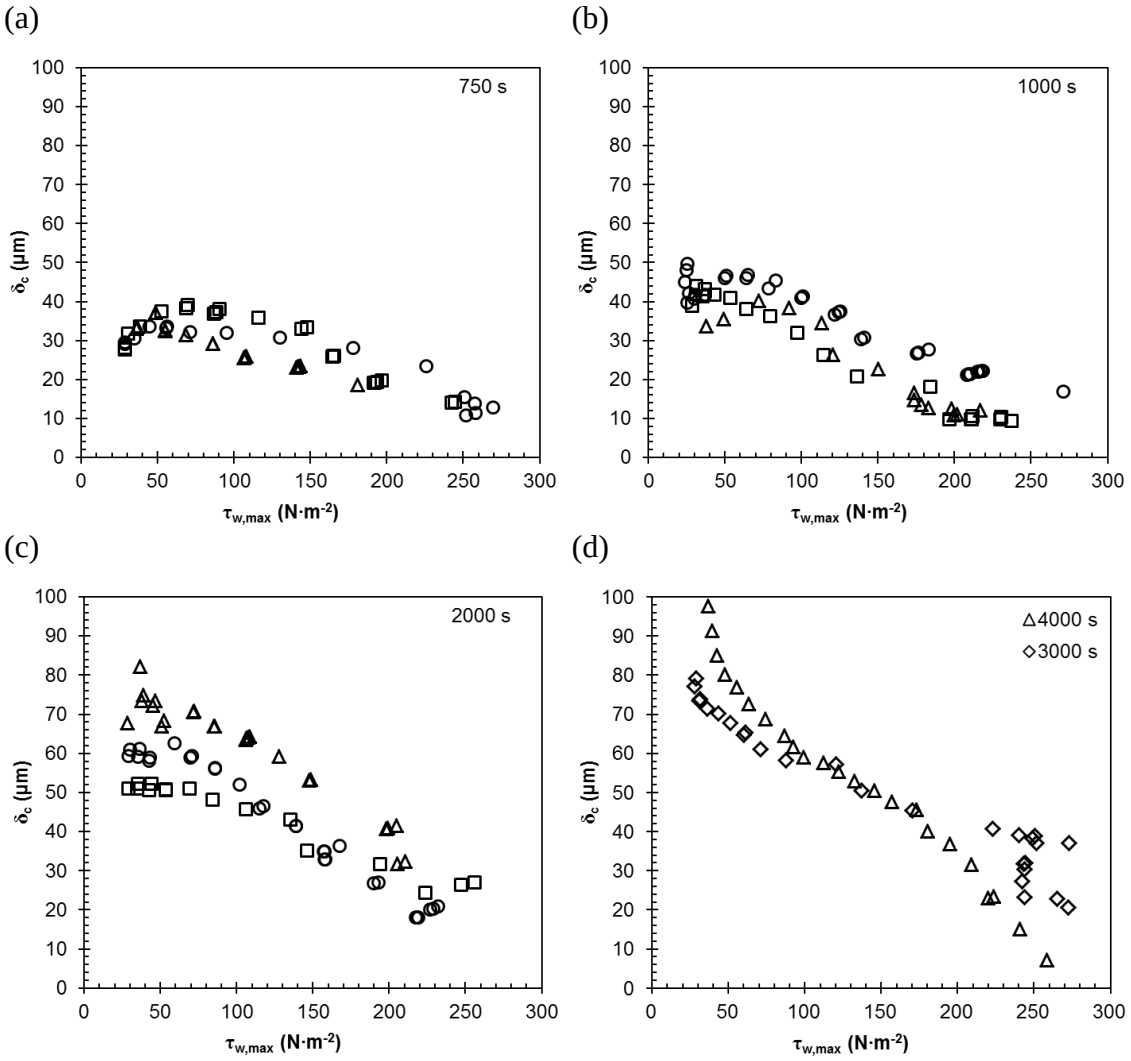

Figure 7.8. Thickness vs. maximum wall shear stress, $\tau_{w,\max}$, for lignin cakes fouled for (a) 750, (b) 1000, (c) 2000, and (d) 3000 and 4000 seconds. Results for all experiments considered valid are shown here.

A general negative trend is seen in all these results, showing that layers of cake closer to the membrane surface are harder to remove than those at the top of the cake i.e. the cohesive strength increases as the cake gets thinner. This is similar to the pattern

reported for ballotini particles in section 5.3. For the 750, 1000, and 2000 s filtrations there is also suggestion of a yield stress beyond which more significant removal of the cake takes place, although this is much less clear cut than that described for ballotini in section 5.3. Obviously a direct comparison cannot be made with those results however, as alongside different membrane pore size and operating conditions, the cakes developed with ballotini particles were much thicker than those measured in this study.

Comparison between Figure 7.8 (a), (b), and (c) clearly shows how thicker cakes, or at least those developed over longer filtrations, exhibit less repeatable results. Some peculiar behaviour is also indicated in (d) for the cake formed over a 3000 s filtration. Here a cake layer of 37 μm thickness remains at a shear stress of 270 N m^{-2}, however the cake is subsequently eroded, decreasing $\tau_{w,max}$. Further increases in shear stress lead to a final cake thickness of 21 μm at the maximum stress measured.

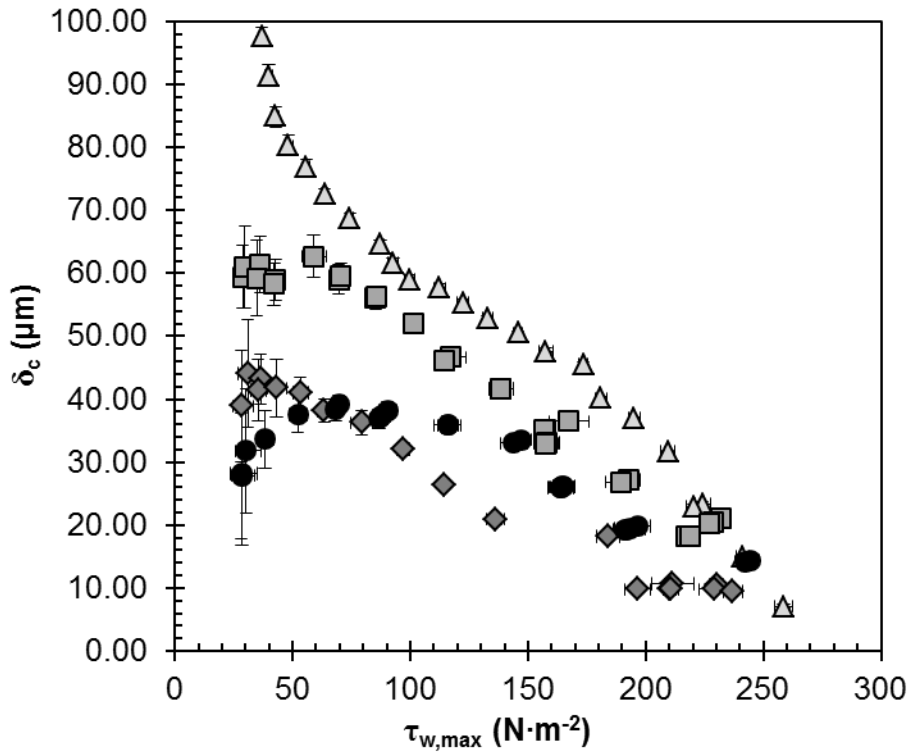

Figure 7.9. Comparison between results of destructive thickness tests for lignin filtrations up to 750 s (circles), 1000 s (diamonds), 2000 s (squares), and 4000 s (triangles). Results for 3000 s are omitted because they were found to becloud the overall comparison.

In no cases did the cake appear to be entirely removed (which was confirmed visually after experiments), as at the maximum imposed shear stress in all these studies a fouling layer of a thickness between about 10 and 20 μm remained. This could be evidence of a denser, less permeable, "skin" layer on the membrane surface, as suggested in section 7.3.3. Another possible explanation is that the larger lignin

particles in the range $10 \leq d_p \leq 20$ become trapped on the surface of the membrane and provide a more solid support around which smaller particles form the rest of the cake.

The yield stress type behaviour can be roughly characterised as occurring between 60 and 80 $N \cdot m^{-2}$; a value which appears to be the same for fouling layers developed over 750, 1000, and 2000 s, however the thickness at which this occurs increases with filtration time. Figure 7.9 suggests that this yield-stress behaviour is not seen for the longer filtrations. This is suggestive of a limiting thickness, above which a weaker cake is deposited.

Defining cake behaviour under fluid shear stress

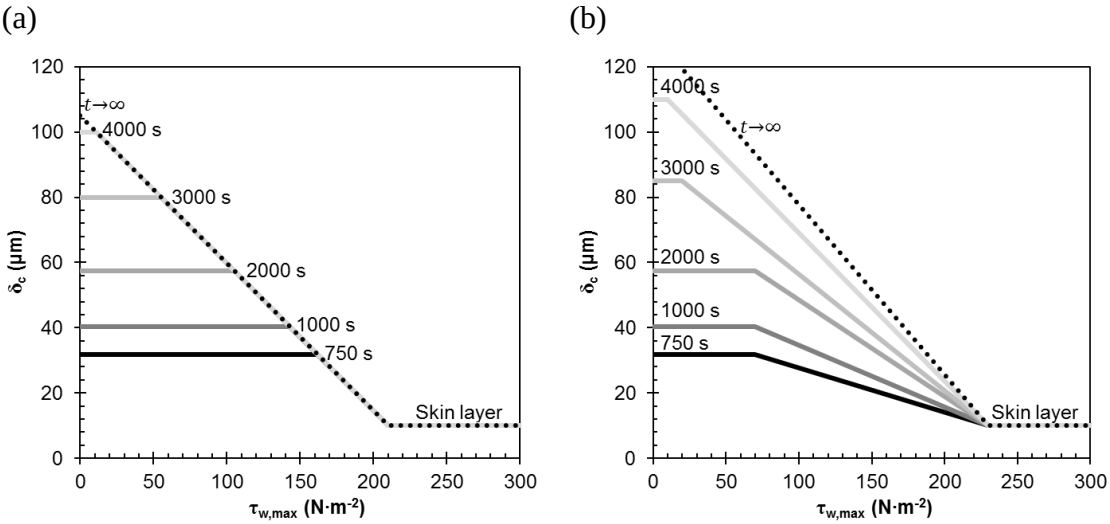

Figure 7.10. Predictions for destructive strength testing results for mechanisms 1 (a), and 2 (b). The filtration time for each is labelled on the graph, $t \rightarrow \infty$ represents the condition approached at a steady state. δ_c for each time is matched to the result plotted in Figure 7.4.

The mechanisms of cake removal by fluid shear have not received much attention in the literature, and there are no existing models to which this type of study can be compared. Two mechanistic models are proposed here, from which trends in δ_c vs $\tau_{w,max}$ could be predicted as shown in Figure 7.10:

1. Successive layers built on the cake surface are weaker than those before. The cake appears to undergo no disruption until a yield stress is reached, which decreases linearly for thicker cakes. There is no alteration to the structure of lower layers over time, meaning that under the same shear stress, the cake will always be removed down to the same thickness. The thickness of the bottom skin layer remains constant. This mechanism would present as illustrated in Figure 7.10a.

2. The yield point of the cake layer remains constant below a limiting thickness, above which the top layers of the cake are more easily removed. Although the thickness of the skin layer remains constant, cakes deposited on top of it rearrange over time, becoming more resilient to fluid shear. This means that after longer filtrations, more stress is required to remove cake down to a particular thickness greater than that of the skin layer. This type of behaviour would result in the graph shown in Figure 7.10b.

As the results shown in Figure 7.9 are quite scattered their interpretation is partially subjective, and either of these models could conceivably fit the data. A yield stress between 60 and 80 $N \cdot m^{-2}$ is seen for cakes developed at 750, 1000, and 2000 s, which supports model 2. An increase in resistance would be expected to coincide with the rearrangement and strengthening of lower layer suggested by this model. If a linear relationship between cake resistance and thickness can be assumed however, as in Figure 7.6, model 1 should be more appropriate.

7.3.6 Critical flux laws

The adaption of Hermia's (1982) dead-end blocking laws to cross-flow filtration by Field *et al.* (1995) (equation (2.20)) was used to analyse the flux decline curves for all lignin filtrations. The method by which this analysis was performed is described in appendix B. . As described in section 2.5.1, a linear correlation between $f(J)$ and J indicates consistence with a particular fouling phenomenon where $n = 0$, 1, or 2. In these studies, such a correlation was only established for the cake filtration model, where $n = 0$. An example of this is shown in Figure 7.11.

Transition flux

A transition point occurs at $J = 365\ L \cdot m^{-2} \cdot h^{-1}$, below which a linear fit is applicable. As this model considers the fouling mechanisms to be sequential and mutually exclusive, this is interpreted as the point at which intermediate fouling (where $n = 1$) ends and cake fouling ($n = 0$) becomes the dominant mechanism. The average value across the valid experiments was $387\ L \cdot m^{-2} \cdot h^{-1}$.According to the additive resistance model (equation (2.3)), this corresponds to a resistance of $9.31 \times 10^{10}\ m^{-1}$, which is slightly less than that calculated for pore blocking, R_p, in section 7.3.3.

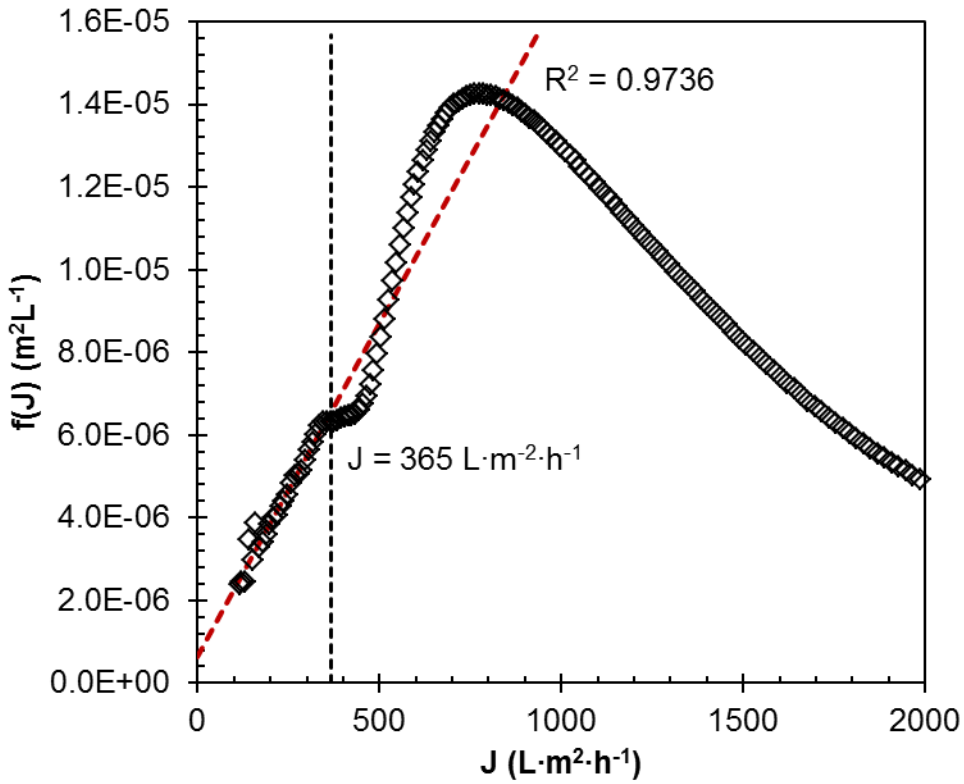

Figure 7.11. $f(J)$ against J using (2.20) where $n = 0$ for a 2000 s filtration.. The vertical dashed line indicates the transition point at J = 365 L·m^{-2}·h^{-1} below which this flux decline model applies. The diagonal dashed line indicates the linear fit for this model, and the coefficient of determination is indicated on the graph.

While this may be an overestimate for such resistance, inspection of Figure 7.11 indicates a second transition point at J = 460 L·m^{-2}·h^{-1}. Analysis of plots for intermediate fouling ($n = 1$) and complete blocking ($n = 2$), which are shown in Figure 7.12, also suggests a transition from one regime to another. This occurs at J = 474, and J = 505 L·m^{-2}·h^{-1} for n = 1 and 2 respectively. This agrees very well with the value for R_p derived in section 7.3.3. This demonstrates, therefore, that using just flux data, it is still possible to estimate the significance of pore fouling phenomena.

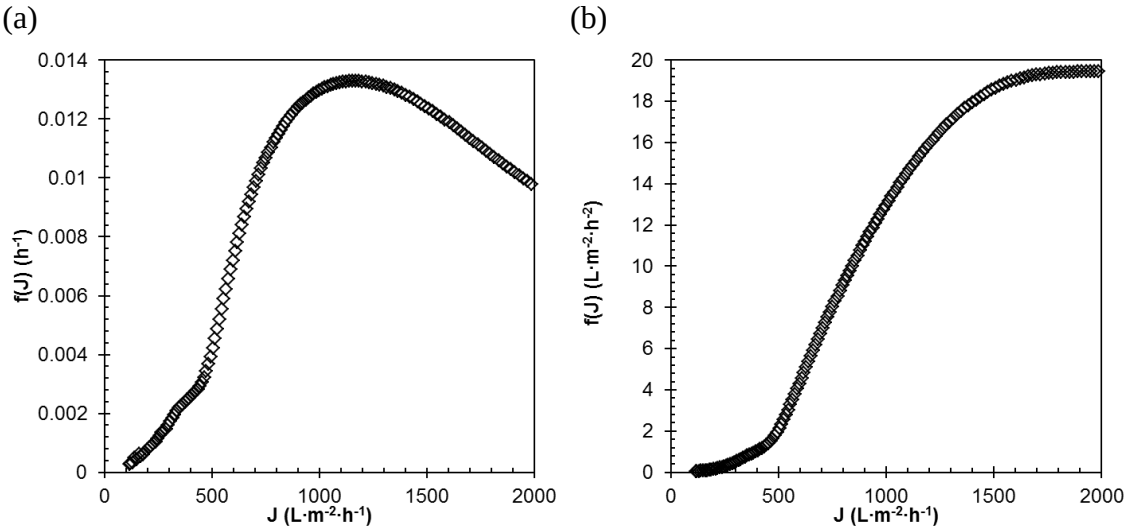

Figure 7.12. $f(J)$ against J using equation (2.20) where (a) $n = 1$, and (b) $n = 2$. Data shown in for the same filtration as in Figure 7.11.

Constants k and J^*

Whilst the transitional flux between different blocking mechanisms can be used quite effectively to indicate the pore blocking resistance, the constants k and J^* can be used to indicate the significance of back-transport phenomena. For the cake fouling law, where $n = 0$, $J^* < 0$ in almost all cases, with an average value of -56 L·m^{-2}·h^{-1}. This is unrealistic as in this case J^* should represent the flux at which there will be no further cake fouling, i.e. a steady-state flux. A possible reason for this is that the steady state flux would actually be very close to zero, and the linear correlation is too rough for it to be defined effectively. Another interpretation of this is that there are some fouling phenomena occurring which are not due to flux, as discussed in section 7.3.2.

For cake filtration:

$$k = \frac{\varphi_c k_c'}{J_0 R_m} \tag{7.5}$$

where, according to Field *et al.* (1995):

$$k_c' = \frac{S}{J^*} \tag{7.6}$$

and S is the rate of cake removal in kg·m^{-2}·s^{-1}, which is assumed to be constant and could be calculated using the data available – φ_c can be determined by a linear fit of R_f against M_c/A_m. Due to the negative sign on J^* however, a positive flux of particles

towards the membrane would be predicted as a result of cross-flow. This is not completely implausible, as shown in Figure 7.5 and discussed in section 7.3.2.

An average value of $k = 2.02\times10^{5}$ was determined for these experiments. Using equations (7.5) and (7.6), plus a specific resistance (determined through linear regression) of $\varphi_c = 5.89\times10^{12}$ m·kg^{-1}, gives $S = -5.38\times10^{-6}$ mg·m^{-2}·s^{-1}. Adapting equation (7.1) to account for this extra deposition leads to:

$$\frac{M_c}{A_m} = \int_0^t (Jc_b - S).dt \qquad (7.7)$$

When applied to the filtration data recorded for 4000 s, the corrected prediction shown in Figure 7.13 shows a much closer match with the measured values than the previous curve. This demonstrates that, despite being a relatively approximate method, interpreting the flux data by the method of Field *et al.* (1995) can provide important and meaningful insights into the fouling mechanisms of this filtration process when combined with observations made by FDG.

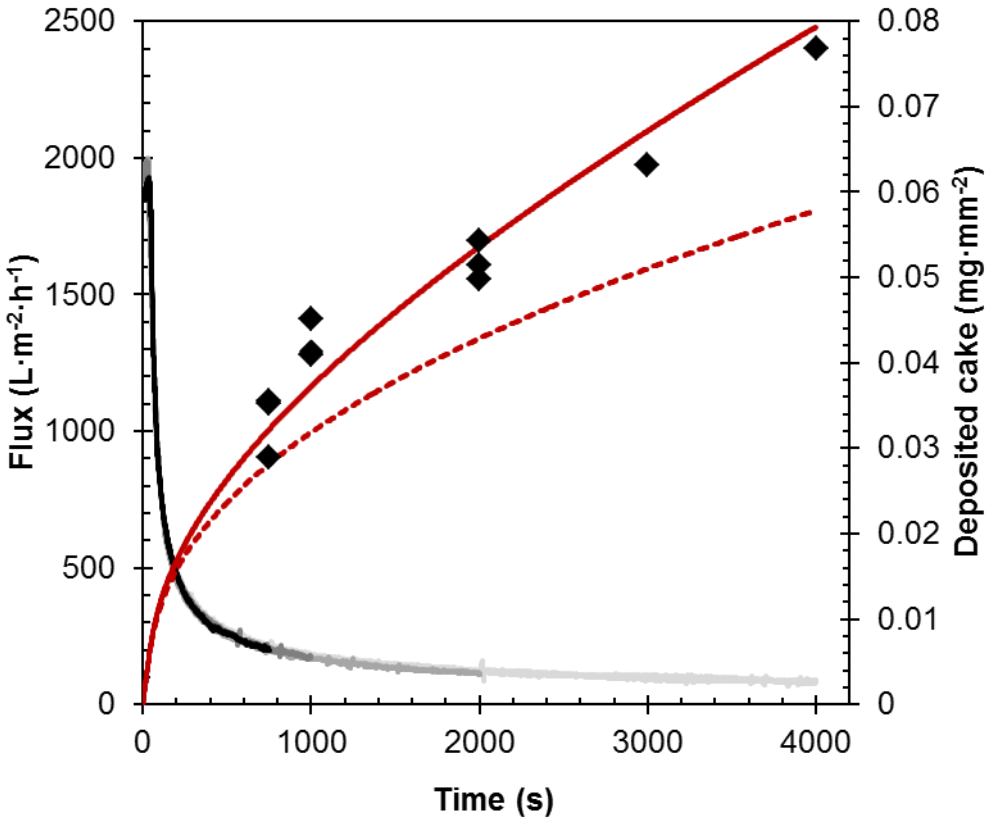

Figure 7.13. Dry cake mass deposited per unit area of membrane (symbols) and flux (lines) against time. Black, dark, medium and light grey lines represent fluxes for 750, 1000, 2000 and 4000 s respectively. The dashed red line indicates the quantity of cake predicted by (7.1) for the 4000 s experiment. The solid red line indicates the corrected curve given by equation (7.7)

7.4 PLF Studies

A comparison between flux decline behaviour is shown in Figure 7.14 for the three different pressures studied. In all cases flux decreased by an order of magnitude within the first 750 s of filtration. After 300 s of rinsing under relaxation (i.e. zero TMP), some flux recovery was observed, which became more pronounced for filtrations performed at higher pressures. This is explored in further depth in section 7.4.2.

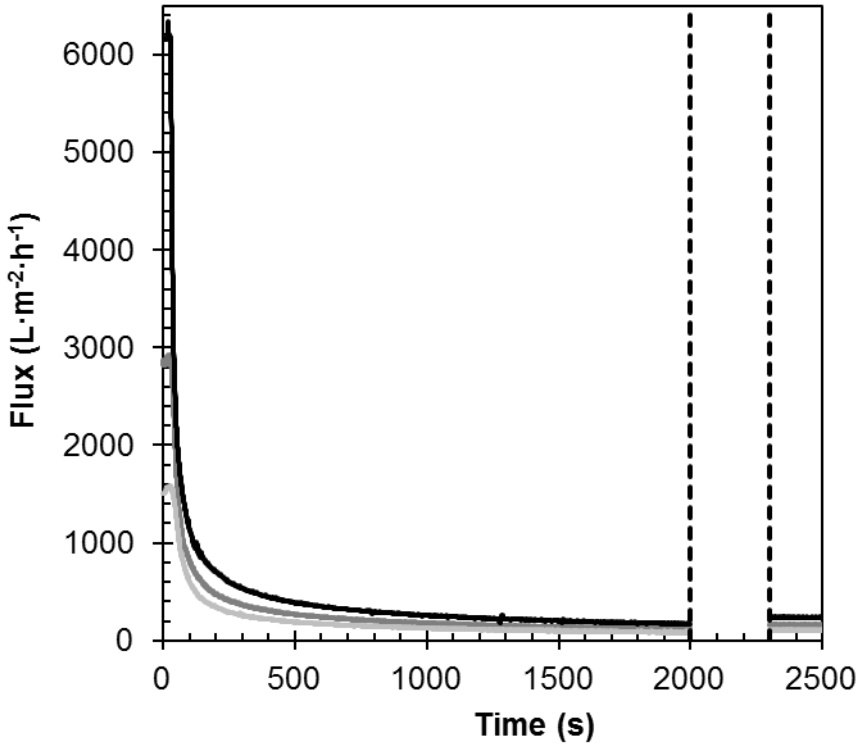

Figure 7.14. Flux decline for lignin fouling experiments run at TMPs of 50 (light grey), 100 (dark grey) and 200 (black) mbar. The area between the dashed lines indicates the 300 s period of rinsing under relaxation.

7.4.1 Data validation

Experiments were repeated for each pressure at least three times. Due to less repeatable flux decline and initial fluxes, more repeats were performed at the highest TMP of 200 mbar. Valid results were determined as before, by comparing flux decline curves. Results from experiments where flux decline or initial flux deviated significantly from the rest were discarded as invalid. A second validation step was performed using mass and thickness data, wherein only measurements for which $0.4 < \phi_c < 0.8$ were considered valid. This relatively wide tolerance was used because some nonlinearity was suspected between thickness and deposited cake mass due to

possible compressibility of the cake. After this elimination three data sets (where one data set represents one experimental run) were used for each TMP.

7.4.2 Recovery flux and cake thickness

Recovery flux

As indicated in Figure 7.14 the flux increases marginally following 300 s of rinsing under relaxation. The flux before and after this rinse is summarised for each TMP in Figure 7.15, which in both cases increases linearly with TMP. The dimensionless flux recovery is expressed as:

$$J'_{rec} = \frac{J_{rinse}}{J_{final}} \tag{7.8}$$

where J_{rinse} is the flux after rinsing, and J_{final} is the flux after 2000 s fouling. J'_{rec} also increases with TMP, as evidenced by a steeper gradient for J_{rinse} compared with J_{final}.

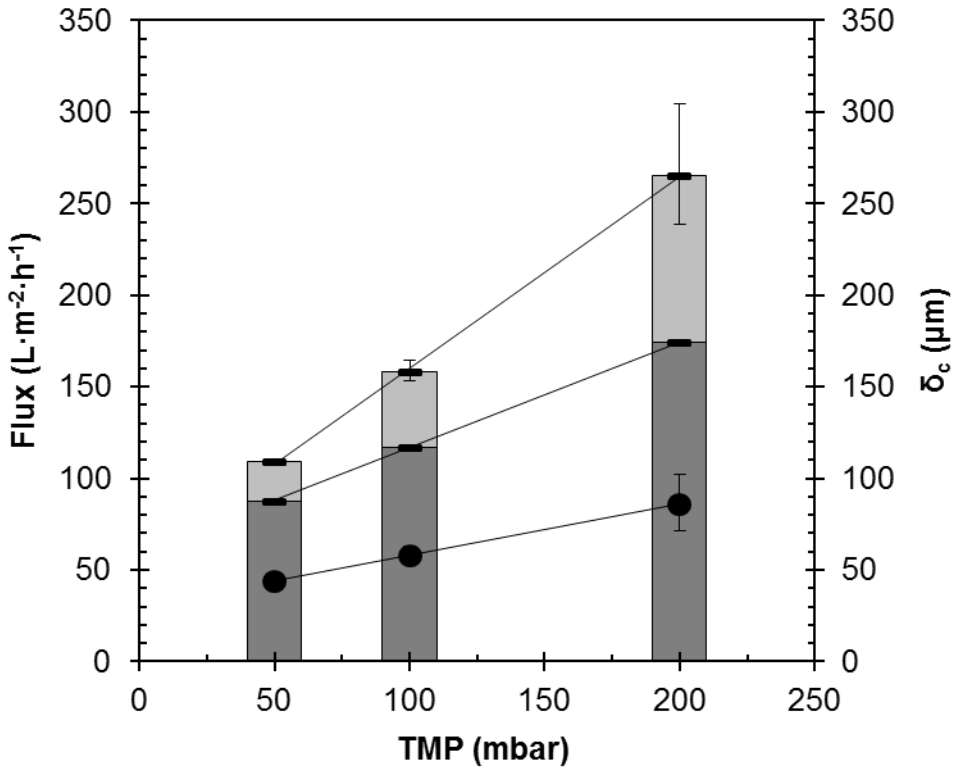

Figure 7.15. Average flux after 2000 s filtration (dark grey) and subsequent recovery after rinsing (additional light grey). Error bars indicate the total span of results. Circles indicate average thickness measurements at each TMP, again error bars indicate the overall span.

Cake deposition

The cake thickness, which is indicated by the circles in Figure 7.15, also increased linearly with pressure. This should be expected if cake growth is directly

linked to flux. For the PLF studies, there was not such a strong linear correlation between the mass of cake deposited and the measured thickness. Figure 7.16 shows a relatively constant mass of cake deposited for thickness values between 40 and 60 μm, which corresponds to results for both 50 and 100 mbar TMP. This suggests that after rinsing, the cake developed at a higher TMP has a lower volume fraction of lignin than the cake developed at lower TMP.

This behaviour could be linked with differing degrees of pore fouling at the different pressures. For example the pressure drop across the majority of the cake layer could be lower at 100 mbar than at 50 mbar if the resistance due to pore blocking (or a skin layer) was sufficiently greater at 100 mbar. If this were the case it would imply that the cake is compressible at these low pressures.

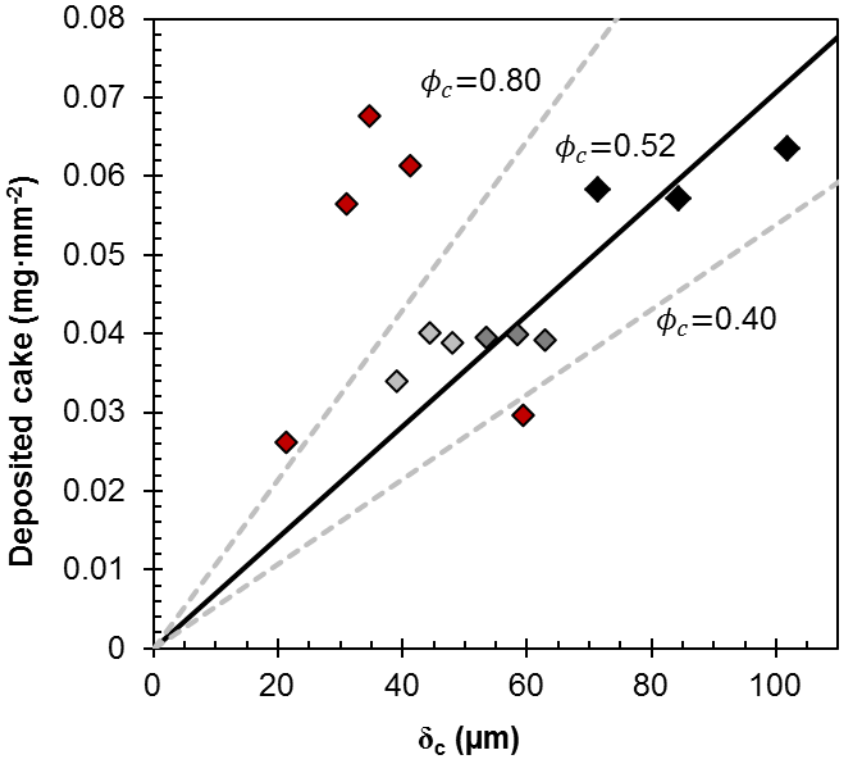

Figure 7.16. Mass of cake per unit area of membrane against measured thickness. The dashed grey lines indicate trends for volume fractions of 0.4 and 0.8. Red symbols indicate data points corresponding to experiments considered invalid, as described in section 7.4.1. The solid black line indicates a linear fit (with an intercept of zero) to the data considered valid. Light grey, dark grey, and black symbols indicate results for TMPs of 50, 100 and 200 mbar respectively.

The thicker cakes, developed under 200 mbar TMP indicate a higher mass of cake per unit area, however there is still little dependence on thickness. The latter observation might indicate instead that weight is still a more repeatable indicator of cake deposition than thickness, potentially due to variability in strength at the top layer of the cake. That there is a significant step-wise increase in deposited mass between 100

and 200 mbar TMP accompanied by a steady growth in cake thickness (as seen in Figure 7.15) suggests a transition in fouling behaviour across the range of TMPs studied.

Cake volume fraction

Using equation (7.4) and the linear fit indicated by the black line in Figure 7.16, the cake volume fraction was estimated to be ϕ_c = 0.52, which is close to that of the wet lignin powder.

7.4.3 Fouling resistance

Estimation of pore blocking resistance

The fouling resistance after rinsing, R_f, is calculated as before using equation (7.2). Figure 7.17 shows a plot of this against cake thickness, for which a linear regression fit gives an estimate for pore blocking resistance of $R_p = 5.64\times10^{10}$ m^{-1}. Although this is similar to the result calculated in section 7.3.3, such a fit is much less certain in light of the previous observations for Figure 7.16 which suggest the possibility of a compressible pore blocking or skin layer at the membrane surface.

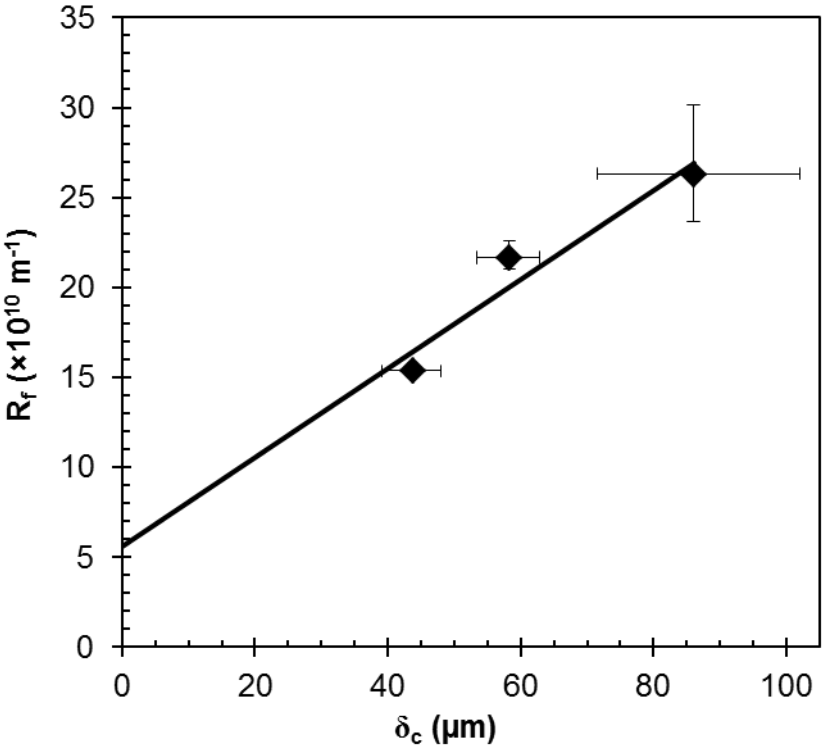

Figure 7.17. Fouling resistance, R_f, after rinsing under relaxation plotted against cake thickness. Here average values are plotted for each TMP and error bars show overall span of results. A linear regression fit extrapolated to δ_c = 0 is shown.

Resistance of the loose layer

The change in flux due to rinsing under relaxation is considered here to be evidence of reversible fouling, hence a reversible resistance, R_{rev} is derived by:

$$R_{rev} = R_{f,final} - R_{f,rinse} \tag{7.9}$$

where $R_{f,final}$ and $R_{f,rinse}$ are the fouling resistances before and after rinsing. A breakdown of the different contributions to the total resistance, R_T, is shown in Figure 7.18, along with the average deposited mass, at each pressure. The resistance contributed by reversible fouling significantly increases at higher pressure, eclipsing the presumed constant pore blocking resistance.

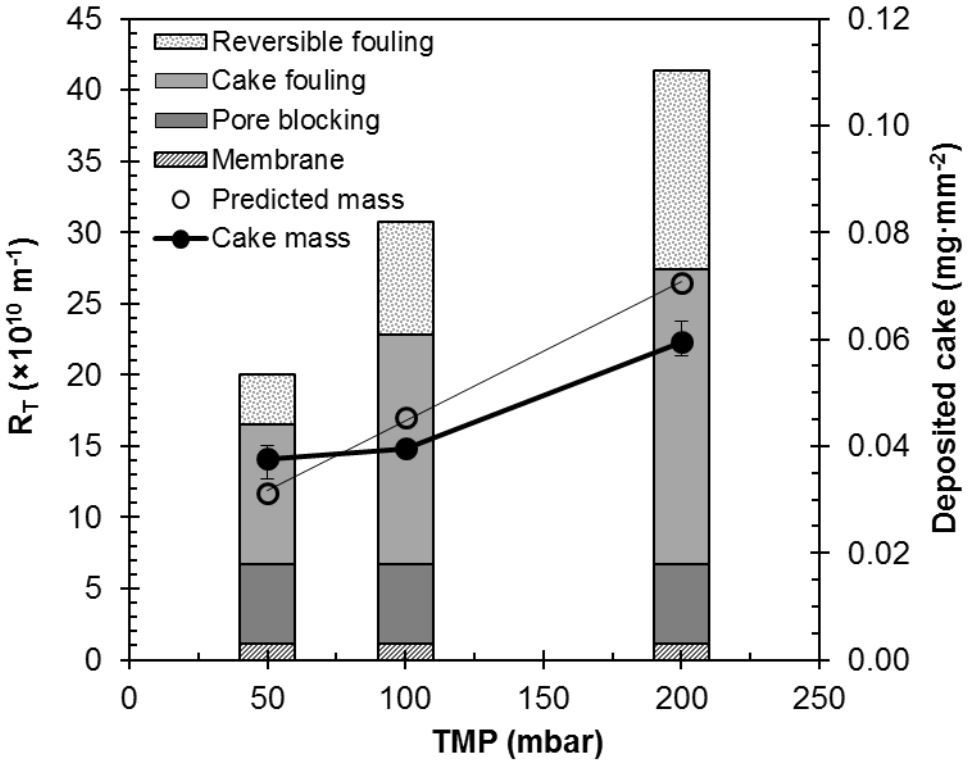

Figure 7.18. Contribution of different resistance mechanisms to total resistance, R_T at each pressure. Closed symbols indicate average deposited cake per unit area of membrane, for which the error bars indicate the overall span of measurements. Open symbols indicate the predicted mass using equation (7.1), for which a linear regression fit (dashed line) is plotted.

Inconsistent mass deposition

Figure 7.18 also demonstrates the nonlinearity between deposited mass and TMP. The irreversible fouling resistance (indicated by the top of the "cake fouling" column) appears to increase asymptotically with pressure, which suggests an inconsistent specific resistance, φ_c, across the TMP range studied. Equation (7.1) was

used to predict the final mass of cake deposited, which indicates a practically linear correlation with TMP. In contrast to the results shown in section 7.3.2, the equation over-predicts mass at TMPs of 100 and 200 mbar as a result of the material lost when rinsed under relaxation.

While a primary factor in this could be a difference in the quantity of material in the reversible fouling layer, this does not explain why the thickness readings increase linearly with pressure (Figure 7.15). One viable explanation is that the pore blocking/skin layer increases resistance with pressure between 50 and 100 mbar, but reaches a threshold pressure before 200 mbar beyond which no further increase in resistance occurs. As a result the flux decreases faster at 100 mbar with little extra deposition compared with that at 50 mbar. This would imply the following:

1. The resulting cake is also slightly less dense, and/or:
2. the cake measured at 50 mbar is too weak and was a similar height to that at 100 mbar.

Performing time-related fouling studies (i.e. TLF studies) at each pressure would allow for pore blocking resistance to be estimated for each individual pressure, such that a plateau in pore blocking resistance could be identified. This would also give a stronger indication of whether the terminal cake thickness measurements are definitely linearly dependent on TMP.

7.4.4 Destructive strength testing

The results of destructive thickness testing at each TMP are compared in Figure 7.19. The thicker cakes developed at 200 mbar (c) show more variation in their removal behaviour than at 50 and 100 mbar (a and b). A similar observation was made for the TLF studies, as highlighted in section 7.3.5. Comparing just the 50 mbar and 100 mbar experiments suggests that the yield stress for the top surface of the cake layer is much lower at 50 mbar. Also, the cake formed at 50 mbar is also almost fully removed at around 250 $N \cdot m^{-2}$, whereas a layer of about 30 μm still remains with an applied shear stress of 300 $N \cdot m^{-2}$ at 100 mbar. This indicates a lower adhesive strength.

Comparison between cakes for the three different pressures, as shown in (d), indicates a similar gradient between δ_c and $\tau_{w,max}$ for 100 and 200 mbar filtrations, whereas the 50 mbar experiment exhibits a steeper gradient and a higher sensitivity of the cake to fluid shear. Due to the variation shown between repeat runs in (a-c) this is somewhat open to interpretation. Aside from the anomalous results shown by circles in (c), the more reliable conclusion to be drawn from Figure 7.19 is that higher pressures

increase the cohesive strength at greater cake thickness. This means that cake strength is strongly dependent on the normal force holding particles to the surface.

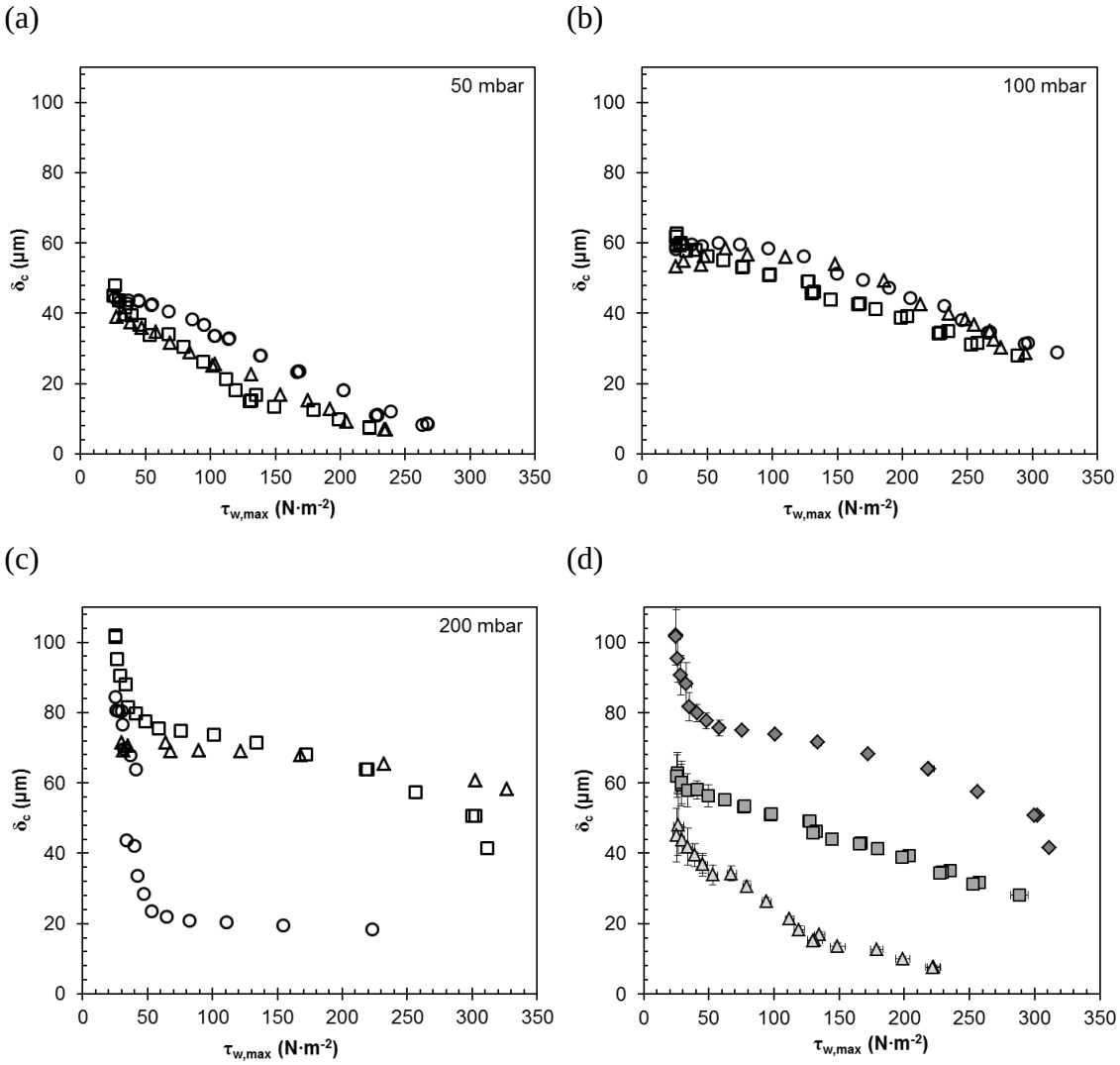

Figure 7.19. Thickness vs. maximum wall shear stress, $\tau_{w,\max}$, for lignin cakes fouled at 50, 100, and 200 mbar TMP (a-c respectively). Different symbols represent repeat runs of the same experiment. (d) shows example results for each pressure, where triangles, squares and diamonds represent 50, 100, and 200 mbar TMP respectively.

Cake removal at 50 mbar

The almost complete cake removal at 50 mbar is likely due to Δp_{13} approaching TMP as $\tau_{w,\max}$ increases. After recovering the membrane, the area just beneath the gauge was imaged using an optical microscope (*Nikon*, AZ100). An image from one experiment is shown in Figure 7.20a. An annular area of almost clean membrane is visible just beneath the nozzle rim. The size and shape of this region proved to be repeatable, and its alignment with the nozzle geometry is indicated in Figure 7.20b. This formation is similar to that seen for ballotini in section 5.3.3, and the decrease in the

quantity of material removed from the surface is in line with the shear stress profile predicted in section 8.7.4.

(a) (b)

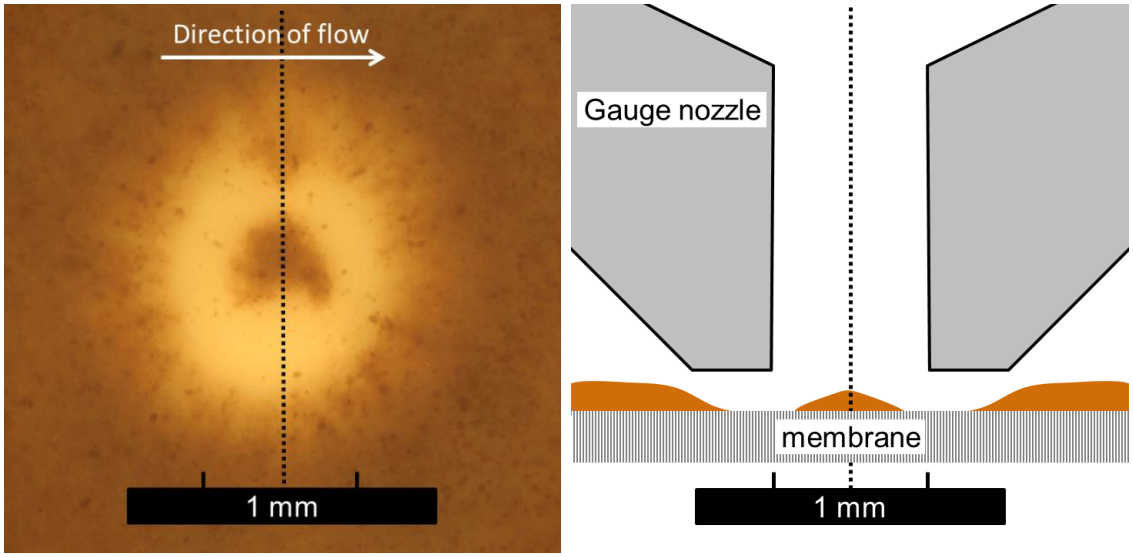

Figure 7.20. (a) Magnified image of the eroded region of the lignin fouling layer beneath the gauge nozzle, after 2000 s filtration at 50 mbar TMP. (b) diagram representing a cross-section through this region where the geometry of the gauge nozzle is shown to scale directly above. The dashed line indicates the position of the gauge centreline, and the ticks on the scale bar indicate the position of the inner edges of the nozzle rim (Thickness of the fouling layer and membrane is not drawn to scale here).

7.4.5 Critical flux laws

Table 7.1 Average values for the critical flux constant, k, limiting flux, J^*, and transitional flux , J_T, all calculated using equation (2.20) where $n = 0$. The pore blocking resistance, R_p is calculated from J_T using equation (7.10).

TMP (mbar)	k ($m^{-2} \cdot s^{-1}$)	J^* ($L \cdot m^{-2} \cdot h^{-1}$)	J_T ($L \cdot m^{-2} \cdot h^{-1}$)	R_p ($\times 10^{10}$ m^{-1})
50	361,800	-36.0	580.6	5.30
100	209,100	-42.6	375.9	8.42
200	83,800	-86.5	278.8	11.35

As described in section 7.3.6, linear correlations were only established for the cake fouling ($n = 0$) model. Example plots for the three different TMPs are shown together in Figure 7.21 and the resulting constants are summarised in Table 6.1. The kinks in the graph are thought to be the effect of minor decreases in TMP during the filtration. The associated TMP change was less than 2 mbar in all cases where this

occurred, however the impact it has is demonstrative of the sensitivity of this method of analysis.

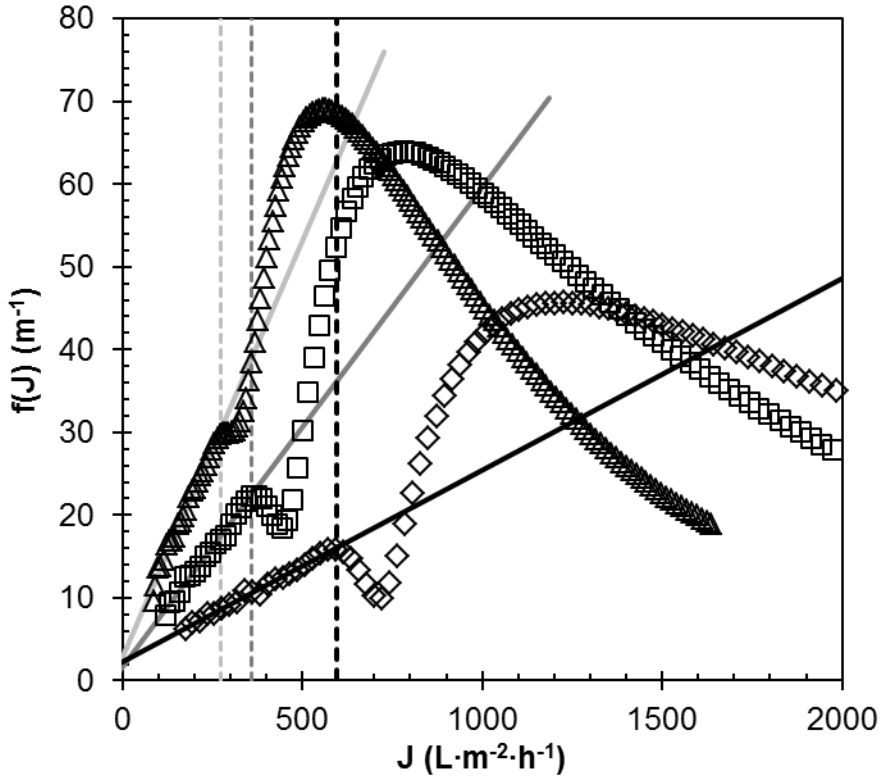

Figure 7.21. $f(J)$ against J using (2.20) where $n = 0$ for 2000 s filtrations at 50 mbar (triangles), 100 mbar (squares) and 200 mbar (diamonds) TMP. Dashed lines indicate the flux at the transition between complete/intermediate fouling and cake fouling mechanisms. Solid lines indicate the linear regression fits below this point. Light grey, dark grey, and black lines correspond to TMPs of 50, 100 and 200 mbar respectively.

Limiting flux, J^*

For all three TMPs the limiting flux was negative, and actually decreased with increasing TMP. This quantity should represent the flux at which no cake fouling would occur, which one could control through adjustment of TMP, so would be expected to remain constant. That this is not the case might indicate a change in the additional transport of particles towards the membrane – represented by S in equation (7.6) – as a result of the increased flux.

Transition flux, J_T

In section 7.4.3 the possibility of a changing pore blocking resistance, R_p, was discussed as an explanation for the inconsistency between deposited mass and cake thickness. This is supported by the results of this analysis, as R_p can be estimated from J_T by:

$$R_p = \frac{TMP}{\mu J_P} - R_m \tag{7.10}$$

and shown in Table 6.1. J_T actually increases linearly with TMP (not shown here), and R_p does indeed show an increase with pressure, however with only 3 data points there would be no clear indication of a plateau between 100 and 200 mbar TMP. The values for R_p in Table 6.1 are likely to represent over-estimates because, as shown in section 7.3.6, the transition flux determined using the $n = 1$, and $n = 2$ laws gave a larger estimate in closer agreement with the estimate using thickness measurements.

Back transport and specific resistance

As previous observations have indicated that specific cake resistance is unlikely to be constant, equations (7.5) and (7.6) cannot be used to predict the rate of back-transport (which would be negative because $J^* < 0$). The changing value for J^* also means that S may also change with TMP, hence this analysis will not be attempted for this set of studies.

7.4.6 Comparison with TLF studies

It is important to note that the membranes used for PLF studies were slightly different to those used in these studies. An interesting comparison can be made with the previous filtration data in section 7.3 with regards to the minor difference in membrane performance. The older Schleicher & Scheull membranes exhibited a higher resistance than the newer ones (see Table 6.2), which resulted in a lower initial flux as shown in Figure 7.22. The graph indicates a perfect match between the flux decline curves, suggesting very similar pore blocking and cake fouling behaviour. Thickness measurements were also consistent between the two.

The flux after rinsing was higher for the older membrane in the TLF studies, and the resistance of the loose flowing layer was calculated to be roughly twice that seen for the PLF studies.

Comparison between the two membranes highlights how a significant difference in membrane resistance ultimately has little influence on the overall filtration performance. Comparison of the results of destructive strength testing (i.e. Figure 7.8c and Figure 7.22b) showed similar behaviour.

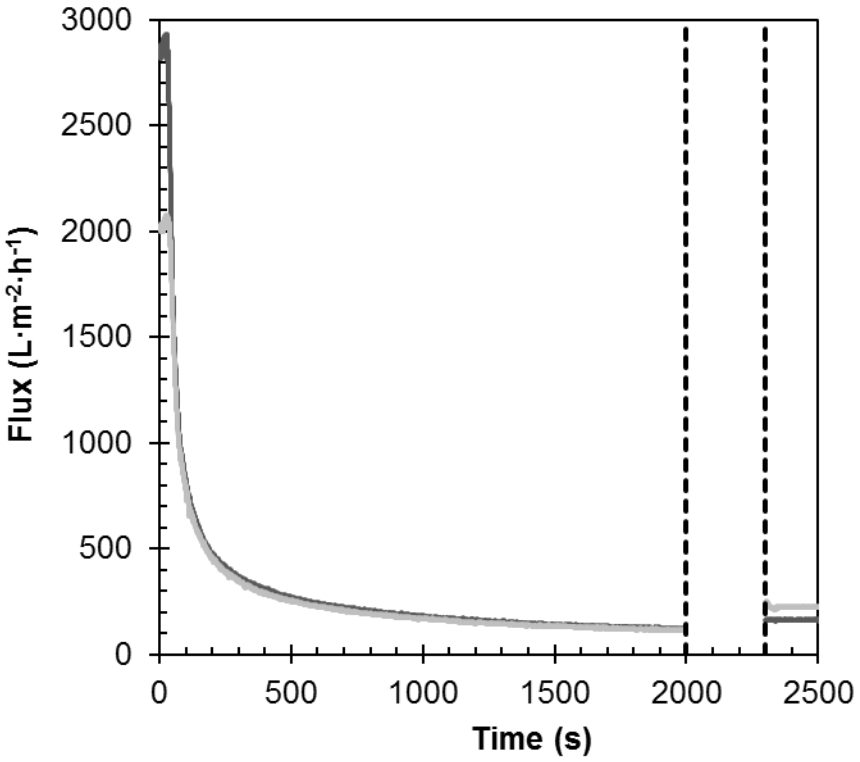

Figure 7.22. Comparison of flux decline behaviour between the TLF studies (light grey) and PLF studies (dark grey). TMP = 100 mbar and Re_{duct} = 1550 in both cases. The area between the dashed lines indicates the 300 s period of rinsing under relaxation.

7.5 BLF Studies

Only one repeat was performed for each experiment of this type and, due to incongruence between flux decline curves or low initial flux, only one from each experiment was deemed viable. Four different types of fouling scheme were used in these experiments, namely:

L: Fouling with lignin only

BL: Ballotini then lignin

M: Filtration of the ballotini and lignin mixture

B: Fouling with ballotini only

Results from L were found to exhibit very different flux decline curves to those seen for the same conditions (100 mbar TMP) in section 7.4, and were thus considered non-viable.

7.5.1 Cake growth and flux decline

Flux Decline

Figure 7.23 shows flux decline curves for BL, M, and B experiments. Immediately evident from the graph is the much slower rate at which ballotini causes flux decline in comparison with lignin. It should be noted that comparison with flux decline curves for a pure lignin feed at the same TMP (i.e. that shown for 100 mbar in Figure 7.14) showed near-perfect concordance. Subsequent to the addition of ballotini particles at 300 s, the flux for the BL experiment declined rapidly and became closely matched with M by 750 s. This shows that the addition of inert ballotini particles, whether in the mixture or as a prefouling layer, did not result in any improvement to the overall filtration performance.

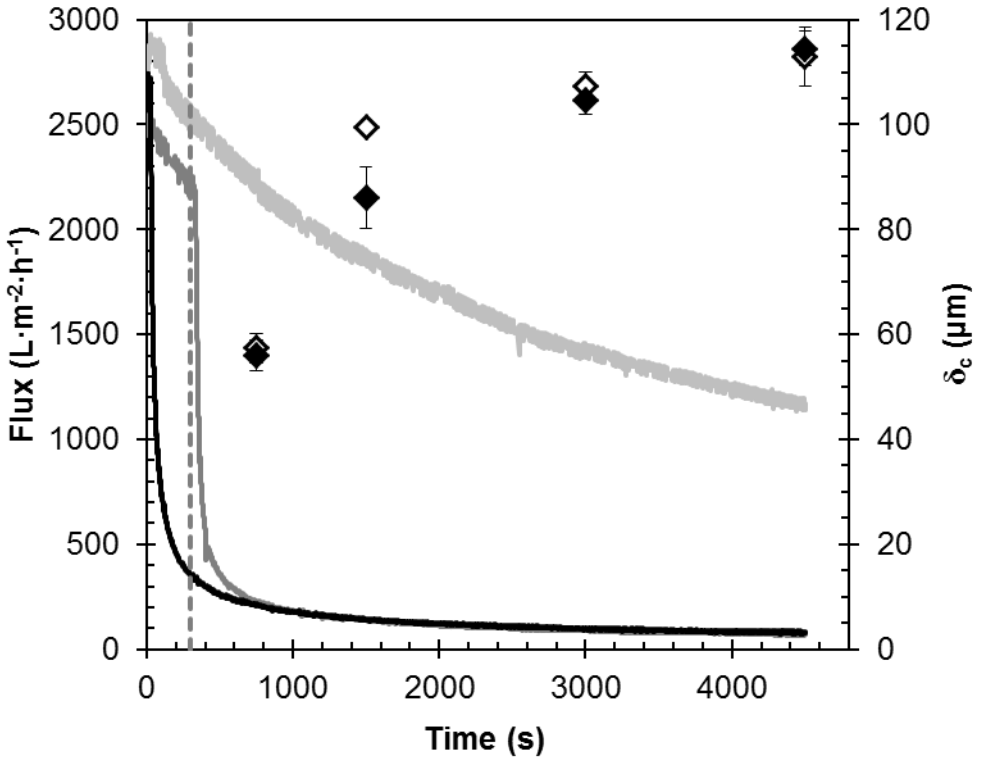

Figure 7.23. Cake thickness (symbols) and flux against time for mixture fouling, M (black line, closed symbols); ballotini then lignin, BL (dark grey line, open symbols); and ballotini, B (light grey line). The dashed grey line indicates the time point at which the lignin was added to the feed tank in BL experiments. Cake thickness for ballotini fouling (B) experiments not shown here.

Cake thickness

An image of the fouling layer formed during a 3000 s BL experiment was acquired using an optical microscope (*Nikon*, AZ100). This fouling layer was also analysed using SEM (*JEOL* SEM6480LV). The resulting images are shown in

Figure 7.24. The cross-section by optical microscope (a) clearly shows a layer consisting predominantly of ballotini particles – which appear white – covered with a mixed layer on top – brown with specular particles. Some permeation of the ballotini layer by brown lignin particles is also evident.

(a)

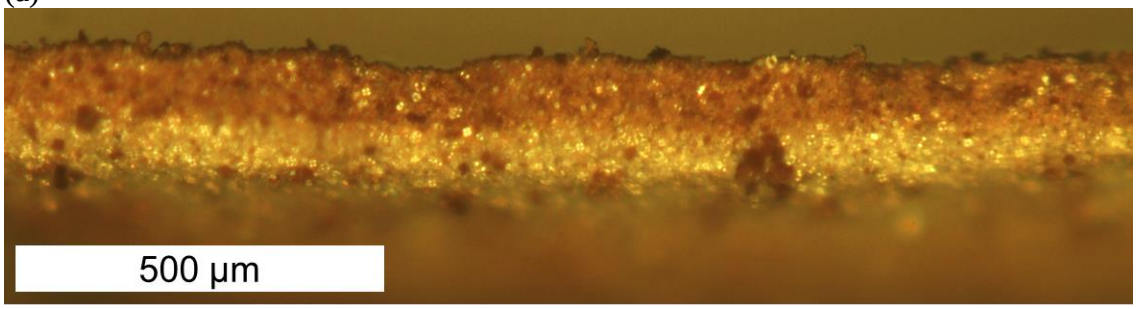

(b)

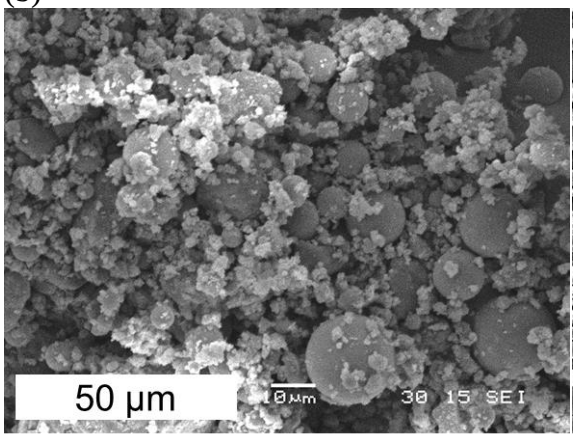

(c)

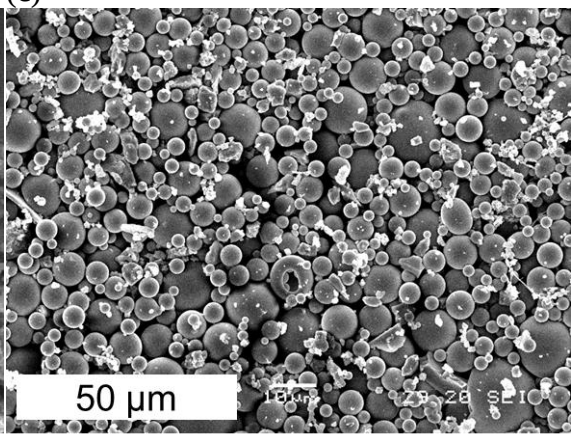

Figure 7.24. Images from of a fouling layer from BL experiments. (a) Cross section retrieved after 3000 s fouling, imaged using an optical microscope, the membrane would be on the bottom, but is not shown. Below shows electron micrographs taken at 10kV of (a) cross section of the upper, mixed region of the layer and (b) underside of ballotini layer in contact with the membrane.

Despite the presence of an initial layer of ballotini, Figure 7.23 shows little difference in cake thickness over time for the BL experiments (open symbols) when compared with the M experiments (closed symbols). In both cases the thickness appears to plateau, which is not so evident for the TLF experiments in which only lignin was used to foul the membrane. The cake layer in the BL experiments does appear to grow slightly faster than in the M experiments as evidenced by the higher point at 1500 s. Although repeat experiments would be required to verify this pattern, this could indicate a sequential fouling mechanism in which:

1. Ballotini cake builds up in the initial 300 s, at which point the lignin is added to the feed tank.
2. Lignin forms a cake on the surface which adds to thickness, however at a slower rate than M because some lignin particles are dragged into the

structure of the ballotini cake. There is evidence that smaller lignin particles permeated the ballotini layer in Figure 7.24c.

3. At 750 s the cake thickness is the same as for the mixture (M), but a significant proportion of this is an initial ballotini layer.
4. Once the ballotini cake has been saturated with lignin particles, the mixed fouling layer continues to build up on the surface at the same rate as in M, the result is a thicker overall cake layer.
5. As the cake height approaches its maximum value, particles are more easily removed due to surface shear; so thickness readings between the two experiments become comparable.

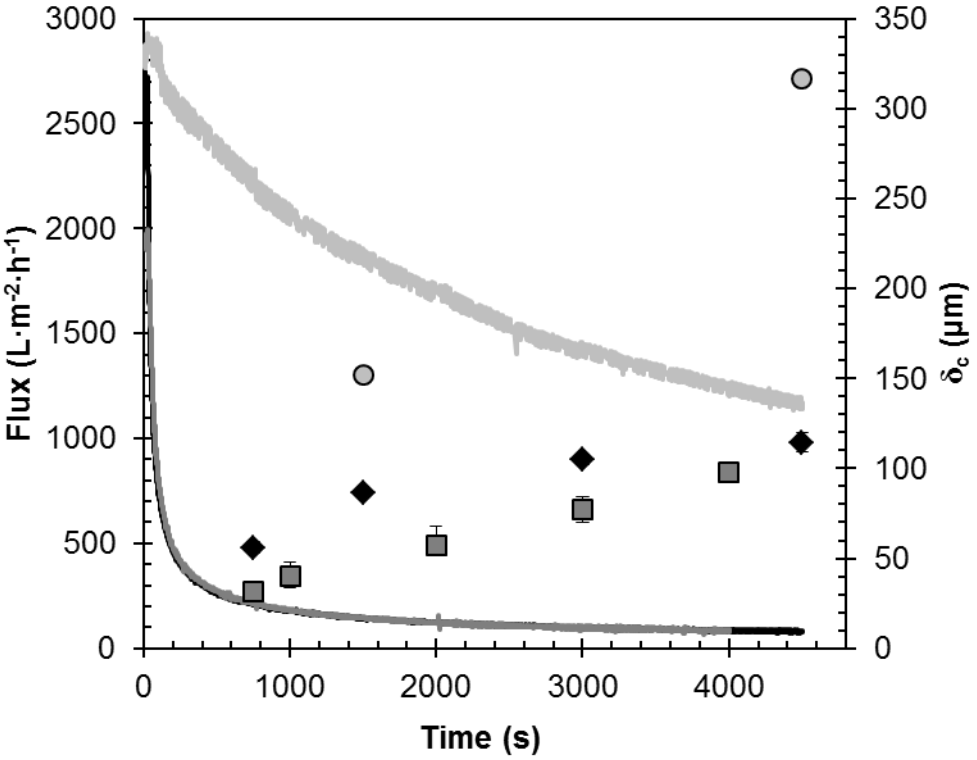

Figure 7.25. Comparison of flux and thickness between M experiments (black line, diamonds), TLF studies (dark grey line, squares), and B experiments (light grey line, circles).

Figure 7.25 shows the thickness and flux readings from the mixed foulant experiment (M) compared with those of the TLF studies (which are shown in Figure 7.4) and from ballotini fouling experiments (B). Immediately obvious from the flux decline curves is that the rate of decline is much slower for ballotini, despite being present at the same volumetric concentration as lignin. This is not entirely surprising as ballotini particles, along with being more perfectly spherical, have a narrower particle size distribution and higher average particle diameter than lignin.

Particle cakes formed by ballotini particles alone were much thicker than for lignin or a mixture of the two, however a growth pattern cannot be established from two data points. The mixed fouling layer was also thicker than the purely lignin fouling layer, although the resistance is the same for each, as indicated by matching fluxes at each time point[*]. Whereas the mixed fouling layer appears to tend towards a limiting thickness, the lignin fouling layer appears to still be increasing at 4000 s. There is a possibility that the two may converge on a similar limiting thickness. The results of destructive thickness tests, as described in 7.3.5, indicated that the top surfaces of fouling layers were progressively easier to remove as they became further from the membrane. This would suggest an eventual limiting thickness, above which FDG measurements cannot be achieved under these fouling conditions. By extension this also implies a thickness at which shear stress due to cross-flow would prevent further cake growth.

7.5.2 Destructive strength testing

Results of the destructive thickness testing for M and BL experiments are shown in Figure 7.26. Comparing bi-layered cakes formed by BL experiments with the ones formed in M experiments indicated that in general, the former are harder to remove. Plots (a) to (d) all show a thicker layer at the highest applied stress compared with the homogeneous cakes. Cakes formed from a single layer (M) actually appeared to be completely removed in some cases (at 750 and 3000 s).

The overall results for the M experiments follow a much more distinct pattern than those for BL, as seen by comparison of (e) and (f). This may reflect a somewhat more random nature in the cohesive strength of bi-layer cakes. As seen in Figure 7.24a the permeation of lignin in the cake is far from regular, neither is the arrangement of the larger, darker lignin particles. The M experiments, summarised in Figure 7.26e, actually follow the pattern suggested by the mechanistic model of Figure 7.10a described in section 7.3.5.

To properly verify these observations would require repeat runs of all experiments, however initial results do suggest that cakes formed from a mixture of ballotini and lignin may me slightly more removable by fluid shear than those purely of lignin.

[*] Although the TLF studies used a membrane of slightly higher resistance, the difference has a negligible impact on overall resistance. At 750 s this equates to a maximum of 3.7% increase in R_f.

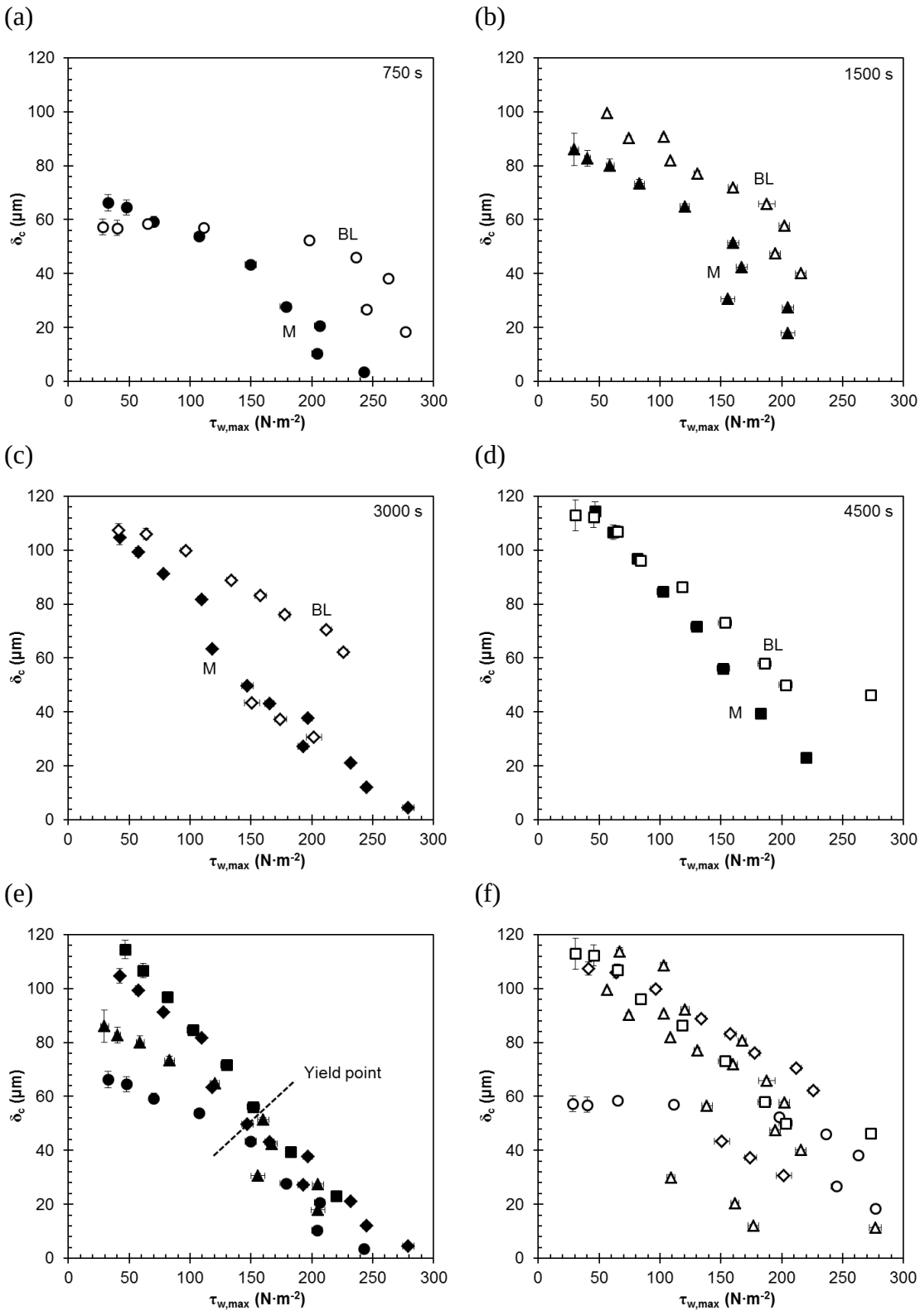

Figure 7.26. Thickness vs. maximum wall shear stress, $\tau_{w,\max}$, for BL (open symbols) and M (closed symbols) cakes fouled for (a) 750 s, (b) 1500 s, (c) 3000 s, and (d) 4500 s. (e) and (f) show all data for M and BL where circles, triangles, diamonds and squares represent 750, 1500, 3000, and 4500 s runs respectively. The estimated yield point is indicated in (e). All experiments performed at TMP = 100 mbar and Re_{duct} = 1550.

7.6 Conclusions

Filtration of a suspension of Kraft Lignin showed fast fouling of the membrane which caused a 10-fold decrease in flux within 500 s and 20-fold by 2000 s. Cake thickness measurements taken at various times indicated a highly resistant fouling layer either caused by a pore blocking phenomenon or highly impermeable skin layer at the cake/membrane interface. A resistance value of R_p = 5.10×10^{10} m^{-1} at TMP = 100 mbar, yet there was evidence to suggest this might vary with pressure. Analysis using the critical flux filtration laws of Field *et al.* (1995) yielded a similar value.

7.6.1 Improvements to lignin filtration

Flux improvement

Introducing an inert species such as ballotini to the suspension ultimately made no difference to the rate of flux decline or steady-state flux, whether as an initial fouling layer or at the same time as the lignin. The destructive strength testing showed that surface layers of thicker cakes were easier to remove than for thinner cakes. Those formed with ballotini were thicker than pure lignin cakes at no greater resistance. Thus it may be possible to improve filtrations through enhancing the overall thickness of the cakes to a higher, threshold value where shear forces due to cross flow limit fouling. This could be achieved either by significantly increasing the ballotini concentration or growing an initial layer for a longer time period.

The first target for improvement would be the elimination of pore blocking resistance, R_p, which could lead to a 20% increase in flux. This may be achieved by selection of membranes with smaller pores, such that the particles cannot rest within the pore structure as easily. Although this would result in a lower initial flux this could limit the system to purely cake fouling mechanisms.

Cleaning improvements

Although further studies are required for confirmation, there is some evidence to suggest that mixing with ballotini particles made lignin suspensions slightly easier to remove from the membrane surface with shear forces. The ability to create initial layers of inert particles on the membrane surface does, however, present an interesting method by which anti-fouling strategies can be approached by functionalising such particles rather than membranes.

Investigations of cake removal under different pressures in the PLF studies, as described in section 7.4.4, indicated that normal force on the surface of the cake played

the most significant role in removal. Hence backflushing is likely to be the most effective physical removal strategy.

7.6.2 Automation of FDG

The incorporation of a syringe pump to control gauging flow, m_g, demonstrates a zero-net-discharge method for performing FDG measurements in a cross-flow membrane filtration. This would be especially important when performing filtrations of sterile or valuable feeds. In addition, the automated calibrations and instantaneous thickness readings show how applicable FDG could be to industrial applications wherein specialist support may not be available to interpret data.

The measures put in place to automate calibrations prior to fouling experiments proved successful in reducing the time and level of input required to set up an FDG experiment. As a result it was possible to perform numerous experiments over a short space of time to quickly assess potential improvements to cleaning or filtration performance while simultaneously characterising their underlying mechanics.

Potential for further automation

It would be possible to fully automate the calibration protocol of the current device such that no user input would be required to specify the h_0/d_t positions at which to make Δp_{13} readings or align them to the calibration curve. Thickness readings could also be made automatically, and include destructive strength testing. These are currently achievable through further programming, which will be discussed in more detail in 9.4.1.

Chapter 8: Computational Fluid Dynamics

8.1 Introduction

As described in 2.7.3, an analytical solution (equation (2.38)) can be used to estimate the surface shear stress directly beneath the tip of the gauging nozzle during FDG measurements. While this has been accepted as a reasonably accurate approximation (Chew *et al.*, 2004a; Gu *et al.*, 2007), it cannot easily be confirmed experimentally. To do so would require the use of complex experimental techniques such as particle imaging velocimetry or laser-doppler anemometry. A more practicable method is to use computational fluid dynamics (CFD), which solves the continuity and Navier-Stokes equations to attain position-specific velocity vectors, and local pressures. Previous researchers have used CFD to predict local fluxes along a tubular membrane (Damak *et al.*, 2004), and predict uneven particle deposition on a flat sheet membrane (Rahimi *et al.*, 2009).

In this work, a commercially available computational modelling package, COMSOL Multiphysics™ ver. 4.2 (and later 4.2a), was used to simulate the conditions of the FDG experiments described in previous sections. In doing this it was not only possible to estimate the fluid shear stress on the surface below the gauge, but also infer its effect on the flow patterns and recirculation caused by its presence. The effect of duct geometry, such as the 3 mm step-down to the membrane surface for the manual duct flow rig, could also be examined. Finally, this technique is useful for predicting the Δp_{13} vs. h/d_t profiles determined experimentally, and indicate the effect (if any) which membrane flow has upon them.

8.2 Components of numerical CFD modelling

Computational fluid dynamics is a means to predict flow behaviour in pre-defined geometries by solving the appropriate constitutive equations for which there is no analytical solution (Fox *et al.*, 2010). The components from which a CFD solution for fluid flow is produced are briefly discussed below. A more detailed explanation of these can be found elsewhere (Tu *et al.*, 2008).

8.2.1 Flow domain

A flow domain is a representation of the geometry which is to be modelled by the CFD system. This can be one-, two- or three-dimensional. In cases where fluid moves around a solid object or obstruction, the domain consists of all the fluid around

this but not the object itself. The outer edges and/or faces of this domain are referred to as *boundaries*, e.g. pipe walls, inlets or outlets.

8.2.2 Mathematical model

A mathematical model is set up which consists of a set of *partial differential equations* (PDEs) and *boundary conditions*.

Partial Differential Equations (PDEs)

PDEs describe the system to be modelled in terms of constitutive equations. These include equations which govern conservation of mass, momentum, and energy; and can also include extra terms which define species diffusion or turbulent kinetics

Boundary conditions

These are used to characterise the system being investigated by constraining variables (such as pressure and velocity) at the boundaries of the flow domain. They must be specified so as to provide a reasonable representation of an experimental system, without over or under-constraining the rest of the model. Two types of boundary condition are generally used in CFD, namely *Dirichlet*, which specify the value of a variable (usually as a function), and *Neumman*, which constrain the derivative of a variable.

8.2.3 Coordinate systems

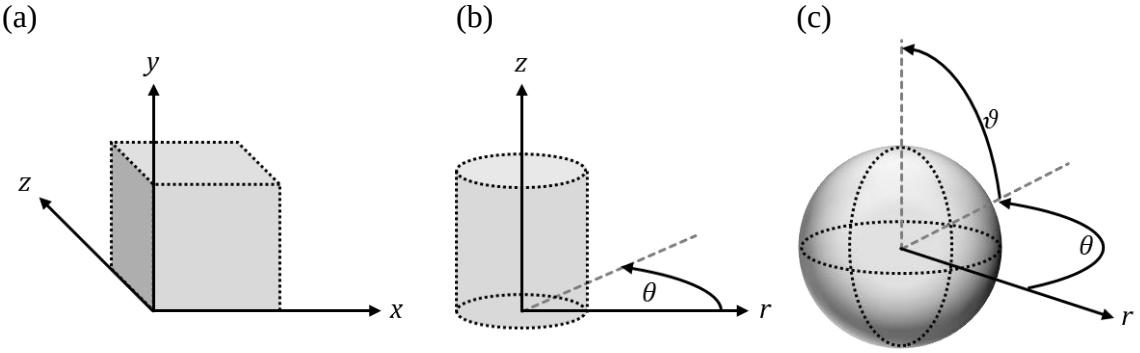

Figure 8.1. Diagrams showing (a) Cartesian, (b) cylindrical, and (c) spherical coordinate systems in three-dimensional space.

A coordinate system defines how the PDEs are defined in relation to three-dimensional space. The coordinate systems available are Cartesian, cylindrical, and spherical; which are illustrated in Figure 8.1 (a), (b), and (c) respectively. Although interchangeable, each has its most appropriate uses. For example, a spherical coordinate system is quite useful for considering particle fluid dynamics when using the centre of

the particle as a reference point. In rotating geometries, or when the system is axisymmetric, a cylindrical coordinate system is sometimes more appropriate.

8.2.4 Discretisation methods

Discretisation is a method of approximating PDEs by a system of algebraic equations. These include terms for variables (e.g. velocity and pressure) at discrete locations within the domain in space and time. Once these discrete locations are specified (by a mesh, as described below) they can be solved by a variety of approaches which include *finite element modelling* (FEM), *finite difference modelling* (FDM), and *finite volume modelling* (FVM).

8.2.5 Computational grid (mesh)

Commonly referred to as a mesh, this splits the domain into a number of cells, or *elements*, between or across which (depending on the method, e.g. FEM, FDM, or FVM) the mathematical model is discretised. The lines which bound these elements are referred to as *vertices*, and the points at which the lines meet are referred to as *nodes*. The shape of the mesh can have a strong influence on the results of a CFD simulation, so its appropriate specification for a particular system is important. The two general forms of mesh are shown in Figure 8.2. A structured mesh consists of regularly sized (usually rectangular) elements, whereas an unstructured mesh consists of a range of irregularly sized elements. In addition, the shapes from which a mesh is constructed can be either triangles or quadrilaterals. These translate into tetrahedrons and hexahedrons when modelling three-dimensional domains.

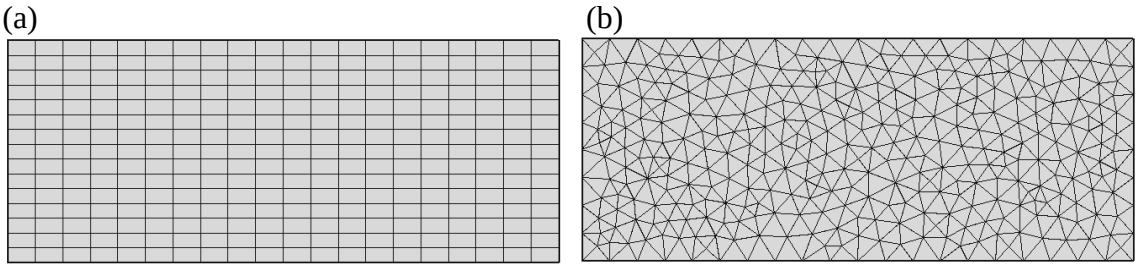

Figure 8.2. Examples of a (a) structured, and (b) unstructured mesh for a 2D rectangular domain.

8.2.6 Solution method and convergence tests

The general purpose of a CFD solver is to identify accurate values for all dependent variables (e.g. pressure and velocity) at each node on the mesh. Aside from values at nodes defined by boundary conditions, this leaves a very large number to

determine, a quantity referred to as the number of *degrees of freedom*. This increases with the number of nodes in the mesh.

CFD solvers can reach a solution by two types of method: *direct* and *iterative*.

Direct methods

In direct solvers, the entire system of equations (i.e. the resulting individual linear equations between every cell in the mesh) is formed into a matrix. This is then solved by Gaussian elimination or a variation thereof. These methods may reach a solution faster than iterative methods but are more computationally intensive.

Iterative methods

Iterative solvers guess values of the dependent variables and use various algorithms and the equation system in place to improve upon these guesses until a desired convergence, as described below, is reached. This requires less computational resources and is usually the preferred technique in 3D simulations.

Convergence criteria

Most iterative solvers use one or more dimensionless measures of convergence. Once this value drops below a specified *tolerance* at the end of an iteration step the solver process is terminated and a solution is deemed to have 'converged'. Most solvers define dimensionless convergence using two methods, sometimes together:

1. The relative combined change in value of all dependent variables at each node from one iteration to the next.
2. The relative residual, this is a measure of the imbalance of the discretised equation for a dependent variable between two nodes, by subtracting the difference determined by the discretised equations from the actual difference. The convergence criteria can be set such that the residual for every single node or sum total of all residuals must be below the specified tolerance.

8.3 Numerical modelling applied to FDG

8.3.1 Equations solved

COMSOL Multiphysics™ was used to solve the continuity and Navier-Stokes equations, namely (in vector form):

$$\rho \nabla \cdot \boldsymbol{u} = 0 \tag{8.1}$$

and

$$\rho\left(\frac{\partial \boldsymbol{u}}{\partial t} + \boldsymbol{u}\cdot\nabla\boldsymbol{u}\right) = -\nabla p + \mu\nabla^2\boldsymbol{u} + \rho\boldsymbol{g} \tag{8.2}$$

where $\boldsymbol{u}$ represents the velocity vector (u, v, w). In these simulations the flow was pressure-driven, so the body force term, $\rho\boldsymbol{g}$, can be ignored from equation (8.2). Steady-state simulations were performed, such that $\partial\boldsymbol{u}/\partial t = 0$. In all simulations described in this section the process fluid was modelled as a single phase liquid, namely water, which is incompressible so $\rho = constant$. The dynamic viscosity, μ, is also considered to be constant because water is Newtonian.

8.3.2 Discretisation method

COMSOL Multiphysics™ uses FEM to discretise the flow domain, which formulates expressions for equations (8.1) and (8.2) along the vertices between nodes on the mesh. These are then solved to find individual values for velocity, $\boldsymbol{u}$, and pressure , p, on each node. In these simulations a first-order discretisation method was used for both pressure and velocity variables.

8.3.3 Solver configuration and convergence criteria

An iterative solver was employed to solve all CFD simulations described in this section. The convergence criteria used is a residual defined in the COMSOL Multiphysics™ software as, as an example for the velocity vector, $\boldsymbol{u}$ (COMSOL, 2011):

$$Residual = \sqrt{\frac{1}{N_{DOF}}\sum_{i=1}^{N_{DOF}}\left(\frac{|\boldsymbol{\epsilon}_i|}{max(|\boldsymbol{u}_i|, S_i)}\right)^2} \tag{8.3}$$

where N_{DOF} is the total number of degrees of freedom, i is the node number, $|\boldsymbol{\epsilon}_i|$ is the modulus of the estimated error in the vector, $|\boldsymbol{u}_i|$ is the modulus of the velocity vector at node i, and S_i is a scale factor determined by the solver. The tolerance for this residual was set to 10^{-4} in all simulations.

8.4 Aims and Objectives

While the underlying aim of performing CFD simulations for FDG was to acquire reasonable predictions of shear stress on the surface below the gauge, a number of other assessments could also be made using this technique. CFD models were used to elucidate the flow disturbances caused by the FDG gauge in a flow stream, investigate

whether various simplifying assumptions can be rationally applied, and predict Δp_{13} vs. h/d_t profiles.

The following objectives were identified for this work, for which a number of different simulations were performed.

Manual duct flow rig (COMSOL ver. 4.2)

1. Simulating flow patterns around the gauge and in the duct when withdrawn from the surface and not in use.
2. Modelling the case with membrane flow to check gauging does not significantly affect flux. This was used to assess whether further simulations could be simplified by neglecting membrane flow from the model.
3. Check Δp_{13} and C_d predictions from simulations against experimental data.
4. Compare τ_w estimates from simulations against values from the analytical model given by equation (2.38).

Objectives 1-4 were achieved by using two simulation geometries, on which a parametric sweep was used to model a range of h/d_t values. The objectives were achieved through post-processing analysis of simulation results. The first geometry was for a section of cross-flow duct, in which membrane flow was included in the model. The second was a more accurate representation of the apparatus, including the recess from the bottom of the duct at which the membrane was situated.

Automated micro-FDG rig (COMSOL ver. 4.2a)

5. Obtain Δp_{13} predictions for calibration of zero-position
6. Check validity of a 2D-axisymmetric model for this gauge geometry and apparatus
7. Further assess viability of Middleman model, specifically for the conditions used in experiments with this apparatus
8. Produce a set of τ_w data for use in strength analysis of fouling layers.

Objective 5 was very critical from a practical perspective. Because the scale of movement for micro-FDG is so small, calibration of the positioning apparatus to identify the position of the gauge positioning apparatus where $h_0 = 0$ is more effectively achieved by comparison with FDG predictions than by manually setting this position against a solid surface, this is discussed in section 6.3.2. Both 3D and 2D models were performed to produce Δp_{13} vs. h/d_t profiles, which were used as calibration data for

FDG experiments using this rig. The 3D model was a representation of the FDG apparatus within the test section, and the 2D model represented the area immediately around the gauge without consideration of duct flow.

Objectives 6 and 8 were also achieved using these 3D and 2D models. In both cases results sets for a full range of h/d_t values were processed to get τ_w values and Δp_{13}.

8.5 Simulation 1: duct flow with d_t = 1 mm gauge (Membrane flow)

This simulation was performed to assess whether membrane flow affected FDG readings and calibration plots.

Objectives: *2,3*

Description:

(a)

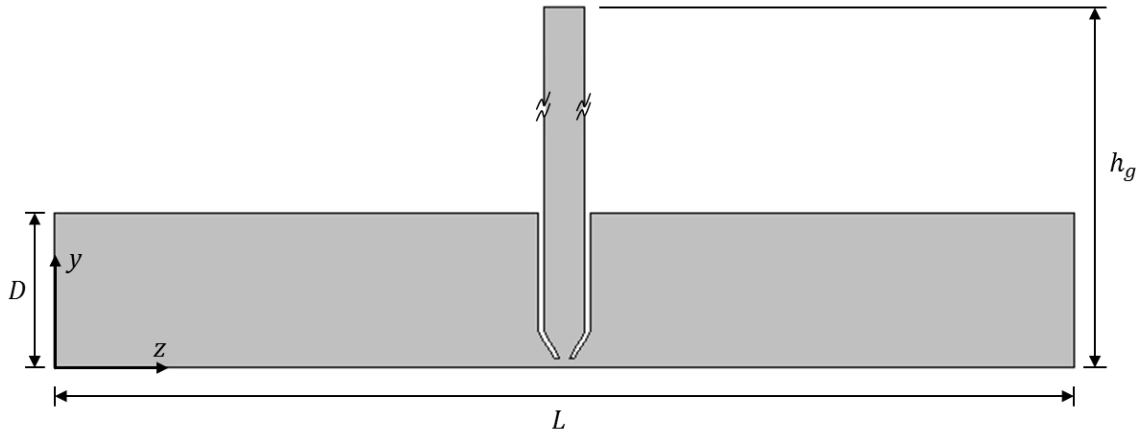

(b)

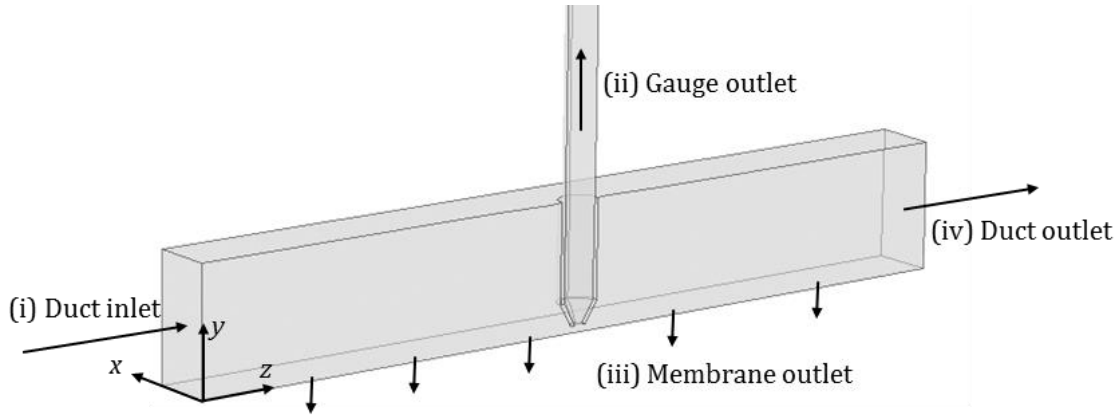

Figure 8.3. Computational domain used to model duct flow FDG with a membrane, shown in (a) 2D and (b) 3D with boundary labels. The origin of the coordinate axes indicate the point where x, y, and z = 0.

Using an idealised geometry for the test chamber (neglecting the recessed position of the membrane described in section 4.1.2), of a 15 × 15 mm square duct, this simulation was used to predict the effect of membrane flow on FDG. The domain, shown in Figure 8.3, modelled a shortened duct of length L = 100 mm to cover part of the length of the membrane, thus reducing computational load. The gauge position was set to the midpoint of this section which, although technically inaccurate in terms of the actual rig geometry, allowed enough room for streamlines to be parallel at the inlet and outlet of the domain (i.e. laminar or near-laminar flow). The gauge dimensions were specified as in described in 4.1.1, where d_t = 1 mm, d = 4 mm, s = 1 mm, and α = 30°. The simulation was solved using parametric studies for values of h/d_t ranging 0.06 to 0.4 and gauging flows where Re_{gauge} (characterised by the gauging tube diameter, d) ranged from 60 to 200.

8.5.1 Simulation parameters

The parameters below were used in this simulation, some of which were varied using a parametric sweep. It should be noted that the membrane resistance, R_m was specified as the lowest at which solutions could be achieved reliably, which was higher than for membranes used in experiments.

Stationary parameters

Transmembrane pressure, TMP = 35 mbar
Fluid viscosity, μ = 0.001 Pa·s
Fluid density, ρ = 1000 kg·m^{-3}
Membrane resistance, R_m = 5×10^{10} m^{-1}
Bulk inlet flowrate, Re_{duct} = 1000

Varied parameters

Dimensionless gauge clearance, h/d_t = 0.06-0.4
Dimensionless gauging flow, Re_g = 60-200 (≈0.2-0.6 g·s^{-1})

8.5.2 Boundary Conditions

(i) Duct inlet, z = 0

This was specified as a pressure-inlet boundary, wherein flow was constrained to a laminar profile. This condition is met internally within the software by modelling a theoretical entry length to develop flow (in this case 0.5 m was used). In the model detailed by Damak *et al.* (2004), and that used for cross-flow FDG by Lister *et al.*

(2011), an inlet velocity condition for with laminar flow was used instead. Using this version of COMSOL Multiphysics™ however, it was not possible to reference the pressure at this boundary when specified as a velocity inlet. This is important to specifying the membrane flow at boundary (iii). Pressure at the inlet was derived iteratively by running simulations at varying p_{in} until $Re_{duct} \approx 1000$. The resulting boundary condition was:

$$p_{in} = 35.3\ mbar \tag{8.4}$$

(ii) Gauge outlet, $y = h_g$, $z = L/2$

This was specified as a laminar flow outlet at the exit of the gauging tube by using a velocity outlet boundary condition where:

$$v = v_{max}\left(1 - \left(\frac{2r}{d}\right)^2\right) \tag{8.5}$$

where $v_{max} = 2v_{av}$, and u and w are zero. The average velocity, w_{av}, is given by:

$$v_{av} = \frac{4m_g}{\rho(\pi d^2)} \tag{8.6}$$

and the radial distance from the centre of the gauge, *r*, is given by:

$$r = \sqrt{x^2 + \left(z - \frac{L}{2}\right)^2} \tag{8.7}$$

The *y*-position of this boundary, h_g, was specified such that a laminar flow profile is fully developed at $0.95h_g$. This was found by running simulations with incrementally increased h_g until the *y*-wise velocity profiles at the outlet (defined by equation (8.5)) and at $0.95h_g$ matched.

(iii) Membrane outlet, y = 0

The conditions at the membrane outlet were specified using the same method as Damak *et al.* (2004) and Lister *et al.* (2011), which is derived from the Darcy's law equation (2.1). *y*-wise velocity at this boundary is given by:

$$v = \frac{p_{in} - TMP - p}{\mu R_m} \tag{8.8}$$

where p is the local pressure at the boundary.

The membrane resistance, R_m, used in this model was the lowest for which a converged solution could be achieved. It is higher than that determined for the membranes used in corresponding experiments, but lower than the total resistance, R_T, observed after fouling.

The surface of the membrane was considered to be non-slip, a condition which is debatable due to its porous nature. Other researchers modelling membrane filtration have concluded this to be a reasonable assumption (Damak *et al.*, 2004; Schmitz and Prat, 1995). The non-slip condition only applies in the *x* and *z* directions, such that:

$$u = 0, w = 0 \tag{8.9}$$

Beavers and Joseph (1967) explored methods by which to estimate the effective slip velocity due to flow over pores. They produce an estimate for slip velocity , u_w, at the wall of a surface with permeability, κ, given by:

$$u_w = -\frac{\kappa}{2\mu}\left(\frac{\vartheta^2 + 2\omega\vartheta}{1 + \omega\vartheta}\right)\frac{dp}{dx} \tag{8.10}$$

where $\vartheta = h/\sqrt{\kappa}$, and dp/dx is the pressure drop tangential to the wall. ω is a dimensionless parameter, which Beavers and Joseph (1967) determined experimentally for specific materials.

Equation (8.10) can be applied by assuming $dp = \Delta p_{13}$ and $dx = s$ (see Figure 2.15a). For FDG, Δp_{13} is dependent on h, which is taken into account here using the calibrations for m_g = 0.4 g·s^{-1} shown in Figure 5.1. From Table 4.2, κ = 2.85×10^{-13} m^2. For ϑ, an estimate of 1 was used. This gave, for a value of h/d_t = 0.1, u_w = 0.06 m·s^{-1}, which is by no means a negligible quantity (roughly 9% of the velocity at the outer edge of the FDG nozzle rim). However, a reasonable estimate for ϑ cannot be obtained and more recent work has suggested slip velocity on membrane surfaces can be considered negligible (Damak *et al.*, 2004; Schmitz and Prat, 1995). Hence wall slip will not be considered in the current simulations.

(iv) Duct outlet, z = L

This was defined as a pressure outlet:

$$p = TMP \tag{8.11}$$

which leaves velocity values unconstrained at all nodes except walls.

Symmetry, x = 0

The *zy*-plane at $x = 0$ was modelled as a plane of symmetry to halve the size of the domain and reduce computational load. The constraint applied on this boundary restricts flow normal to the boundary, which in this case is:

$$u = 0 \tag{8.12}$$

Walls, all remaining boundaries

The remaining boundaries which correspond to impermeable surfaces internal to the test cell i.e. the duct walls and gauge nozzle and tube. The condition here is:

$$\boldsymbol{u} = 0 \tag{8.13}$$

8.5.3 Finite element grid (mesh)

A relatively coarse, unstructured mesh was used for the domain, with smaller elements in the crucial area around the gauge nozzle. An image of the mesh is shown in Figure 8.4. Working from the findings by Lister *et al.* (2011), who performed a mesh sensitivity study and found ~40,000 to be sufficient, a similar target number was approached. The total elements varied between h/d_t values.

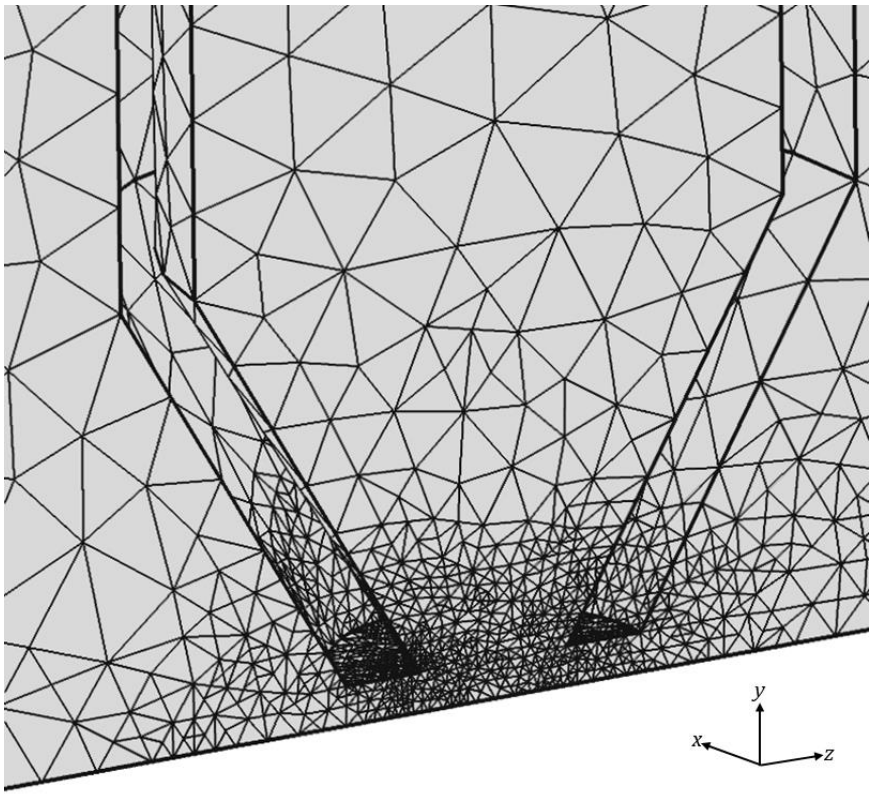

Figure 8.4. Image of the mesh in the area around the gauge nozzle.

8.5.4 Results

The simulation was run using an iterative solver, and reached a converged solution for each value of h/d_t within 15 minutes using an operating system with a dual-core 3.2 GHz CPU (*Intel*® Core™ i5) and 4 Gb RAM.

Calibration plot

Figure 8.5 shows simulated calibration plots of discharge coefficient against h/d_t for three different gauging flowrates. The data is plotted alongside experimental results for FDG over a 5 µm mixed cellulose ester membrane at similar conditions. The simulations predict a slightly lower gradient in the incremental region of the graph, and tend towards an asymptotic value of C_d more slowly. Discrepancies between the experiments and simulations could be attributed to the coarseness of the mesh, for which further refinements in the region around the gauge nozzle would be an appropriate solution. The limitations of the experimental apparatus, such as precision of h_0 and the flatness and alignment of the gauge nozzle tip and membrane, may also be partly responsible.

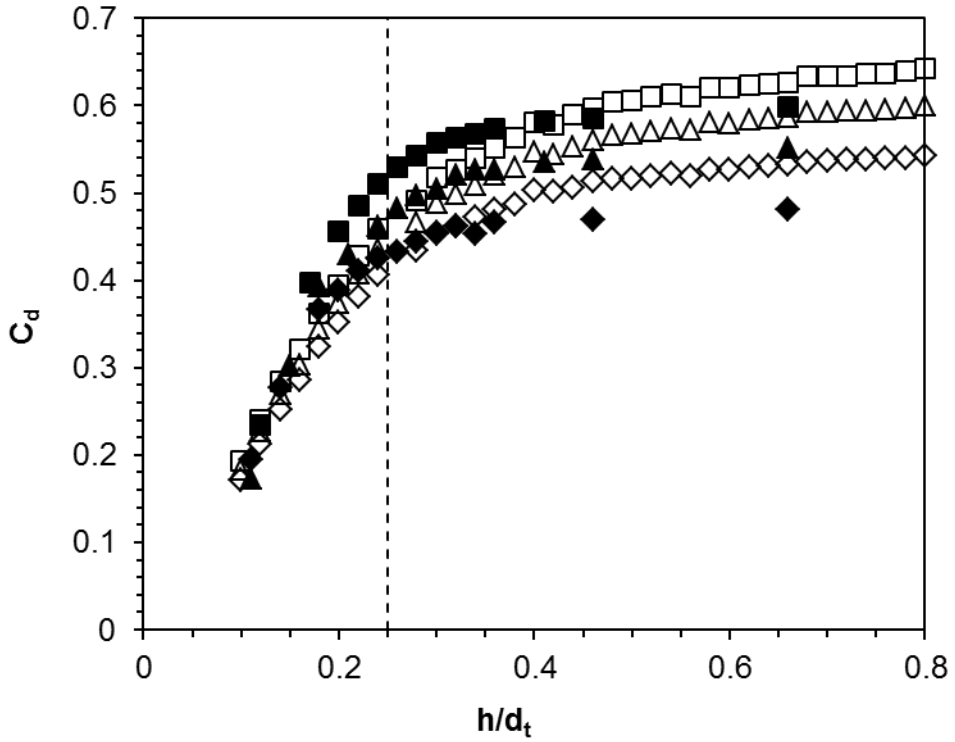

Figure 8.5. C_d vs. h/d_t for simulations (open symbols) and experiments (closed symbols), at gauging flows, mg, of 0.3 g·s-1 (diamonds), 0.4 g·s-1 (triangles), and 0.5 g·s-1 (squares). The dashed vertical line at h/dt = 0.25 represents the transition between the linear and asymptotic zone of the Cd curve. Experiments were performed as described in section 4.3.1, where TMP = 35 mbar and Reduct = 1000.

Shear Stress profiles

Shear stress profiles for the surface beneath the gauge, at $(x, y) = (0,0)$, are shown in Figure 8.6. The profiles predicted by CFD significantly under-predict fluid shear stress compared with the analytical model given by equation (2.38). Few data points are available along the z axis due to the coarseness of the mesh, however, these initial results are at least of a similar order of magnitude to the analytical model. Improvements to the accuracy of such estimations are detailed in later sections within this chapter, at this stage, however, the analytical model was deemed more appropriate than the CFD model for stress estimations when using the d_t = 1 mm gauge. As a result equation (2.38) was used to estimate shear stress in all destructive strength tests reported in Chapter 5.

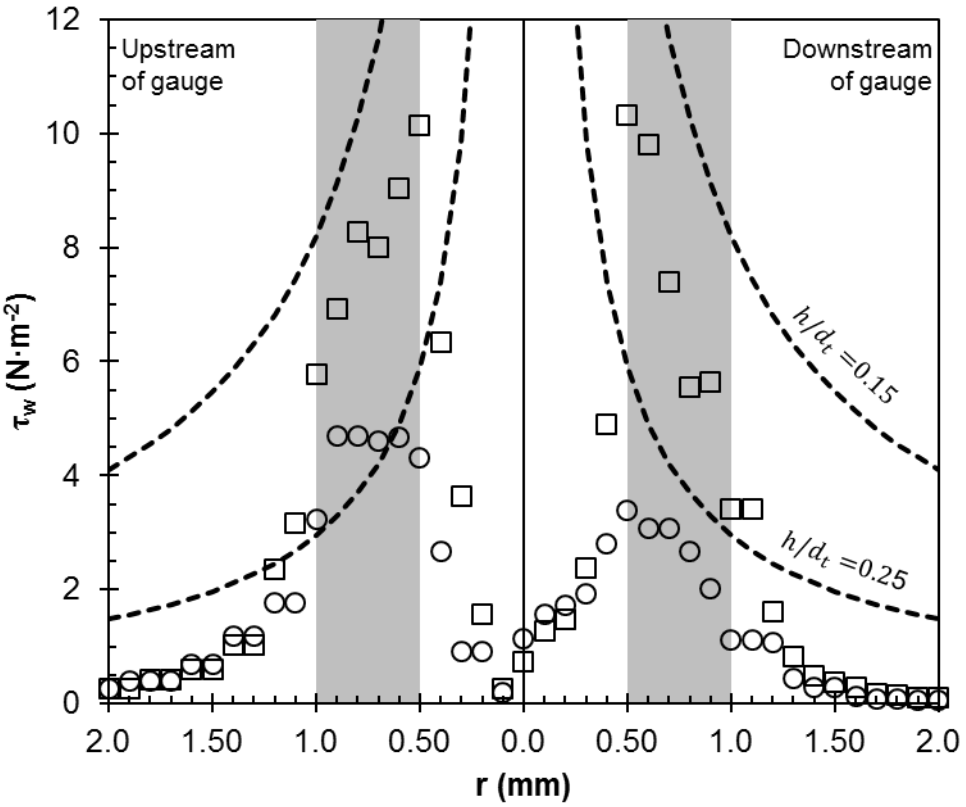

Figure 8.6. Simulated shear stress distributions at $h\ /\ d_t$ = (squares) 0.15, and (circles) 0.25 for data along the z axis. The central axis of the gauge is positioned where r = 0, and the shaded areas on the graph indicate the region directly under the gauge nozzle tip. The dashed lines indicate the stress predicted by equation (2.38) at the indicated clearance.

The shape presented by the data does, however, match well with the formation seen in the eroded region of the cake reported for ballotini particles in section 5.3.3. These indicated a ring of removed particles on the surface, which became deeper towards the inner edges of the nozzle, where r = 0.5 mm in this case. The presence of a

small pile of particles at the centre is explained by the reduction in shear stress in the centre of the graph in Figure 8.6 between the two shaded regions.

Effect on membrane flux

Figure 8.7 shows the local flux at the lowest h/d_t modelled. The flux profile clearly matches well with the shape of the gauge. From the figure, it can be seen that at the lowest gauge clearance, where $h/d_t = 0.06$, the flux through the membrane is reversed. Here the pressure drop caused by the clearance of the nozzle, Δp_{12} (as described in section 2.7.1) is greater than TMP, causing suction on the surface below the gauge orifice. The highest reverse flux is predicted to occur at the location just inside the inner edge of the gauge nozzle, as indicated by the darker region of the reverse flux profile at the centre of the diagram. Due to the small area in which reverse flux taxes place, the overall flux through the membrane remains unaffected. This would imply that a sensible minimum h/d_t used in experiments should be defined as that for which $\Delta p_{13} \leq TMP$.

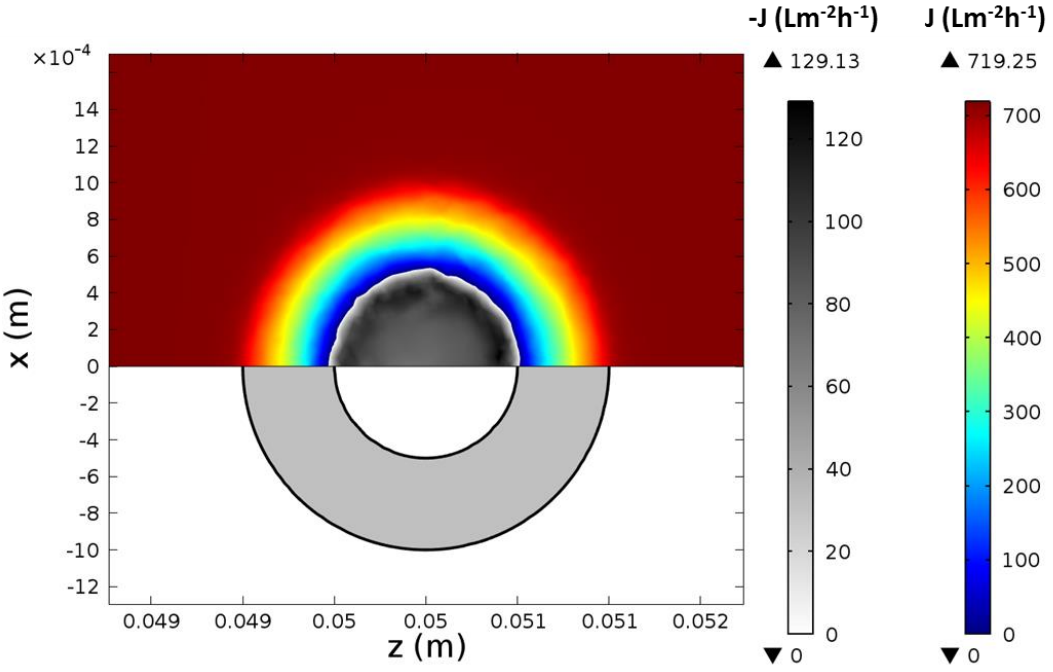

Figure 8.7. Flux through the membrane just below the gauge at $h/d_t = 0.06$. Positive flux, J, is plotted in colour, whilst reverse flux, $-J$, is plotted in black and white. The legends on the right hand side indicate these two quantities, with the maximum of each displayed above. The position of the region directly beneath the nozzle tip (as indicated by the region of interest in Figure 2.15 and shaded area in Figure 8.7) is indicated in the negative x-direction.

The same simulation was run with membrane flow boundary (iii) replaced with a non-slip wall boundary (i.e. no membrane flux). This yielded exactly the same results for C_d vs. h/d_t and the shear stress profile. It is therefore reasonable to conclude that,

despite the flux reversal shown in Figure 8.7, the operability of FDG over a membrane remains the same as for an impermeable surface.

8.6 Simulation 2: duct flow with d_t = 1 mm gauge (complete geometry)

This simulation was performed to investigate the effect caused by the 3 mm recess to the membrane in the duct flow apparatus, which is shown in Figure 4.1a. This model was also intended for use with membrane flow to formulate stress and Δp_{13} predictions for FDG, however due to the size of the domain and increased complexity of the geometry such simulations were not performed successfully. With the bottom surface modelled as a wall, with no membrane flux, C_d vs. h/d_t predictions were the same as observed in Figure 8.5.

Objective: *1*

Description:

The simulation domain, shown in Figure 8.8, comprised the entire test section geometry (less 25 mm from the entry and exit) used in duct flow experiments with the 1 mm gauge described in section 4.1. This included the 3 mm recess from the bottom of the duct entry to the membrane surface, and also accurately represented the shape of the membrane surface at the bottom of the test section. The total length, L, of the membrane along the central axis was 150 mm. No flow into the FDG gauge was modelled, so as to replicate the situation between successive readings when the gauge was withdrawn. This was the system used to monitor ballotini fouling in experiments described in section 4.3.3. No membrane flow was modelled.

8.6.1 Simulation parameters

The following parameters were used in this simulation.

Stationary parameters

Static pressure, p_{static} = 50 mbar

Fluid viscosity, μ = 0.001 Pa·s

Fluid density, ρ = 1000 kg·m^{-3}

Membrane resistance, R_m = 5×10^{10} m^{-1}

Bulk inlet flowrate, Re_{duct} = 1000

Dimensionless gauge clearance, h/d_t = 10 (h_0 = 10 mm)

(a)

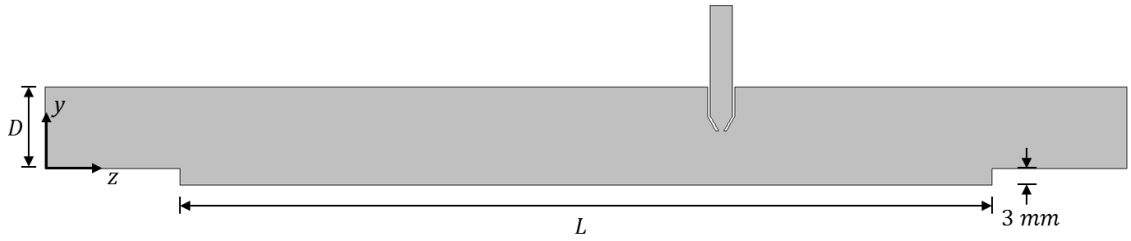

(b)

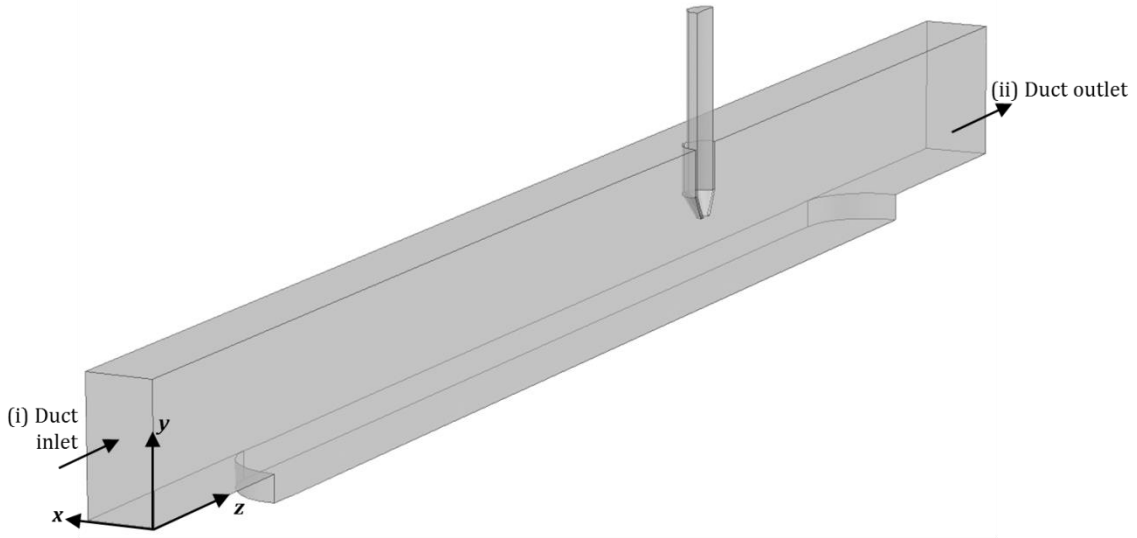

Figure 8.8. Computational domain used to investigate flow disturbance cause by the membrane and gauge positions. (a) shows a 2D view of the symmetry plane, and (b) shows a 3D view of the whole domain including labels for boundary conditions. The origin of the coordinate axes indicate the point where x, y, and $z = 0$.

8.6.2 Boundary Conditions

(i) Duct inlet, z = 0

Because the model did not consider membrane flow, inlet flow to the duct was specified directly using the laminar flow equation for a square duct (Gu *et al.*, 2009b):

$$w = \frac{16 w_{max} \left((x + 0.5D)\big(D - (x + 0.5D)\big) \right) y(D - y)}{D^4} \tag{8.14}$$

where:

$$w_{max} = 2 w_{av} = 2 \frac{\mu Re_{duct}}{\rho D} \tag{8.15}$$

Implicit in equation (8.14) is the assumption of non-slip walls at the edges of the inlet plane.

(ii) Duct outlet, z = 250 mm

This was defined as a pressure outlet:

$$p = p_{static} \tag{8.16}$$

which leaves velocity values unconstrained at all nodes except walls.

Symmetry, x = 0

The *zy*-plane at $x = 0$ was modelled as a plane of symmetry to halve the size of the domain and reduce computational load. The constraint applied on this boundary restricts flow normal to the boundary, which in this case is:

$$u = 0 \tag{8.17}$$

Walls, all remaining boundaries

The remaining boundaries which correspond to impermeable surfaces internal to the test cell i.e. the duct walls and gauge nozzle and tube. The condition here is:

$$\boldsymbol{u} = 0 \tag{8.18}$$

8.6.3 Finite element grid (mesh)

The meshing scheme used for this simulation was the same as for the previous, which used smaller elements around the gauge nozzle. Due to the increase size of the domain, however, the total number of elements was much higher, at 127,300.

8.6.4 Results

Resulting flow patterns and disturbance

The resulting streamline plot from this simulation, shown in Figure 8.9a, indicates some recirculation towards the inlet where flow reaches the sudden 3 mm recess to the membrane surface. The effect of this recess is more clearly seen by plotting the mean velocity, $|\boldsymbol{u}|$, which is given by:

$$|\boldsymbol{u}| = \sqrt{u^2 + v^2 + w^2} \tag{8.19}$$

This is plotted in Figure 8.9b on the symmetry boundary at the centre of the duct. This plot indicates a large dead-zone where flow is very slow (as indicated by dark blue shading) at the inlet side of the test section where it reaches the 3 mm recess to the

membrane surface. A smaller dead zone is also visible at the outlet end of the membrane surface.

In addition to this the FDG gauge also caused some disturbance to flow. This occurred both downstream of the gauge, where recirculation is evident in Figure 8.9a, and at the membrane surface where streamlines in (a) are marginally closer to the membrane surface beneath the gauge nozzle. This latter effect is evidenced more clearly in (b), where the higher velocity contours are closer to the bottom surface below the gauge.

(a)

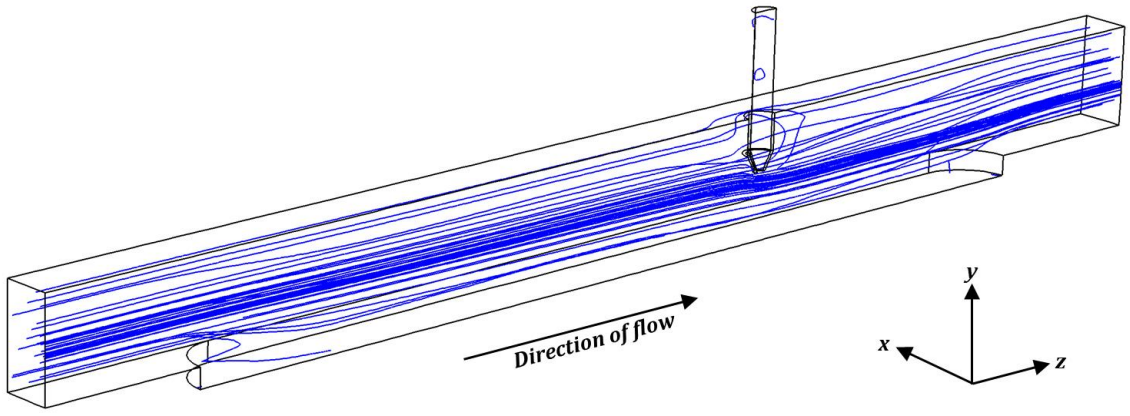

(b)

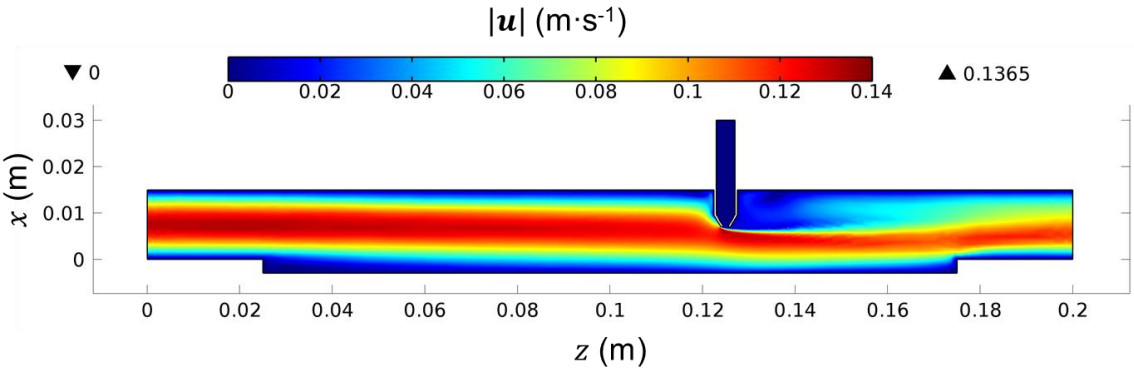

Figure 8.9. (a) Streamlines in the 3D domain, and (b) mean velocity profile at the symmetry plane down the centre of the duct. Flow moves in the positive z-direction.

Resulting surface stress

The fluid shear stress, τ_w, determined from this simulation on the bottom surface is shown in Figure 8.10. The highest stress predicted is 0.0394 N·m^{-2}, which is almost double that which occurs down at the centre-point at $z = 0.1$, $x = 0$. This occurs downstream of the FDG gauge. It is unsurprising, therefore, that in observations of yeast and ballotini fouling layer, described in sections 5.2.3 and 5.3.3, the fouling on the membrane surface was so uneven. In fact the shape seen in Figure 8.10 bears strong

similarity to the observed distribution of foulant on the membrane. (see Figure 5.6). It is therefore clear that, even with the gauge far removed from the membrane surface during the course of an experiment, FDG measurements of filtration cake thickness are representative of an area where higher stress occurs than along the rest of the membrane surface. This was taken into consideration when designing the new automated cross-flow apparatus described in section 6.2.

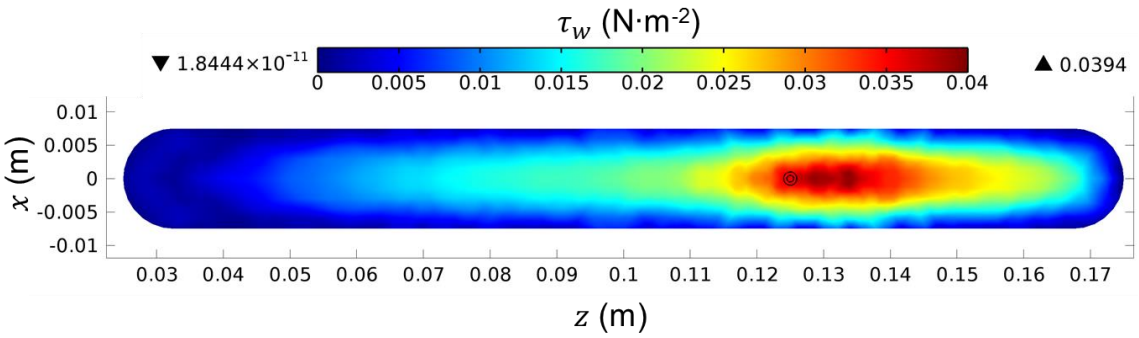

Figure 8.10. Fluid shear stress, τ_w, from simulation, along the bottom surface representing the membrane. The location of the FDG nozzle tip above the surface is indicated by the concentric circles. Flow travels in the positive z-direction.

8.7 Simulation 3: duct flow with d_t = 0.5 mm gauge

This simulation was performed in order to determine Δp_{13} vs. h/d_t profiles for the automated FDG apparatus, these were crucial to experiments because they turned out to be a more accurate method of determining the h_0 position than experimental techniques. In addition, it was used to predict shear stress profiles on the membrane surface and assess their viability in relation to the analytical model of equation (2.38).

Objectives: *5,7,8*

Description:

This simulation neglected the slightly recessed position of the membrane below the duct entrance (although in this case much less significant than for the original apparatus) when modelling the geometry for the domain, which is shown in Figure 8.11. A square duct of cross-section D = 15 mm and length of L = 150 mm was constructed with the gauge in the centre. The geometry of the gauge was matched to the design specifications shown in E. and Figure 6.1, where d_t = 0.5 mm, d = 3 mm, s = 0.25 mm, and α = 45°. The gauge position was matched to that of the existing rig, 75 mm down the length of the duct. Because, as described earlier, membrane flow was found not to affect C_d or τ_w predictions it was not modelled in this simulation so that solutions could

be reached more reliably. A parametric sweep was used to obtain results for a range of h/d_t values.

(a)

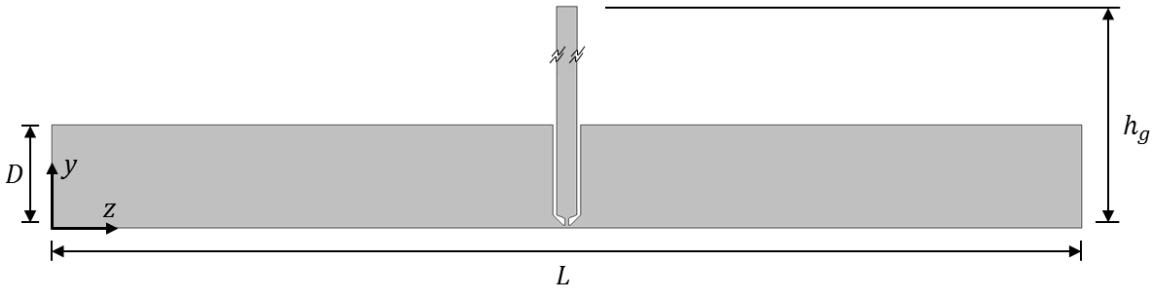

(b)

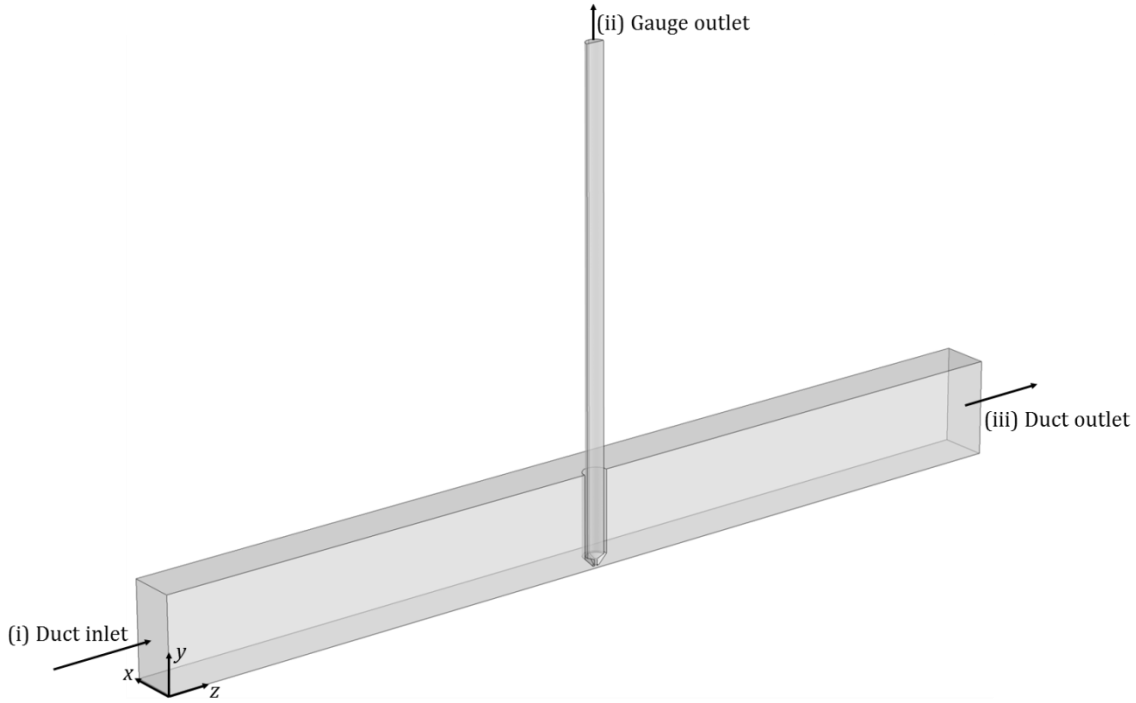

Figure 8.11. Computational domain used to model FDG in the new apparatus, shown in (a) 2D and (b) 3D with boundary labels. The origin of the coordinate axes indicate the point where x, y, and z = 0.

8.7.1 Simulation parameters

Stationary parameters

Static pressure, p_{static} = 100 mbar

Fluid viscosity, μ = 0.001 Pa·s

Fluid density, ρ = 1000 kg·m^{-3}

Duct flow Reynolds number, Re_{duct} = 1550

Gauging flowrate, m_g = 0.1 g·s^{-1}

Varied parameters

Dimensionless gauge clearance, h/d_t = 0.06-0.6

8.7.2 Boundary conditions

(i) Duct inlet

Because there was no need to model membrane flow, inlet flow to the duct was specified as described in equation (8.14):

$$w = \frac{16w_{max}\left((x+0.5D)\big(D-(x+0.5D)\big)\right)y(D-y)}{D^4} \tag{8.20}$$

(ii) Gauge outlet, y = h_g

Exactly the same as condition (ii) given in 8.5.2, the flow through the gauge is given by:

$$v = v_{max}\left(1-\left(\frac{2r}{d}\right)^2\right) \tag{8.21}$$

where $v_{max} = 2v_{av}$, and the average velocity, v_{av} is given by:

$$v_{av} = \frac{4m_g}{\rho(\pi d^2)} \tag{8.22}$$

and the radial distance from the centre of the gauge, *r*, is given by:

$$r = \sqrt{x^2+\left(z-\frac{L}{2}\right)^2} \tag{8.23}$$

For this boundary, the minimum h_g for flow stabilisation in the gauge tube was found to be 80 mm. This was performed where the flow stabilisation requires the greatest distance, at the lowest nozzle clearance where h/d_t = 0.06.

(iii) Duct outlet, z = L

This was defined as a pressure outlet, with no other constraints to the velocity variables.

$$p = p_{static} \tag{8.24}$$

Symmetry, x = 0

The *zy*-plane at $x = 0$ was modelled as a plane of symmetry, with the condition:

$$u = 0 \tag{8.25}$$

Walls, all remaining boundaries

The remaining boundaries are considered to be impermeable non-slip surfaces, for which the condition is:

$$\boldsymbol{u} = 0 \tag{8.26}$$

8.7.3 Mesh

The meshing scheme described in section 8.5.3 was improved upon for these simulations to provide improved accuracy, in light of the smaller gauge dimensions used. The meshing in the region near the gauge nozzle is displayed Figure 8.12 The methods by which this was achieved are detailed below.

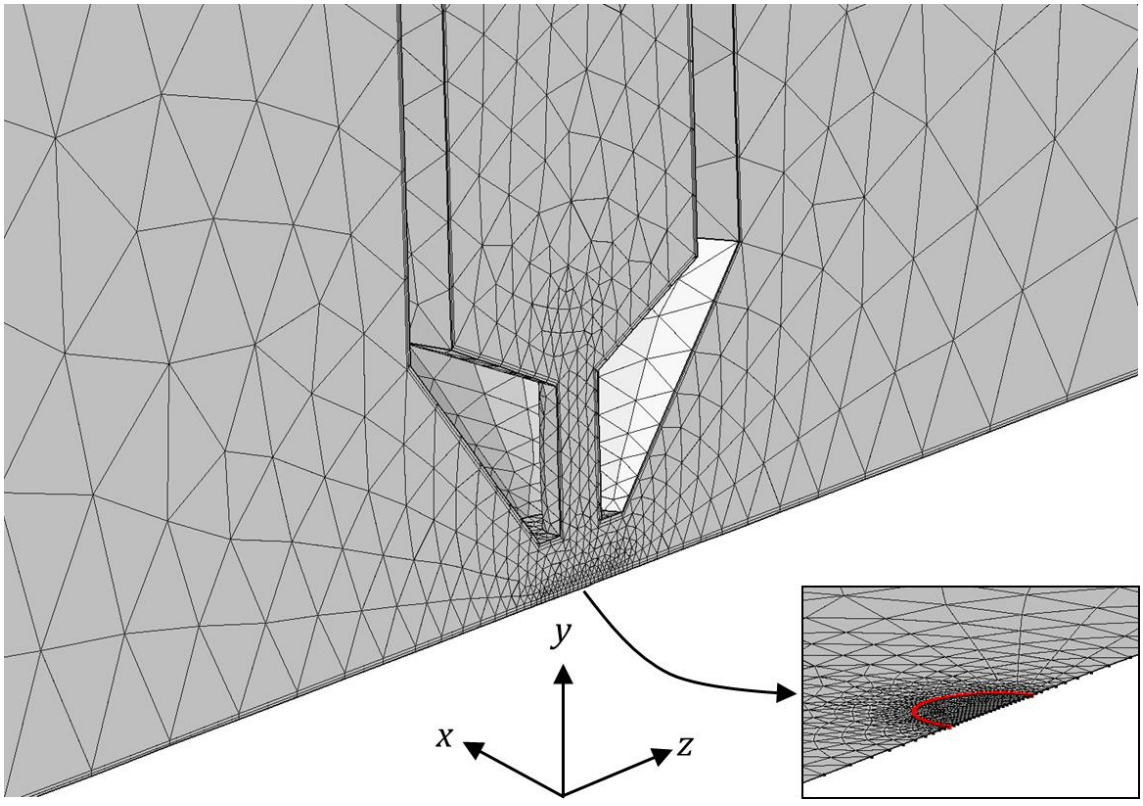

Figure 8.12. Mesh configuration around the FDG nozzle region. (inset) semi-circular area directly beneath the gauge on the bottom face (where $y = 0$), wherein maximum mesh element size was constrained. The highlighted curve indicates the boundary line for this region.

Sizing and refinement

Due to the inclusion of a parametric sweep for the geometry parameter h/d_t, the mesh needed to be reconstructed for each individual simulation. The mesh element density at the gauge nozzle was controlled by specifying size parameters for a semi-circular region on the surface just below it (see Figure 8.12). Such parameters include maximum and minimum vertex length, and maximum element growth rate.

Boundary layers

Mesh refinements were carried out perpendicular to wall surfaces in the simulation. Two extra 10 µm layers were used, ensuring at least two mesh elements between the gauge tip and the surface below for all values of h/d_t.

8.7.4 Results

Post-processing methods

The solutions did not converge at h/d_t values of 0.28, 0.31, and 0.35-0.37. This did not affect other results, and still provided ample data for a calibration plot of Δp_{13} vs. h/d_t. Pressure values at the inlet (i) and gauge tube exit (ii) boundaries were obtained by averaging p across the nodes on each boundary. Δp_{13} was obtained by calculating Δp_{34} using equation (2.35), where l_{eff} was taken to be the exact distance between the top of the tapered section of the nozzle and boundary (ii).

Three additional radial lines were plotted at 45° (clockwise) intervals on the bottom surface ($y = 0$) – where 0° is located upstream along the z axis – from the centre

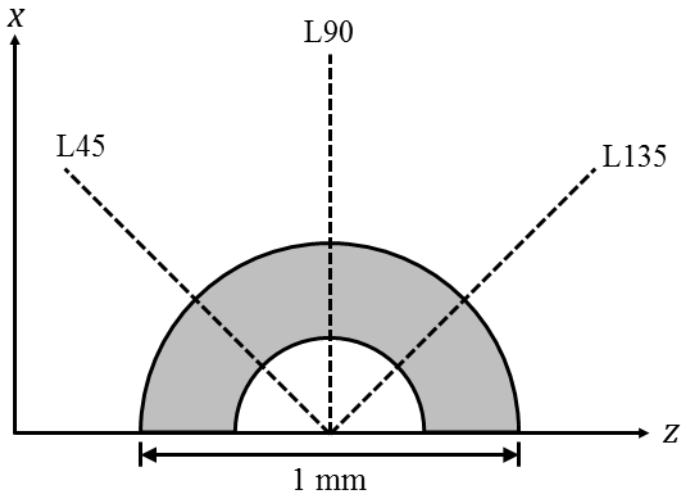

Figure 8.13. Positioning of the additional radial lines on the y = 0 plane plotted during post-processing. The shaded region represents the position of the gauging nozzle. Each line is 1 mm long.

of the gauge nozzle at $x = 0$, $z = L/2$, to a radial position 1 mm from this point. The positioning of these lines, hereafter referred to as L45, L90, and L135, is shown in Figure 8.13.

Shear stress values were obtained using the formula:

$$\tau_w = \mu\dot{\gamma} \tag{8.27}$$

where the shear rate, $\dot{\gamma}$, is calculated within COMSOL from the strain rate tensors, ε_{ij}, in 3D space (where i is the direction normal to the surface, and j is the direction of tensor movement). At the membrane surface this corresponds to the resultant vector from τ_{yx} and τ_{yz}. Stress values on the membrane surface for lines L45, L90, L135, and along the *z* axis were exported, along with a full set of *z*, *x*, τ_w data representing a value for every mesh node.

Calibration plot

Figure 8.14 shows the results of this simulation plotted alongside some selected sample data representing calibrations performed prior to fouling experiments. Each set of sample data has been offset in the *x* and *y* directions, as in the experimental procedure

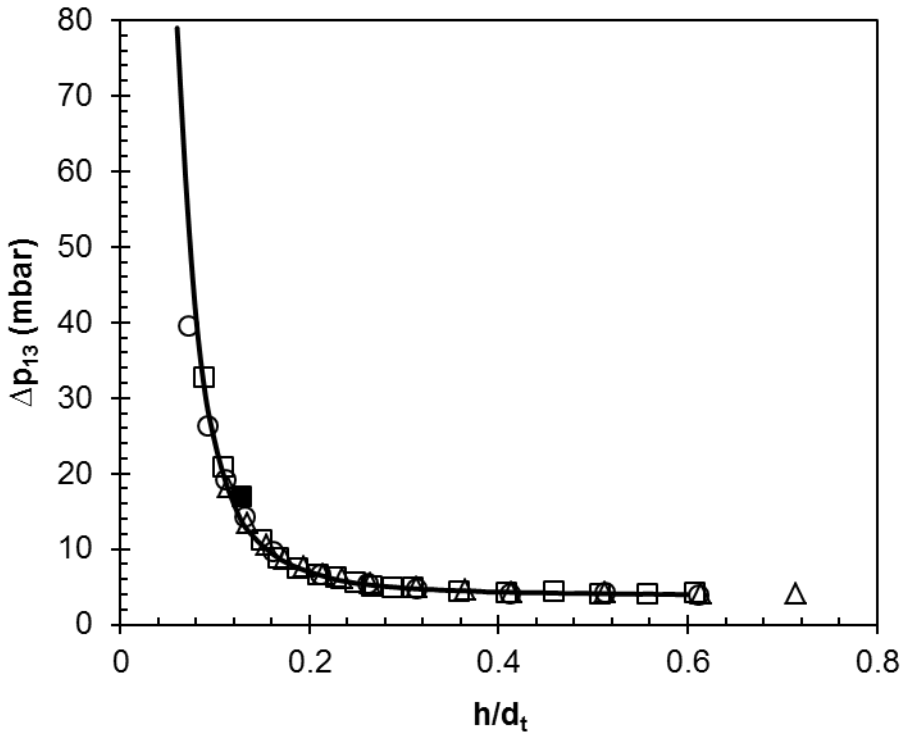

Figure 8.14. 3D simulation results (solid line) plotted against 3 randomly selected membrane calibrations (open symbols) at conditions matching those simulated. Error bars are contained within the symbols. The filled square symbol shows an outlier.

described in 6.6.2, such that a good fit is achieved. The resulting Δp_{13} vs h/d_t profiles show great repeatability and match closely with the curve obtained using CFD. Aside from the outlier at $h/d_t = 0.13$ (indicated by the filled square), the difference in h/d_t between data points and the CFD curve was less than 0.01, corresponding to 5 µm, for all cases where $h/d_t < 0.3$. Using Matlab, a spline was fitted to the CFD data, which was used to infer h/d_t values from Δp_{13} for fouling data. This was also used to correct h_0 values recorded by the apparatus (section 6.6.2).

Surface stress distributions

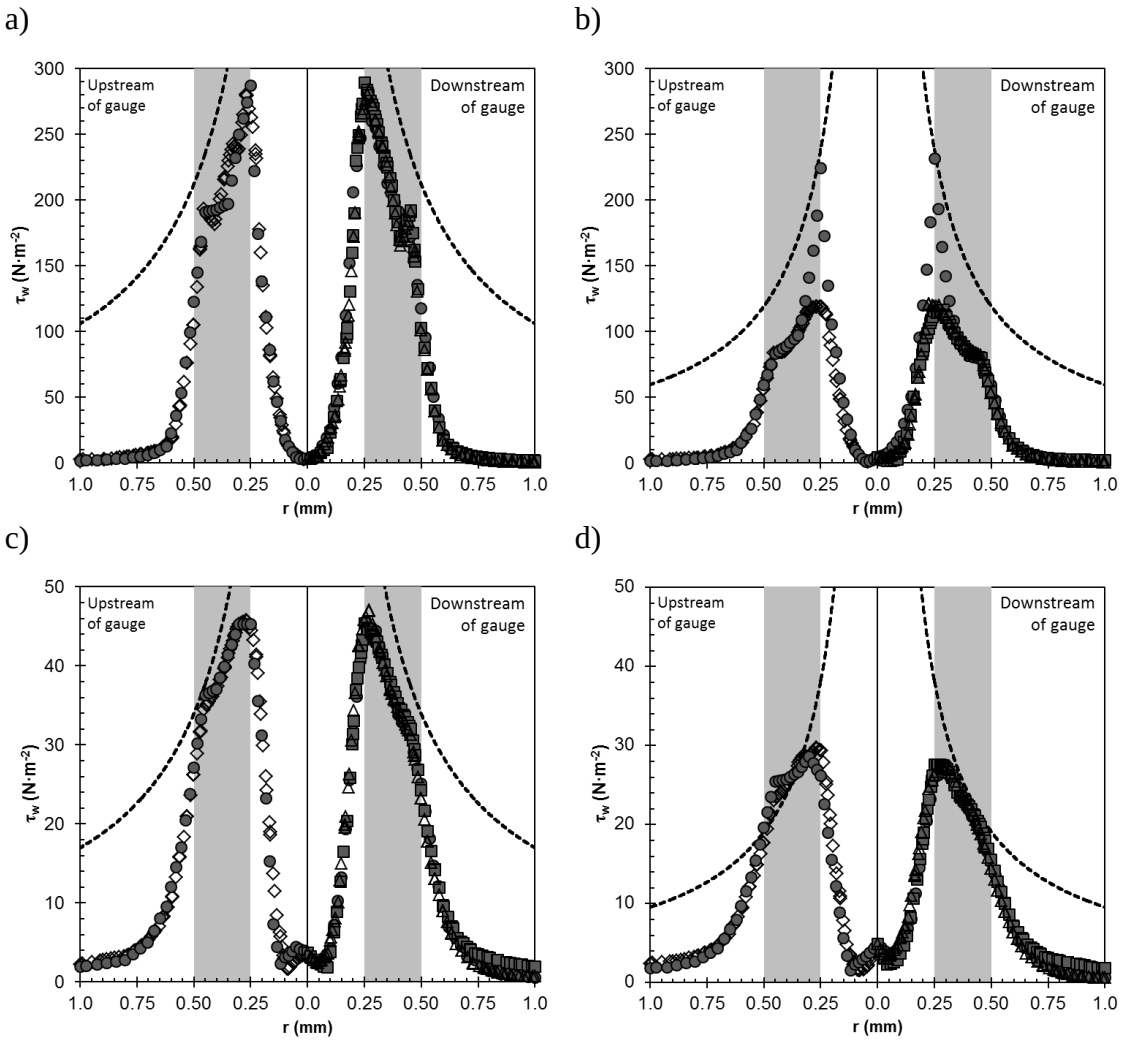

Figure 8.15. Simulated shear stress distributions at h/d_t = (a) 0.06, (b) 0.08, (c) 0.15, and (d) 0.2. Stresses are plotted for lines L45 (open diamonds), L90 (closed squares), L135 (open triangles), and along the *z* axis (closed circles). The central axis of the gauge is positioned where r = 0, the shaded areas on the graph indicate position of the bottom edge of the gauge nozzle. The dashed lines indicate the stress given by the equation (2.38) at the same clearance.

Simulated surface shear stress, τ_w, is shown in Figure 8.15 for h/d_t values of 0.06 (the lowest simulated clearance), 0.08, 0.15, and 0.20. It is clearly evident in graph (a) that the shear stress predicted by equation (2.38) is higher than that estimated using CFD. In fact the maximum stress, $\tau_{w,max}$, which occurs near the inner edge of the gauging nozzle ($r = d_t/2$), is around 290 N·m^{-2} for simulated data, but equation (2.38) actually predicts a value of 424 N·m^{-2} at this position. From Figure 8.15 and Figure 8.16 it is evident that the gap between the simulation and analytical solution narrows as h/d_t increases, which is demonstrated for the full set of data in Figure 8.17a. This makes sense because at a lower clearance the system is more accurately represented by equation (2.38).

The gap reduces with increasing clearance in both magnitude and as a percentage of the simulation result. Where $h/d_t > 0.4$, $\tau_{w,max}$ predicted by simulations actually becomes slightly larger than the analytical prediction. For most values of h/d_t, the stresses along the L90, L135, and downstream *z* axis lines (plotted on the downstream side) match quite closely to each other, with the maxima also occurring at

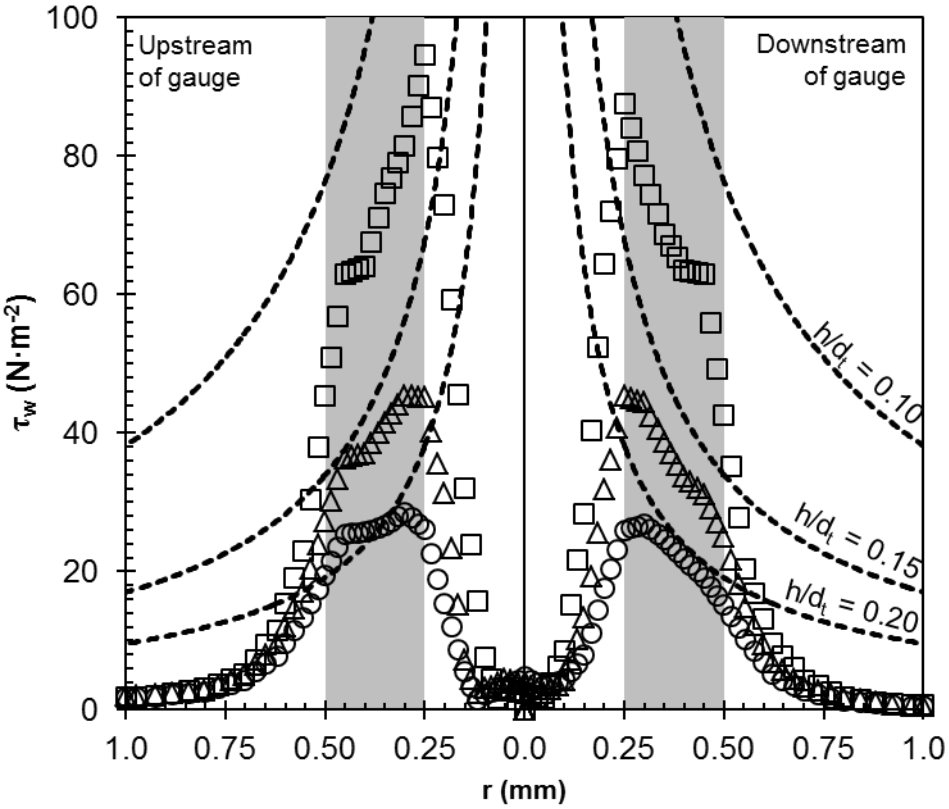

Figure 8.16. Simulated shear stress distributions at h/d_t = (squares) 0.10, (triangles) 0.15, and (circles) 0.20 for data along the *z* axis. The central axis of the gauge is positioned where r = 0, the shaded areas on the graph indicate position of the bottom edge of the gauge nozzle. The dashed lines indicate the stress given by equation (2.38) at the indicated clearance.

approximately the same place and value. The upstream values also indicate very similar maximum stresses to those downstream.

In exceptional cases (e.g. Figure 8.15b), data along one or more of these plot lines did not show such good agreement with the rest of the data, specifically where h/d_t = 0.07, 0.08, and 0.09, and to a lesser extent in a few others. This is likely to be a combined effect of the relatively low mesh density and the way in which a solution is found. To conform to the continuity (8.1), and Navier-Stokes (8.2) equations, an improbable, yet converged solution may be achieved. In this case it appears as though small areas of high localised converging flow are predicted by the simulation. In the case of Figure 8.15b this occurs along the *z*-axis, however this is not the case for the other two exceptions.

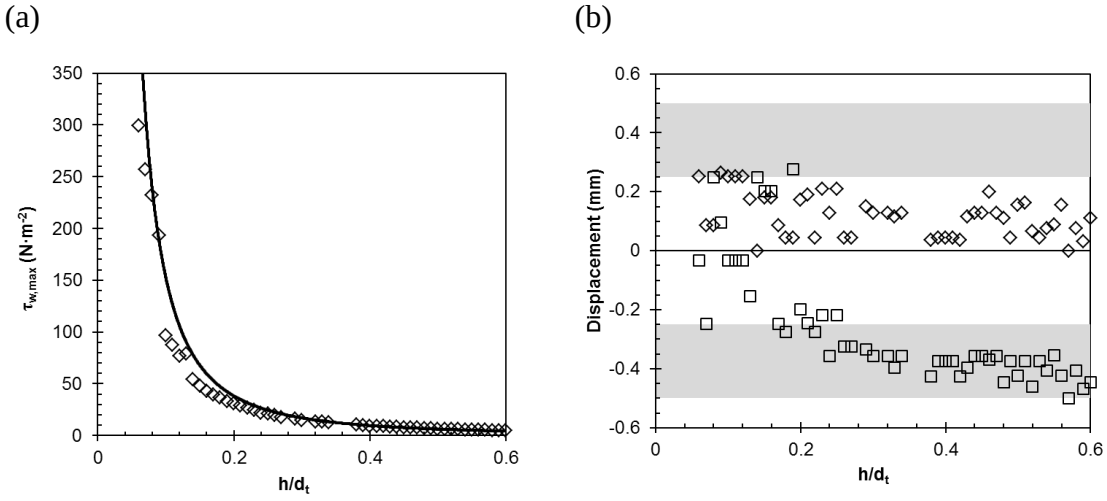

Figure 8.17. 3D simulations results for (a) maximum shear stress (symbols) against prediction by equation (2.38) (solid line). (b) *x*-wise (diamonds), and *z*-wise (squares) displacement of maximum shear stress, $\tau_{w,max}$, from central axis of the gauge. The shaded regions in (b) indicate the area under the nozzle rim (in terms of the x and z Cartesian coordinates).

Analysis of the full set of surface data demonstrates this effect more clearly. Figure 8.19 shows surface plots for stress shear stress at h/d_t values of 0.06, 0.07, 0.08, and 0.09. The stress appears even all around the peak of the plot for h/d_t = 0.06 (a), however in the subsequent 3 plots (b-d) there are outlying single peaks. Whether this occurs or not can to some extent be predicted by inspection of Figure 8.17a, wherein the maximum shear stress, τ_w, predicted by simulations appears to follow a rough inverse-square curve, deviating further from the analytical model of equation (2.38) at lower h/d_t values. Those values which appear to deviate from the apparent trend in the data tend to present a less even stress distribution around the peak of the 3D surface plots of the type shown in Figure 8.19.

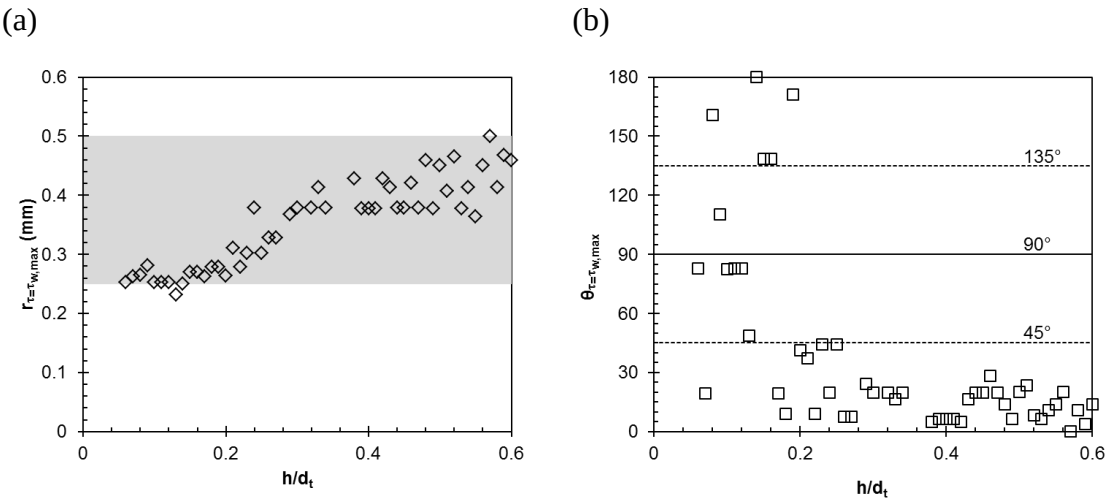

Figure 8.18. Cylindrical coordinates of $\tau_{w,max}$ against h/d_t. (a) shows r-coordinate, $r_{\tau=\tau_{w,max}}$, with the gauge nozzle rim indicated by the shaded region. (b) shows the displacement angle, $\theta_{\tau=\tau_{w,max}}$, measured from the *z*-axis downstream of the gauge (see Figure 8.13).

The small peak on the outer edge of the volcano-like formation shown in Figure 8.19a is due to an entry effect related to the inertia of fluid reaching the surface below the gauge and changing direction. This is more pronounced for lower h/d_t values. Such effects cannot be predicted by equation (2.38), which assumes stokes flow and does not account for entry and exit effects to the region considered. The *z*, *x* position of $\tau_{w,max}$ is also indicative of the deviations from equation (2.38) caused by entry and exit effects. Figure 8.17b highlights how this position varies in both the z- and x-wise displacement from the centre of the gauge. While no clear trend can be seen for the x displacement, which is scattered between 0 and 0.25 mm, $\tau_{w,max}$ occurs further upstream as h/d_t increases. The corresponding cylindrical coordinates to these are shown in Figure 8.18. (a) demonstrates how, at higher h/d_t, $\tau_{w,max}$ occurs further from the gauge centreline. Its position remains near the inner edge of the nozzle at $h/d_t < 0.2$ until a transition point in the region $0.2 < h/d_t < 0.25$, after which point it occurs further out, towards the outer edge. From (b) it is evident, as with Figure 8.17b, that this maxima occurs upstream, which can be attributed to flow in the *z*-direction within the duct.

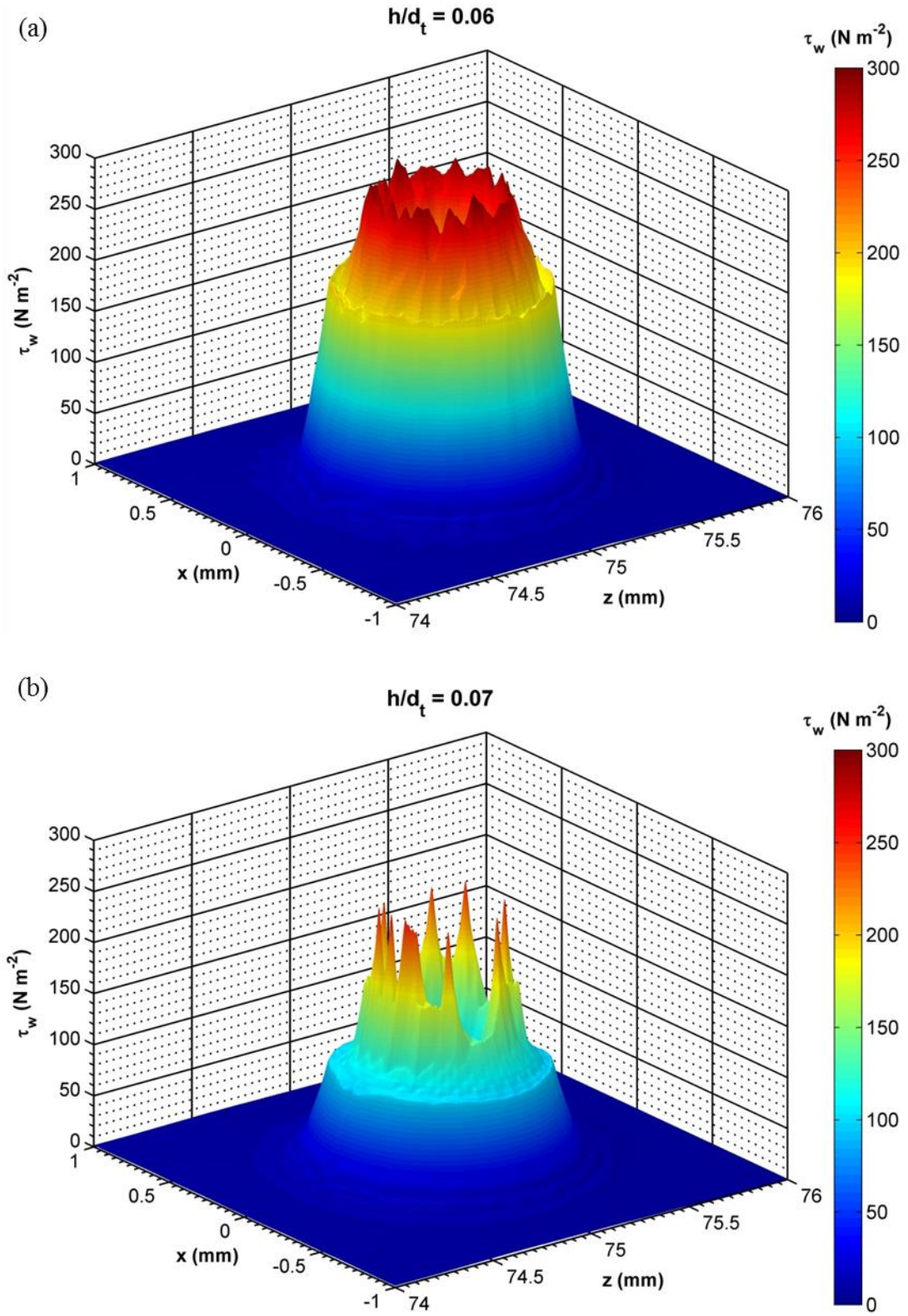

Figure 8.19. 3D surface plots of simulated shear stress, τ_w, on the membrane surface at h/d_t = (a) 0.06, (b) 0.07, (c) 0.08, and (d) 0.09. The magnitude of the stress is represented by both the colour and the height. Data is mirrored across $x = 0$, and smoothed using an interpolation method built into Matlab®. Here the central axis of the gauge ($r = 0$) is at $x = 0$, $z = 75$ mm.

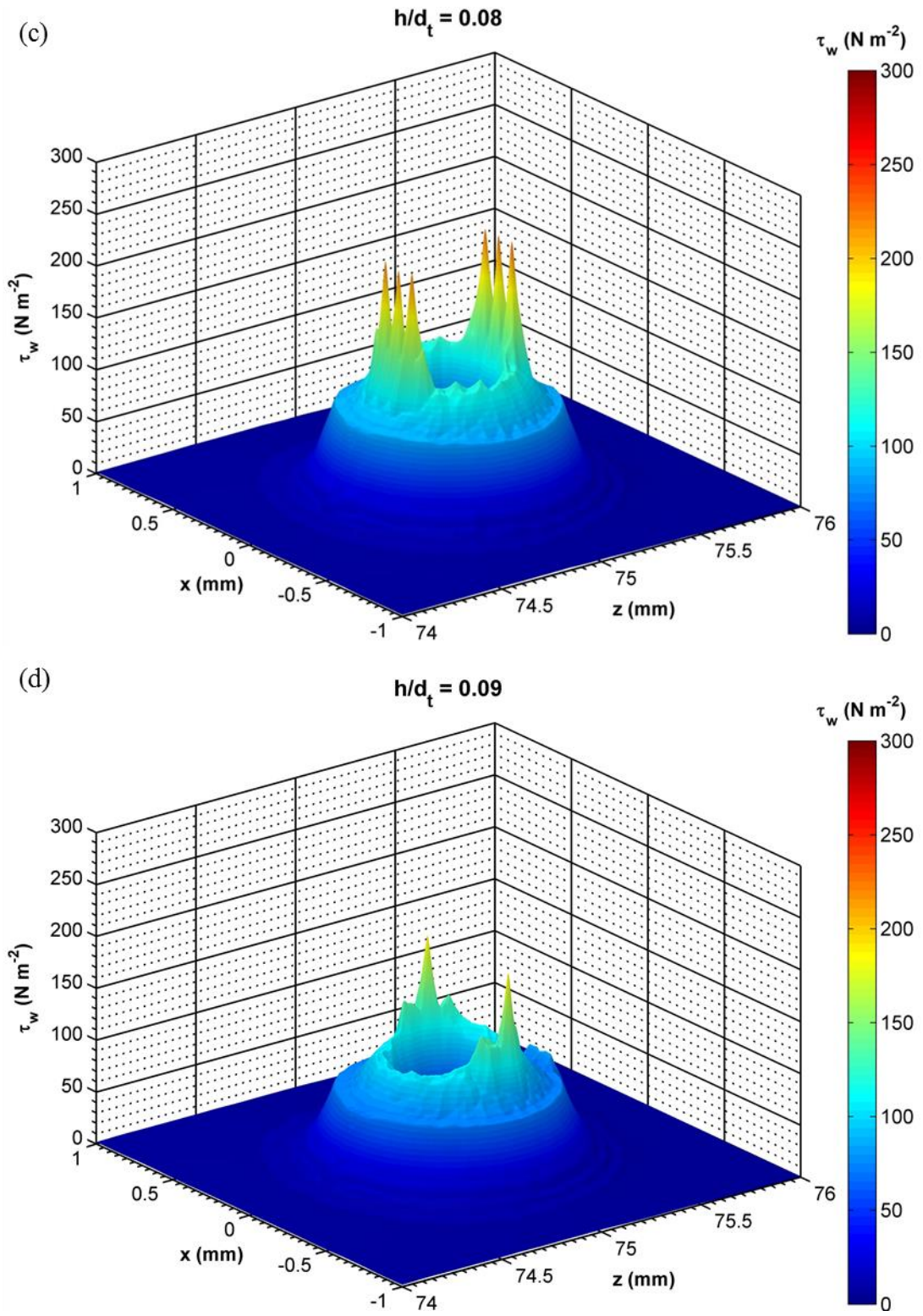

Figure 8.19. 3D surface plots of simulated shear stress, τ_w, on the membrane surface at h/d_t = (a) 0.06, (b) 0.07, (c) 0.08, and (d) 0.09. The magnitude of the stress is represented by both the colour and the height. Data is mirrored across x = 0, and smoothed using an interpolation method built into Matlab®. Here the central axis of the gauge (r = 0) is at x = 0, z = 75 mm.

Comparison with fouling layer

The eroded region observed after destructive strength testing of lignin filter cakes, displayed in Figure 7.20, shows remarkable conformity with the shape of the shear stress profiles described here. There is significant erosion of the fouling layer in the region directly below the tip of the gauge nozzle; but in the centre, above the orifice, there remains a thicker layer of cake. This conforms inversely to high and low stress regions indicated by 3D plot in Figure 8.19.

8.7.5 Conclusions

A very good match is achieved between simulated pressures and those recorded in experiments, once experimental data is adjusted for systematic error. This means simulation data can be used confidently for calibration plots and adjustment for h/d_t correction. There is strong evidence to suggest that the analytical solution of equation (2.38) employs too many assumptions to make it valid for estimating surface stress in this FDG set-up, however some doubt is cast on the accuracy of results from this 3D model. The considerable scatter shown in Figure 8.17b and Figure 8.18 shows a somewhat oscillatory pattern. This is characteristic of a sub-optimal meshing scheme, where mesh elements are becoming stretched, then split, as the geometry of the simulation domain changes with increasing h/d_t. The discrete high-stress peaks in 3D plots (Figure 8.19b-d) also suggest a strong influence of the mesh on the converged solution.

From this it is possible to conclude that, for the purpose of accurate τ_w predictions, a denser mesh would be required, so that equations (8.2) and (8.1) are linearized across smaller distances where the greater velocity gradients occur. Unfortunately this was not possible in the current 3D simulation, as increasing the mesh density resulted in failed simulations. These failures are potentially a result of poor mesh quality at specific h/d_t values, or due to software and/or hardware limitations. A convenient simplification to the simulation would be to make it axisymmetric. While not true of the conditions within the apparatus, it is not a completely unreasonable assumption in the context of estimating stress at lower h/d_t, as Figure 8.15 shows reasonable symmetry about the centreline of the gauge. The use of axisymmetric simulations is assessed in the next section.

8.8 Simulation 4: 2D Axisymmetric flow with d_t = 0.5 mm gauge

This simulation was performed to identify the differences between stress, τ_w and gauging pressure, Δp_{13} predictions when working with a 2D axisymmetric coordinate frame rather than in 3D Cartesian. This method allows for a much finer mesh to be developed, which should lead to more accurate results.

Objectives: *6,7,8*

Description:

In this model only the area immediately surrounding the gauge is considered. As before, the exact gauge geometry is modelled, as specified in the design documents (appendix E.) and section 6.2.1. Using a 2D axisymmetric model allowed for a much greater mesh element density, and hence more accurate and detailed results. The domain modelled is shown in Figure 8.20. Membrane flow was not considered in this simulation in order to make a direct comparison to simulation 3. Again a parametric sweep was used to run this simulation for a range of h/d_t values from 0.02 to 0.8.

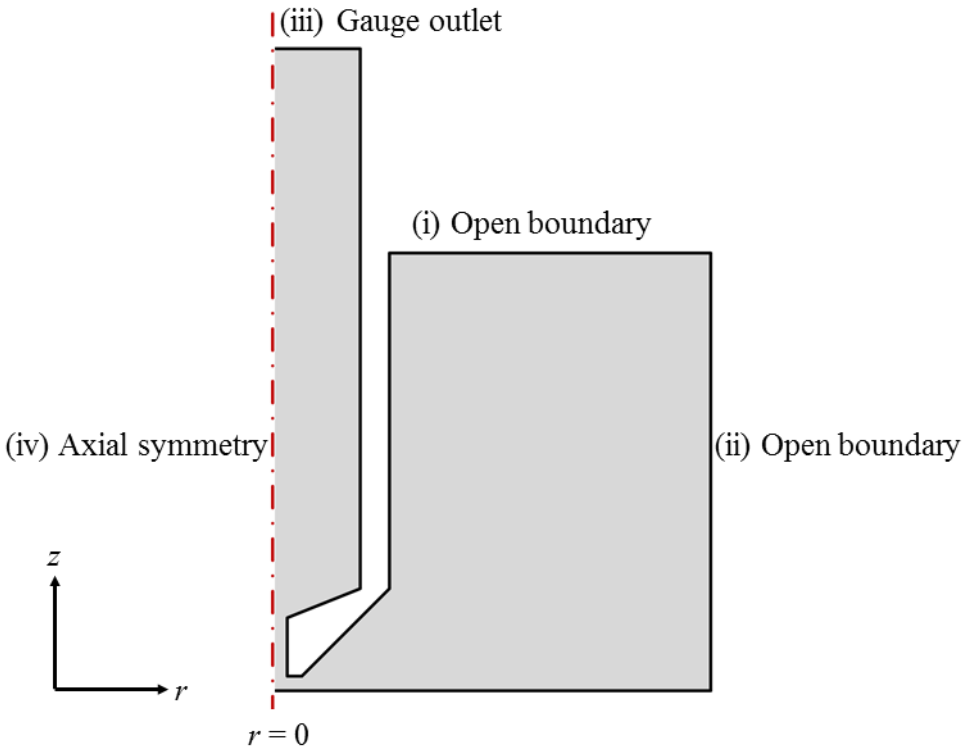

Figure 8.20. Axisymmetric domain modelled in this simulation

8.8.1 Simulation Parameters

Stationary parameters

Static pressure, p_{static} = 100 mbar

Fluid viscosity, μ = 0.001 Pa·s

Fluid density, ρ = 1000 kg·m^{-3}

Duct flow Reynolds number, Re_{duct} = 1550

Gauging flowrate, m_g = 0.1 g·s^{-1}

Varied parameters

Dimensionless gauge clearance, h/d_t = 0.02-0.8 in 0.001 steps

8.8.2 Boundary Conditions

A diagram of the domain modelled in this simulation is shown in Figure 8.20, where boundaries (i) to (iv) are labelled, and all remaining boundaries are modelled as non-slip, impermeable walls.

(i) Open boundary, r = d_o/2 to D/2, z = D/2

An open boundary condition was used, such that velocity vectors were completely unconstrained along the boundary. The only constraint applied was of a constant pressure:

$$p = 0 \tag{8.28}$$

This boundary condition represents a fluid plane in the centre of the duct, so fluid can move freely across it in any direction.

(ii) Open boundary, r = D/2

This condition was specified identically to (ii), again representing a fluid plane. Technically this would not be true for the walls of the duct, however in similar simulations, Chew *et al.* (2004a) have reported negligible effects when changing how boundaries (i) and (ii) operate (i.e. walls, non-slip planes or inlets). Thus the use of a free boundary in this case should be justified for both this and (i).

(iii) Gauge outlet, z = h_g

Exactly the same as condition (ii) given in section 8.7.2, the flow through the gauge is given by a laminar flow equation:

$$v = v_{max}\left(1 - \left(\frac{2r}{d}\right)^2\right) \tag{8.29}$$

As in section 8.7.2, the value of v_{max} is derived from m_g, which is 0.1 g·s^{-1}. h_g was also found through the same methodology as in the 3D simulation. Here h_g was $200d_t$.

(iv) Axial symmetry, r = 0

The constraint applied on this boundary prevents flow across it:

$$u = 0 \tag{8.30}$$

Walls

All other surfaces were modelled as non-slip impermeable surfaces, so:

$$u = 0, \qquad w = 0 \tag{8.31}$$

8.8.3 Mesh

A very fine, unstructured triangular mesh was used throughout the domain, with constraints in place to ensure particularly small elements around the important area in the region of the FDG nozzle. Vertex lengths along the base of the nozzle, and the area from $r = d_t/2$ to $r = d_t$ on the surface below, were constrained to a maximum of 1 µm. Those on the walls of the nozzle, and at locations $r = 0$ to $d_t/2$ and $r = d_t$ to $r = d_t + s$ were constrained to a maximum of 5 µm, as were the lines on the bottom surface from $r = 0$ to $d_t/2$, and $r = d_t$ to $d/2$. Additionally, 3 boundary element layers of 0.5 µm each were fixed to all walls. The overall mesh, and a close-up view of the area around the gauge are shown in Figure 8.21.

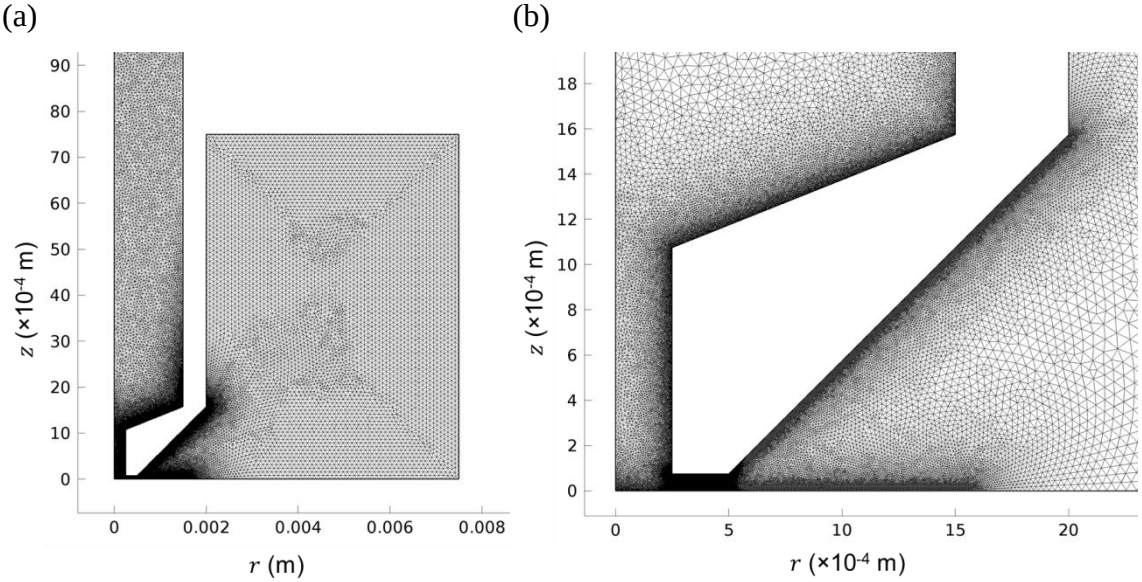

Figure 8.21. Mesh structure for a simulation where h/d_t = 0.15. (a) shows the whole domain except for the gauge tube (which is too tall to show here), and (b) shows a close-up view of the structure around the gauge nozzle. Dark patches indicate areas where mesh density is higher.

The resulting meshes ranged from approximately 160,000 (at $h/d_t = 0.6$) to 188,000 (at $h/d_t = 0.8$) total elements, depending on the h/d_t value. Due to the simplifications of a 2D simulation and the boundary conditions used in this study, solutions converged much faster compared with the 3D simulation.

8.8.4 Results

Calibration plot

The 2D simulation results for Δp_{13} vs. h/d_t did not match those for the 3D data directly, as shown in Figure 8.22a. The shapes of the two curves in this figure are very similar however. The 3D data was offset along the Δp_{13} axis by -0.81 mbar, which gave the minimum average absolute difference (0.011) in h/d_t between the two data sets; this adjusted plot is shown in Figure 8.22b. One might posit that the 0.81 mbar discrepancy might be due to the asymmetry of the system and arise from pressure drop along the duct before the gauge in the 3D model, however this is not the case. The pressure drop along the duct in simulation 3 was found to be only about 0.02 mbar at the location of the gauge.

(a)

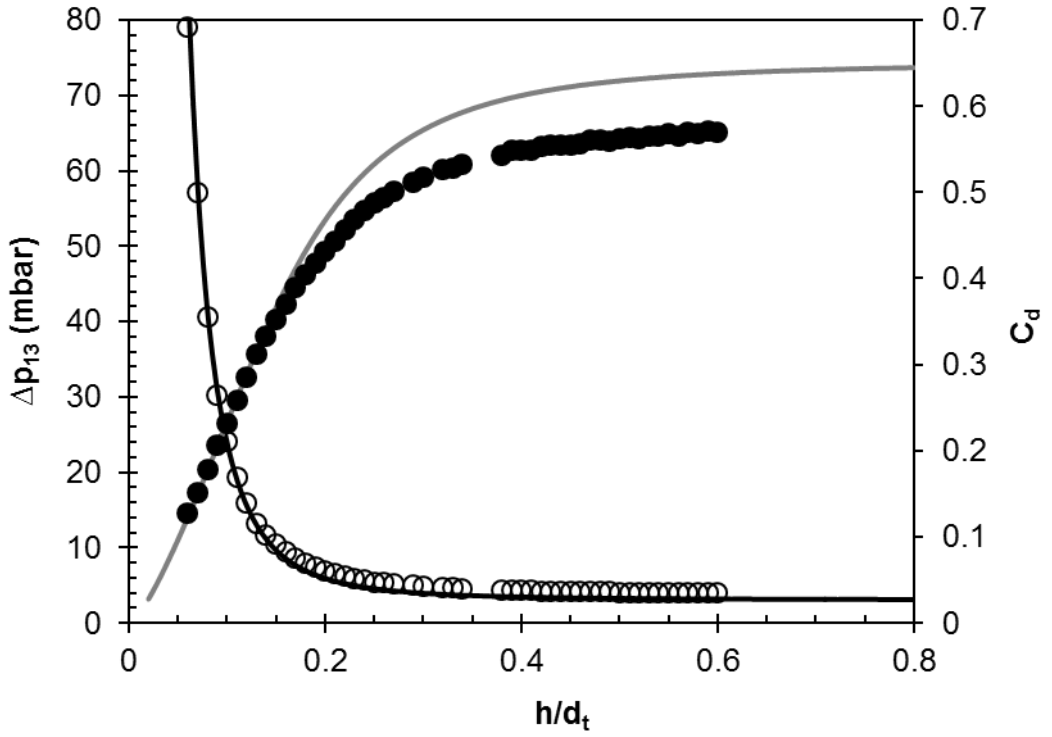

Figure 8.22. 2D (lines) and 3D (symbols) simulation results for Δp_{13} (black lines, open symbols) and C_d (grey lines, closed symbols) versus h/d_t. (a) shows data prior to Δp_{13} adjustment, and (b) shows data from 3D simulations (as reported in Figure 8.14) for which Δp_{13} has been reduced by 0.81 mbar.

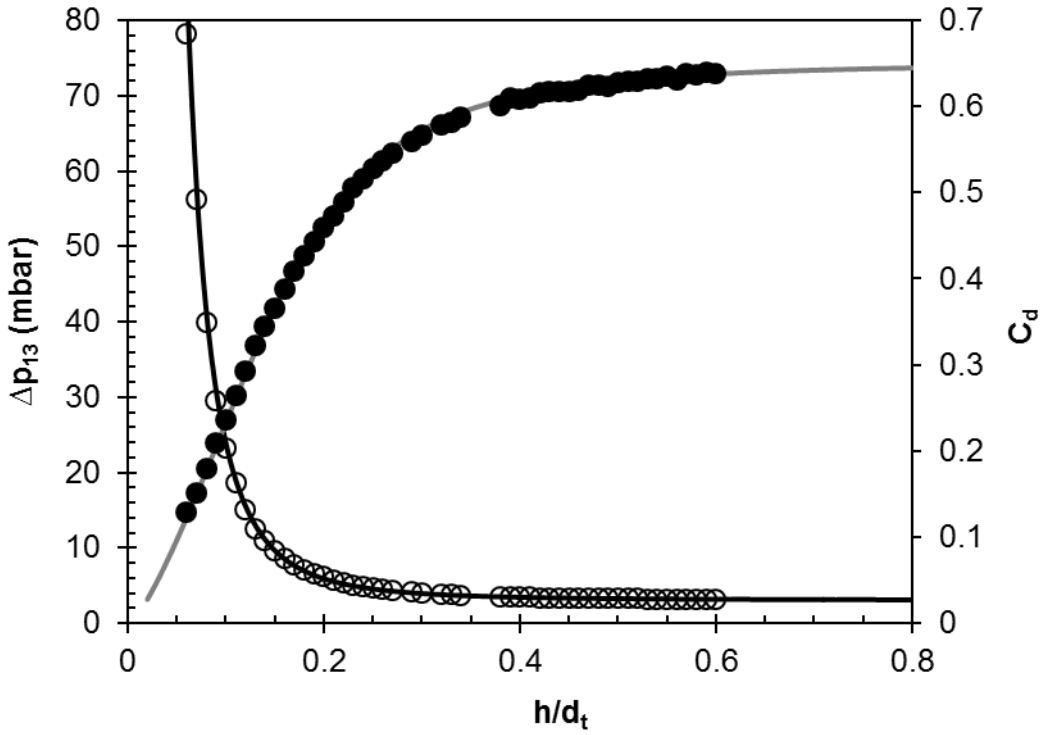

Figure 8.22. 2D (lines) and 3D (symbols) simulation results for Δp_{13} (black lines, open symbols) and C_d (grey lines, closed symbols) versus h/d_t. (a) shows data prior to Δp_{13} adjustment, and (b) shows data from 3D simulations (as reported in Figure 8.14) for which Δp_{13} has been reduced by 0.81 mbar.

Shear stress, τ_w profiles

Looking at the estimates for shear stress at the surface it becomes immediately obvious why this increased pressure drop arises, given that the shear stress on the tip of the nozzle and the surface below accounts for the pressure drop Δp_{12} (see section 2.7.1). The stress predicted by 3D simulations was considerably lower than the analytical prediction of (2.38). By contrast, results shown in Figure 8.23 show that τ_w predicted by this axisymmetric simulation actually exceeds it around the middle of the nozzle region. Hence in the 3D simulations it appears as though the pressure drop, Δp_{12}, in the region between the tip of the gauge nozzle and the surface below, has been consistently underestimated.

Despite clear discrepancies between local stresses underneath the gauge, the maximum stress predicted by the simulation for each h/d_t is similar to that predicted by the analytical model at $r = d_t/2$. In Figure 8.25a the dashed black line representing the analytical model of equation (2.38) is almost identical to the grey line showing the simulation results. $\tau_{w,max}$ from equation (2.38) was consistently higher than that predicted in this 2D simulation, however for all values where $h/d_t > 0.06$ the difference is negligible, at less than 4 N·m^{-2}. This difference, as a percentage of the

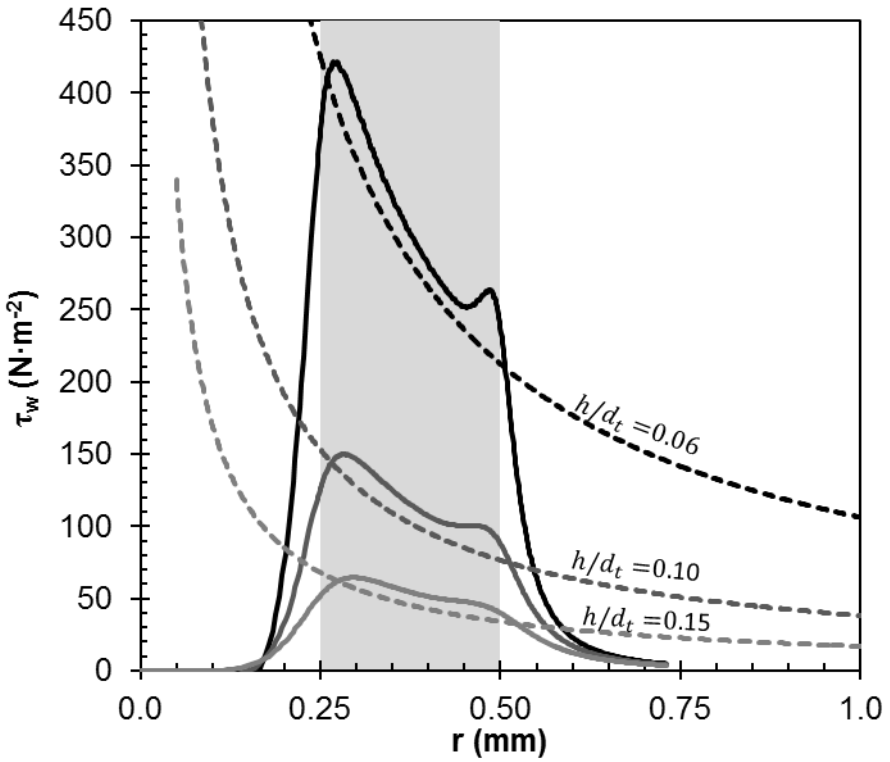

Figure 8.23. 2D axisymmetric simulation results for τ_w vs. r at h/d_t = 0.06 (black), 0.10 (dark grey), and 0.15 (light grey). Dashed lines indicate the analytical prediction of equation (2.38). The shaded region indicates the position of the nozzle tip above the surface.

simulation value, increases with h/d_t however. This is likely to be due to exit effect near the inner edge of the gauging nozzle, where flow direction changes from radial to axial, moving into the nozzle orifice. This presents in Figure 8.23 as a drop from the peak shear stress within the shaded area which represents the surface below the tip of the gauge nozzle. The reason behind this is indicated in the streamline plots of Figure 8.24. As Chew *et al.* (2004a) have previously noted, the small peak in shear stress seen in Figure 8.23, which occurs where $r \approx d_t + s$ (i.e 0.5 mm), is due to inertial effects as fluid enters the suction region between the nozzle tip and the surface below. In Figure 8.24a there is significant flow convergence towards the nozzle which must carry momentum through the suction region, which will increase the shear rate as it enters. (b) shows a more detailed view of the suction region and nozzle tip. The streamlines diverge from upwards in the z–direction before reaching the inner edge of the nozzle throat (where $r = 0.5d_t$).

This simulation also demonstrates the shifting of this peak more clearly than the 3D simulations. Here Figure 8.25b shows how the position at which $\tau_{w,max}$ occurs varies with h/d_t. For 2D simulations, the trend seen is almost one of two distinct linear regions, transitioning at around $h/d_t = 0.3$. The slightly scattered nature of the 2D

results is most likely due to shifting mesh density (described in section 8.8.3), although the reason behind the general trend here is not entirely clear.

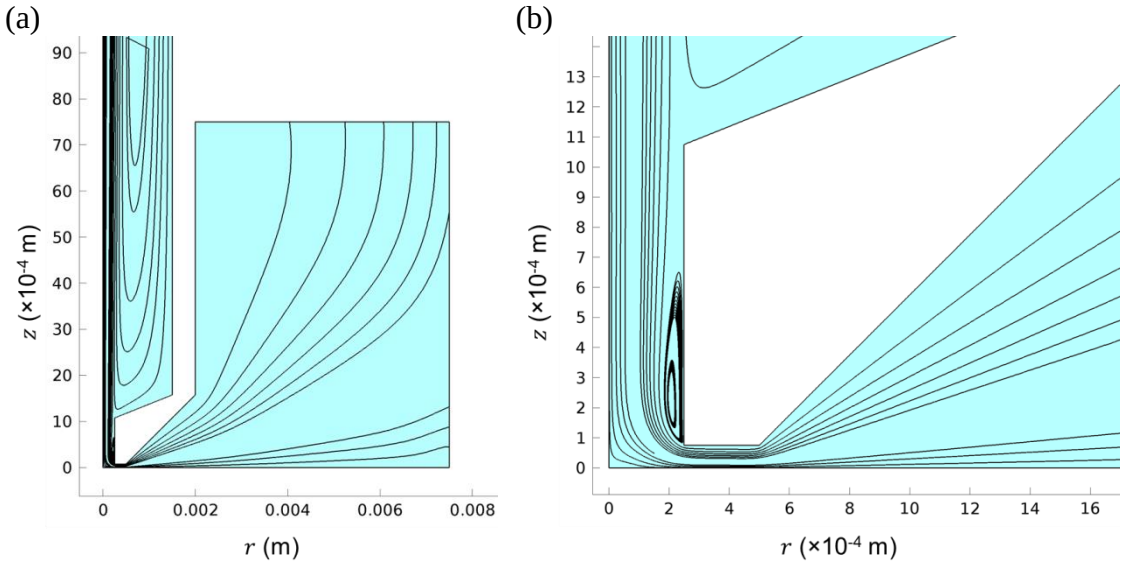

Figure 8.24. Streamlines for a simulation at $h/d_t = 0.15$ showing (a) flow streams from the free boundaries and recirculation in the gauge tube downstream of the nozzle, and (b) close-up of the flow patterns around the tip of the gauge nozzle. The fluid domain has been shaded to indicate the position of the flow boundaries more clearly.

It would be reasonable to assume that the results of the 2D simulation should be more accurate than those of the 3D one due to the much higher mesh density employed. In this case, as opposed to the 3D simulations, the analytical solution of equation (2.38) appears to be a reasonable approximation for maximum shear stress on the surface below the gauge. Despite this, it does not accurately predict the local stress variation in this area, due to entry and exit effects in the gauging region.

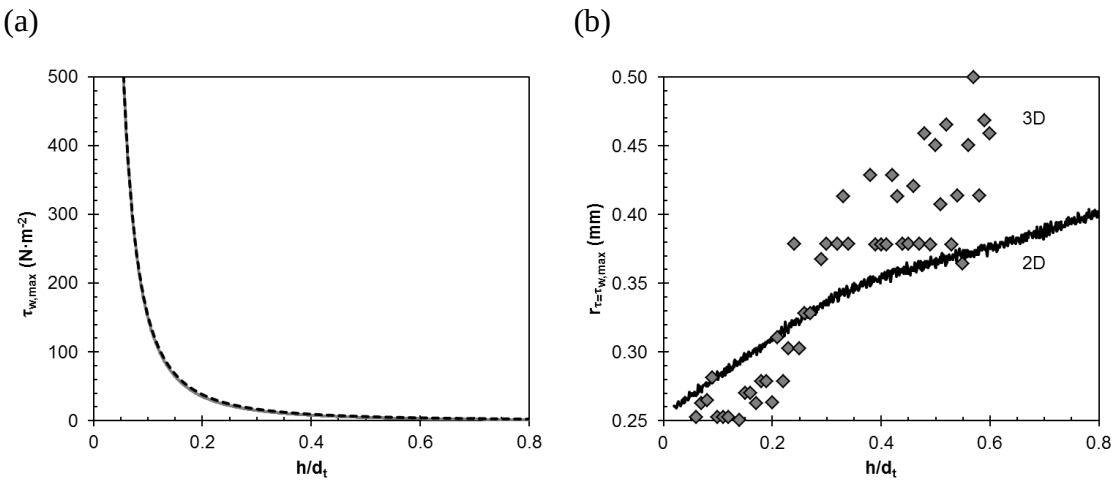

Figure 8.25. (a) Simulation (solid grey) and analytical (dashed black) predictions for $\tau_{w,max}$ at varying h/d_t and (b) r-coordinate, $r_{\tau=\tau_{w,max}}$, at which this occurs in 2D (line) and 3D (symbols) simulations, where the position of inner edge of the gauge nozzle is bound by the vertical axis limits.

It is therefore necessary to question the validity of the equation (2.38) in terms of both its assumptions and whether it can be reproduced in COMSOL. For the former: all simulation results meet the criteria for creeping flow set by equation (2.39), with the maximum value of this dimensionless group being 1×10^{-4} when h/d_t=0.3. Stress estimates above this clearance value are of little use, because they are outside the region wherein accurate thickness measurements can be made. The latter is evident by the increasing conformity to equation (2.38) as h/d_t decreases and equation (2.39) becomes increasingly applicable.

8.9 Conclusions

Early 3D simulations for the d_t = 1 mm gauge showed that it is reasonable to assume no membrane flow in further simulations, which allowed them to be solved much more easily. 2D and 3D numerical simulations of FDG for the 0.5 mm gauge have demonstrated very good agreement with experimental data. The predictions of 3D simulations for Δp_{13} vs. h/d_t proved reliable for calibrating the gauge position relative to a surface, where experimental techniques proved insufficient due to the minute scale of movement required to do so.

3D simulations were inappropriate for determining shear stress imposed on the surface beneath the gauge during thickness and strength measurements because of limitations to mesh size. Critical analysis of the analytical model of equation (2.38) indicated that it does not accurately describe the shear stress distribution on the surface below the gauge due to entrance and exit effects around the gauging region and inertia effects. Despite this it does provide a reasonable estimate for maximum shear stress, however not for the radial position at which it occurs.

Unfortunately simulations for FDG are not yet at a point where stresses can be reliably estimated for a duct flow environment. To achieve this would require simulations with a much higher mesh density, which would require more computing power and more advanced adaptions to the solution algorithms. Alternative CFD packages such as ANSYS Fluent, CFX, or OpenFoam may also achieve less computationally intensive solutions.

Chapter 9: Conclusions and Future Perspectives

9.1 Implementation of FDG

Fluid dynamic gauging has been successfully applied to microfiltrations of four different types of suspension with various cellulosic membranes, namely:

1. Yeast, a food-type foulant, filtered through a mixed cellulose ester membrane;
2. Ballotini, an ideal suspension of inert hollow silica spheres of uniform size, filtered through regenerated cellulose membranes;
3. Lignin, a sticky substance which forms large and small agglomerates, filtered through regenerated cellulose membranes; and
4. Mixed foulant, a mixture of lignin and ballotini in suspension, filtered through regenerated cellulose membranes.

During the course of these experiments the technique of FDG for membrane filtrations was refined, and led to an improved apparatus which was constructed between filtration of suspensions 2 and 3. A summary of the findings from these filtrations studies is given below.

9.1.1 Yeast, filtered by mixed cellulose ester membranes

In these initial studies, transient thickness data was produced using two different methods (M2 and M3). Significant fouling of the membrane was found to occur very quickly, accompanied by a sharp rise in cake thickness; both of which reached a near steady-state within about 10 minutes of commencing the filtration. M2, wherein the gauge height, h_0, was adjusted with cake growth, was found to provide more reliable thickness estimates across the entire range of cake thickness. M3, in which the gauge was maintained at a constant clearance, showed much better characterisation of initial growth. On application of destructive strength tests, M1, to preformed fouling layers, it was found that the constant thickness measurement systems of M2 and M3 caused significant interference with cake growth. This was confirmed by visual analysis of the fouling layers. As a result, a different method for estimating transient cake thickness was employed in subsequent ballotini filtrations.

9.1.2 Ballotini filtered by regenerated cellulose membranes

Transient thickness studies were performed for two types of ballotini suspension. One of these (110P8) contained mostly neutrally buoyant particles, and the other

(60P18) contained larger, mostly buoyant particles. As with the yeast filtration the flux declined rapidly at first, tending towards a near steady-state. This was coupled with an initially sharp increase in cake thickness, which levelled off towards a steadier limiting thickness. The cake thicknesses observed in these experiments were much greater than for yeast filtrations and flux declined at a much slower rate. Comparisons were made between experiments at different cross-flow velocities (CFVs) and TMPs. The results indicated that varying the CFV within the laminar flow region had little or no influence on flux, however an increased CFV resulted in a thicker cake developing on the membrane surface. TMP was found to increase cake thickness and flux, as well as the time taken to reach a steady-state cake thickness.

Comparison between the 110P8 and 60P18 suspensions showed a thicker cake developed during filtration of the smaller, neutrally buoyant particles. The flux also declined further when filtering these particles and a steady-state cake thickness was reached more slowly. These phenomena were all deemed congruent with current theory.

Attempts were made to reduce disturbance to cake growth by performing thickness measurements periodically, keeping the gauge retracted from the surface in-between readings. Destructive strength tests of preformed filter cakes, along with cross-sections of extracted cakes, indicated that there was still interference with the fouling layer during filtration, resulting in significant underestimation of transient cake thickness. The initial thickness readings provided by destructive tests were found to produce a reasonable estimate for cake thickness.

Highly uneven deposition was observed on the membrane surface due to the filtration rig geometry, which cast some doubt over the trends observed for ballotini and yeast filtrations. This was taken into account when designing a newer FDG apparatus for cross-flow membrane filtrations.

9.1.3 Lignin filtered by regenerated cellulose membranes

Cross-flow fouling experiments using a suspension of Kraft lignin were performed using the newer, automated FDG apparatus. The problem of uneven fouling across the membrane surface was significantly reduced, allowing for gravimetric analyses of fouling layers. The technique for measuring transient cake thickness was also refined, resulting in much more reliable estimates.

The results of lignin fouling experiments showed an interesting contrast to the previous work. Here the flux decline was severe early on; but cake growth did not follow the same pattern, and thickness increased significantly without a corresponding

drop in flux. The reason for this was concluded to be due to either pore fouling or a thin fouling layer formed close to the membrane surface with a much higher resistance than the rest of the cake layer. Further analysis estimated the resistance due to this phenomenon. Resistance estimates were also made for a flowing layer which was easily removed by cross-flow at zero-flux. The resistance of this flowing layer was found to be more significant for filtrations at higher transmembrane pressures.

Destructive thickness testing yielded evidence of a persistent layer 10-20 μm thick on the membrane surface, which was irremovable under the highest fluid shear stress applied by the gauge. There was also indication that the resilience of the cake at higher thicknesses increased with filtration time up to a limiting thickness between 60 and 100 μm, above which it seemed more easily deformable.

9.1.4 Mixed foulant systems filtered by regenerated cellulose membranes

Although no improvement to overall flux was observed as a result of combining ballotini with lignin in the filtered suspension, there appeared to be some reduction in the shear stress required to remove the fouling layer from the membrane surface. Although the results were not conclusive, this is a novel area of study and warrants further investigation.

It was also possible to produce a layer of ballotini particles on the membrane surface prior to the lignin, which rejected most of the lignin particles during the filtration. This opens up new possibilities for pre-treatment for membrane filtrations. Instead of attempting to functionalise membranes for anti-fouling properties, inert particles could be modified and used to foul the membrane surface. This would create a replenishable, modified filtration surface, and increase the versatility of a membrane filtration unit.

9.1.5 Use of mathematical models

FDG was used to investigate the viability of the models discussed in section 2.5. Both the particle capture (section 2.5.2) and inertial lift (section 2.5.3) models were found to significantly underestimate the stress required to remove the fouling layer – the former to a much greater degree than the latter. This was proposed to be a result of the inter-particle interactions within a pre-formed fouling layer which are not considered in these models.

The most useful analysis for cross-flow filtrations was the more general critical flux model (section 2.5.1) for cross-flow filtrations derived by Field *et al.* (1995). This

demonstrated a remarkably good prediction of the extent of pore-blocking phenomena in lignin filtrations, and also demonstrated clearly that the flux decline during ballotini filtrations was, as should be expected, due to cake development.

9.2 Limitations of current apparatus

The newer FDG apparatus described in section 6.2 featured significant improvements over the older one (described in section 4.1), in terms of operability, automation and control. The membrane was positioned such that a more uniform flow over the surface could be expected, and the implementation of a smaller gauge nozzle reduced flow disturbance while providing a higher precision for thickness measurements. Automated calibrations and gauge adjustments built into the control system also greatly reduced the time required to conduct experiments.

There are still a number general limitations to the use of the new system however. These include limits to operating conditions, as well as more fundamental aspects of the FDG procedure which are crucial to understanding fouling mechanisms.

9.2.1 Operating conditions

Limiting ranges to operating conditions and their reasons are provided below.

Transmembrane Pressure

Reading: 30-370 mbar

Operating: 30-1000 mbar

The minimum transmembrane pressure is currently limited by the hydrostatic pressure of fluid above the test section as it returns to the feed tank. Theoretically it would be possible to operate at lower TMP, by controlling flux from the permeate side. Another limit applies however, wherein gauging pressure, Δp_{13} should not exceed TMP, as this will reverse membrane flow. By setting a minimum h/d_t of 0.15, for which Δp_{13} = 10.35 mbar, a sensible absolute minimum TMP would therefore be 15 mbar, however this would limit destructive strength tests.

The maximum measurable TMP is limited by a differential transducer (*Omega*, PX26-005DV). With a different pressure transducer it would be possible to read higher transmembrane pressures. The unit has been leak tested up to 1 bar. Use at pressures above this risks detaching the viewing window, and is likely to force fluid through the seals of the test section.

One caveat of this limit is that with the current set-up, fast fouling rates will be accompanied by an increase in TMP. This will be more significant as the following ratio increases:

$$\frac{JA_m}{Q_{duct}} \tag{9.1}$$

where Q_{duct} is the volumetric flowrate at the inlet of the test section.

Cross-flow velocity (Re_{duct})

Reading: 100-2200

Operating: 100-Unknown

The FDG apparatus used in this work was designed for operation at cross-flow velocities within the laminar region. It should, however, be possible to operate at much higher values, in the turbulent region. Flow measurement would require different instrumentation however. The minimum is dependent on a low enough flow through the membrane. By definition, the ratio defined by equation (9.1) cannot exceed 1, at which point the system becomes a dead-end filtration.

Suspension particle size

Operating: unknown-250 μm

A maximum particle size of 250 μm, half the nozzle throat diameter, d_t is suggested in order to avoid blocking of the gauging nozzle. The minimum is dependent on the nature of the filtration and membrane used to perform it.

Chemical and temperature tolerances

Temperature: 10-50°C

Due to the thermal expansion properties of polycarbonate, from which the test section is constructed, extremes of temperature should be avoided. The list of compatibility properties of polycarbonate with individual chemicals is available elsewhere (Cole-Parmer, 2014) and too long to include here. Some common fluids to avoid the use of are listed below, and still allows for most pretreatment and cleaning protocols which might be required for membrane studies.

- Acetone
- Alcohols (chains shorter than C_2H_5OH)
- Ammonia
- Benzene (and most benzene compounds)
- Chlorine (and most reactive chlorine-containing compounds)

- Concentrated acids (>10%)
- NaOH (>10%)
- Reactive ketones

Flux limitation

Operation: $\rho_L J A_m$ < 0.06 kg·s^{-1}

The limit above is determined mainly for convenience. A maximum load on the balance used to measure flux is 1.8 kg, and minimum time period allowed for this to be reached is 30 s.

9.2.2 Membrane offset

As described in section 6.6.2, a calibration step was required prior to each fouling experiment to adjust for variations in the membrane position. When mounting membranes in the test section it is unsurprising that their position adjusts slightly. It was found, however, that the position of the membrane varied with TMP. This would present issues if constant flux filtrations were required. An appropriate fix for this might be to adapt the membrane support to make it more rigid, and establish a minimum TMP, above which no significant movement of the membrane occurs.

9.2.3 Developing flow on a membrane surface

The duct flow rig (section 4.1) contained a 3 mm recess from the entry duct to the membrane surface which, as discussed in section 8.6.4, was likely to be responsible for uneven surface fouling on the membrane. Efforts were made to reduce this effect in the new apparatus (section 6.2). Despite this there still remains the possibility that the 1 mm recess (although this occurs over a bevelled surface) and the presence of the gauge nozzle may influence flow over the membrane enough to affect fouling. This would mean the FDG readings may not be representative of the entire fouling layer.

9.2.4 Limitations of the FDG procedure

Limitations specific to FDG measurement are discussed here. Some of these can be addressed in future work, both experimentally and through further CFD studies.

Thickness and strength measurements of an uneven surface

The region tested by FDG was examined for both ballotini and lignin filtrations using microscopy. The results (sections 5.3.3 and 7.4) indicated that the region of the fouling layer directly beneath the FDG nozzle took a form similar to the inverse of the

shear stress profiles in this region elucidated thorough CFD (section 8.7.4). In this work, the thickness readings made by FDG have either presumed that the surface in this region is completely flat or that the clearance, h, is that from the lowest point on the fouling layer as indicated in Figure 9.1. The increased constriction at the outer edges of the nozzle tip may result in an underestimation of h, and hence over-estimation of δ_c.

CFD could be used to address the significance of this, which would also give an indication of the change to shear stress profiles on the surface. A more detailed study of the eroded region after FDG measurements would help to identify the geometry to be studied. Improvements upon the techniques used in this work (section 5.2.3) such as non-contact surface profilometry, would be necessary in this case.

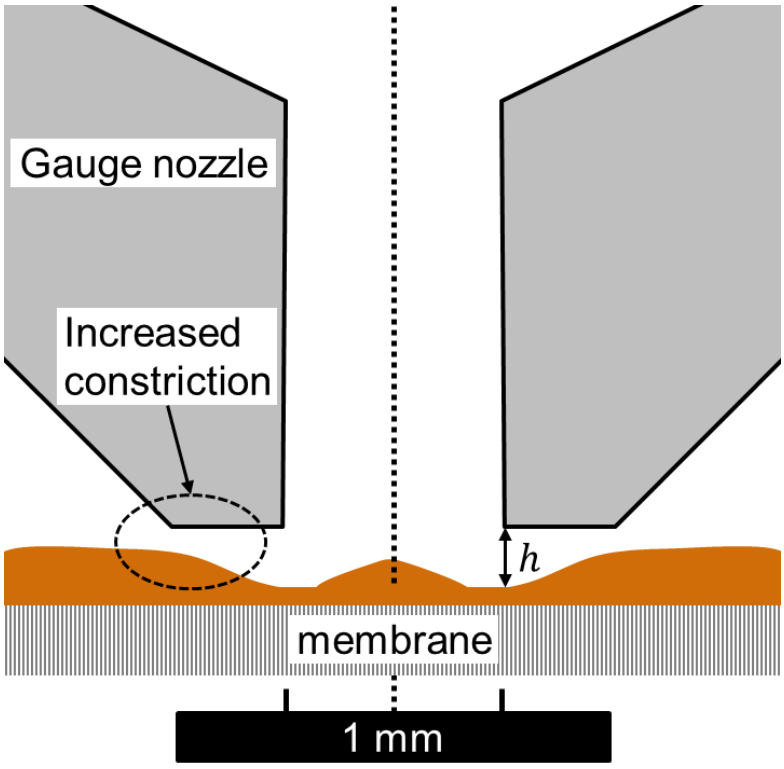

Figure 9.1. Presumed clearance, h, measured by FDG, over an uneven surface. The area of increased constriction, which might contribute to inaccuracy in h measurements, is indicated. The dashed vertical line indicates the centreline of the gauge.

Single location readings

FDG measurements have so far only taken place at 2/3 the length of the membrane for yeast and ballotini filtrations, and 1/2 the length for lignin. This only gives a thickness reading for a very small area of the fouling layer, which may not be representative of the whole layer. This has been addressed in the new apparatus, as two extra fixing points for the FDG system, upstream and downstream of the current position, have been included. There is space on the current apparatus for up to two

simultaneous FDG systems. This adaption does not, however, account for the difference in thickness which may occur across the width of the membrane, perpendicular to flow, as all three fixing points place an FDG gauge directly in the centre of the channel.

Disturbance to the fouling layer

FDG cannot be described as a non-invasive technique to measure the thickness of a fouling layer, as it involves a physical probe which disturbs flow in the test section. Although non-contact, the process is also partially destructive due to the shear stress imposed by the gauge on the membrane surface. In laminar flow conditions this is approximately two orders of magnitude higher than the stress on the membrane surface due to duct flow. This means that FDG measurements are not a direct representation of the thickness of the fouling layer but, as is the case with destructive thickness tests, the thickness of the cake layer which remains undisturbed at the shear stress applied during readings.

9.3 Future studies using current apparatus

There is scope to expand the studies reported in this work in a number of directions. Having optimised the procedure for FDG readings using the new apparatus, it is now possible to explore numerous areas of research.

9.3.1 Optimisation of cross-flow lignin filtrations

Change of membrane

Both the FDG measurements and the analysis based on Field *et al.'s* (1995) critical flux laws indicated a significant degree of pore fouling. Although the nominal pore size of the membrane used was smaller than the filtered particles, SEM micrographs of the membrane indicated pore structures on the membrane surface which could become blocked by smaller lignin particles. Perhaps counter-intuitively, a less porous membrane may actually eliminate this effect, resulting in an overall higher terminal flux.

Adjustment of pH and ionic concentration

Gravimetric analysis, supported by results of the critical flux equations, suggested that cake deposition occurred faster than should be expected by convection due to flux or settling. This, along with the high cohesive strength observed in the cakes (section 7.3.5), implies that inter-particle forces influence cake deposition as well as removal. Net charge on the surface of particles will increase the concentration of

counter-ions in the stagnant fluid region surrounding them, forming an electrical double layer around each one. This results in repulsion between individual particles. Zeta-potential measurements are commonly used as a measure of the magnitude of inter-particle interactions and stability in colloidal suspensions, where higher positive or negative charge means a stronger repulsion. Conversely, suspensions with a lower zeta-potential will tend to agglomerate more easily.

Lignin is known to precipitate from solution in acidic conditions (Öhman *et al.*, 2007b), and other researchers (Wang and Chen, 2013) have shown how the magnitude of the zeta-potential decreases with pH. It may therefore be possible to promote agglomeration subsequent to precipitation by one of two methods:

1. Further decrease of pH, to reduce electrostatic repulsion between particles
2. Increasing concentration of monovalent ions by addition of a suitable buffer. The additional ions has the effect of reducing the Debye length, a measure of the distance across which inter-particle electrostatic forces are active.

Increasing agglomeration could result in larger individual particles, which, according to the Carman-Kozeny equation (2.7) would result in a more permeable cake layer.

9.3.2 Further investigations of pre-fouling layers

Section 7.5 shows results for filtrations of lignin which were preceded by, or mixed directly with ballotini particles. Although there was no significant reduction in flux decline, there was some evidence to suggest the cake became more weakly attached to the membrane with the addition of ballotini. A more detailed study of this as a means to coat membranes would be appropriate, as initial fouling layers of ballotini have thus far been formed during only five minute periods. Thicker pre-fouling layers such as this may have a more significant impact on the terminal flux in a filtration system, or greatly improve the ease at which more complex foulants (e.g. lignin or yeast) are removed.

Using inert particles in this way also means that, if functionalised appropriately, they could be used as antimicrobial or species selective layers which can be regenerated or replaced based on the needs of the process. This could be especially important in ceramic membrane units, extending the range of separations they could perform.

9.3.3 Fouling by TiO_2 particles

Anatase (TiO_2) powder has been used as a model foulant material in a number of previous studies (Mattsson *et al.*, 2011; Wakeman, 1994) because of its availability and

non-reactive properties. In addition, Mattsson *et al.* (2011) have used it to demonstrate the impact of zeta-potential on cake porosity in dead-end filtrations.

Anatase particles offer an advantage over ballotini particles as an inert foulant because the particle density is likely to be more consistent (Variability in buoyancy was observed for ballotini, see section 4.2.3). There is also scope for performing studies on the effect of pH change on foulant removal using strength tests, whilst also verifying the aforementioned studies by Mattsson *et al.* (2011).

9.4 Future developments of membrane FDG devices

This work has identified key protocols for performing pressure-mode FDG in cross-flow membrane systems, as well as some of the limitations of the existing apparatus. Progressing from this it is possible to recommend some peripheral enhancements to existing apparatus, as well as developing a new variation on membrane FDG which draws on some of the most recent studies on gauge geometry. The way in which FDG could be used as an industrial tool is also discussed here.

9.4.1 Enhancements to the automated FDG apparatus

Dual feed/cleaning tanks

The gravimetric analyses of lignin cakes reported in section 7.3.2 showed evidence of excess deposition on the membrane surface which could have been partly due to lignin still in suspension when the apparatus was drained. In order to produce more reliable fouled membrane samples for gravimetric analysis the fouling layer was rinsed at zero TMP with foulant-free water, as described in section 6.6.7. This also appeared to remove some loose particles from the cake surface, making thickness readings more repeatable. The drawback of this procedure, however, was that due to the release and reapplication of TMP to the membrane, the position may have been altered slightly. A secondary calibration was performed after rinsing the membrane with NaOH to dissolve and remove lignin. This indicated little or no change to the membrane following rinsing under relaxation and reapplying TMP, however the current method still risks altering the fouling layer before thickness and strength tests. Additionally there was an inevitable resting time between fouling and rinsing whilst the media in the feed tank was changed.

Addition of an extra feed unit to the current apparatus would provide instantaneous switching between feed and a rinsing or cleaning liquid. Not only would this allow for rinsing the fouling layer without changing TMP, but also facilitate

sequential fouling and cleaning studies. Because preparation, membrane mounting and priming of the apparatus (steps described in section 6.6.1) contribute a large proportion of the overall time required to perform experiments, it also would be very advantageous to develop a protocol in which cleaning steps could be performed instead of renewing the membrane between experiments. As a result, much more extensive repetition of experimental studies could be performed.

Automated FDG measurements

Automation of FDG readings in calibration procedures has already been demonstrated in this work, the methods for which are summarised in section 6.3.4. It follows that automation of the FDG measurements themselves can also be performed, which would greatly reduce the user input required and potentially improve the speed at which they are achieved. This would be a significant step towards an FDG device which can perform measurements autonomously during the course of repeated fouling/cleaning cycles.

A proposed control flowchart for automated thickness and/or strength measurements, similar to those discussed in section 6.3.4, is shown in Figure 9.3. This can be built into the current software control system, the following notes are appropriate to the numbers marked on the figure:

1. A guess value for the maximum thickness needs to be made in order to position the gauge near the surface of the fouling layer. Using this estimate, the gauge is moved into a position where h/d_t = 0.2 at this thickness.
2. Using the estimate given for h/d_t by the VI, the required movement to reach h/d_t = 0.2 is calculated here. The movement should be multiplied by a factor of 0.8 and constrained to a sensible maximum distance to avoid overshooting. It will also be necessary to apply a minimum movement distance, and also a reasonable tolerance to the target position of h/d_t = 0.2 in order to prevent the movement process taking too long.
3. The target value of h/d_t = 0.2 can be altered. At higher gauging flow, m_g, it may be appropriate to use h/d_t = 0.25 instead.
4. The minimum h/d_t to reach during strength measurements should be prescribed such that Δp_{14} is less than TMP and within the range of transducer readings.
5. The step size between strength measurements can be defined either as a constant value, or as a constant step change in $\tau_{w,max}$.

6. It may be necessary to include a sequence which increases the allowable error in Δp_{13} at lower h/d_t values, as this has been found to fluctuate more in this region.

The control flowchart for the two separate processes, "End sequence" and "Fail sequence" is shown in Figure 9.2. The only difference between the two is that the fail sequence includes a restart of the process.

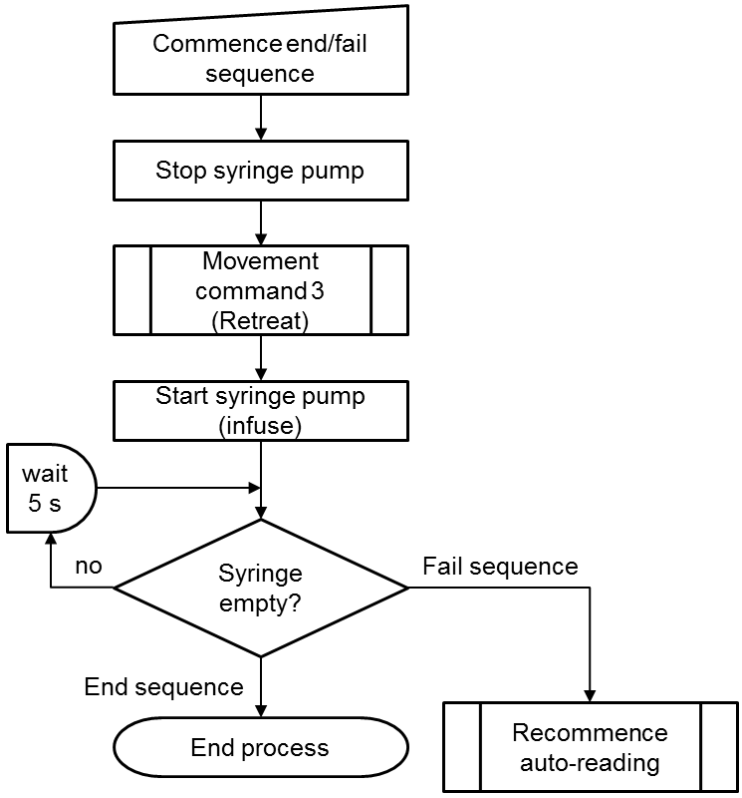

Figure 9.2. Flowchart for end and fail sequences. Movement command 3 is detailed in section 6.3.3.

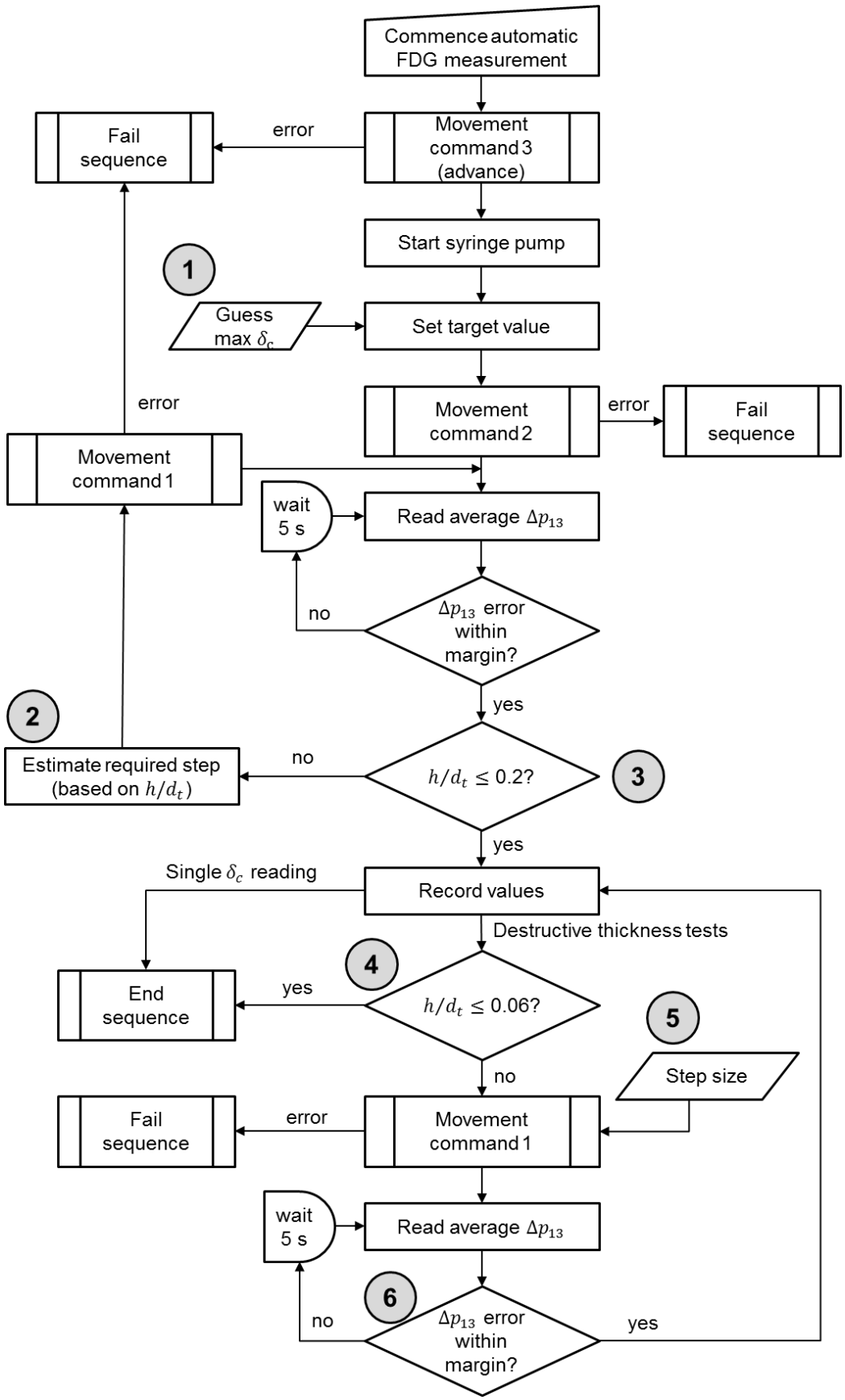

Figure 9.3. Control flowchart for automated FDG readings and destructive strength tests. End and Fail sequences are shown in Figure 9.2. Movement commands 1, 2, and 3 are detailed in section 6.3.3.

Multiple FDG attachments

Other researchers have noted that cake layers are unlikely to be uniform across the entire length of a cross-flow cell (Davis and Sherwood, 1990). In this work such a phenomenon has also been apparent. An interesting extension to the current studies would be to install an additional FDG system on to the current test section (an adaption which has already been accounted for in the design) to observe any difference in the rate of fouling, thickness, and strength of cake layers towards the entrance and exit of the test section.

9.4.2 Radial cross-flow FDG

Figure 9.4 shows a concept schematic for a proposed new FDG system which is intended to address some of the drawbacks listed above in section 9.2.4. Specifically, it deals with two key issues, *disturbance to the fouling layer*, and *single location readings*.

The design comprises a cylindrical vessel with a removable bottom plate which contains a circular disc membrane. The membrane is supported on a solid porous spacer, which rests over coarse packing to distribute flow should backflushing be required. Feed flow runs through the cylinder, with TMP controlled by a needle valve. Flow across the membrane is generated and controlled by gauging flow. This means that rather than the stress imposed by FDG exceeding that caused by cross-flow velocity, the stress is controlled accurately by FDG, whilst simultaneously providing a constant measure of the fouling layer thickness. In addition, FDG readings now give a measure of cake thickness across an entire cake layer.

Provided that the feed flow through the cylinder is fast enough, the suspension drawn over the membrane by the gauge will be representative of the bulk feed. A rugged construction of this using stainless steel for the cylinder, gauge and bottom plate would allow for high pressure membrane applications.

The shape of the gauging nozzle draws upon recent studies by Peralta *et al.* (2011a, b) into the various nozzle geometries. They established that a near-constant shear stress profile can be achieved by using a more complex nozzle geometry. This would be very advantageous, allowing this equipment to perform studies at constant, precisely controlled shear stresses. In order to maintain a constant shear stress, h/d_t would need to be constant.

The exact specification of d_t, d, and other dimensions is not proposed here, but can be optimised first using CFD studies. A stronger stepper assembly may be required to adjust the height of what is envisioned to be a wider outlet tube than previous

devices. Additionally, this apparatus provides scope for multiple gauge attachments, so that dead-end filtration studies, and detailed destructive thickness testing can be performed.

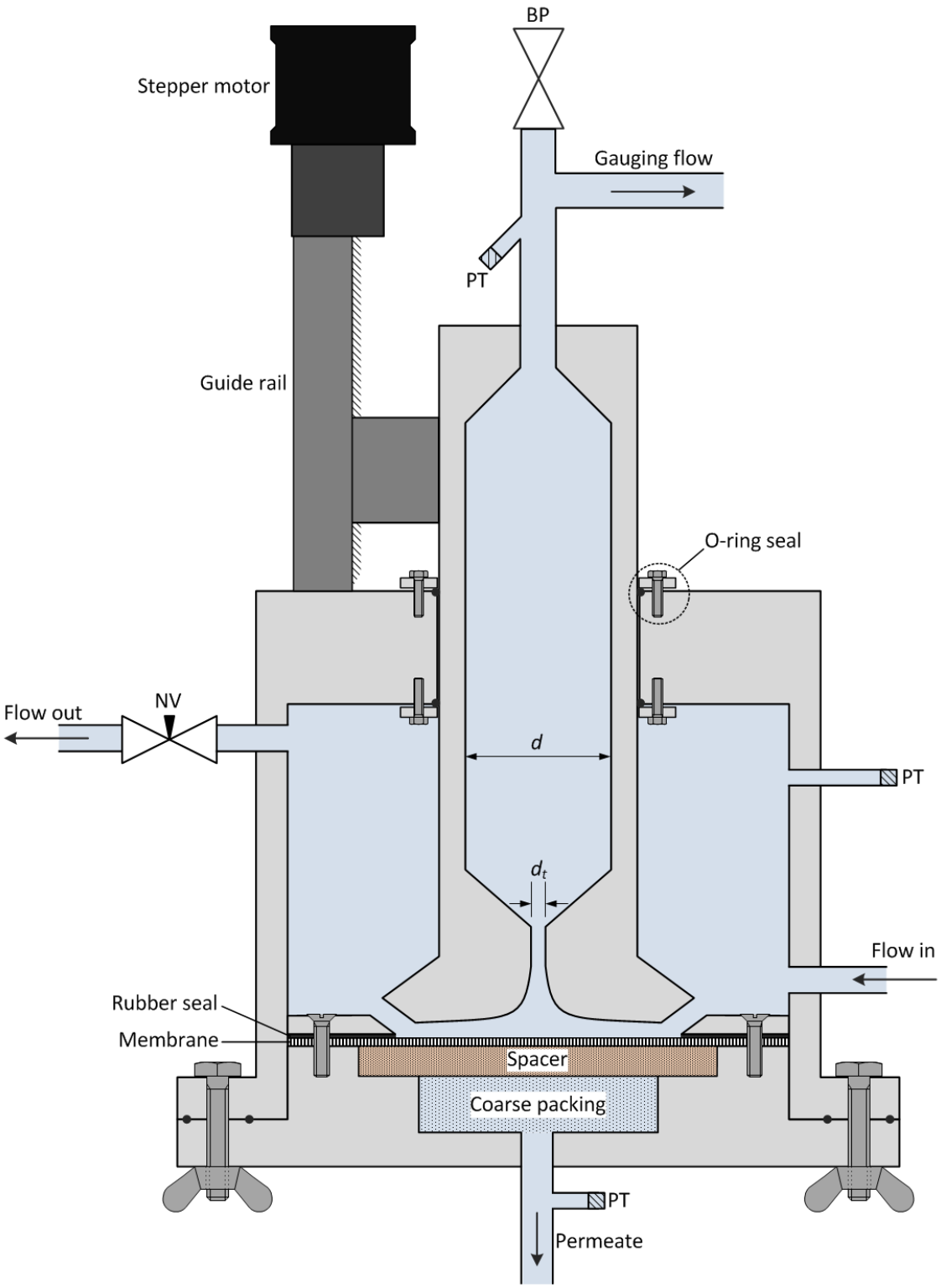

Figure 9.4. Concept schematic for a radial cross-flow FDG system. BP represents a bleed point, NV is a needle valve, and PT represents pressure tappings. The design constitutes a cylindrical vessel, in which an FDG gauge is suspended above a membrane. The membrane is held in a removable bottom place, which attaches to the main vessel and is secured with wingnuts.

9.4.3 Practical application in industry

One of the key objectives of this work was to develop FDG as a versatile tool for studying fouling in membrane operations. As highlighted in section 9.2.4, there are limitations and caveats to the measurements produced by FDG in cross-flow membrane systems. While other techniques (section 2.6) such as laser triangulometry and UTDR can provide can provide completely non-destructive and non-invasive estimates of cake thickness, both have practical limitations. The former requires that a laser beam is transmissible through the process fluid and reflected from the fouling surface, and the latter involves complex signal processing which appears to require specific technical expertise. The advantage that FDG holds over these is that it is more versatile and can provide thickness measurements on-the-fly if required.

In an industrial setting it is proposed that, rather than installing an FDG system on to existing apparatus, the most useful application would be as a separate side-stream, as shown in Figure 9.5. Here a separate filtration cell, which includes an FDG system, is placed as a parallel side-stream to the main membrane unit. This configuration would facilitate autonomous FDG readings to take place during a normal filtration without affecting the main system. If effective cleaning in place (CIP) procedures are available to the FDG unit, during the course of a single filtration through the main unit, it would be possible to perform multiple tests of the same feed stream using FDG. This would allow operators to characterise feed fouling and cleaning behaviour during filtrations, and directly relate results to the behaviour of the main filtration unit.

Examples where this could be particularly useful are in waste processing and food process streams, where the properties of the feed may change over time or between

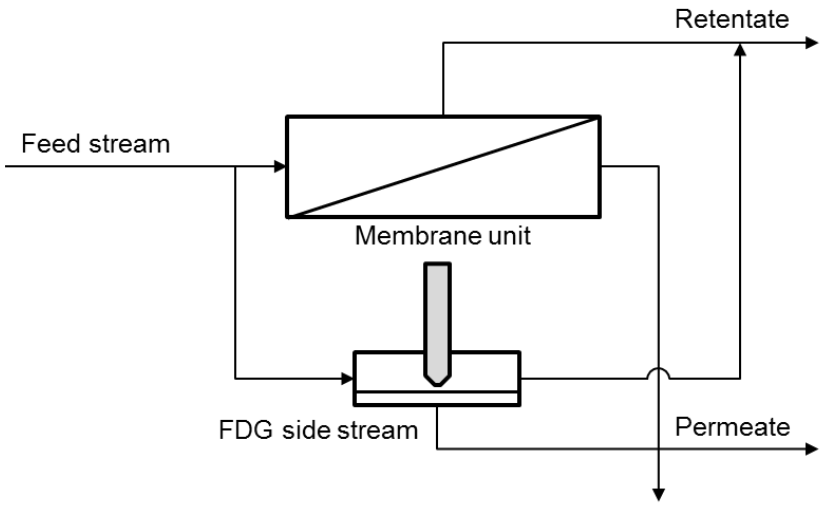

Figure 9.5. Proposed implementation of FDG within an existing industrial process.

batch operations. Using FDG as a means to characterise whether fouling layers are thick and relatively porous, or thinner and highly impermeable, may provide useful information of the type of cleaning procedure required. This would allow a targeted and more efficient approach towards CIP to be developed in-house and with very little lag time between useful observations, improvements, and their implementation.

9.5 Concluding Remarks

The technique of fluid dynamic gauging (FDG) has been further developed for membrane systems in this work, taking an approach towards automation and facile use. It was used to investigate various models which describe fouling phenomenon by studying fouling and removal during filtrations of inert, spherical particles. Two models which describe back-transport of particles from a membrane surface, namely particle capture (section 2.5.2) and inertial lift (section 2.5.3), were investigated. These were found to poorly describe particle removal under fluid shear, as they do not appropriately model the effect of packing in filter cakes.

It is apparent that considering individual particle dynamics cannot yet lead to an effective means to predict the fouling properties of a filtration. An accurate, all-encompassing equation to predict the rate of flux decline purely from characteristic data for the feed is probably a long way off, not least because of the mounting error which might be incurred in attempting to determine, individually, all of the parameters which it would need to take into account. An alternative method therefore, is to develop a means to produce more general data about a filtration using choice analytical procedures. FDG has demonstrated that for a filtration of lignin - which was found to form thin, but relatively impermeable filter cakes on membrane surfaces - it is possible to generate data which indicates the influence of pore blocking type phenomena. The way in which this can be supported by analysis of flux vs. time data has also been established. The response of filter cakes to fluid shear was studied, and the technique of destructive thickness testing provides another means by which improvements to cleaning protocols can be investigated.

Compared to other analytical methods for monitoring cake fouling on membranes, FDG is not necessarily the optimum tool for elucidating the mechanics of a system. This is mainly because it is both invasive and destructive in its measuring process. It is, however, a very promising tool for quickly and effectively procuring qualitative data for enhancing membrane filtrations. Its scope for full automation and

on-the-fly readings could lead to it becoming a robust and reliable tool used to monitor and improve membrane filtration operations in a range of industries.

Chapter 10: Bibliography

Airey, D., Yao, S., Wu, J., Chen, V., Fane, A.G. & Pope, J.M. 1998. An investigation of concentration polarization phenomena in membrane filtration of colloidal silica suspensions by nmr micro-imaging. *Journal of Membrane Science,* 145**,** 145-158.

Al-Akoum, O., Ding, L., Chotard-Ghodsnia, R., Jaffrin, M.Y. & Gésan-Guiziou, G. 2002. Casein micelles separation from skimmed milk using a vsep dynamic filtration module. *Desalination,* 144**,** 325-330.

Al-Amoudi, A. & Lovitt, R.W. 2007. Fouling strategies and the cleaning system of nf membranes and factors affecting cleaning efficiency. *Journal of Membrane Science,* 303**,** 4-28.

Ali, A., Chapman, G.J., Chew, Y.M.J., Gu, T., Paterson, W.R. & Wilson, D.I. 2013. A fluid dynamic gauging device for measuring fouling deposit thickness in opaque liquids at elevated temperature and pressure. *Experimental Thermal and Fluid Science,* 48**,** 19-28.

Altena, F.W. & Belfort, G. 1984. Lateral migration of spherical particles in porous flow channels: Application to membrane filtration. *Chemical Engineering Science,* 39**,** 343-355.

Altmann, J. & Ripperger, S. 1997. Particle deposition and layer formation at the crossflow microfiltration. *Journal of Membrane Science,* 124**,** 119-128.

An, G., Lin, J., Li, J., Li, X. & Jian, X. 2011. Non-invasive measurement of membrane scaling and cleaning in spiral-wound reverse osmosis modules by ultrasonic time-domain reflectometry with sound intensity calculation. *Desalination,* 283**,** 3-9.

Antony, A., Chilcott, T., Coster, H. & Leslie, G. 2013. In situ structural and functional characterization of reverse osmosis membranes using electrical impedance spectroscopy. *Journal of Membrane Science,* 425–426**,** 89-97.

Argyle, I.S., Pihlajamäki, A. & Bird, M.R. 2012. Structural and surface modification of polymeric ultrafiltration membranes by alcohol pre-treatment and subsequent fouling implications. *Procedia Engineering,* 44**,** 1168-1171.

Atkinson, S. 2002. Us membrane separation technology markets analysed. *Membrane Technology,* 2002**,** 10-12.

Balakrishnan, M., Dua, M. & Bhagat, J.J. 2000. Effect of operating parameters on sugarcane juice ultrafiltration: Results of a field experience. *Separation and Purification Technology,* 19**,** 209-220.

Beavers, G.S. & Joseph, D.D. 1967. Boundary conditions at a naturally permeable wall. *Journal of Fluid Mechanics,* 30**,** 197-207.

Belfort, G., Davis, R.H. & Zydney, A.L. 1994. The behavior of suspensions and macromolecular solutions in crossflow microfiltration. *Journal of Membrane Science,* 96**,** 1-58.

Bergström, L. 1992. Sedimentation of flocculated alumina suspensions: Γ-ray measurements and comparison with model predictions. *Journal of the Chemical Society, Faraday Transactions,* 88**,** 3201-3211.

Bhosle, B.M. & Subramanian, R. 2005. New approaches in deacidification of edible oils--a review. *Journal of Food Engineering,* 69**,** 481-494.

Bowen, W.R., Calvo, J.I. & Hernández, A. 1995. Steps of membrane blocking in flux decline during protein microfiltration. *Journal of Membrane Science,* 101**,** 153-165.

Broeckmann, A., Busch, J., Wintgens, T. & Marquardt, W. 2006. Modeling of pore blocking and cake layer formation in membrane filtration for wastewater treatment. *Desalination,* 189**,** 97-109.

Buetehorn, S., Utiu, L., Küppers, M., Blümich, B., Wintgens, T., Wessling, M. & Melin, T. 2011. Nmr imaging of local cumulative permeate flux and local cake growth in submerged microfiltration processes. *Journal of Membrane Science,* 371**,** 52-64.

Cañas, A., Ariza, M.J. & Benavente, J. 2001. Characterization of active and porous sublayers of a composite reverse osmosis membrane by impedance spectroscopy, streaming and membrane potentials, salt diffusion and x-ray photoelectron spectroscopy measurements. *Journal of Membrane Science,* 183**,** 135-146.

Cassano, A., Donato, L. & Drioli, E. 2007. Ultrafiltration of kiwifruit juice: Operating parameters, juice quality and membrane fouling. *Journal of Food Engineering,* 79**,** 613-621.

Chen, V., Li, H. & Fane, A.G. 2004. Non-invasive observation of synthetic membrane processes - a review of methods. *Journal of Membrane Science,* 241**,** 23-44.

Cheng, L.-H., Yang, Y.-C., Chen, J., Lin, Y.-H. & Wang, S.-H. 2011. A new view of membrane fouling with 3d ultrasonic imaging techniques: Taking the canola oil with phospholipids for example. *Journal of Membrane Science,* 372**,** 134-144.

Cheryan, M. & Cheryan, M.U.h. 1998. *Ultrafiltration and microfiltration handbook,* Lancaster, Pa.: Technomic.

Chew, J.Y.M. 2004. *Development of fluid dynamic gauging for cleaning studies.* PhD, University of Cambridge.

Chew, J.Y.M., Cardoso, S.S.S., Paterson, W.R. & Wilson, D.I. 2004a. Cfd studies of dynamic gauging. *Chemical Engineering Science,* 59**,** 3381-3398.

Chew, J.Y.M., Paterson, W.R. & Wilson, D.I. 2004b. Fluid dynamic gauging for measuring the strength of soft deposits. *Journal of Food Engineering,* 65**,** 175-187.

Chew, J.Y.M., Paterson, W.R. & Wilson, D.I. 2010. Application of fluid dynamic gauging and optical imaging to membrane fouling. *In:* Wilson & Chew (eds.) *Fouling & Cleaning in Food Processing 2010.* Cambridge, UK: Department of Chemical Engineering, Cambridge.

Chew, J.Y.M., Paterson, W.R., Wilson, D.I., Höufling, V. & Augustin, W. 2005a. A method for measuring the strength of scale deposits on heat transfer surfaces. *Developments in Chemical Engineering and Mineral Processing,* 13**,** 21-30.

Chew, J.Y.M., Tonneijk, S.J., Paterson, W.R. & Wilson, D.I. 2005b. Mechanisms in the solvent cleaning of emulsion polymerization reactor surfaces. *Industrial & Engineering Chemistry Research,* 44**,** 4605-4616.

Chew, J.Y.M., Tonneijk, S.J., Paterson, W.R. & Wilson, D.I. 2006. Solvent-based cleaning of emulsion polymerization reactors. *Chemical Engineering Journal,* 117**,** 61-69.

Chew, Y.M.J., Paterson, W.R. & Wilson, D.I. 2007. Fluid dynamic gauging: A new tool to study deposition on porous surfaces. *Journal of Membrane Science,* 296**,** 29-41.

Chilcott, T.C., Chan, M., Gaedt, L., Nantawisarakul, T., Fane, A.G. & Coster, H.G.L. 2002. Electrical impedance spectroscopy characterisation of conducting membranes: I. Theory. *Journal of Membrane Science,* 195**,** 153-167.

Cole-Parmer 2014. Chemical compatibility database.

COMSOL 2011. *Comsol multiphysics reference guide,* ver. 4.2a.

Coster, H.G.L., Chilcott, T.C. & Coster, A.C.F. 1996. Impedance spectroscopy of interfaces, membranes and ultrastructures. *Bioelectrochemistry and Bioenergetics,* 40**,** 79-98.

Creber, S.A., Pintelon, T.R.R., Graf von der Schulenburg, D.A.W., Vrouwenvelder, J.S., van Loosdrecht, M.C.M. & Johns, M.L. 2010a. Magnetic resonance imaging and 3d simulation studies of biofilm accumulation and cleaning on reverse osmosis membranes. *Food and Bioproducts Processing,* 88**,** 401-408.

Creber, S.A., Vrouwenvelder, J.S., van Loosdrecht, M.C.M. & Johns, M.L. 2010b. Chemical cleaning of biofouling in reverse osmosis membranes evaluated using magnetic resonance imaging. *Journal of Membrane Science,* 362**,** 202-210.

Cui, Z.F., Jiang, Y. & Field, R.W. 2010. Chapter 1 - fundamentals of pressure-driven membrane separation processes. *In:* Cui & Muralidhara (eds.) *Membrane technology.* Oxford: Butterworth-Heinemann.

Cui, Z.F. & Muralidhara, H.S. 2010. *Membrane technology,* Amsterdam ; London: Elsevier/Butterworth-Heinemann.

Damak, K., Ayadi, A., Zeghmati, B. & Schmitz, P. 2004. A new navier-stokes and darcy's law combined model for fluid flow in crossflow filtration tubular membranes. *Desalination,* 161**,** 67-77.

Davies, J.L. & Smith, M.P. 2010. Membrane applications in monoclonal antibody production. *In:* Muralidhara & Cui (eds.) *Membrane technology : A practical guide to membrane technology and applications in food and bioprocessing.* Amsterdam ; London: Elsevier/Butterworth-Heinemann.

Davis, R.H. & Leighton, D.T. 1987. Shear-induced transport of a particle layer along a porous wall. *Chemical Engineering Science,* 42**,** 275-281.

Davis, R.H. & Sherwood, J.D. 1990. A similarity solution for steady-state crossflow microfiltration. *Chemical Engineering Science,* 45**,** 3203-3209.

De, B.K., Das, R., Dutta, B.K. & Bhattacharyya, D.K. 1998. Membrane degumming and dewaxing of rice bran oil and its refining. *Lipid / Fett,* 100**,** 416-421.

De Bruijn, J., Venegas, A. & Borquez, R. 2002. Influence of crossflow ultrafiltration on membrane fouling and apple juice quality. *Desalination,* 148**,** 131-136.

de Morais Coutinho, C., Chiu, M.C., Basso, R.C., Ribeiro, A.P.B., Gonçalves, L.A.G. & Viotto, L.A. 2009. State of art of the application of membrane technology to vegetable oils: A review. *Food Research International,* 42**,** 536-550.

Drew, D.A., Schonberg, J.A. & Belfort, G. 1991. Lateral inertial migration of a small sphere in fast laminar flow through a membrane duct. *Chemical Engineering Science,* 46**,** 3219-3224.

Eckstein, E.C., Bailey, D.G. & Shapiro, A.H. 1977. Self-diffusion of particles in shear flow of a suspension. *Journal of Fluid Mechanics,* 79**,** 191-208.

Elander, R.P. 2003. Industrial production of ß-lactam antibiotics. *Applied Microbiology and Biotechnology,* 61**,** 385-392.

Endo, Y., Chen, D.-R. & Pui, D.Y.H. 2002. Theoretical consideration of permeation resistance of fluid through a particle packed layer. *Powder Technology,* 124**,** 119-126.

Evans, J.C. & Morgan, I.G. 1964. *Principles of pneumatic gauging,* National Physical Laboratory (UK): H.M.S.O.

Evans, P.J., Bird, M.R., Pihlajamäki, A. & Nyström, M. 2008. The influence of hydrophobicity, roughness and charge upon ultrafiltration membranes for black tea liquor clarification. *Journal of Membrane Science,* 313**,** 250-262.

FiberCell. 2008. Hollow fiber bioreactors and related products. Available: http://www.nbsbio.co.uk/downloads/fibercell_brochure.pdf [Accessed 26th November 2014].

Field, R.W., Wu, D., Howell, J.A. & Gupta, B.B. 1995. Critical flux concept for microfiltration fouling. *Journal of Membrane Science,* 100**,** 259-272.

Field, R.W. & Wu, J.J. 2011. Modelling of permeability loss in membrane filtration: Re-examination of fundamental fouling equations and their link to critical flux. *Desalination,* 283**,** 68-74.

Foley, G. 2006. A review of factors affecting filter cake properties in dead-end microfiltration of microbial suspensions. *Journal of Membrane Science,* 274**,** 38-46.

Foley, G.a. 2013. *Membrane filtration : A problem solving approach with matlab*.

Fox, R.W., Pritchard, P.J. & McDonald, A.T. 2010. *Introduction to fluid mechanics,* Hoboken, N.J.: John Wiley.

Freedonia. 2013. World membrane separation technologies to 2017. Available: http://www.reportsnreports.com/reports/250063-world-membrane-separation-technologies-to-2017.html [Accessed 17/12/2014].

Fryer, P.J., Slater, N.K.H. & Duddridge, J.E. 1985. Suggestions for the operation of radial flow cells in cell adhesion and biofouling studies. *Biotechnology and Bioengineering,* 27**,** 434-438.

Gordon, P.W., Brooker, A.D.M., Chew, J.Y.M., Peralta, J.M., York, D.W. & Wilson, D.I. 2011a. Using scanning fluid dynamic gauging to study the mechanisms and kinetics of enzyme-based cleaning. *In:* Taoukis, Stoforos, Karathanos & Saravacos (eds.) *11th International Congress of Engineering and Food (ICEF11).* Athens, Greece: Cosmosware, Ag. Ioannou 53, Athens, Greece, 00302106013922.

Gordon, P.W., Brooker, A.D.M., Chew, Y.M.J., Letzelter, N., York, D.W. & Wilson, D.I. 2011b. Elucidating enzyme-based cleaning of protein soils (gelatine and egg yolk) using a scanning fluid dynamic gauge. *Chemical Engineering Research and Design,* In Press, Corrected Proof.

Gordon, P.W., Brooker, A.D.M., Chew, Y.M.J., Letzelter, N., York, D.W. & Wilson, D.I. 2012. Elucidating enzyme-based cleaning of protein soils (gelatine and egg yolk) using a scanning fluid dynamic gauge. *Chemical Engineering Research and Design,* 90**,** 162-171.

Gordon, P.W., Brooker, A.D.M., Chew, Y.M.J., Wilson, D.I. & York, D.W. 2010. Studies into the swelling of gelatine films using a scanning fluid dynamic gauge. *Food and Bioproducts Processing,* 88**,** 357-364.

Graf von der Schulenburg, D.A., Vrouwenvelder, J.S., Creber, S.A., van Loosdrecht, M.C.M. & Johns, M.L. 2008. Nuclear magnetic resonance microscopy studies of membrane biofouling. *Journal of Membrane Science,* 323**,** 37-44.

Greenlee, L.F., Lawler, D.F., Freeman, B.D., Marrot, B. & Moulin, P. 2009. Reverse osmosis desalination: Water sources, technology, and today's challenges. *Water Research,* 43**,** 2317-2348.

Gu, T., Albert, F., Augustin, W., Chew, Y.M.J., Mayer, M., Paterson, W.R., Scholl, S., Sheikh, I., Wang, K. & Wilson, D.I. 2011a. Application of fluid dynamic gauging to annular test apparatuses for studying fouling and cleaning. *Experimental Thermal and Fluid Science,* 35**,** 509-520.

Gu, T., Albert, F., Augustin, W., Chew, Y.M.J., Paterson, W.R., Scholl, S., Sheikh, I., Wang, K. & Wilson, D.I. 2011b. Fluid dynamic gauging applied to annular test apparatuses for fouling and cleaning. *Heat Transfer Engineering,* 32**,** 339-348.

Gu, T., Chew, J.Y.M., Paterson, W.R. & Wilson, D.I. 2007. Fluid dynamic gauging in duct flows - experiments and cfd simulations. *In:* Müller-Steinhagen, Malayeri & Watkinson (eds.) *7th International Conference on Heat Exchanger Fouling and Cleaning.* Tomat, Portugal.

Gu, T., Chew, Y.M.J., Paterson, W.R. & Wilson, D.I. 2009a. Experimental and cfd studies of fluid dynamic gauging in annular flows. *AIChE Journal,* 55**,** 1937-1947.

Gu, T., Chew, Y.M.J., Paterson, W.R. & Wilson, D.I. 2009b. Experimental and cfd studies of fluid dynamic gauging in duct flows. *Chemical Engineering Science,* 64**,** 219-227.

Guillemot, G., Vaca-Medina, G., Martin-Yken, H., Vernhet, A., Schmitz, P. & Mercier-Bonin, M. 2006. Shear-flow induced detachment of saccharomyces cerevisiae from stainless steel: Influence of yeast and solid surface properties. *Colloids and Surfaces B: Biointerfaces,* 49**,** 126-135.

Hamachi, M. & Mietton-Peuchot, M. 2001. Cake thickness measurement with an optical laser sensor. *Chemical Engineering Research and Design,* 79**,** 151-155.

Hamachi, M. & Mietton-Peuchot, M. 2002. Analysis of deposit behaviour in crossflow microfiltration by means of thickness measurement. *Chemical Engineering Journal,* 86**,** 251-257.

Hermia, J. 1982. Constant pressure blocking filtration laws-application to power law non-newtonian fluids. *Transactions of the Institution of Chemical Engineers,* 60**,** 183-187.

Hooper, R.J., Paterson, W.R. & Wilson, D.I. 2006. Comparison of whey protein model foulants for studying cleaning of milk fouling deposits. *Food and Bioproducts Processing,* 84**,** 329-337.

Huang, X., Guillen, G.R. & Hoek, E.M.V. 2010. A new high-pressure optical membrane module for direct observation of seawater ro membrane fouling and cleaning. *Journal of Membrane Science,* 364**,** 149-156.

Hughes, D., Tirlapur, U.K., Field, R. & Cui, Z. 2006a. In situ 3d characterization of membrane fouling by yeast suspensions using two-photon femtosecond near infrared non-linear optical imaging. *Journal of Membrane Science,* 280**,** 124-133.

Hughes, D.J., Cui, Z., Field, R.W. & Tirlapur, U.K. 2006b. In situ three-dimensional characterization of membrane fouling by protein suspensions using multiphoton microscopy. *Langmuir,* 22**,** 6266-6272.

Hughes, D.J., Cui, Z., Field, R.W. & Tirlapur, U.K. 2007. Membrane fouling by cell-protein mixtures: In situ characterisation using multi-photon microscopy. *Biotechnology and Bioengineering,* 96**,** 1083-1091.

IST. 2014. *Middle east climate* [Online]. Israel Science and Technology. Available: http://www.science.co.il/Weather/Middle-East-Climate/ [Accessed 22nd April 2014].

James Watkins, E. & Pfromm, P.H. 1999. Capacitance spectroscopy to characterize organic fouling of electrodialysis membranes. *Journal of Membrane Science,* 162**,** 213-218.

Jeon, K.-J. & Jung, Y.-W. 2004. A simulation study on the compression behavior of dust cakes. *Powder Technology,* 141**,** 1-11.

Johansson, C. & Theliander, H. 2007. Validation of predicted local profiles in cake filtration. *Chemical Engineering Research and Design,* 85**,** 220-228.

Jones, S.A., Bird, M.R., Chew, J.Y.M. & Wilson, D.I. 2010a. The application of fluid dynamic gauging in the investigation of synthetic membrane surface phenomena. *In:* Wilson & Chew (eds.) *Fouling & Cleaning in Food Processing 2010.* Cambridge, UK: Department of Chemical Engineering, Cambridge.

Jones, S.A., Chew, Y.M.J., Bird, M.R. & Wilson, D.I. 2010b. The application of fluid dynamic gauging in the investigation of synthetic membrane fouling phenomena. *Food and Bioproducts Processing,* 88**,** 409-418.

Jones, S.A., Chew, Y.M.J., Wilson, D.I. & Bird, M.R. 2012. Fluid dynamic gauging of microfiltration membranes fouled with sugar beet molasses. *Journal of Food Engineering,* 108**,** 22-29.

Ju, L.-K. & Ho, C.S. 1988. Correlation of cell volume fractions with cell concentrations in fermentation media. *Biotechnology and Bioengineering,* 32**,** 95-99.

Kavanagh, J.M., Hussain, S., Chilcott, T.C. & Coster, H.G.L. 2009. Fouling of reverse osmosis membranes using electrical impedance spectroscopy: Measurements and simulations. *Desalination,* 236**,** 187-193.

Kindasa. 2014. *Production plant* [Online]. Kindasa Water Services. Available: http://www.kindasa.com/plant.php [Accessed 22nd April 2014].

Knutsen, J.S. & Davis, R.H. 2006. Deposition of foulant particles during tangential flow filtration. *Journal of Membrane Science,* 271**,** 101-113.

Köseoglu, S. & Engelgau, D. 1990. Membrane applications and research in the edible oil industry: An assessment. *Journal of the American Oil Chemists' Society,* 67**,** 239-249.

Kroll, S., Treccani, L., Rezwan, K. & Grathwohl, G. 2010. Development and characterisation of functionalised ceramic microtubes for bacteria filtration. *Journal of Membrane Science,* 365**,** 447-455.

Krstićś, D.M., Tekić, M.N., Carić, M.D. & Milanović, S.D. 2004. Static turbulence promoter in cross-flow microfiltration of skim milk. *Desalination,* 163**,** 297-309.

Kuberkar, V.T. & Davis, R.H. 2001. Microfiltration of protein-cell mixtures with crossflushing or backflushing. *Journal of Membrane Science,* 183**,** 1-14.

Ladhe, A.R. & Krishna Kumar, N.S. 2010a. Application of membrane technology in vegetable oil processing. *In:* Muralidhara & Cui (eds.) *Membrane technology : A practical guide to*

membrane technology and applications in food and bioprocessing. Amsterdam ; London: Elsevier/Butterworth-Heinemann.

Ladhe, A.R. & Krishna Kumar, N.S. 2010b. Chapter 5 - application of membrane technology in vegetable oil processing. *In:* Cui & Muralidhara (eds.) *Membrane technology.* Oxford: Butterworth-Heinemann.

Laurichesse, S. & Avérous, L. 2014. Chemical modification of lignins: Towards biobased polymers. *Progress in Polymer Science,* 39**,** 1266-1290.

Leighton, D. & Acrivos, A. 1986. Viscous resuspension. *Chemical Engineering Science,* 41**,** 1377-1384.

Lewis, W.J.T., Chew, Y.M.J. & Bird, M.R. 2011. Experimental and cfd studies of fluid dynamic gauging in cross-flow microfiltration systems. *In:* Taoukis, Stoforos, Karathanos & Saravacos (eds.) *11th International Congress of Engineering and Food (ICEF11).* Athens, Greece: Cosmosware.

Lewis, W.J.T., Chew, Y.M.J. & Bird, M.R. 2012. The application of fluid dynamic gauging in characterising cake deposition during the cross-flow microfiltration of a yeast suspension. *Journal of Membrane Science,* 405–406**,** 113-122.

Li, H. & Chen, V. 2010. Chapter 10 - membrane fouling and cleaning in food and bioprocessing. *In:* Cui & Muralidhara (eds.) *Membrane technology.* Oxford: Butterworth-Heinemann.

Li, H., Fane, A.G., Coster, H.G.L. & Vigneswaran, S. 1998. Direct observation of particle deposition on the membrane surface during crossflow microfiltration. *Journal of Membrane Science,* 149**,** 83-97.

Li, H., Fane, A.G., Coster, H.G.L. & Vigneswaran, S. 2000. An assessment of depolarisation models of crossflow microfiltration by direct observation through the membrane. *Journal of Membrane Science,* 172**,** 135-147.

Li, H., Fane, A.G., Coster, H.G.L. & Vigneswaran, S. 2003a. Observation of deposition and removal behaviour of submicron bacteria on the membrane surface during crossflow microfiltration. *Journal of Membrane Science,* 217**,** 29-41.

Li, J.-X., Sanderson, R.D. & Chai, G.Y. 2006. A focused ultrasonic sensor for in situ detection of protein fouling on tubular ultrafiltration membranes. *Sensors and Actuators B: Chemical,* 114**,** 182-191.

Li, J., Hallbauer, D.K. & Sanderson, R.D. 2003b. Direct monitoring of membrane fouling and cleaning during ultrafiltration using a non-invasive ultrasonic technique. *Journal of Membrane Science,* 215**,** 33-52.

Li, J. & Sanderson, R.D. 2002. In situ measurement of particle deposition and its removal in microfiltration by ultrasonic time-domain reflectometry. *Desalination,* 146**,** 169-175.

Li, J., Sanderson, R.D., Hallbauer, D.K. & Hallbauer-Zadorozhnaya, V.Y. 2002a. Measurement and modelling of organic fouling deposition in ultrafiltration by ultrasonic transfer signals and reflections. *Desalination,* 146**,** 177-185.

Li, J., Sanderson, R.D. & Jacobs, E.P. 2002b. Non-invasive visualization of the fouling of microfiltration membranes by ultrasonic time-domain reflectometry. *Journal of Membrane Science,* 201**,** 17-29.

Li, X., Li, J., Wang, J., Wang, H., Cui, C., He, B. & Zhang, H. 2014. Direct monitoring of sub-critical flux fouling in a horizontal double-end submerged hollow fiber membrane module using ultrasonic time domain reflectometry. *Journal of Membrane Science,* 451**,** 226-233.

Li, X., Li, J., Wang, J., Zhang, H. & Pan, Y. 2012. In situ investigation of fouling behavior in submerged hollow fiber membrane module under sub-critical flux operation via ultrasonic time domain reflectometry. *Journal of Membrane Science,* 411–412**,** 137-145.

Lin, C.L. & Miller, J.D. 2000. Network analysis of filter cake pore structure by high resolution x-ray microtomography. *Chemical Engineering Journal,* 77**,** 79-86.

Lin, Y.-H., Tung, K.-L., Wang, S.-H., Zhou, Q. & Shung, K.K. 2013. Distribution and deposition of organic fouling on the microfiltration membrane evaluated by high-frequency ultrasound. *Journal of Membrane Science,* 433**,** 100-111.

Linkhorst, J. & Lewis, W.J.T. 2013. Workshop on membrane fouling and monitoring: A summary. *Desalination and Water Treatment,* 51**,** 6401-6406.

Lipnizki, F. 2010. Membrane processes for the production of bulk fermentation products. *In:* Cui & Muralidhara (eds.) *Membrane technology : A practical guide to membrane technology and applications in food and bioprocessing.* Amsterdam ; London: Elsevier/Butterworth-Heinemann.

Lipnizki, F., Boelsmand, J. & Madsen, R.F. 2002. Concepts of industrial-scale diafiltration systems. *Desalination,* 144**,** 179-184.

Lister, V.Y., Lucas, C., Gordon, P.W., Chew, Y.M.J. & Wilson, D.I. 2011. Pressure mode fluid dynamic gauging for studying cake build-up in cross-flow microfiltration. *Journal of Membrane Science,* 366**,** 304-313.

Liu, J.-x., Li, J.-x., Chen, X.-m. & Zhang, Y.-z. 2006. Monitoring of polymeric membrane fouling in hollow fiber module using ultrasonic nondestructive testing. *Transactions of Nonferrous Metals Society of China,* 16**,** s845-s848.

Loulergue, P., Andréd, C., Lauxd, D., Ferrandisd, J.Y., Guigui, C. & Cabassud, C. 2011. In-situ characterization of fouling layers: Which tool for which measurement? *Desalination and Water Treatment,* 34**,** 156-162.

Luo, J., Ding, L., Chen, X. & Wan, Y. 2009. Desalination of soy sauce by nanofiltration. *Separation and Purification Technology,* 66**,** 429-437.

Mackley, M.R. & Sherman, N.E. 1992. Cross-flow cake filtration mechanisms and kinetics. *Chemical Engineering Science,* 47**,** 3067-3084.

Mairal, A.P., Greenberg, A.R. & Krantz, W.B. 2000. Investigation of membrane fouling and cleaning using ultrasonic time-domain reflectometry. *Desalination,* 130**,** 45-60.

Mairal, A.P., Greenberg, A.R., Krantz, W.B. & Bond, L.J. 1999. Real-time measurement of inorganic fouling of ro desalination membranes using ultrasonic time-domain reflectometry. *Journal of Membrane Science,* 159**,** 185-196.

Majid, R.A., Baharin, B.S., Ahmadun, F.L.-R. & Man, Y.B.C. 2000. Processing of crude palm oil with ceramic microfiltration membrane. *Journal of Food Lipids,* 7**,** 113-126.

Makardij, A., Chen, X.D. & Farid, M.M. 1999. Microfiltration and ultrafiltration of milk: Some aspects of fouling and cleaning. *Food and Bioproducts Processing: Transactions of the Institution of of Chemical Engineers, Part C,* 77**,** 107-113.

Malone, M.A., Jr. 2010. *Infrared microspectroscopy: A study of the single isolated bread yeast cell.* MSc Thesis, Ohio State University.

Manjula, S. & Subramanian, R. 2006. Membrane technology in degumming, dewaxing, deacidifying, and decolorizing edible oils. *Critical Reviews in Food Science and Nutrition,* 46**,** 569-592.

Marselina, Y., Le-Clech, P., Stuetz, R. & Chen, V. 2008. Detailed characterisation of fouling deposition and removal on a hollow fibre membrane by direct observation technique. *Desalination,* 231**,** 3-11.

Marselina, Y., Lifia, Le-Clech, P., Stuetz, R.M. & Chen, V. 2009. Characterisation of membrane fouling deposition and removal by direct observation technique. *Journal of Membrane Science,* 341**,** 163-171.

Mattsson, T., Martínez, E.L., Sedin, M. & Theliander, H. 2013. Local solidosity of microcrystalline cellulose during dead-end filtration and sedimentation. *Chemical Engineering Research and Design,* 91**,** 1155-1162.

Mattsson, T., Sedin, M. & Theliander, H. 2011. Zeta-potential and local filtration properties: Constitutive relationships for tio2 from experimental filtration measurements. *Chemical Engineering Science,* 66**,** 4573-4581.

Mattsson, T., Sedin, M. & Theliander, H. 2012a. Filtration properties and skin formation of micro-crystalline cellulose. *Separation and Purification Technology,* 96**,** 139-146.

Mattsson, T., Sedin, M. & Theliander, H. 2012b. On the local filtration properties of microcrystalline cellulose during dead-end filtration. *Chemical Engineering Science,* 72**,** 51-60.

McCarthy, A.A., Conroy, H., Walsh, P.K. & Foley, G. 1998a. The effect of pressure on the specific resistance of yeast filter cakes during dead-end filtration in the range 30–500kpa. *Biotechnology Techniques,* 12**,** 909-912.

McCarthy, A.A., O'Shea, D.G., Murray, N.T., Walsh, P.K. & Foley, G. 1998b. Effect of cell morphology on dead-end filtration of the dimorphic yeast kluyveromycesmarxianus var. Marxianus nrrly2415. *Biotechnology Progress,* 14**,** 279-285.

McCarthy, A.A., Walsh, P.K. & Foley, G. 2002. Characterising the packing and dead-end filter cake compressibility of the polymorphic yeast kluyveromyces marxianus var. Marxianus nrrly2415. *Journal of Membrane Science,* 198**,** 87-94.

Meireles, M., Clifton, M. & Aimar, P. 2002. Filtration of yeast suspensions: Experimental observations and modelling of dead-end filtration with a compressible cake. *Desalination,* 147**,** 19-23.

Mendret, J., Guigui, C., Schmitz, P. & Cabassud, C. 2009. In situ dynamic characterisation of fouling under different pressure conditions during dead-end filtration: Compressibility properties of particle cakes. *Journal of Membrane Science,* 333**,** 20-29.

Mendret, J., Guigui, C., Schmitz, P., Cabassud, C. & Duru, P. 2007. An optical method for in situ characterization of fouling during filtration. *AIChE Journal,* 53**,** 2265-2274.

Meng, F., Chae, S.-R., Drews, A., Kraume, M., Shin, H.-S. & Yang, F. 2009. Recent advances in membrane bioreactors (mbrs): Membrane fouling and membrane material. *Water Research,* 43**,** 1489-1512.

Merry, A. 2010. Chapter 3 - membrane processes in fruit juice processing. *In:* Cui & Muralidhara (eds.) *Membrane technology.* Oxford: Butterworth-Heinemann.

Middleman, S. 1998. *An introduction to fluid dynamics : Principles of analysis and design,* New York ; Chichester: Wiley.

Millipore. 2014. *Mf-millipore™ membrane filters* [Online]. Available: http://www.millipore.com/catalogue/module/C152#1 [Accessed 24th April 2014].

Miradlidhara, H.S. 2010. Challenges of membrane technology in the xxi century. *In:* Cui & Muralidhara (eds.) *Membrane technology : A practical guide to membrane technology and applications in food and bioprocessing.* Amsterdam ; London: Elsevier/Butterworth-Heinemann.

Mores, W.D. & Davis, R.H. 2001. Direct visual observation of yeast deposition and removal during microfiltration. *Journal of Membrane Science,* 189**,** 217-230.

Mores, W.D. & Davis, R.H. 2002a. Direct observation of membrane cleaning via rapid backpulsing. *Desalination,* 146**,** 135-140.

Mores, W.D. & Davis, R.H. 2002b. Yeast foulant removal by backpulses in crossflow microfiltration. *Journal of Membrane Science,* 208**,** 389-404.

Mulder, M. 1996. *Basic principles of membrane technology,* Dordrecht ; London: Kluwer.

Muralidhara, H.S. 2010. Chapter 2 - challenges of membrane technology in the xxi century. *In:* Cui & Muralidhara (eds.) *Membrane technology.* Oxford: Butterworth-Heinemann.

Murase, T., Ohn, T. & Kimata, K. 1995. Filtrate flux in crossflow microfiltration of dilute suspension forming a highly compressible fouling cake-layer. *Journal of Membrane Science,* 108**,** 121-128.

Muthukumaran, S., Kentish, S., Lalchandani, S., Ashokkumar, M., Mawson, R., Stevens, G.W. & Grieser, F. 2005. The optimisation of ultrasonic cleaning procedures for dairy fouled ultrafiltration membranes. *Ultrasonics Sonochemistry,* 12**,** 29-35.

Muthukumaran, S., Kentish, S.E., Stevens, G.W., Ashokkumar, M. & Mawson, R. 2007. The application of ultrasound to dairy ultrafiltration: The influence of operating conditions. *Journal of Food Engineering,* 81**,** 364-373.

Nakanishi, K., Tadokoro, T. & Matsuno, R. 1987. On the specific resistance of cakes of microorganisms. *Chemical Engineering Communications,* 62**,** 187-201.

Narong, P. & James, A.E. 2006. Effect of ph on the [zeta]-potential and turbidity of yeast suspensions. *Colloids and Surfaces A: Physicochemical and Engineering Aspects,* 274**,** 130-137.

Nghiem, L.D. & Schäfer, A.I. 2006. Fouling autopsy of hollow-fibre mf membranes in wastewater reclamation. *Desalination,* 188**,** 113-121.

Ochoa, N., Pagliero, C., Marchese, J. & Mattea, M. 2001. Ultrafiltration of vegetable oils: Degumming by polymeric membranes. *Separation and Purification Technology,* 22-23**,** 417-422.

Öhman, F., Theliander, H., Tomani, P. & Axegard, P. 2008. *Method for separating lignin from black liquor* US patent application 11/659,733.

Öhman, F., Wailmo, H. & Theliander, H. 2007a. A novel method for washing lignin precipitated from kraft black liquor - laboratory trials. *Nordic Pulp and Paper Research Journal,* 22**,** 9-16.

Öhman, F., Wallmo, H. & Theliander, H. 2007b. Precipitation and filtration of lignin from black liquor of different origin. *Nordic Pulp and Paper Research Journal,* 22**,** 188-193.

Okamoto, Y., Ohmori, K. & Glatz, C.E. 2001. Harvest time effects on membrane cake resistance of escherichia coli broth. *Journal of Membrane Science,* 190**,** 93-106.

Panco-GmbH. 2012. High resolution characterisation: Membrane applications. Available: http://www.inphaze.com.au/pubs/INPHAZE_WaterApp_RevA_4pages.pdf [Accessed 31st October 2012].

Park, J.-S., Choi, J.-H., Yeon, K.-H. & Moon, S.-H. 2006. An approach to fouling characterization of an ion-exchange membrane using current-voltage relation and electrical impedance spectroscopy. *Journal of Colloid and Interface Science,* 294**,** 129-138.

Pearce, G.K. 2007. The case for uf/mf pretreatment to ro in seawater applications. *Desalination,* 203**,** 286-295.

Pearce, G.K. 2012. Quantifying the benefit of membrane improvement on the total water cost of drinking water production. *Procedia Engineering,* 44**,** 204-205.

Peck, O.P.W., Bird, M.R., Bolhuis, A. & Chew, Y.M.J. 2013. Application of fluid dynamic gauging in the characterisation and removal of biofouling deposits. *In:* Malayeri, Müller-Steinhagen & Watkinson (eds.) *International Conference on Heat Exchanger Fouling and Cleaning*. Budapest, Hungary: Publico.

Peralta, J.M., Chew, Y.M.J. & Wilson, D.I. 2011a. An analytical method for selecting the optimal nozzle external geometry for fluid dynamic gauging. *Chemical Engineering Science,* 66**,** 3579-3591.

Peralta, J.M., Chew, Y.M.J. & Wilson, D.I. 2011b. Effect of nozzle external geometry on the pressure and shear stress exerted on the surface being gauged in fluid dynamic gauging. *Chemical Engineering Research and Design,* 89**,** 2540-2551.

Perry, R.H., Green, D.W. & Maloney, J.O. 1984. *Perry's chemical engineers' handbook,* London: McGraw-Hill.

Pope, J.M., Yao, S. & Fane, A.G. 1996. Quantitative measurements of the concentration polarisation layer thickness in membrane filtration of oil-water emulsions using nmr micro-imaging. *Journal of Membrane Science,* 118**,** 247-257.

Potters. 2011. Sphericel typical product characteristics. Available: http://www.pottersbeads.com/egm/NorthAmerica/Products/HollowInorganicMicrospheres/SPHERICEL.aspx.

Rahimi, M., Madaeni, S.S., Abolhasani, M. & Alsairafi, A.A. 2009. Cfd and experimental studies of fouling of a microfiltration membrane. *Chemical Engineering and Processing: Process Intensification,* 48**,** 1405-1413.

Richardson, J.F., Harker, J.H. & Backhurst, J.R. 2007a. Coulson and richardson's chemical engineering. *Particle Technology and Separation Processes.* 5th ed.: Elsevier.

Richardson, J.F., Harker, J.H. & Backhurst, J.R. 2007b. *Particle technology and separation processes,* Amsterdam; Boston: Butterworth-Heinemann.

Romero, C.A. & Davis, R.H. 1991. Experimental verification of the shear-induced hydrodynamic diffusion model of crossflow microfiltration. *Journal of Membrane Science,* 62**,** 249-273.

Sahoo, P.K., Chew, Y.M.J., Mercade-Prieto, R., Wilson, D.I. & Dai, X.W. 2008. Fluid dynamic gauging studies of swelling behaviour of whey protein gels in naoh/nacl solutions. *International Journal of Food Science and Technology,* 43**,** 1901-1907.

Santos, A., Ma, W. & Judd, S.J. 2011. Membrane bioreactors: Two decades of research and implementation. *Desalination,* 273**,** 148-154.

Sanz, M.A., Bonnélye, V. & Cremer, G. 2007. Fujairah reverse osmosis plant: 2 years of operation. *Desalination,* 203**,** 91-99.

Schluep, T. & Widmer, F. 1996. Initial transient effects during cross flow microfiltration of yeast suspensions. *Journal of Membrane Science,* 115**,** 133-145.

Schmitz, P. & Prat, M. 1995. 3-d laminar stationary flow over a porous surface with suction: Description at pore level. *AIChE Journal,* 41**,** 2212-2226.

Sedin, P., Johansson, C. & Theliander, H. 2003. On the measurement and evaluation of pressure and solidosity in filtration. *Chemical Engineering Research and Design,* 81**,** 1393-1405.

Sherwood, J.D. 1988. The force on a sphere pulled away from a permeable half-space. *Physicochemical Hydrodynamics,* 10**,** 3-12.

Sim, L.N., Wang, Z.J., Gu, J., Coster, H.G.L. & Fane, A.G. 2013a. Detection of reverse osmosis membrane fouling with silica, bovine serum albumin and their mixture using in-situ electrical impedance spectroscopy. *Journal of Membrane Science,* 443**,** 45-53.

Sim, S.T.V., Chong, T.H., Krantz, W.B. & Fane, A.G. 2012. Monitoring of colloidal fouling and its associated metastability using ultrasonic time domain reflectometry. *Journal of Membrane Science,* 401–402**,** 241-253.

Sim, S.T.V., Suwarno, S.R., Chong, T.H., Krantz, W.B. & Fane, A.G. 2013b. Monitoring membrane biofouling via ultrasonic time-domain reflectometry enhanced by silica dosing. *Journal of Membrane Science,* 428**,** 24-37.

Sondhi, R. & Bhave, R. 2001. Role of backpulsing in fouling minimization in crossflow filtration with ceramic membranes. *Journal of Membrane Science,* 186**,** 41-52.

Subramani, A. & Hoek, E.M.V. 2008. Direct observation of initial microbial deposition onto reverse osmosis and nanofiltration membranes. *Journal of Membrane Science,* 319**,** 111-125.

Suki, A., Fane, A.G. & Fell, C.J.D. 1984. Flux decline in protein ultrafiltration. *Journal of Membrane Science,* 21**,** 269-283.

Sun, C., Fiksdal, L., Hanssen-Bauer, A., Rye, M.B. & Leiknes, T. 2011. Characterization of membrane biofouling at different operating conditions (flux) in drinking water treatment using confocal laser scanning microscopy (clsm) and image analysis. *Journal of Membrane Science,* 382**,** 194-201.

Tien, C.H.J. & Chiang, B.E.H. 1992. Filtration of soy sauce by ceramic membrane. *Journal of Food Science,* 57**,** 740-742.

Tu, J., Yeoh, G.H. & Liu, C. 2008. *Computational fluid dynamics : A practical approach*, Boston ; Oxford: Butterworth-Heinemann.

Tuladhar, T.R., Paterson, W.R., Macleod, N. & Wilson, D.I. 2000. Development of a novel non-contact proximity gauge for thickness measurement of soft deposits and its application in fouling studies. *Canadian Journal of Chemical Engineering,* 78**,** 935-947.

Tuladhar, T.R., Paterson, W.R. & Wilson, D.I. 2002a. Investigation of alkaline cleaning-in-place of whey protein deposits using dynamic gauging. *Food and Bioproducts Processing,* 80**,** 199-214.

Tuladhar, T.R., Paterson, W.R. & Wilson, D.I. 2002b. Thermal conductivity of whey protein films undergoing swelling: Measurement by dynamic gauging. *Food and Bioproducts Processing,* 80**,** 332-339.

Tuladhar, T.R., Paterson, W.R. & Wilson, D.I. 2003. Dynamic gauging in duct flows. *Canadian Journal of Chemical Engineering,* 81**,** 279-284.

Uchymiak, M., Bartman, A.R., Daltrophe, N., Weissman, M., Gilron, J., Christofides, P.D., Kaiser, W.J. & Cohen, Y. 2009. Brackish water reverse osmosis (bwro) operation in feed flow reversal mode using an ex situ scale observation detector (exsod). *Journal of Membrane Science,* 341**,** 60-66.

Uchymiak, M., Rahardianto, A., Lyster, E., Glater, J. & Cohen, Y. 2007. A novel ro ex situ scale observation detector (exsod) for mineral scale characterization and early detection. *Journal of Membrane Science,* 291**,** 86-95.

van der Sman, R.G.M., Vollebregt, H.M., Mepschen, A. & Noordman, T.R. 2012. Review of hypotheses for fouling during beer clarification using membranes. *Journal of Membrane Science,* 396**,** 22-31.

Vrouwenvelder, J.S., Bakker, S.M., Wessels, L.P. & van Paassen, J.A.M. 2007. The membrane fouling simulator as a new tool for biofouling control of spiral-wound membranes. *Desalination,* 204**,** 170-174.

Vrouwenvelder, J.S., van Paassen, J.A.M., Wessels, L.P., van Dam, A.F. & Bakker, S.M. 2006. The membrane fouling simulator: A practical tool for fouling prediction and control. *Journal of Membrane Science,* 281**,** 316-324.

Wakeman, R.J. 1994. Visualization of cake formation in cross-flow microfiltration. *Chemical Engineering Research & Design,* 72**,** 530-540.

Wallberg, O., Jönsson, A.-S. & Wimmerstedt, R. 2003. Fractionation and concentration of kraft black liquor lignin with ultrafiltration. *Desalination,* 154**,** 187-199.

Wan, Y., Luo, J. & Cui, Z. 2010. Chapter 4 - membrane application in soy sauce processing. *In:* Cui & Muralidhara (eds.) *Membrane technology.* Oxford: Butterworth-Heinemann.

Wang, G. & Chen, H. 2013. Fractionation of alkali-extracted lignin from steam-exploded stalk by gradient acid precipitation. *Separation and Purification Technology,* 105**,** 98-105.

WHO 2008. Guidelines for drinking-water quality. Geneva: World Health Organisation.

Wicaksana, F., Fane, A.G., Pongpairoj, P. & Field, R. 2012. Microfiltration of algae (chlorella sorokiniana): Critical flux, fouling and transmission. *Journal of Membrane Science,* 387–388**,** 83-92.

Wung, N., Acott, S., Tosh, D. & Ellis, M. 2014. Hollow fibre membrane bioreactors for tissue engineering applications. *Biotechnology Letters,* 36**,** 2357-2366.

Xu, X., Li, J., Li, H., Cai, Y., Cao, Y., He, B. & Zhang, Y. 2009a. Non-invasive monitoring of fouling in hollow fiber membrane via utdr. *Journal of Membrane Science,* 326**,** 103-110.

Xu, X., Li, J., Xu, N., Hou, Y. & Lin, J. 2009b. Visualization of fouling and diffusion behaviors during hollow fiber microfiltration of oily wastewater by ultrasonic reflectometry and wavelet analysis. *Journal of Membrane Science,* 341**,** 195-202.

Yang, Q., Ali, A., Shi, L. & Wilson, D.I. 2014. Zero discharge fluid dynamic gauging for studying the thickness of soft solid layers. *Journal of Food Engineering,* 127**,** 24-33.

Yao, S., Costello, M., Fane, A.G. & Pope, J.M. 1995. Non-invasive observation of flow profiles and polarisation layers in hollow fibre membrane filtration modules using nmr micro-imaging. *Journal of Membrane Science,* 99**,** 207-216.

Ye, Y., Chen, V. & Le-Clech, P. 2011. Evolution of fouling deposition and removal on hollow fibre membrane during filtration with periodical backwash. *Desalination,* 283**,** 198-205.

Zamani, F., Wicaksana, F., Taheri, A.H., Law, A.W.K., Fane, A.G. & Krantz, W.B. 2014. Generalized criterion for the onset of particle deposition in crossflow microfiltration via dotm – modeling and experimental validation. *Journal of Membrane Science,* 457**,** 128-138.

Zhang, Y.P., Fane, A.G. & Law, A.W.K. 2006. Critical flux and particle deposition of bidisperse suspensions during crossflow microfiltration. *Journal of Membrane Science,* 282**,** 189-197.

Zhang, Y.P., Fane, A.G. & Law, A.W.K. 2010. Critical flux and particle deposition of fractal flocs during crossflow microfiltration. *Journal of Membrane Science,* 353**,** 28-35.

Zhang, Z.X., Greenberg, A.R., Krantz, W.B. & Chai, G.Y. 2003. Study of membrane fouling and cleaning in spiral wound modules using ultrasonic time-domain reflectometry. *In:* Dibakar & Butterfield (eds.) *Membrane science and technology.* Elsevier.

Zydney, A.L. & Colton, C.K. 1986. A concentration polarization model for the filtrate flux in cross-flow microfiltration of particulate suspensions. *Chemical Engineering Communications,* 47**,** 1-21.

Appendix

List of Appendices

A. Derivations for calculations relevant to sections 4.2.3 and 7.3.2

B. Explanation of algorithm applied to critical flux analysis (sections 5.3.5, 7.3.6, and 7.4.5)

C. Details of membrane permeability experiment

D. Data acquisition calculations used in VIs for both sets of experimental apparatus

E. Design documents for automated cross-flow rig.

A. Derivations for calculations

A1. Calculation of ballotini particle density

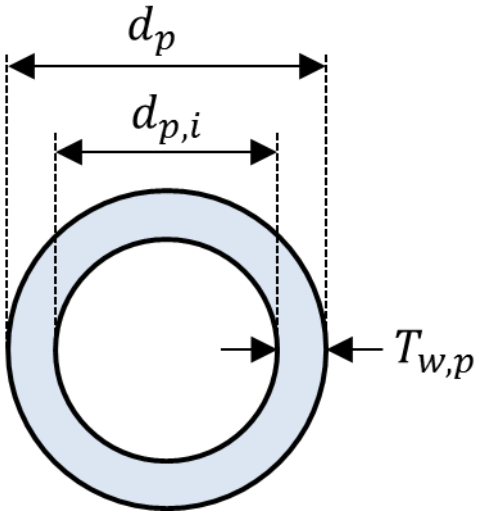

Figure A1. Dimensions of hollow spherical particle, where d_p and $d_{p,i}$ are the total and inner diameters respectively, and $T_{w,p}$ is the wall thickness. The shaded region indicates the actual glass material of the particle.

A hollow spherical particle is represented in Figure A1. The wall thickness of the particle is given by:

$$T_{w,p} = \frac{1}{2}\left(d_p - d_{p,i}\right) \tag{A1}$$

The total volume of material in a single particle is given by:

$$V_{material} = \frac{4}{3}\pi\left(\left(\frac{d_p}{2}\right)^3 - \left(\frac{d_{p,i}}{2}\right)^3\right) \tag{A2}$$

$$V_{material} = \frac{1}{6}\pi\left(d_p^3 - d_{p,i}^3\right) \tag{A3}$$

and the total volume of the particle itself, V_p, is:

$$V_p = \frac{1}{6}\pi d_p^3 \tag{A4}$$

Given the density for borosilicate glass, ρ_{glass} = 2230 kg·m^{-3} *, it is possible to compute the actual particle density, ρ_p by:

$$\rho_p = \frac{\rho_{glass} V_{material}}{V_p} = \frac{\rho_{glass}\left(d_p^3 - d_{p,i}^3\right)}{d_p^3} \tag{A5}$$

Hence the inner particle diameter can be given by:

$$d_{p,i} = d_p \left(1 - \frac{\rho_p}{\rho_{glass}}\right)^{\frac{1}{3}} \tag{A6}$$

$d_{p,i}$ was estimated for each type of ballotini using $d_p = d_{3,2}$ for each particle, and ρ_p was given by the manufacturer, as stated in Table 4.4. The minimum d_p at which particles were considered buoyant was calculated using the lower wall thickness, $T_{w,p}$, of the two types of ballotini, whilst the maximum d_p for the buoyant region was calculated using the higher wall thickness.

A2. Correction for mass over-estimation

The estimation of extra lignin deposition on the cake surface, discussed in section 7.3.2, is estimated by assuming the entire length of the test section is full of lignin suspension (with the extra 1 mm recess discounted). This gives a total chamber volume, $V_{chamber}$, of:

$$V_{chamber} = 15 \times 250 \times 15\ [mm] = 5.6 \times 10^{-5}\ m^3 \tag{A7}$$

Given that the concentration of lignin was ϕ_b = 0.02 vol%, the bulk concentration of dry lignin is given by:

$$c_b = \phi_b \rho_p \tag{A8}$$

which gives: c_b = 0.27 kg·m^{-3}. Hence the extra mass per unit area is given by:

$$\frac{M_c}{A_m} = \frac{c_b V_{chamber}}{A_m} \tag{A9}$$

This gives 0.675 mg·mm^{-2}.

*Compound Summary for: CID 24261, http://pubchem.ncbi.nlm.nih.gov/, accessed 23/09/2014

B. Algorithm for critical flux analysis

The results shown in sections 5.3.5, 7.2.6, and 7.3.5 required an algorithmic process in order to determine a transition flux, J_T, and locate the region wherein a reasonable linear fit to equation (2.20) exists between $f(J)$ and J. The algorithm described below was processed using a set of Matlab® scripts. Beginning with raw flux data, this determined $f(J)$ for each value of n, and subsequently used an iterative process to determine J_T, J^*, and k.

B1. Smoothing of flux data

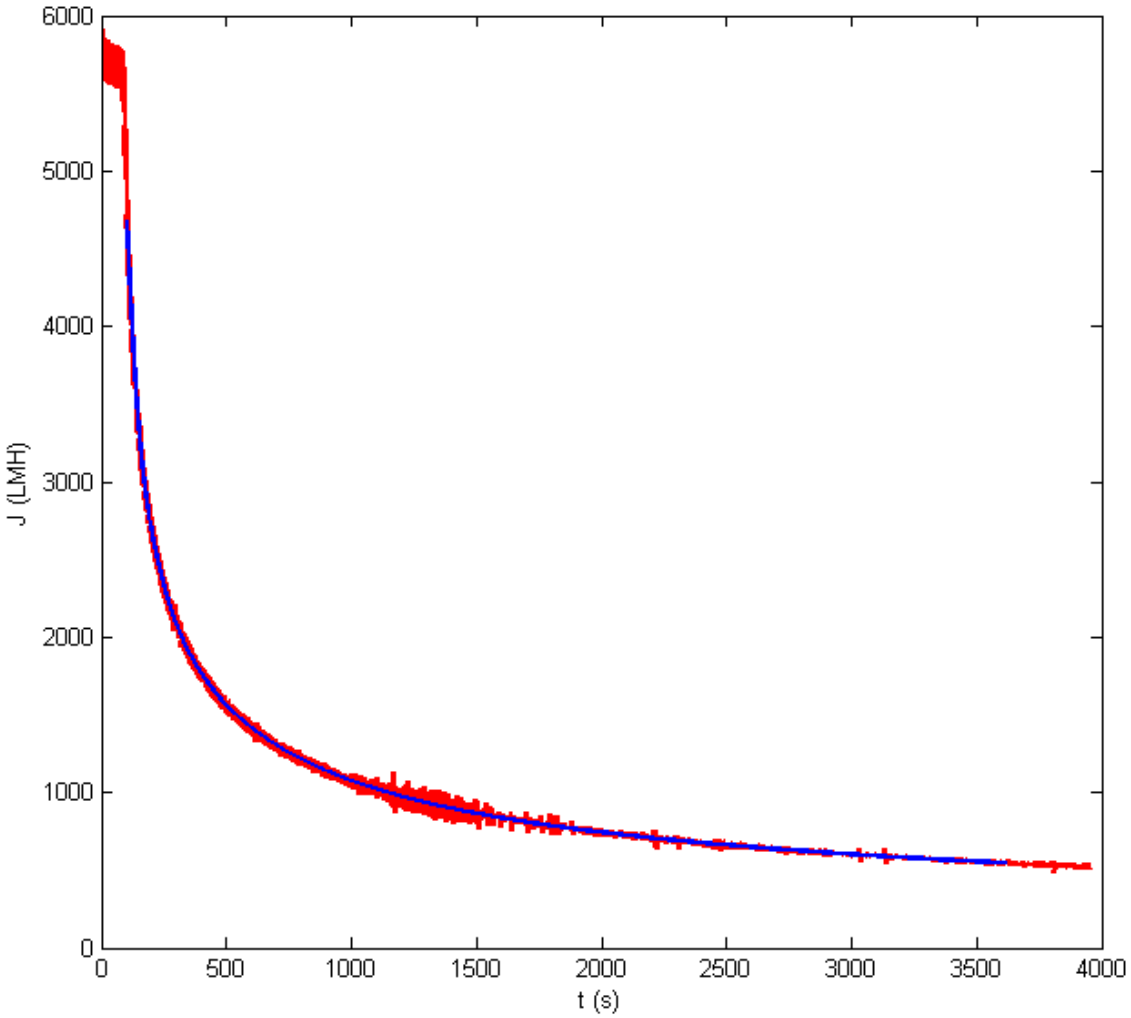

Figure A2. Example of raw flux data (shown in red) and smoothing spline (blue) as displayed by Matlab®. This data is from a 60P18 ballotini filtration at Re_{duct} = 1550 and TMP = 50 mbar

The first step required reducing noise in the flux data. This was achieved by fitting a spline curve to the J vs. t data provided by experiments using the following steps:

1. Loading J vs. t data from the raw spreadsheet file
2. Removing data before the first 100 seconds
3. Removing data after the termination time of the experiment (usually at 3620 s)
4. Using the inbuilt curve-fitting functions a smoothing spline curve was fitted to the remaining J vs. t data using a smoothing parameter of 1×10^{-5}.
   An example of the resulting curve is shown in Figure A2.

B2. Processing of $f(J)$

Equation (2.20) was used to produce a set of $f(J)$ vs. J data from the smoothing spline curve (as shown in Figure A2) by the following method:

1. The a set of J vs. t data was produced for 10,000 graduations of t.
2. Regular intervals of J were specified by:

$$J_{interval} = \frac{J_{max} - J_{min}}{200} \tag{A10}$$

3. Across each interval, dJ/d_t was determined by linear regression. This was matched to corresponding values of t and J at the mid-point of each interval.
4. Three different values for $f(J)$, for $n = 0$, 1, and 2, were determined according to equation (2.20).
5. The resulting data provided an array of 200 J values with a corresponding $f(J)$ array for each n value.

B3. Determine linear fit parameters where $n = 0$

For the cake filtration law, where $n = 0$, the values of J_T, and subsequently J^* and k, were derived as described below. This step was performed using $f(J)$ vs. J data attained as described above, an example of which is shown in Figure A3. Example data for $f(J)$ vs. J where $n = 0$. Dashed lines indicate (blue) $J_{T,max}$ and (green) J_T from iterative method. The solid lines indicate the corresponding linear fit for each. This data is from a 60P18 ballotini filtration at Re_{duct} = 1550 and TMP = 50 mbar.Figure A3. In this step, $f(J)$ vs. J was assumed to produce a linear fit between the minimum value of J and J_T.

1. The maximum and minimum values for $f(J)$ were determined, along with corresponding J values.
2. An maximum guess value for the transition flux, J_T, was given by:

$$J_{T,max} = 0.9\, max\big(f(J)\big) \tag{A11}$$

3. A minimum guess for J_T was given by:

$$J_{T,min} = 0.5\, max\big(f(J)\big) \tag{A12}$$

4. Iterating between $J_{T,min}$ and $J_{T,max}$, linear regression between $f(J)$ and J was performed for the range $J_{min} \rightarrow J_T$, where J_{min} is the minimum J value for the current data. From each fit, the goodness of fit, R^2, was recorded. This resulted in arrays of k, J^*, and R^2, each corresponding to s specific guess value for J_T.
5. The best fit data for J_T, J^*, and k was determined as that which corresponded to the maximum R^2 value.
6. This fit, along with that where $J_T = J_{T,max}$ was presented to the user; an example of this plot is shown in Figure A3.

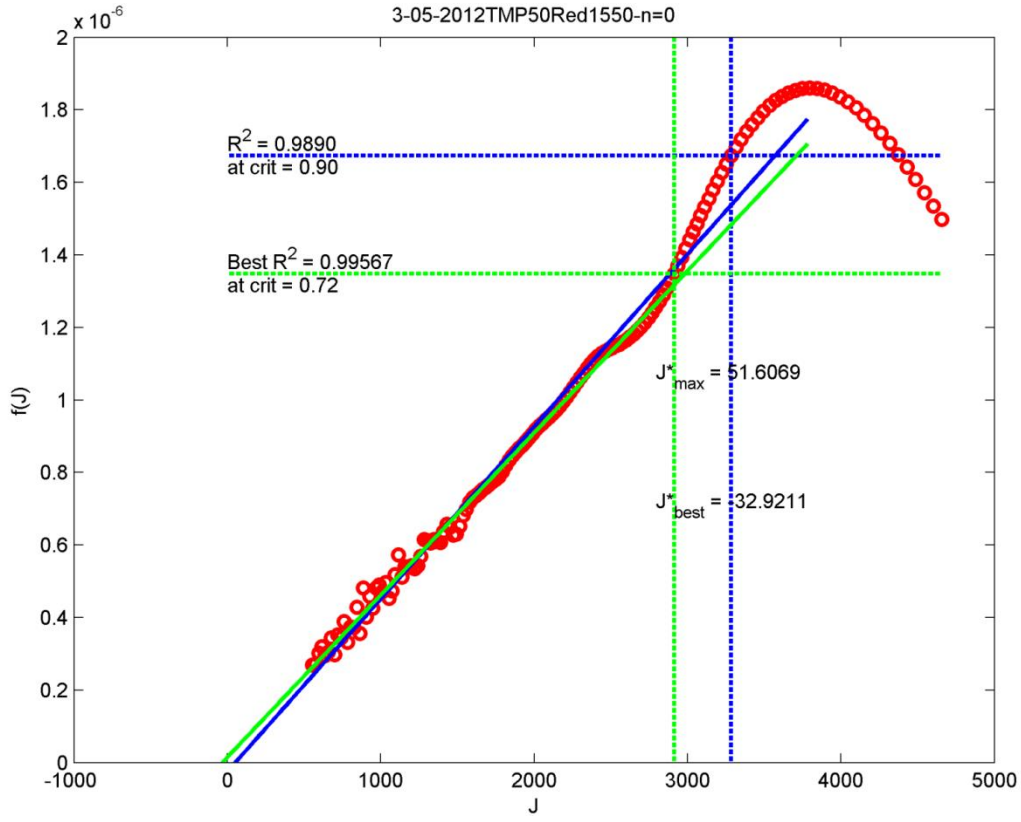

Figure A3. Example data for $f(J)$ vs. J where n = 0. Dashed lines indicate (blue) $J_{T,max}$ and (green) J_T from iterative method. The solid lines indicate the corresponding linear fit for each. This data is from a 60P18 ballotini filtration at Re_{duct} = 1550 and TMP = 50 mbar.

7. User input was required to determine one of the following options:
    a. Accept the best fit determined by maximum R^2

b. Use fit for $J_T = J_{T,max}$

c. Set J_T manually

8. In almost all cases, option a was selected. On rare occasions, a more appropriate fit was given where $J_T = J_{T,max}$, or by setting manually, for which an adjustments to J_T could be viewed by an additional plot line (not shown on figure).

B4. Determine linear fit parameters where n = 1 or 2

A similar method as that described above was used to determined parameters for the intermediate and standard blocking laws where n = 1 and 2 respectively. Here a linear fit could not be assumed to extend from the minimum value of J. A reasonable assumption, given that these laws should apply towards the start of the filtrations, was that a linear fit region exists between J_T (to be determined) and a maximum limit for J. Example plots for these two laws are shown in Figure A4.

(a) (b)

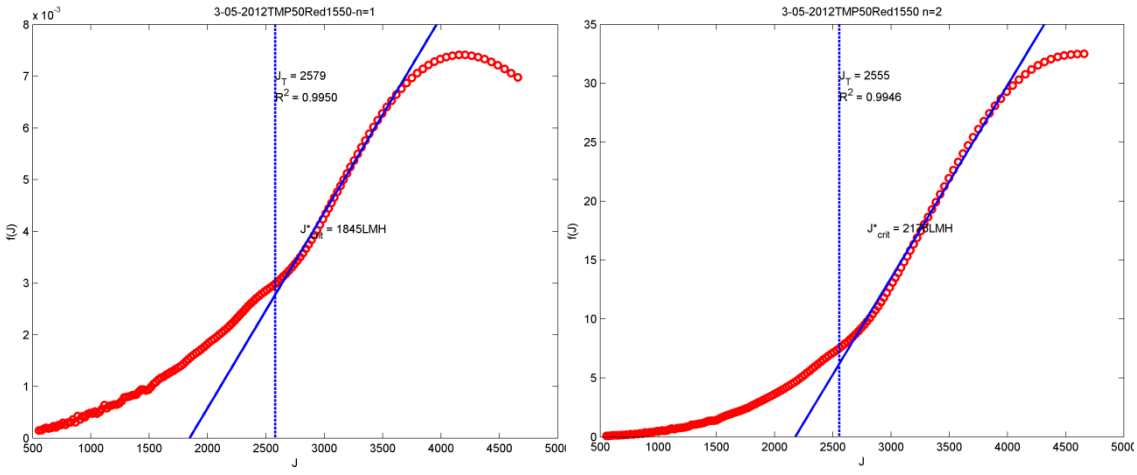

Figure A4. Example data for $f(J)$ vs. J where (a) n = 1, and (b) n = 2. Dashed lines indicate J_T as derived by the iterative method described below, and solid lines indicate the resulting linear fit.

1. An maximum guess value for the transition flux, J_T, was given by:

$$J_{T,max} = 0.9\, max\big(f(J)\big) \tag{A13}$$

2. An iterative method was performed to find J_T by reducing stepwise from $J_{T,max}$, starting a minimum of five steps from $J_{T,max}$. This used the array of J produced as described in section B2. A linear fit was performed within the range $J_T \rightarrow J_{T,max}$. The iterations were halted when $R^2 < 0.995$. In effect, this

is aimed to produce a value for J_T where the experimental data begins to deviate from the blocking law as described by equation (2.20).

3. Iterating between $J_{T,min}$ and $J_{T,max}$, linear regression between $f(J)$ and J was performed within the range $J_{T,min} < J_T \leq J_{T,max}$ From each fit, the goodness of fit, R^2, was recorded. This resulted in arrays of k, J^*, and R^2, each corresponding to s specific guess value for J_T.
4. The best fit data for J_T, J^*, and k was determined as that which corresponded to the maximum R^2 value.
5. This fit was presented to the user, an example of this plot is shown in Figure A4.
6. User input was used to determine one of the following options:
    a. Use fit determined automatically
    b. Set J_T manually
7. In almost all cases, a was selected. On rare occasions, a more appropriate fit was given by setting J_T manually, for which an adjustments to J_T could be viewed by an additional plot line (not shown on figure). This also included the option to alter the value of $J_{T,max}$.

C. Membrane permeability tests

C1. Method

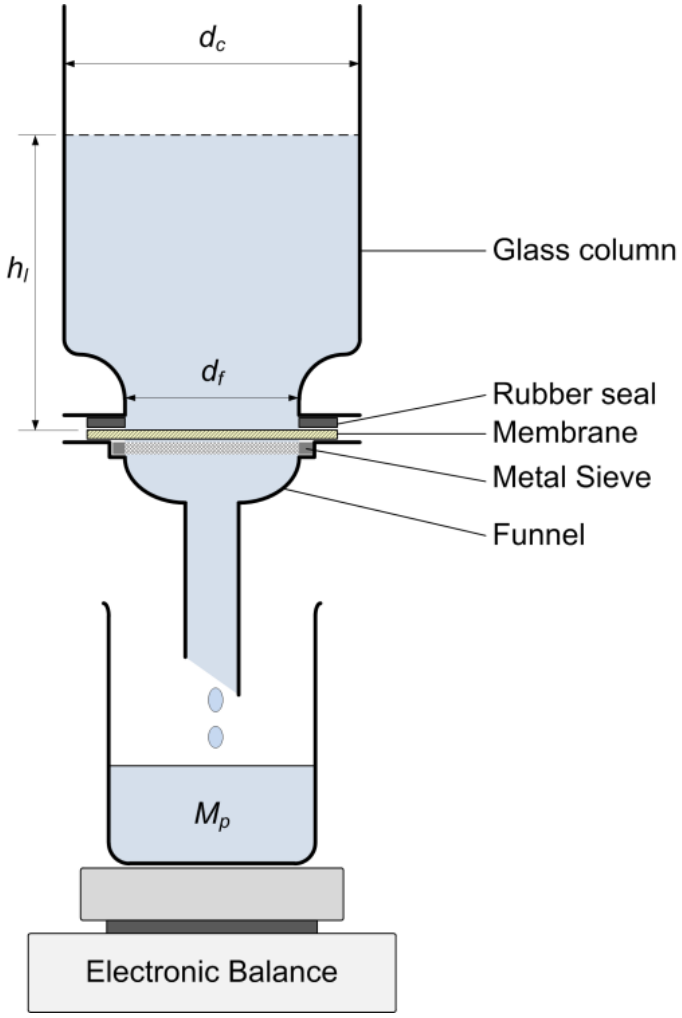

Figure A5. Dead-end filtration apparatus used to determine R_m, where d_c is the internal diameter of the glass column, d_f is the diameter of the membrane filter, h_l is the liquid level above the membrane, and M_p is the permeate mass on the balance.

Membrane resistance was characterised using dead-end filtration apparatus as shown in Figure A5, using a similar technique to that employed by Lister *et al.* (2011). The mass of RO water, M_p, flowing through the membrane was measured by an electronic balance connected to a data-logging PC, and used to estimate R_m through linear regression using the following equation:

$$\therefore ln\left(\frac{h_l}{h_{l,0}}\right) = -\left(\frac{d_f^2}{d_c^2}\right)\frac{\rho g}{\mu}\frac{1}{R_m}t \tag{A14}$$

where $h_{l,0}$ is the height of liquid, h_l, above the membrane at time t = 0. From the above equation R_m can be estimated from the inverse gradient of a linear plot of $\ln(h_l/h_{l,0})$ vs. t. The liquid level is calculated from M_p by:

$$h_l = h_{l,0} - \frac{(M_p - M_{p,0})}{\rho}\frac{\pi d_c^2}{4} \tag{A15}$$

where $M_{p,0}$ is the mass of permeate recorded by the balance at time t = 0. In all test, the initial liquid level, $h_{l,0}$, was set to 100 mm.

C2. Derivation for equation (A15)

The flow through the dead-end filtration apparatus shown in Figure A5 can be described by Darcy's law, where pressure is given by static head, h_l:

$$J = -\left(\frac{d_c^2}{d_f^2}\right)\frac{dh_l}{dt} = \frac{TMP}{\mu R_m} = \frac{\rho_L g h_l}{\mu R_m} \tag{A16}$$

This can be integrated to give:

$$\int_{h_{l_0}}^{h_l} \frac{1}{h_l}.dh_l = -\left(\frac{d_f^2}{d_c^2}\right)\frac{\rho g}{\mu}\frac{1}{R_m}\int_0^t .dt \tag{A17}$$

$$\therefore ln\left(\frac{h_l}{h_{l0}}\right) = -\left(\frac{d_f^2}{d_c^2}\right)\frac{\rho g}{\mu}\frac{1}{R_m}t \tag{A18}$$

D. Data acquisition and error calculation

Both the duct flow apparatus described in section 4.1 and the automated apparatus described in section 6.2 required the processing of large datasets. This section describes how pressure, flow, and thickness values were derived within the VIs along with their associated error.

D1. Data acquisition for duct flow rig

Data was acquired in a control loop which repeated at a frequency of $1/t_{CL}$, where t_{CL} is an adjustable control loop time. For the experiments described in this work, t_{CL} = 750 ms. The variables were calculated for a constantly updating array of values, represented in Figure A6, with a width defined by the number of different readings taken, and a length N. For each command loop iteration the oldest value on the array at the point $i = N$, was deleted, and a new row of data was added to the array at i = 1. This meant that for each iteration of the command loop, new values of measured variables would be produced based on those in the updated array.

t_1	$M_{g,1}$	$M_{p,1}$	$\Delta p_{14,1}$	TMP_1
…	…	…	…	…
t_i	$M_{g,i}$	$M_{p,i}$	$\Delta p_{14,i}$	TMP_i
…	…	…	…	…
t_N	$M_{g,N}$	$M_{p,N}$	$\Delta p_{14,N}$	TMP_N

Figure A6. Array used for calculation of variables in LabView™ VI for duct flow rig.

The individual variables were calculated as described below and fed into a new array which included error estimates and other calculations.

D1.1 Time, t

Because the readings taken were representative for a timespan of $N \times t_{CL}$ the corresponding time for each of these readings was given by the mid-point of this timespan:

$$t = \frac{(t_1 + t_N)}{2} \tag{A19}$$

D1.2 Gauging flow, m_g:

m_g was determined using linear regression method as the following gradient:

$$m_g = \frac{dM_g}{dt} \tag{A20}$$

error was given by the root mean squared residual divided by t_{CL}

D1.3 Permeate flow, m_p:

$m_p$was determined using linear regression method as the following gradient:

$$m_g = \frac{dM_g}{dt} \tag{A21}$$

error was given by the root mean squared residual divided by t_{CL}

D1.4 Gauging pressure, Δp_{14}:

This was determined as the average pressure across the array:

$$\Delta p_{14} = \frac{1}{N}\sum_{i=1}^{N} \Delta p_{14,i} \tag{A22}$$

and error was given by standard deviation.

D1.5 Transmembrane pressure, TMP:

This was determined as the average pressure

$$TMP = \frac{1}{N}\sum_{i=1}^{N} TMP_i \tag{A23}$$

and error was given by standard deviation

D1.6 Discharge Coefficient, C_d:

This was calculated from the values above, using equations (2.34) and (2.35).

D1.7 Apparent height, h, and deposit thickness, δ_c:

This was estimated by linear interpolation of the calibration profile (C_d vs. h/d_t and later Δp_{13} vs. h/d_t) to find the closest estimate for h/d_t. This was the multiplied by d_t to give h. Cake thickness, δ_c was then given by:

$$\delta_c = h_0 - h \tag{A24}$$

D2. Data acquisition for automated cross-flow rig

The LabView™ VI used to control and monitor the automated cross-flow filtration apparatus described in section 6.2 produced data through similar methods as described above for the duct flow rig. The key difference for this one was that the number of data points across which flowrates and averages were calculated could be varied for each different variable recorded.

Data was acquired in a control loop which repeated at a frequency of $1/t_{CL}$, where t_{CL} is an adjustable control loop time. For the experiments described in this work, t_{CL} = 500 ms. The variables were calculated for a constantly updating array of values, represented in Figure A7, with a width defined by the number of different readings taken, and a total length N. A total length of N = 20 was used, and for each loop iteration, the first row was deleted to maintain this array size.

t_1	$M_{p,1}$	$\Delta p_{14,1}$	TMP_1
…	…	…	…
t_i	$M_{p,i}$	$\Delta p_{14,i}$	TMP_i
…	…	…	…
t_N	$M_{p,N}$	$\Delta p_{14,N}$	TMP_N

Figure A7. Array used for calculation of variables in LabView™ VI for automated rig.

The individual variables were calculated as described below and transferred into a new array which included error estimates and other calculations.

D2.1 Time, t

Each variable calculated from the array in Figure A7 was determined across an individually controlled time period, t_{var}. This required that the returned value be

realigned to the correct time, t_i for each. This was achieved by reinserting them into a new array at the correct location offset from t_1.

D2.2 Data points specific to each variable, N_{var}

The number of data points across which each variable was calculated, N_{var} is defined by:

$$N_{var} = \frac{t_{var}}{t_{CL}} \tag{A25}$$

which was rounded to the nearest odd number. This meant that the dataset used, defined as the array $1{:}\,N_{var}$, was always symmetric about a central value at i, which determined the time point to which the derived variable corresponded.

D2.3 Permeate flow, m_p

Permeate flow was calculated from the difference in permeate mass, M_p, across a time period defined on the VI (item 7 on Figure 6.6):

$$m_p = \frac{M_{p,N_{var}} - M_{p,1}}{t_{N,var} - t_1} \tag{A26}$$

The error was defined as:

$$\delta(m_p) = \frac{\delta M_p}{t_{N,var} - t_1} \tag{A27}$$

D2.4 Average differential pressure, $\overline{\Delta p_{14}}$

Δp_{14} was averaged across the range defined on the VI (item 4 on Figure 6.6). This was given by the following formula:

$$\overline{\Delta p_{14}} = \frac{1}{N_{var}} \sum_{i=1}^{N_{var}} \Delta p_{14,i} \tag{A28}$$

The error in Δp_{14} readings was taken to be the standard deviation across this range.

D2.5 Average TMP:

TMP was averaged across the range defined on the VI (item 8 on Figure 6.6). This was given by the following formula:

$$\overline{TMP} = \frac{1}{N_{var}} \sum_{i=1}^{N_{var}} TMP_i \tag{A29}$$

The error in TMP readings was taken to be the standard deviation across this range.

D2.6 Gauging pressure, Δp_{13}

This was calculated from the above values, using equation (2.35).

D2.7 Apparent height, h, and deposit thickness, δ_c:

This was estimated by linear interpolation of the calibration profile (Δp_{13} vs. h/d_t) to find the closest estimate for h/d_t. This was the multiplied by d_t to give h. Cake thickness, δ_c was then given by:

$$\delta_c = h_0 - h \tag{A30}$$

D3. Error calculation for δ_c measurements

The overall error in δ_c measurements is given by:

$$\delta(\delta_c) = \sqrt{(\delta h_0)^2 + (\delta h)^2} \tag{A31}$$

where for the original duct flow apparatus: δh_0 = ± 5 μm, and for the newer, automated apparatus: δh_0 = ± 0.5 μm. These values assume no error due to positioning of the membrane.

The error in estimated clearance, h, is given by the upper and lower interpolated values from C_d vs. h/d_t or Δp_{13} vs. h/d_t calibration profiles. This results in a difference between positive and negative errors due to the shape of calibration profiles. An example of the process for a thickness measurement using Δp_{13} is shown in Figure A8, wherein it is evident that the negative error in h is smaller than the positive error, despite equal error margins for Δp_{13}.

The error in Δp_{13} is defined as:

$$\delta(\Delta p_{13}) = \sqrt{\left(\delta(\Delta p_{14})\right)^2 + \left(\delta(\Delta p_{34})\right)^2} \tag{A32}$$

for which the error in Δp_{34} is defined by:

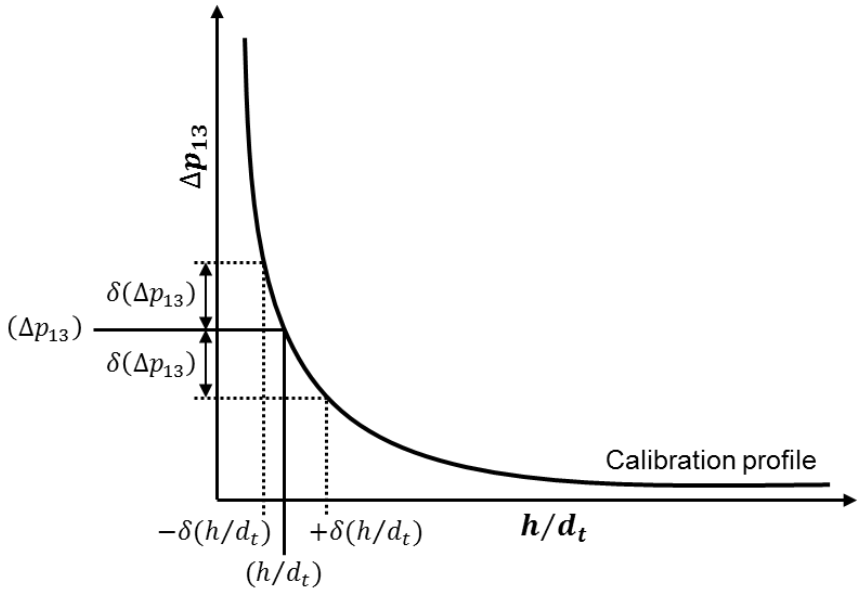

Figure A8. Derivation of error in h/d_t from a Δp_{13} vs. h/d_t calibration profile.

$$\delta(\Delta p_{34}) = \Delta p_{34}\sqrt{\left(\frac{\delta(\mu)}{\mu}\right)^2 + \left(\frac{\delta(m_g)}{m_g}\right)^2 + \left(\frac{\delta(\rho_L)}{\rho_L}\right)^2} \tag{A33}$$

in which error in μ and ρ_L are considered negligible. The error in m_g is also considered negligible for experiments performed using the automated apparatus.

When using calibration plots with C_d to predict h/d_t, the following error is applied:

$$\delta(C_d) = C_d\sqrt{\left(\frac{\delta(m_g)}{m_g}\right)^2 + \left(\frac{1}{2}\frac{\delta(\rho_L)}{\rho_L}\right)^2 + \left(\frac{1}{2}\frac{\delta(\Delta p_{13})}{\Delta p_{13}}\right)^2} \tag{A34}$$

where error in ρ_L is considered negligible.

D4. Error calculation for τ_w

The results of destructive strength measurements used an analytical estimation for maximum fluid shear stress given by equation (2.38). The error in this is calculated by:

$$\delta(\tau_w) = \tau_w\sqrt{\left(\frac{\delta(\mu)}{\mu}\right)^2 + \left(\frac{\delta(m_g)}{m_g}\right)^2 + \left(\frac{\delta(\rho)}{\rho}\right)^2 + \left(2\frac{\delta(h)}{h}\right)^2} \tag{A35}$$

in which errors for μ and ρ_L are considered negligible, as is the error in m_g for results using the automated cross-flow rig.

E. Design documents for automated cross-flow rig

Pages A-18 to A-38 contain design documents produced by Paul Frith for the apparatus described in section 6.2. A total of 21 drawings are provided here, which are summarised in Table A2.

Table A2. Descriptions of design drawings for automated cross-flow rig

Number	Description	Page
922/GA	Full design assembly for the test section, where annotations 1 to 20 refer to subsequent drawings	A-18
922/1	Upper part of test section	A-19
922/2	Removable lower part of test section	A-20
922/3	Stationary lower end piece of test section	A-21
922/4	Stationary lower end piece of test section	A-22
922/5	500 mm entry section (15 mm square duct)	A-23
922/6	50 mm exit section (15 mm square duct)	A-24
922/7	Tapping screw used to secure bleed pipe beneath membrane	A-25
922/8	Outlet tube for permeate	A-26
922/9	Pressure tapping tube(s)	A-27
922/10	Viewing window for test section	A-28
922/11	Bottom plate of membrane cassette (see section 6.2.2)	A-29
922/12	Top plate of membrane cassette (see section 6.2.2)	A-30
922/13	Curved spacer for membrane cassette (see section 6.2.2)	A-31
922/14	Flat spacer for membrane cassette (see section 6.2.2)	A-32
922/15	FDG gauge nozzle and tube	A-33
922/16	Outer part of gauge clamp (for fixing to linear guide rail)	A-34
922/17	Inner part of gauge clamp (for fixing to linear guide rail)	A-35
922/18	Bracket for fixing linear guide rail to test section (N.B. this was replaced with a thicker bracket to reduce flexibility)	A-36
922/19	Blanking plate to seal unused FDG tapping holes	A-37
922/20	Sealing plate to secure o-ring around moving FDG gauging tube	A-38

922/GA: Full design assembly

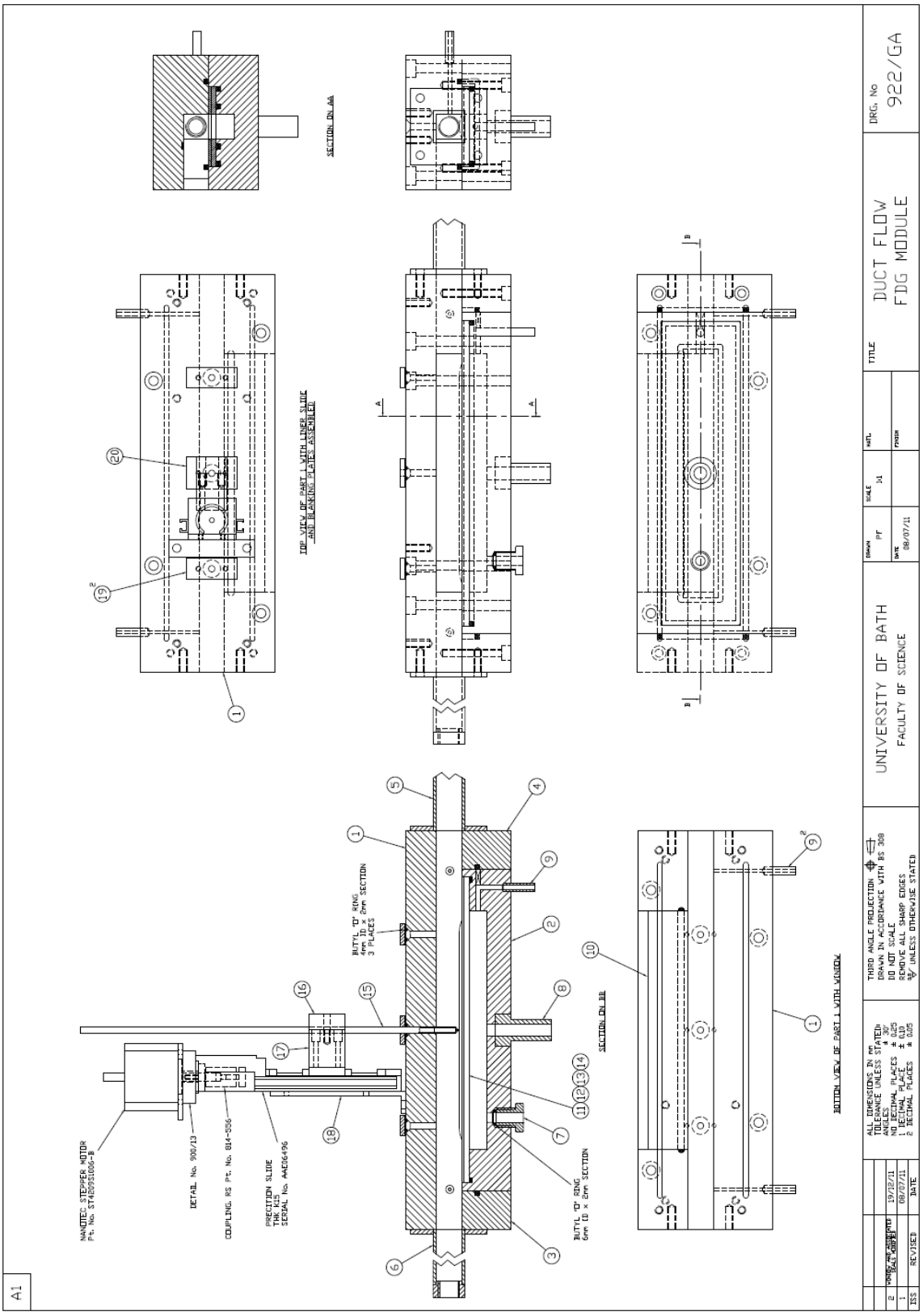

922/1: Top of test section

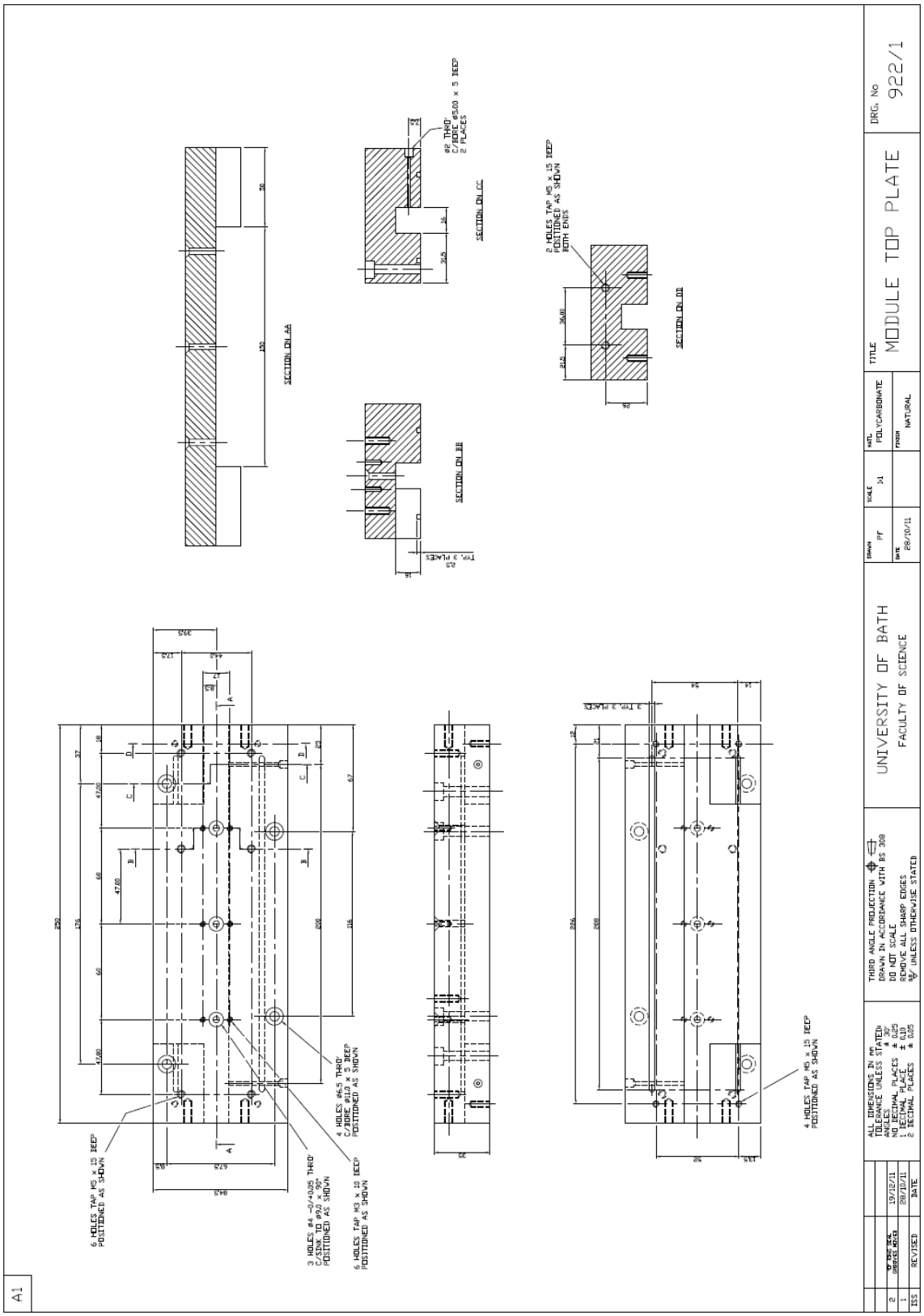

922/2: Removable base of test section

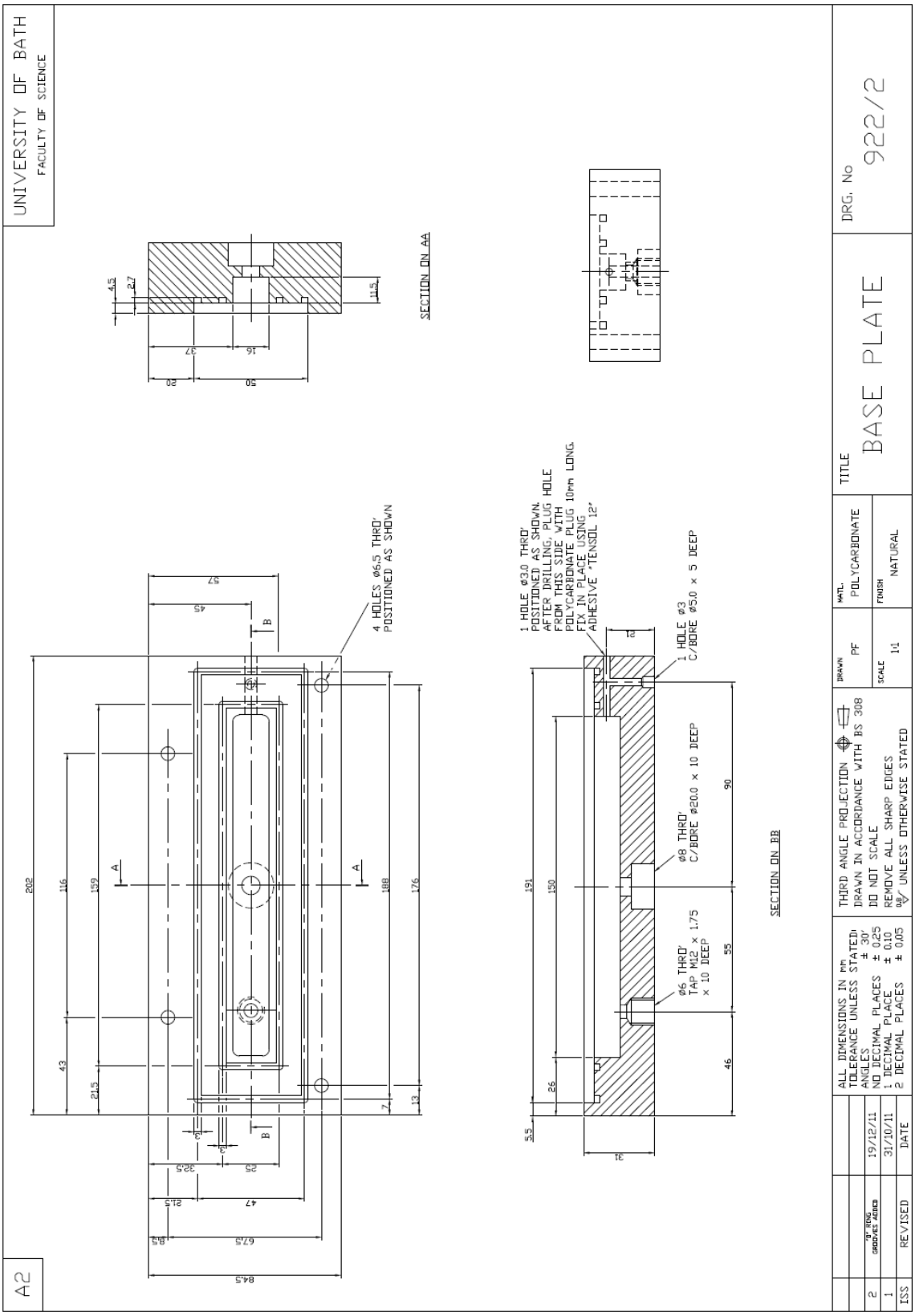

922/3: Non-removable side of test section base

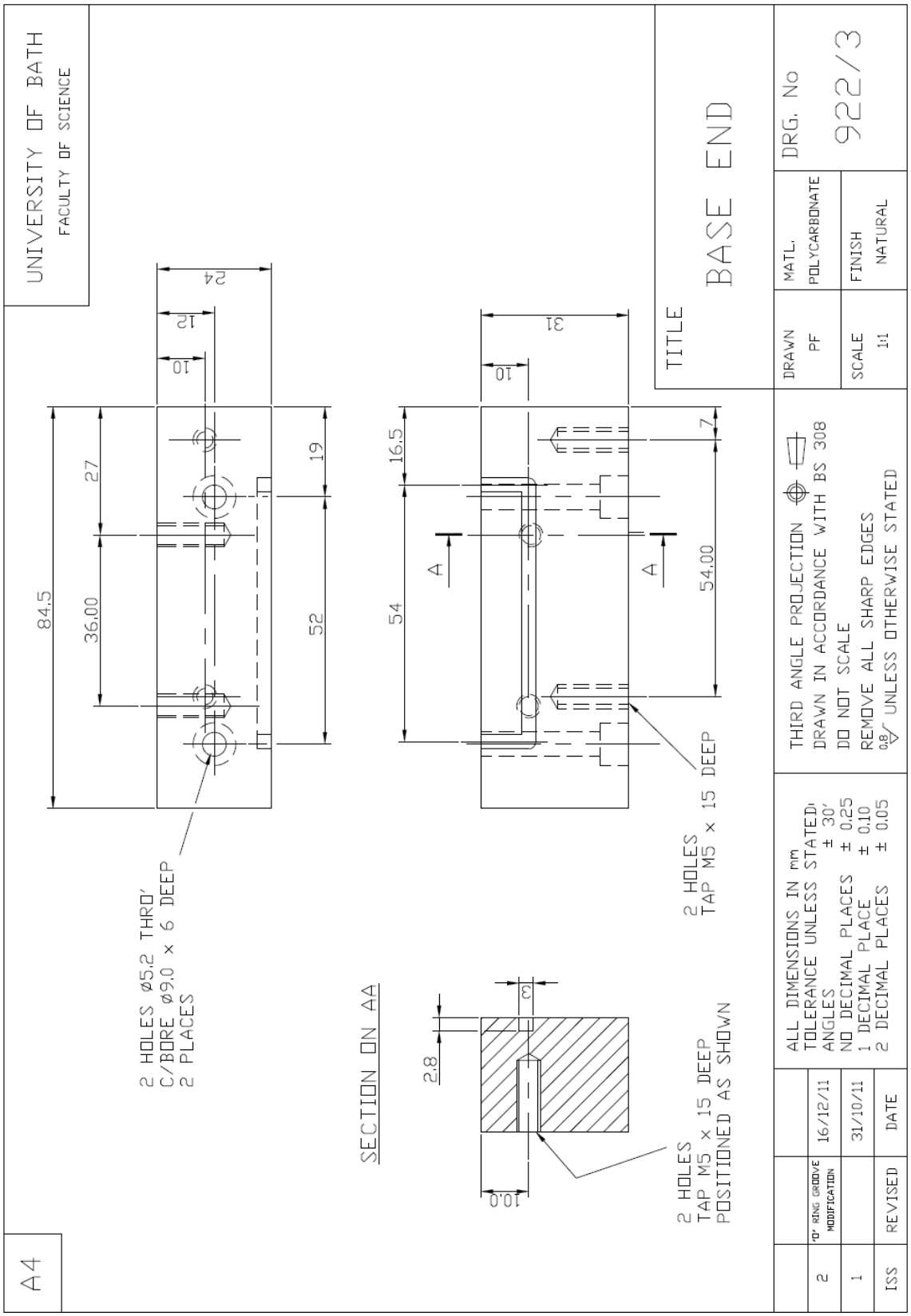

922/4: Non-removable side of test section base

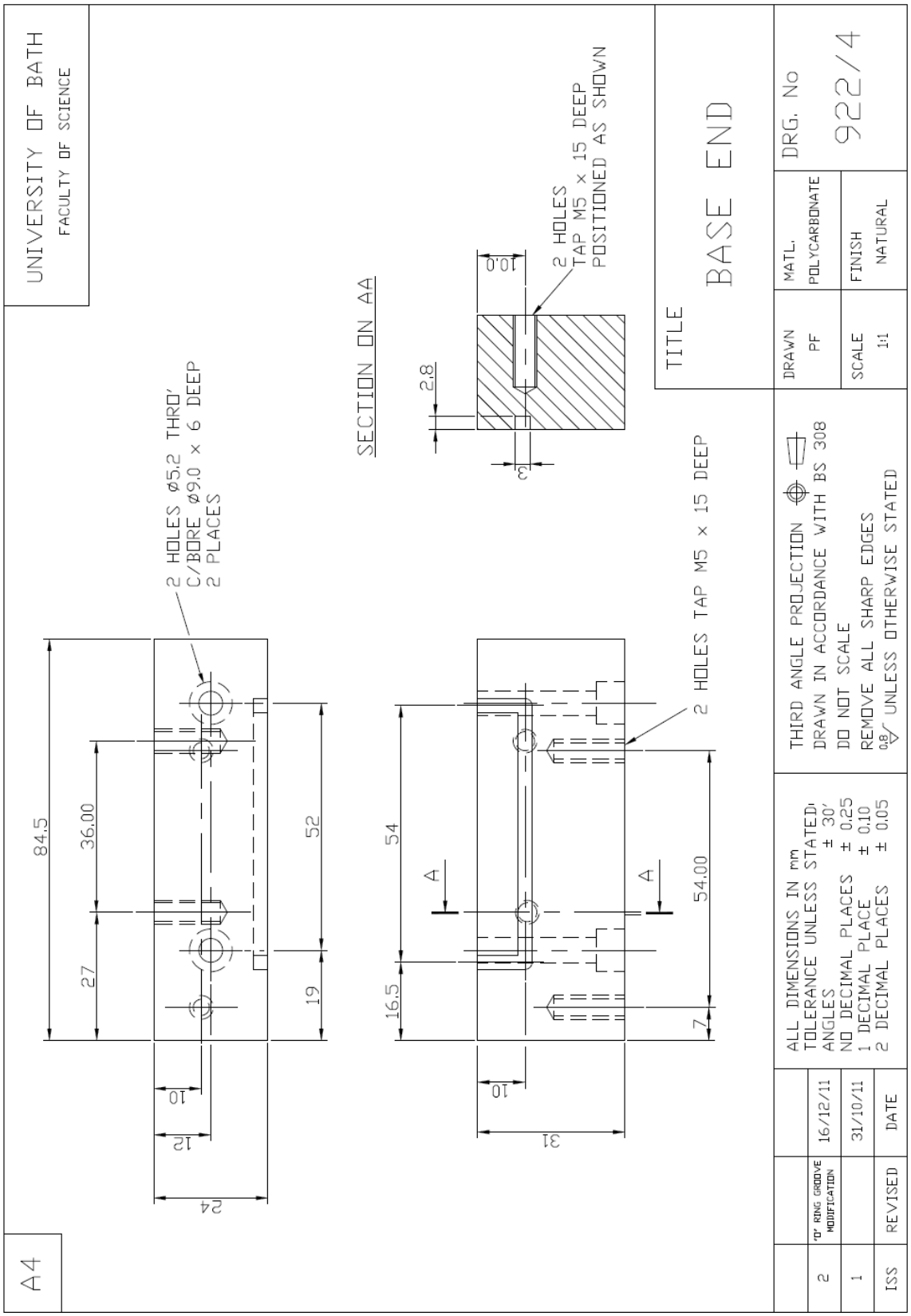

922/5: Square entry section

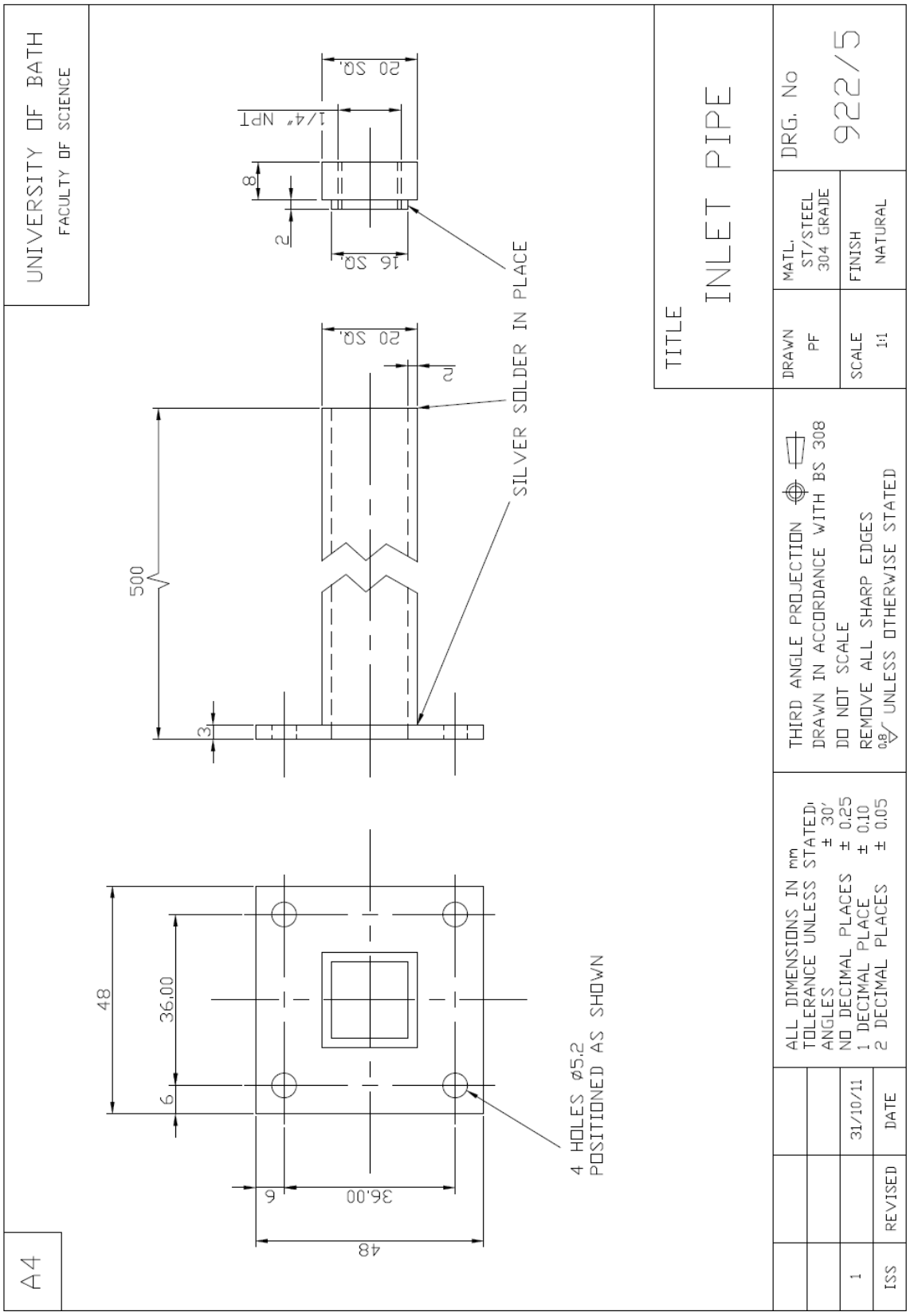

922/6: Square exit section

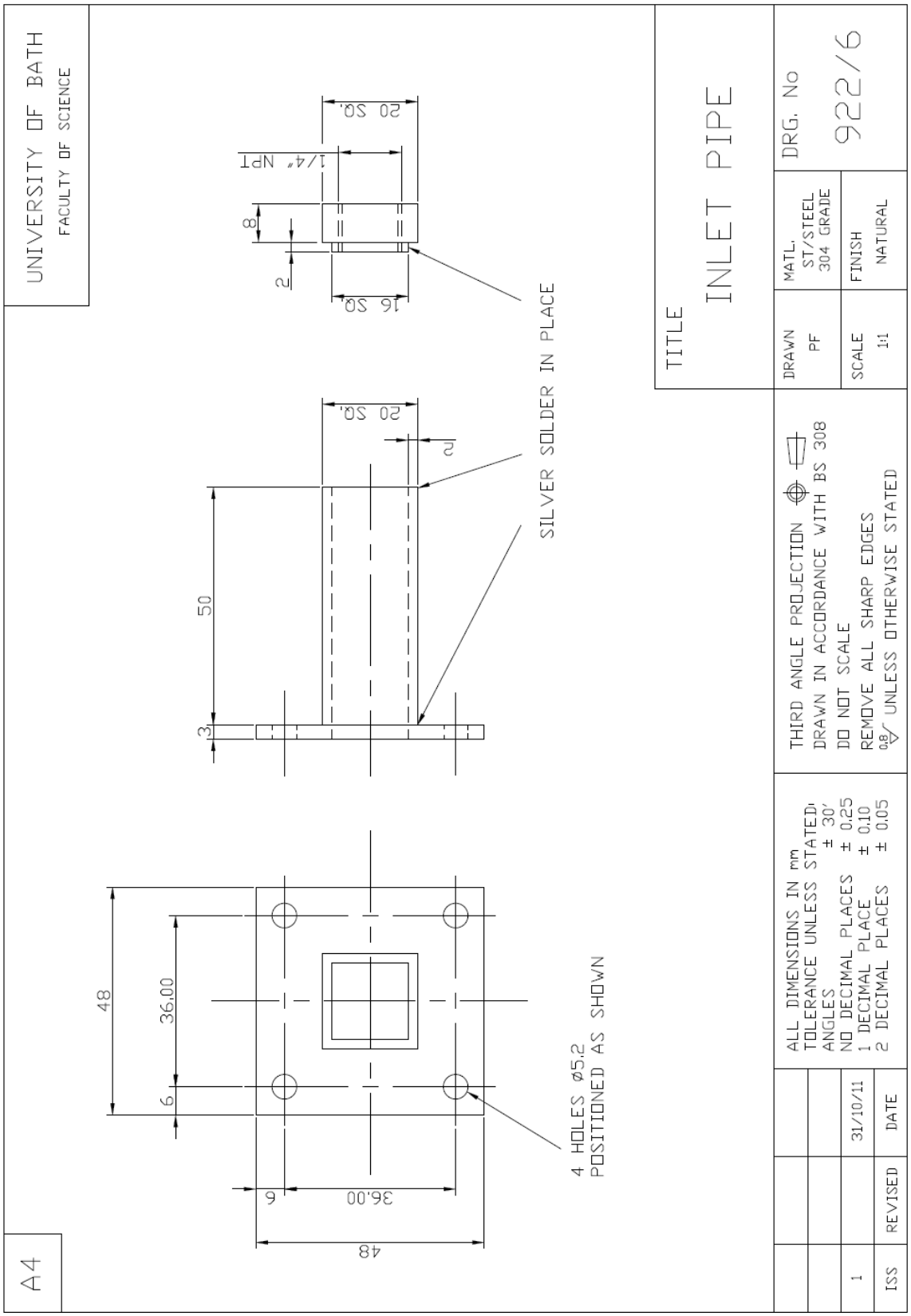

922/7: Tapping screw for adjustable height bleed tube

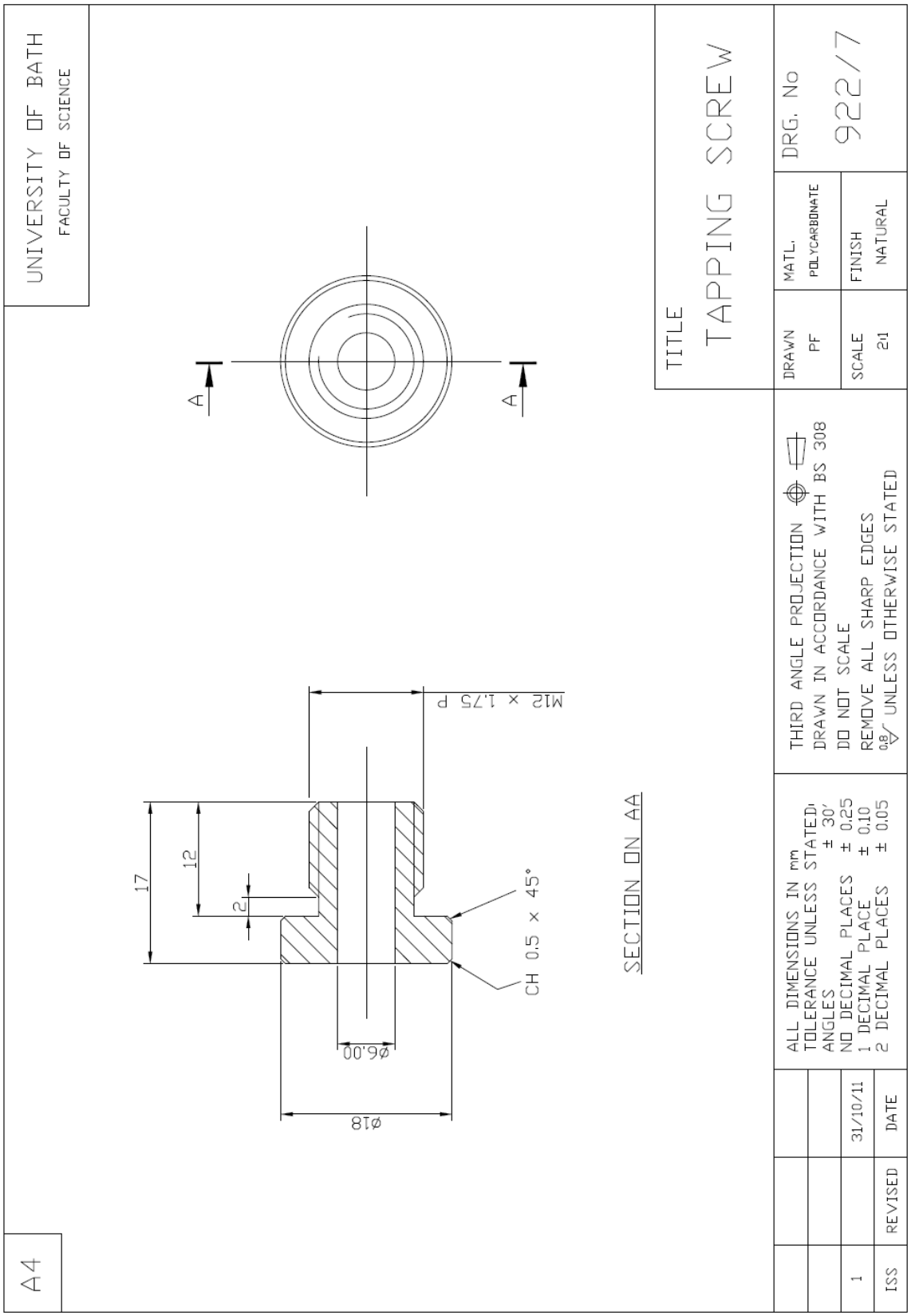

922/8: Outlet tube for permeate

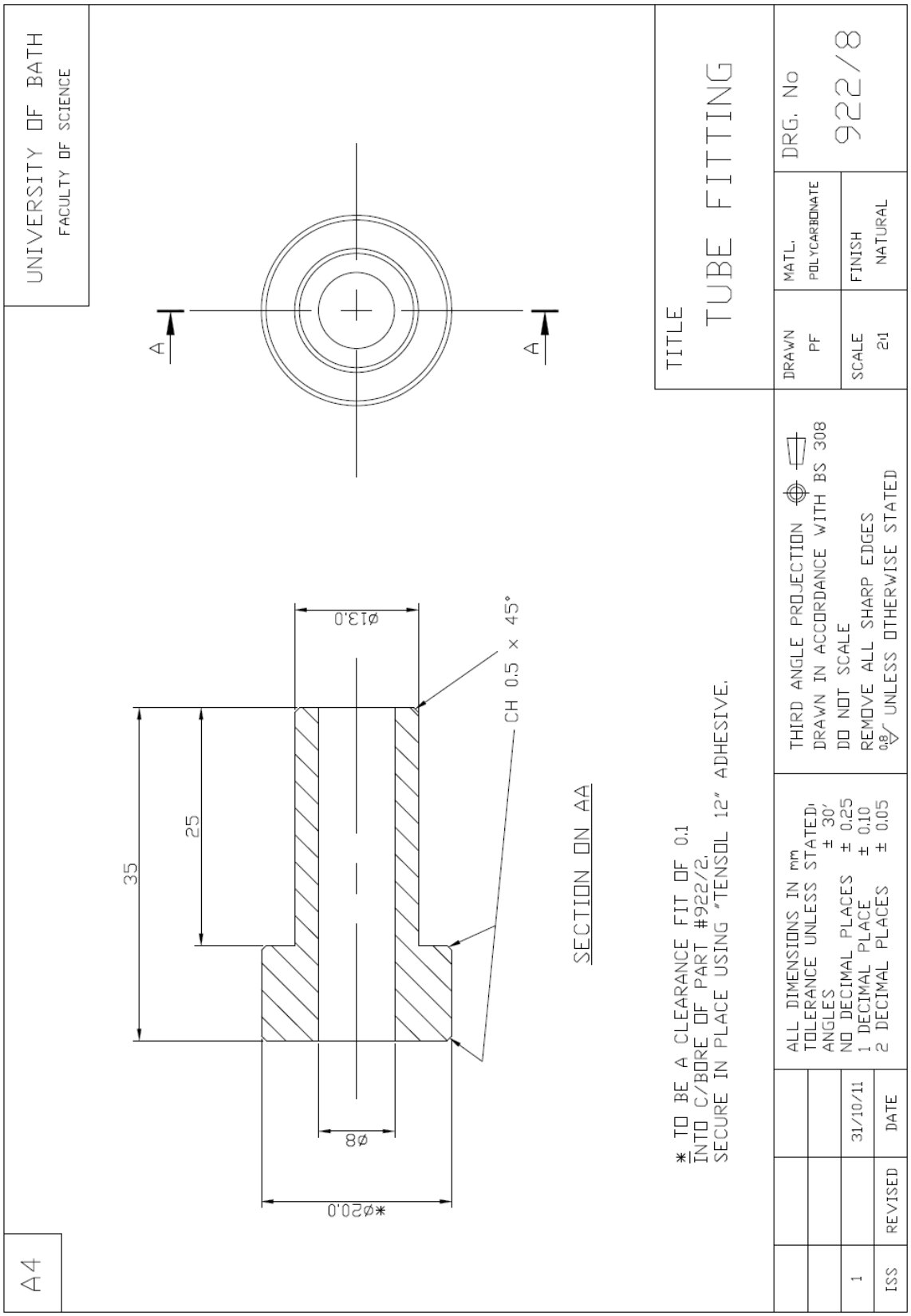

922/9: Pressure tapping tube

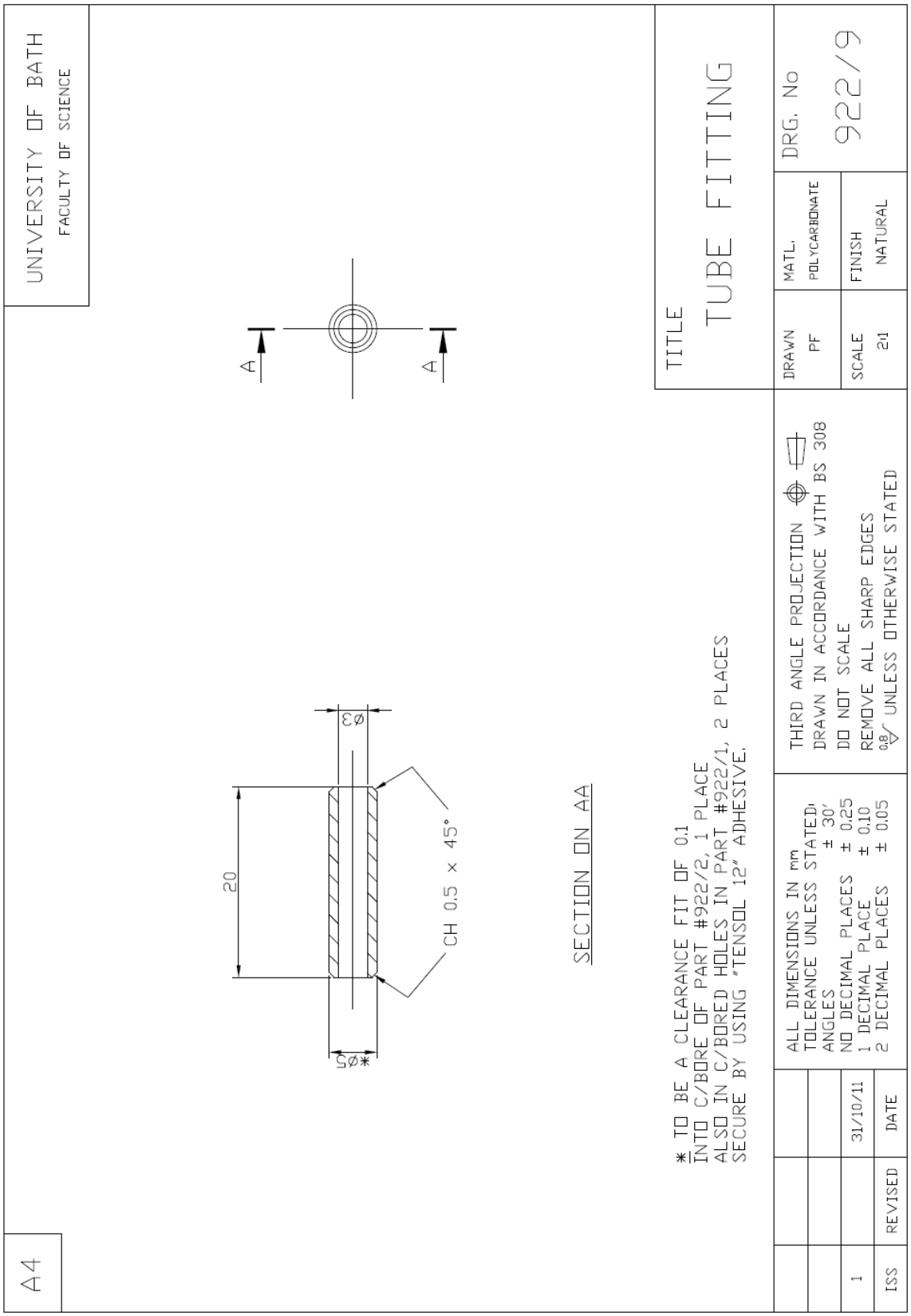

922/10: Test section viewing window

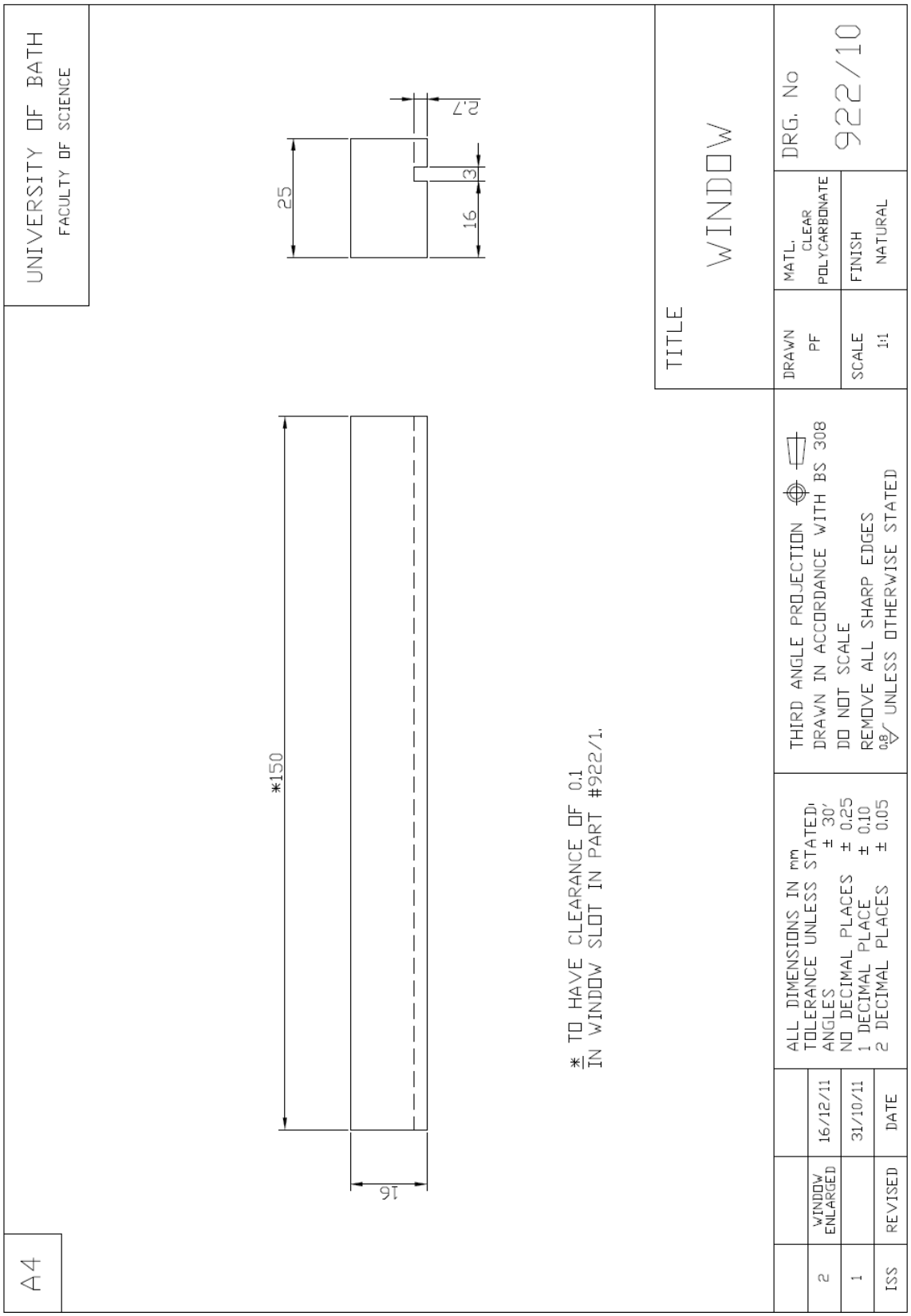

922/11: Membrane cassette base section

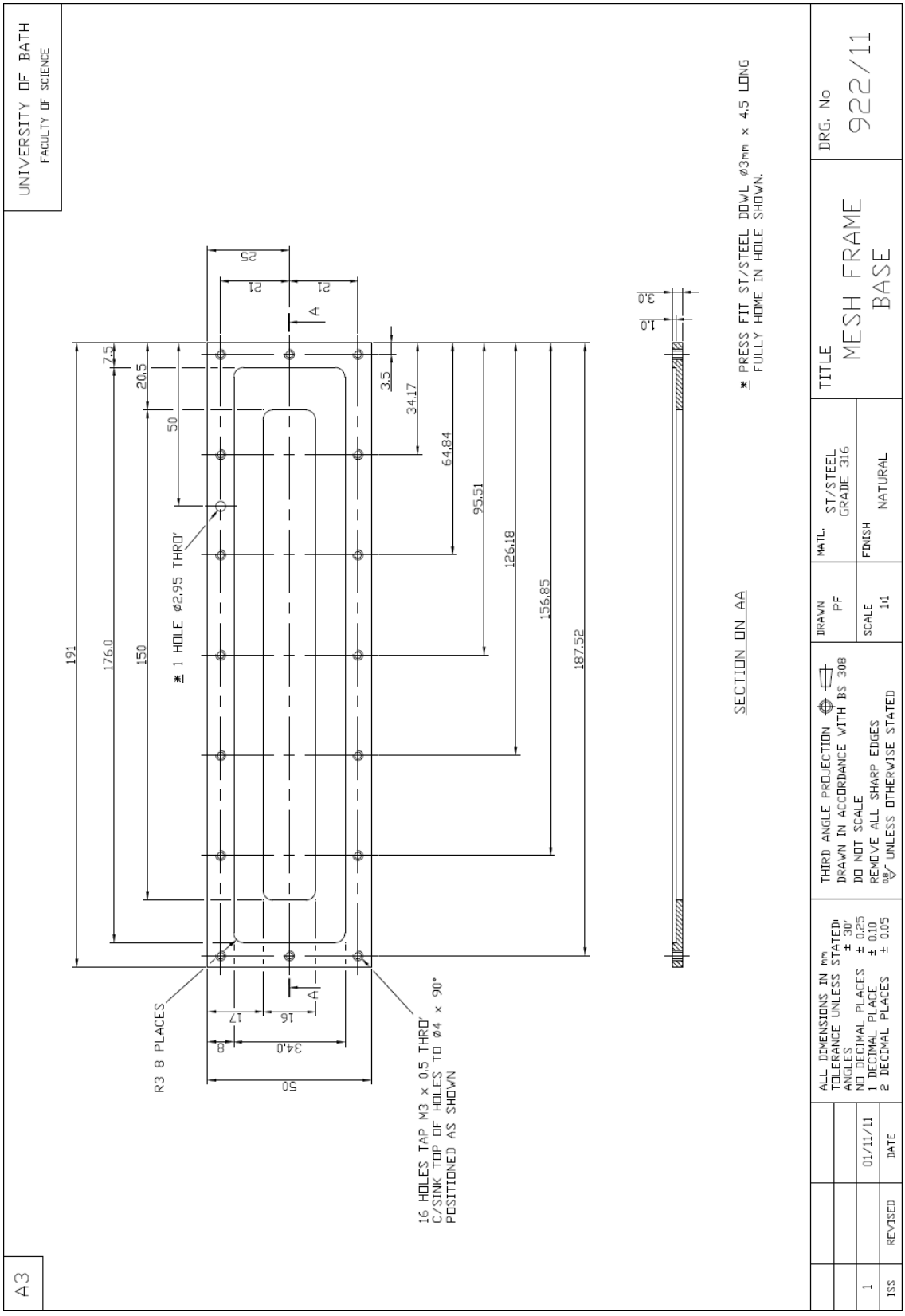

922/12: Membrane cassette top plate

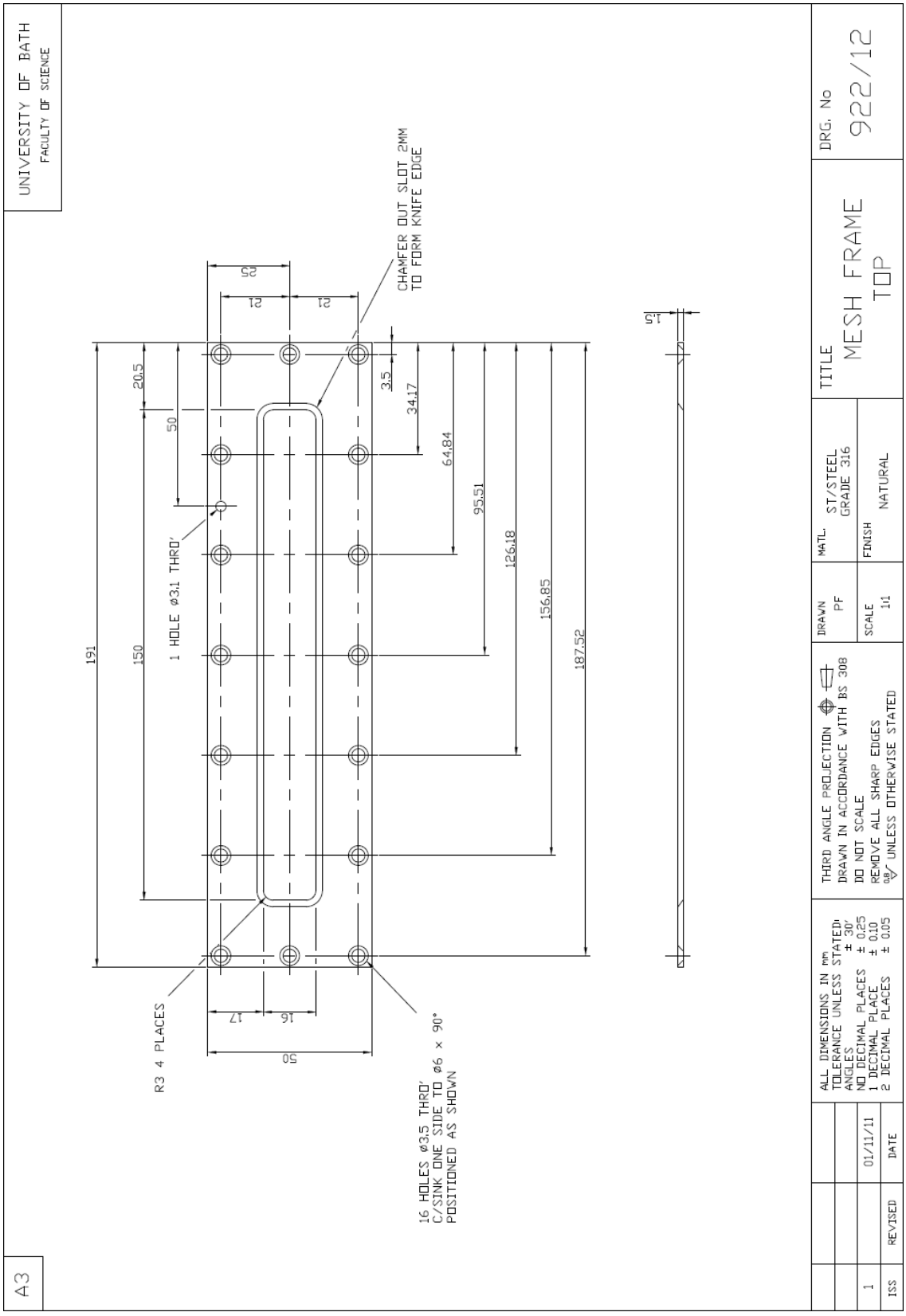

922/13: Curved membrane support

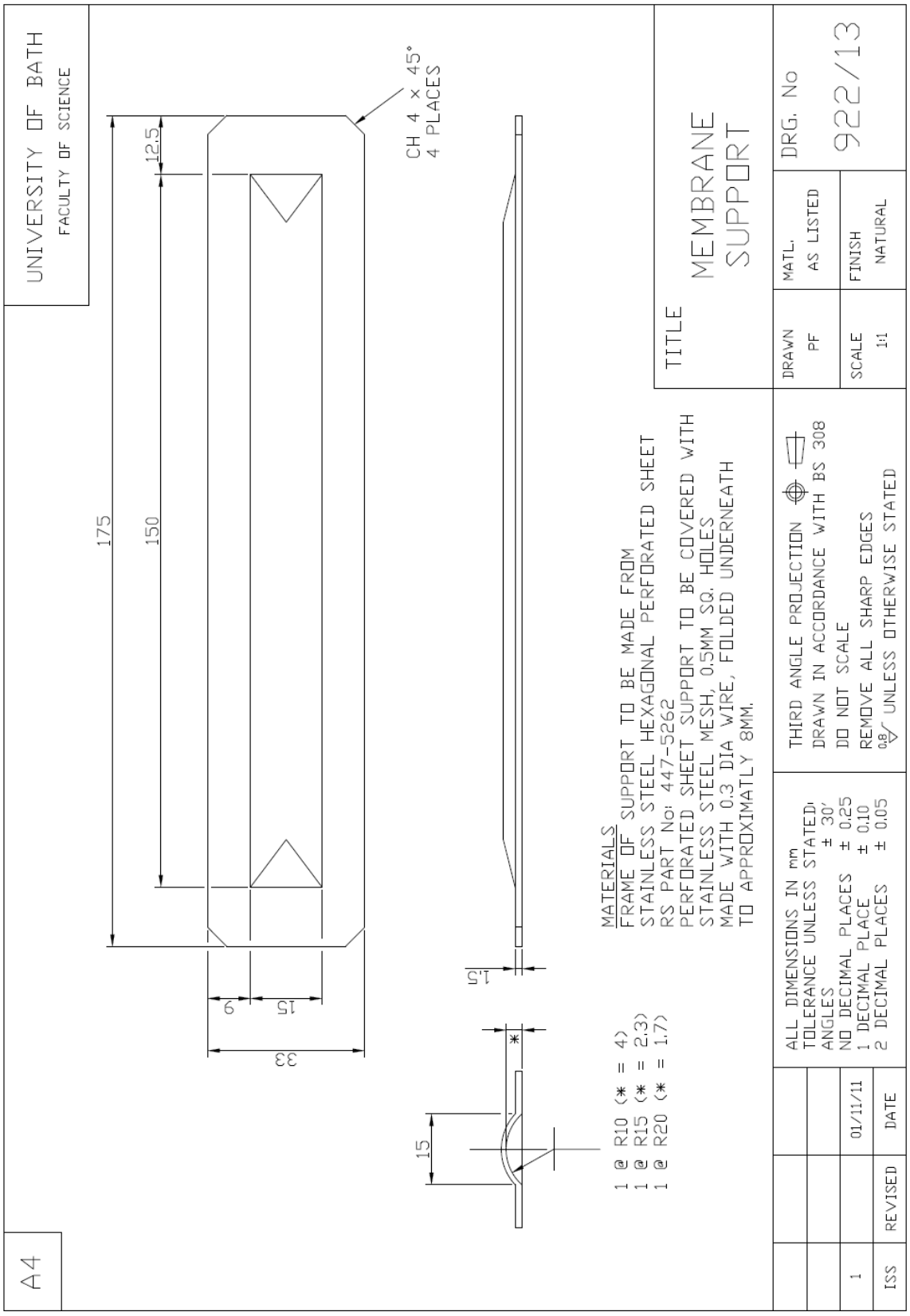

922/14: Flat membrane support

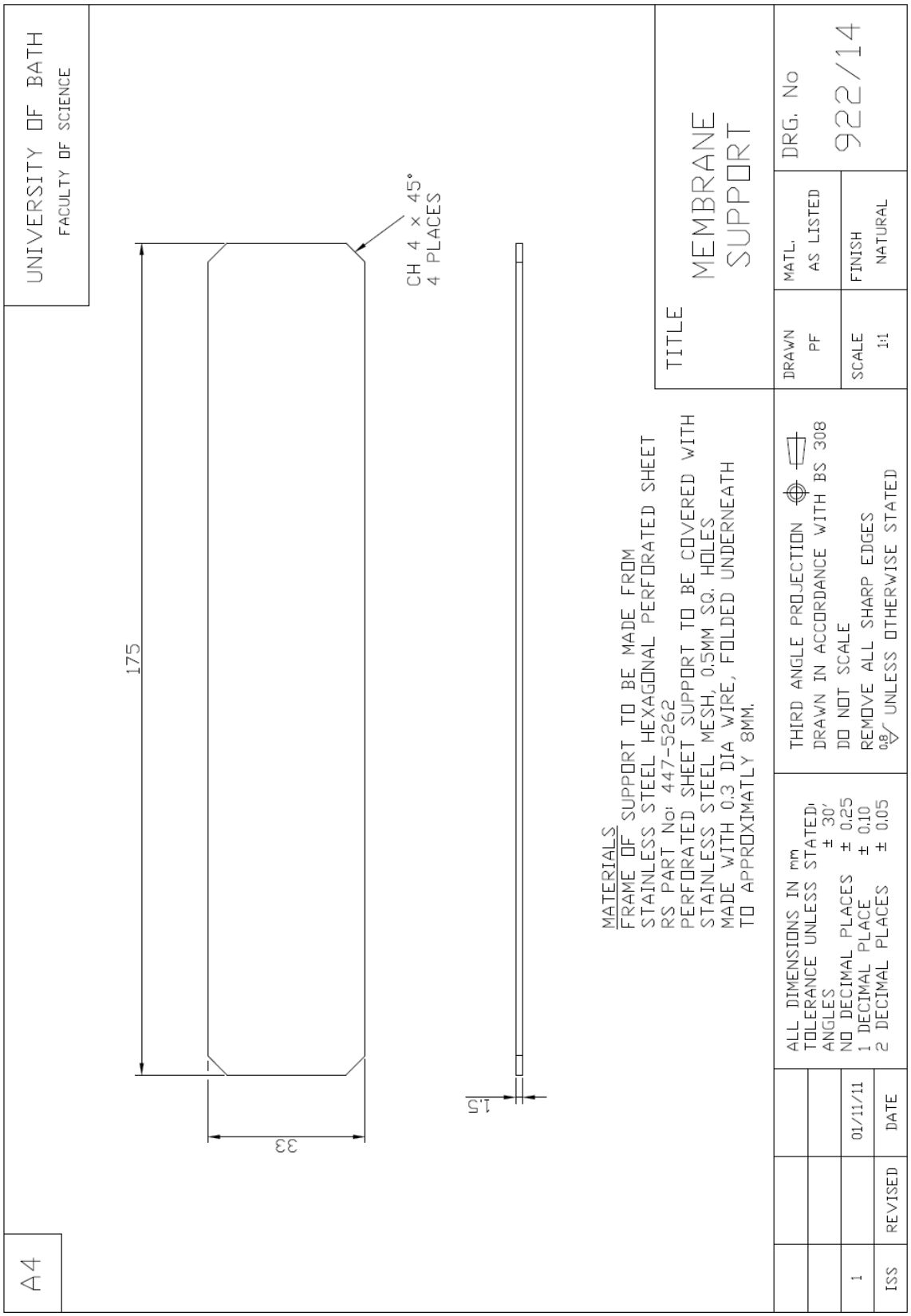

922/15: FDG gauge

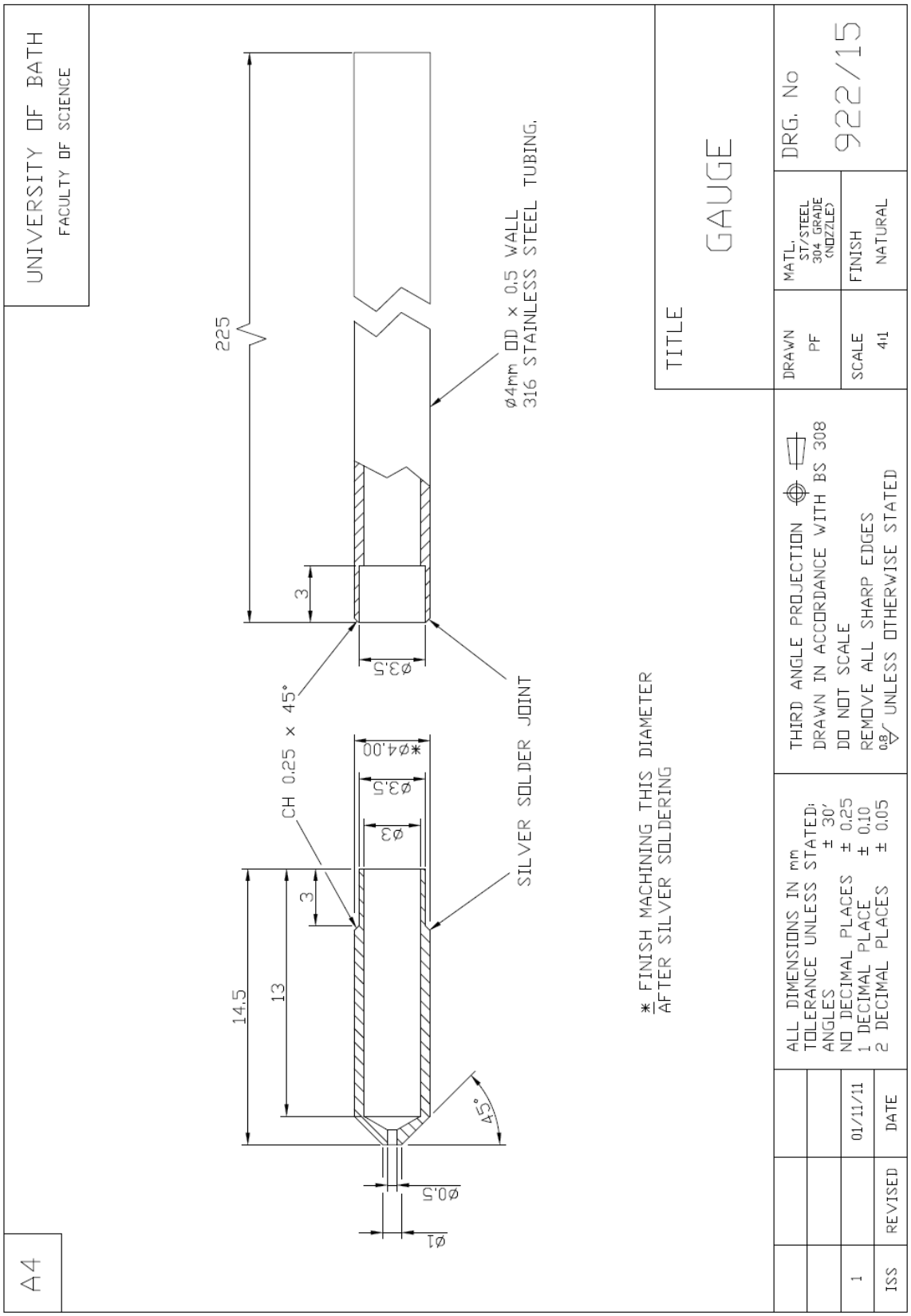

922/16: FDG tube clamp part A

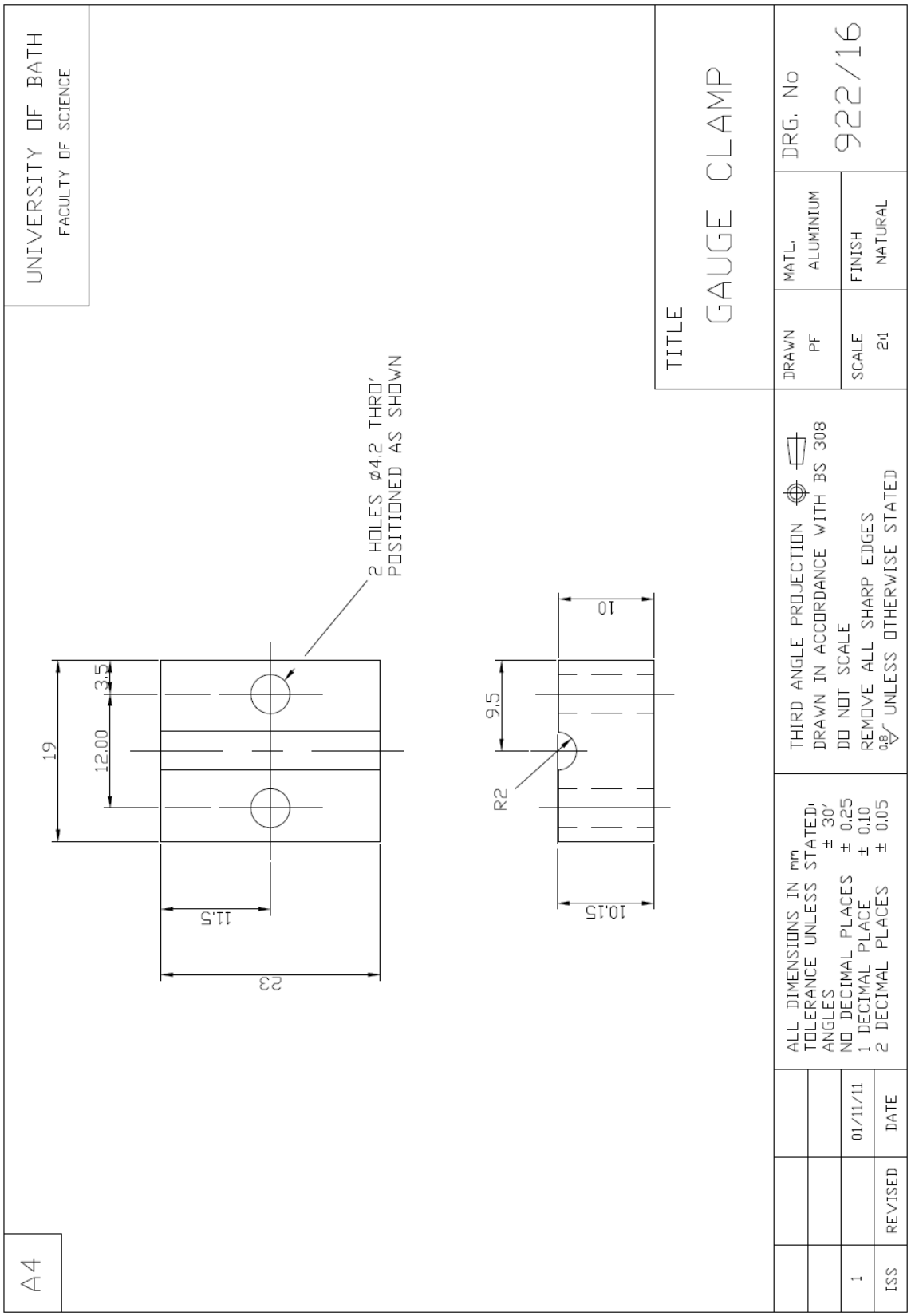

922/17: FDG tube clamp part B

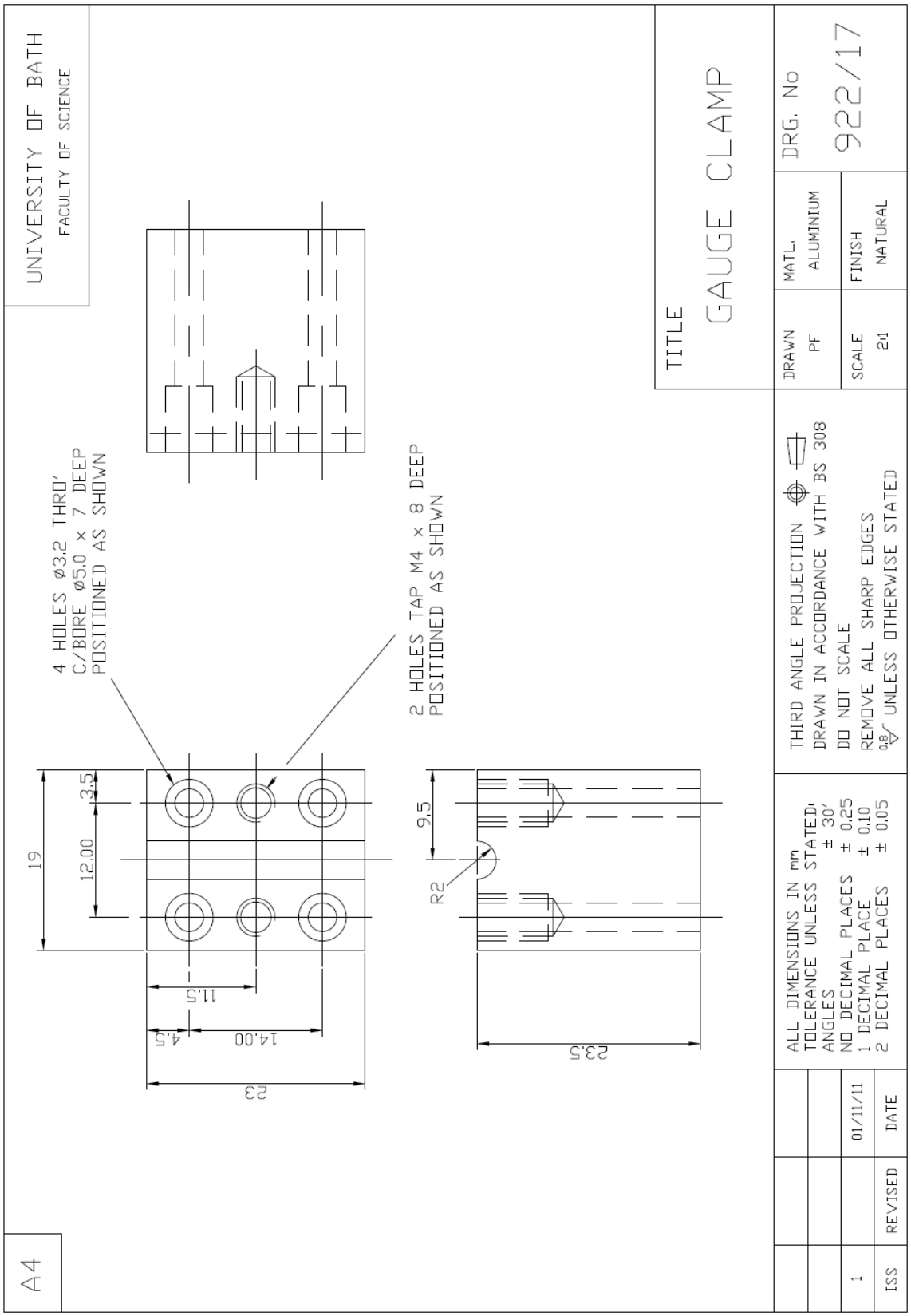

922/18: Fixing bracket for linear guide rail

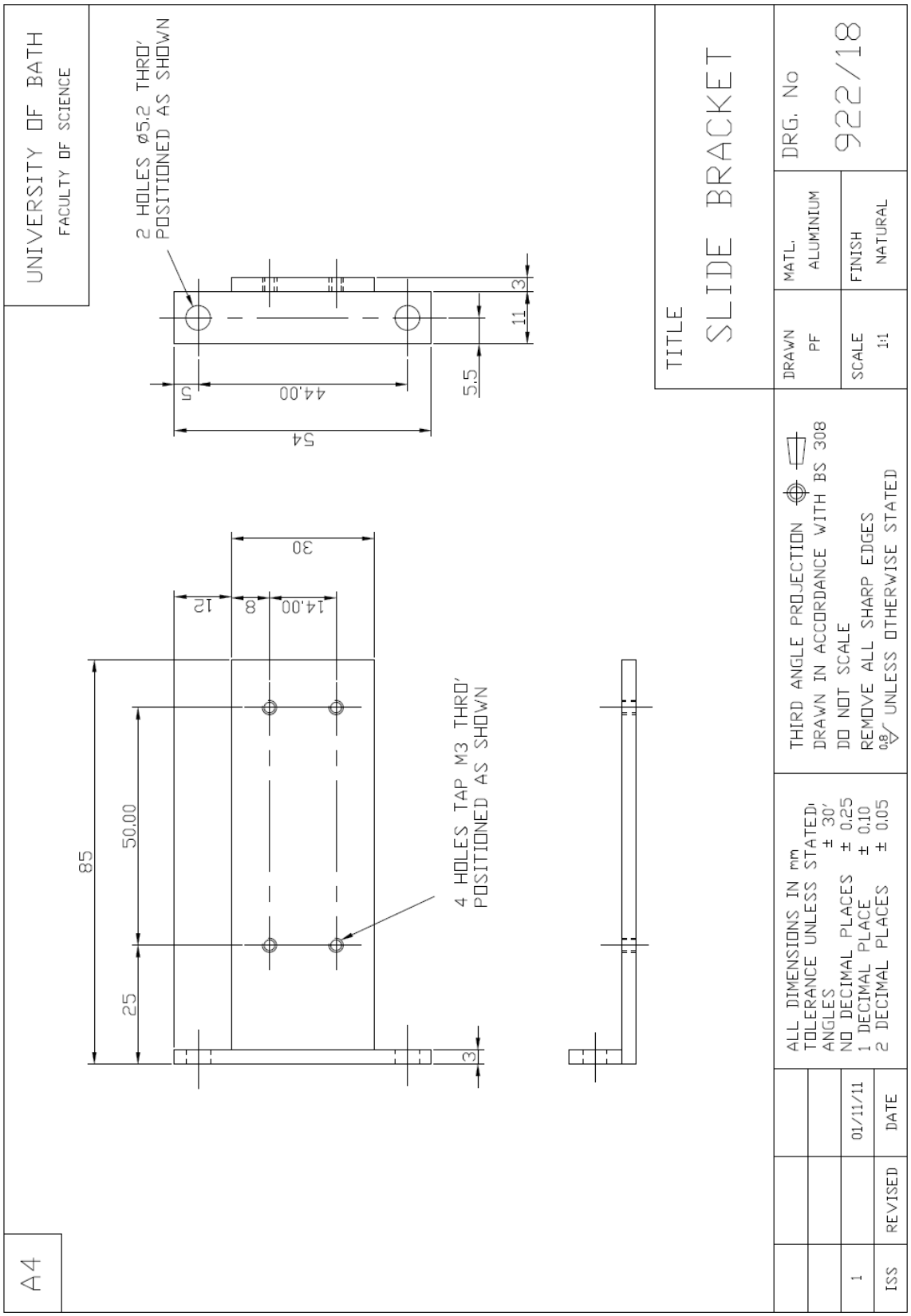

922/19: Cover plate for unused FDG tapping holes in test section

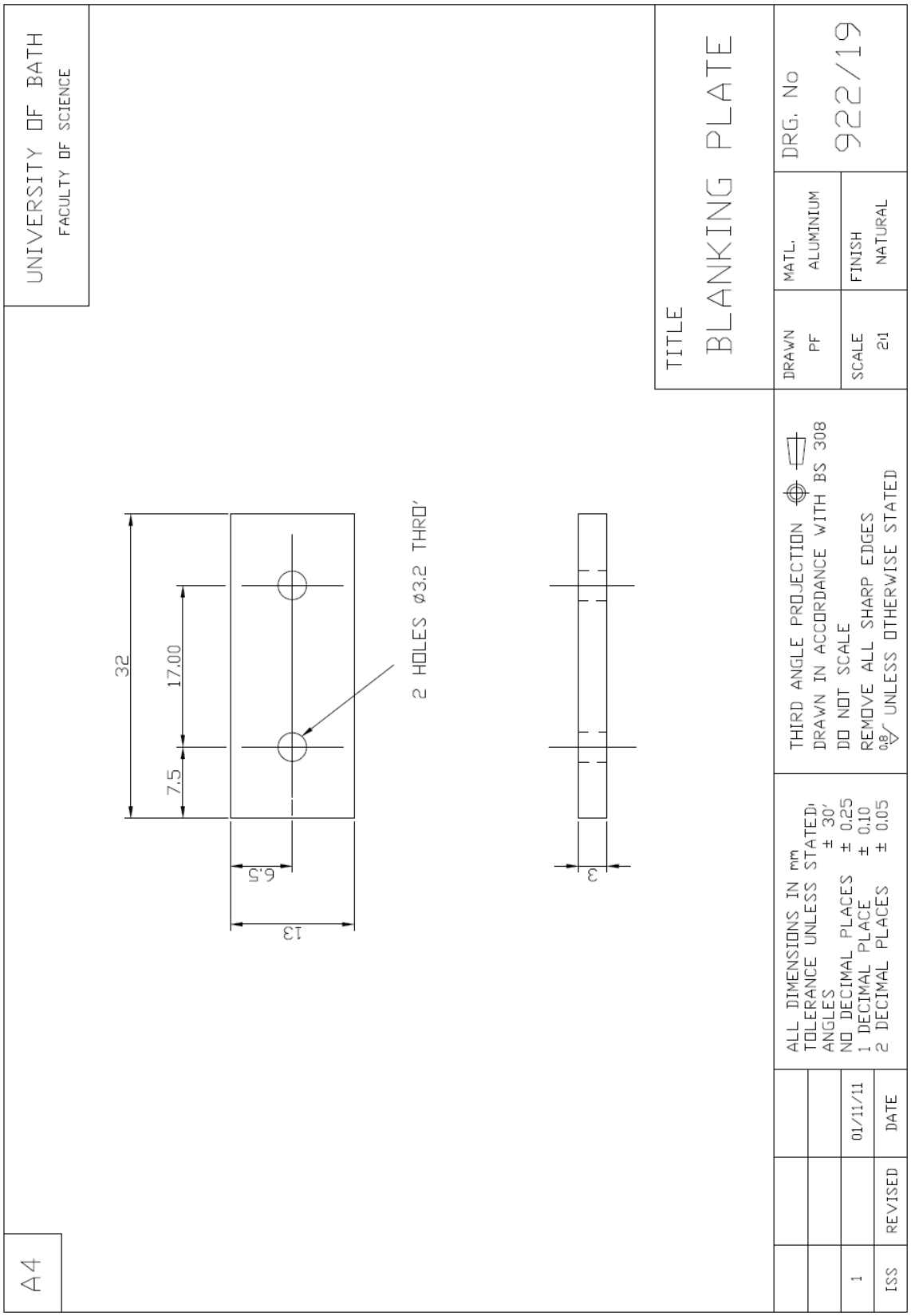

922/20: Sealing plate for FDG tapping point